NTNU
Norwegian University of
Science and Technology

Seismic Wave Attenuation in Partially Saturated Sandstone and AVO Analysis for Carbon Dioxide Quantification at Sleipner

Veronica Alejandra Torres Caceres

Petroleum Geosciences
Submission date: June 2017
Supervisor: Alexey Stovas, IGP
Co-supervisor: Bastien Dupuy, SINTEF Petroleum Research

Norwegian University of Science and Technology
Department of Geoscience and Petroleum

ABSTRACT

Sleipner field (North Sea) is the first largest CO_2 storage site, where the Carbon Dioxide is reinjected into the Utsira Sandstone. The main aim of this work is to obtain an estimate of the CO_2 saturation by using AVO techniques. Some other effects responsible for the energy loss, amplitude reduction and phase shift of the wave due to scattering and intrinsic attenuation, might mislead quantitative results if they are not considered. In order to account those effects. The study of reflection and transmission coefficients for elastic/elastic and elastic/viscoelastic models are performed. Secondly, several attenuation models are simulated increasing their complexity from a three layers model with a thick partially saturated sandstone (viscoelastic and poroelastic) embedded into shales, to a 28 layers model of sandstones with variable thickness and CO_2 saturations interbedded with thinner shales. Results show that viscoelastic and poroelastic sandstones are equivalent to elastic ones. Therefore, attenuation effects can be neglected. Elastic AVO analysis is carried out using the OptAVO tool. First, a feasibility study is performed based on well log and rock physics information, where three different fluid distributions are tested using Biot's theory and Brie's equation (e exponent equal to 1, 5 and 40). Then, the AVO inversion is performed via least squares fitting of the seismic amplitudes with the optimal reference curves. As expected, the AVO results are strongly influenced by the type of fluid distribution. For instance, patchy saturation (e=1) shows the highest saturations levels, while an average mixing law (e=5) suggests much lower saturations. The CO_2 estimation ambiguity from the elastic reflectivity results need to be addressed in the future and better constraints must be included into the modeling stage in order to mitigate it.

DEDICATION

To my lovely family: my mom, dad, brother and Nucita.

ACKNOWLEDGEMENT

First of all, I would like to give my deepest appreciation to my Supervisor Alexey Stovas, for his encouragement to go out of my comfort zone, since he believed and thrusted on my capability to discover and find the proper pathway by my own. I really appreciate his valuable comments and right directions to improve this work. In the same way, I want to express my gratitude to him for his patient and encouragement to research.

I would like to express my sincere thanks to SINTEF Petroleum (Geophysical Department) for the opportunity to be part of their team and collaboration in order to make this project possible, by providing me with the data, tools, new ideas and guidance. I would like to gratitude especially to my co-supervisor Bastien Dupuy for all his interesting ideas, relevant suggestions and discussion during meetings, enthusiasm and valuable feedback in order to improve this work. In the same way, I would like to thank Etor Querendez for his support, always friendly willing to collaborate and his guidance.

Furthermore, the full wave propagation numerical simulations were possible with the collaboration of Stéphane Garambois, Michel Dietrich and Louis De Barros, who developed the FORTRAN code in the Laboratoire de Geophysique Interne et de Tectonophysique, Université Joseph Fourier and CNRS in Grenoble France. My sincere gratitude to them for allow us to use their code for academic purposes

I am thankful to my family for all their support during all my career and encouragement to move forward in all aspect of my life. I really appreciated their love and the example they have given me from where I always found inspiration and motivation.

Finally, I want to say thanks to all my new friends and my flatmates, for making these two years such a nice experience from different points of view and make my state in Norway great.

Table of Contents

List of Figures

Figure Number Page

List of Tables

Table Number Page

Chapter 1 Introduction

Nowadays, more attention is focused on the environmental impact of industrial activities, therefore several projects in Carbon dioxide capture and storage (CCS) are running, in order to reduce the gas emissions to the atmosphere. Saline aquifers are known as an excellent and suitable reservoir to carry out these storage activities, because of their large scale volume and common occurrence in nature. The first industrial scale CO_2 sequestration project was launched in 1996 at the Sleipner gas field in the Norwegian North Sea. From its natural gas production, millions of tons of CO_2 has been separated and reinjected into the Utsira saline aquifer at an average rate of one million tons per year.

Monitoring of these kind of activities could be a challenging task that must be carried out carefully due to its environmental implications. Indeed the goal of this procedure is to assess the injection process, detect and prevent CO_2 leakage and obtain a better understanding of CO_2 migration patterns. Several technologies are developed and applied to achieve this goal, which will be briefly mentioned hereafter.

For the specific case of oil industry activities, during a field production, the changes in fluid saturation and pressure produce changes in the seismic reflection properties. This effect is a key factor for applying what is known as time-lapse reservoir monitoring or 4D seismic. That is the process of acquiring repeated surveys through time, to detect changes in the fluid flow within a production reservoir (Lumley, 2001). 4D seismic technique has been widely used for reservoir monitoring purposes, because the variation in amplitude and time shift among the different seismic vintages is large enough to obtain some estimates of velocity and thickness changes over time (Ghaderi and Landrø, 2009). However, there are some limitations associated to the properties of the host material (reservoir). For instance, in a low porosity and low permeability rock the changes in CO_2 levels are not detectable as is the case of the carbonate reservoirs in McElroy field west Texas, which was studied by Wang et al. (1998).

On the other hand, Amplitude Versus Offset or Amplitude versus Angle (AVO/AVA) techniques are capable to detect slight changes in the seismic properties for a stiff rock (low porosity and low permeability limestone, for example) that has been flooded by CO_2. That is the reason why AVO is a good alternative method, due to its higher sensitivity to determine both the presence and level of CO_2 saturation in the reservoir (Brown et al., 2007). In addition, by using empirical formulation.

Landrø (2001), has shown that AVO attributes can help to discriminate between pore pressure and saturation effects. A real case study was carried out in the Weybur-Midale Field in southeast Saskatchewa, where an AVO inversion for Time-Lapse data was implemented, and the difference in intercept and gradient allowed the quantification of CO_2 saturation and pressure changes in the reservoir (Gao and Morozov, 2011).

Several studies have been done in order to quantify the CO_2 injected into the Utsira formation. For instance, a post-stack stratigraphy inversion applied to 1994 and 2006 vintages by Delépine et al. (2011), which shows a 3D P-wave impedance volume where the low values follow the stratigraphy configuration of the CO_2 interpreted layers. Model driven pre-stack seismic inversion has also implemented, from where it was possible to extract S-wave impedance volume in addition to P-wave impedance, those also represent pretty well the areas with the CO_2 has been accumulated. However, a definitive quantification of the CO_2 is still a matter of discussion, since they found that a given rock physics model in areas with medium to high saturation present the same range of impedance that those accumulations at the upper part of the plume, where is expected to find the highest saturations (Clochard et al., 2010). Other seismic techniques have been applied to constrain the uncertainty regarding the ability to quantify the gas accumulations, for instance, spectral decomposition by using Wigner-Ville Distribution (WVD) and Continuous Wavelet Transform (CWT) suggested an approximate temporal thickness of the thin CO_2 layers about 15ms and 6ms. Additionally, Chadwick et al. (2010) applied AVO optimal tools to estimate the thickness of the CO_2 layers and analyze the tuning effect due to the thin layers below the seismic resolution. They found that the real data from Sleipner inside the CO_2 plume is consistent with the modeled curves corresponding to a thickness range from 1 up to 20m as the most likely ones. Layers whose thickness is greater than 7.5m cannot be distinguished from the thinner layers, since their reflection coefficients response starts to overlap (Chadwick et al., 2010).

Although, the work done by Ghosh et al. (2015) is one of the most recent published in terms of quantification of the CO_2 plume, the estimations in P-impedance results from post-stack inversion were carried out in 2001 seismic vintage, which corresponds to 5 years after the injection process started. Due to the high level of uncertainty regarding how the gas is being allocated into the pore space the assessment was done for each distribution (patchy and uniform) through a dual porosity model that accounts for the viscoelasticity effects and a pressure-dependent differential effective medium (PDEM). They concluded that the most likely concentration of CO_2 is around 20 to 80% and it is dependent on the fluid distribution type. For instance, the highest saturations are associated to patchy distribution and lower saturation corresponds to uniform distribution. (Ghosh et al., 2015).

Besides the attempts to quantify the amount of CO_2 that has been injected into the saline aquifer, other researchers have pointed out the possible impact of intrinsic attenuation due to mesoscale heterogeneities into the porous medium. This could have an important effect that might influence the amplitude analysis and lead to erroneous quantification and interpretation if it is not addressed properly. (Carcione et al., 2006a, Germán Rubino and Velis, 2011, Rubino et al., 2011). Carcione et al. (2006) simulated numerically a simple model for the Utsira formation, where the saline aquifer is presented as visco-poroelastic reservoir and the overburden, inter-layers and underlying shales are assumed to be elastic. In this case, Carcione accounted for the attenuation at mesoscale by using White's model (1975) of patchy saturation, whereas the viscoelasticity is introduced by generalized solid/fluid coupling complex modulus to relaxation functions (Zener model). In this work, he showed that it is possible to have high levels of attenuation into the seismic frequency range (30 Hz). In this case, the attenuation peak was found at 80% CO_2 saturation.

De Barros (2008) also analyzed the behavior of the possible attenuation simulating the wave propagation via reflectively theories develop by Garambois and Dietrich (2002). In his research, the geological poroelastic properties were taken from Carcione et al. (2006), but in this case the Utsira formation was simulated as poroelastic medium to investigate the influence of the CO_2 in the slow P-wave (Biot wave) among other sensitivity analysis as a function of the poroelastic properties.

Previous work (Torres, 2016) shows that even though the quality factor for an anelastic partially saturated rock is quite large, this might have some significant impact in the amplitude response at zero offset in time domain. In the same way, it was shown that this anelasticity effects for the simulated Utsira sand are independent of the fluid distribution model (either patchy model by White (1975) or the effective fluid average by Brie et al. (1995)). Based on these results, some simulation cases are run to investigate the effects of viscoelasticity and poroelasticity within a medium when a seismic wave is propagated through it. In order to do this, firstly the evaluation of the reflection and transmission coefficients as a function of incident angle from two half-space in a perfectly elastic and anelastic case are estimated and analyzed. The anelasticity is introduced through partial saturation at mesoscale heterogeneity into the porous media, whereas the viscoelasticity is introduced by a constant quality factor, regardless the physical mechanisms that induced it. Secondly, a full wave propagation through simple conceptual model of three layers is tested for elastic/elastic and elastic/viscoelastic interfaces. For more realistic cases of periodically layered medium as it is the Utsira sandstone an elastic/elastic, elastic/viscoelastic and elastic/poroelastic cases are investigated. Similarly, a zero offset response in the frequency domain for the more realistic case is carried out for comparisons, since as it was presented by Stovas and Roganov (2010) the difference between purely elastic and anelastic reflection and transmission response (R/T) in time and frequency domain could differ. The outcome of this work could give us an insight about whether or not the dispersion and attenuation effects for the Sleipner case under poroelasticity theory could have an important impact on the AVO response.

Additionally, it was shown that AVO attributes ability to discriminate different lithofacies such as shales, brine sands and partially saturated sands (CO_2 – brine) can be successful or not, depending on the type of fluid distribution model that is considered. For instance, a saturation modeled by the effective fluid equation from Brie e=5 does not distinguish between brine sands and 5% CO_2 saturated sands. The contrary occurs with the patchy model of White (1975). For higher CO_2 saturation above 60%, both models give the same results without being able to discriminate among sandstones within this range (Torres, 2016). Based on this findings the main purpose of this study is to apply an Optimal AVO inversion to a real data set from the Sleipner field with the aim of having an estimation of the CO_2 saturation that can be compared with rock physics inversion and Full Waveform Inversion results. For this purpose, 2 seismic sections, one across the injection point (Inline 1838) and another one where a current FWI approach is being applied (Inline 1880) are selected from 2008 seismic vintage. Similarly to previous work, three possible fluid distribution are modelled with Brie's equation to analyses their impact in the quantification of CO_2. Then from the AVO inversion it is possible to obtain 2D sections of acoustic impedance, shear wave impedance and density reflectivity for qualitative interpretation purposes.

The outline of this work starts out by presenting the geological settings of the cap-rock shales (Norland Group) and the Utsira formation followed by theoretical concepts regarding attenuation mechanisms, zero offset reflectivity, full wave propagation through a poroleastic medium, rock physics models, reflection and transmission coefficient and Amplitude Versus Offset (AVO) technique. Those are presented in Chapter 3 and Chapter 4, respectively. Afterwards, all the procedures and considerations for both, attenuation models and real data AVO applications are described in Chapter 5. Results and discussion are presented and finally the most important remarks and conclusions are summarized.

Chapter 2 Geological Settings

The following chapter presents the location and a brief description of the study area, as well as, the most important geological aspects. The main focus is to point out the most important characteristic for the saline aquifer of Utsira Formation and its cap-rock shale, which is well-known as the Nordland Group Shales.

The area of study is the Sleipner gas field, which is located in the Norwegian North Sea (block 15/9). This field is at the west of Stavanger area, whose coordinates are between 58° 15’ and 58° 40’ N and 1° 40’ and 3° E in latitude and longitude, respectively (see Figure 2.1). Sleipner field has been divided as Sleipner east and west. Both are currently producing gas and light oil from a reservoir sandstone located at about 2300m depth. As a part of the first CO_2 sequestration project, from its hydrocarbon production, millions of tons of CO_2 have been captured and reinjected into the shallower Miocene-Pliocene Utsira sand in which the CO_2 has migrated upwards mainly driven by buoyancy.

As a result of the CO_2 migration, eight amplitude anomalies have been observed by seismic time lapse allowing the interpretation of very thin interlayer shales, previously detected only by well log data. However, before the injection process, these layers were not identified in seismic survey, since their thickness (1-3m approximately) is under the seismic resolution. So far, there are no evidences of CO_2 migration beyond the top of Utsira sandstone, hence the injected gas is being trapped by the shale dominated Nordland Group (Zweigel et al., 2000).

2.1 Nordland Group Shales

In general the cap-rock shale above the sand wedge is in average several hundred meters thick. Its lower and upper Pliocene parts, have been subdivided into three subunits from top to bottom, according to seismic data and well log information (Zweigel et al., 2000).The subdivision is presented as follow and is shown in Figure 2.2.

- The upper Upper Pliocene is characterized by its high to regular seismic amplitude, as well as, high density, resistivity and compressional velocity compared with the underlying and overlaying sequences. This unit is locally seen in the central part of the basin. Around Sleipner area, it reaches a thickness of 70 up to 100m (Bøe and Zweigel, 2001).

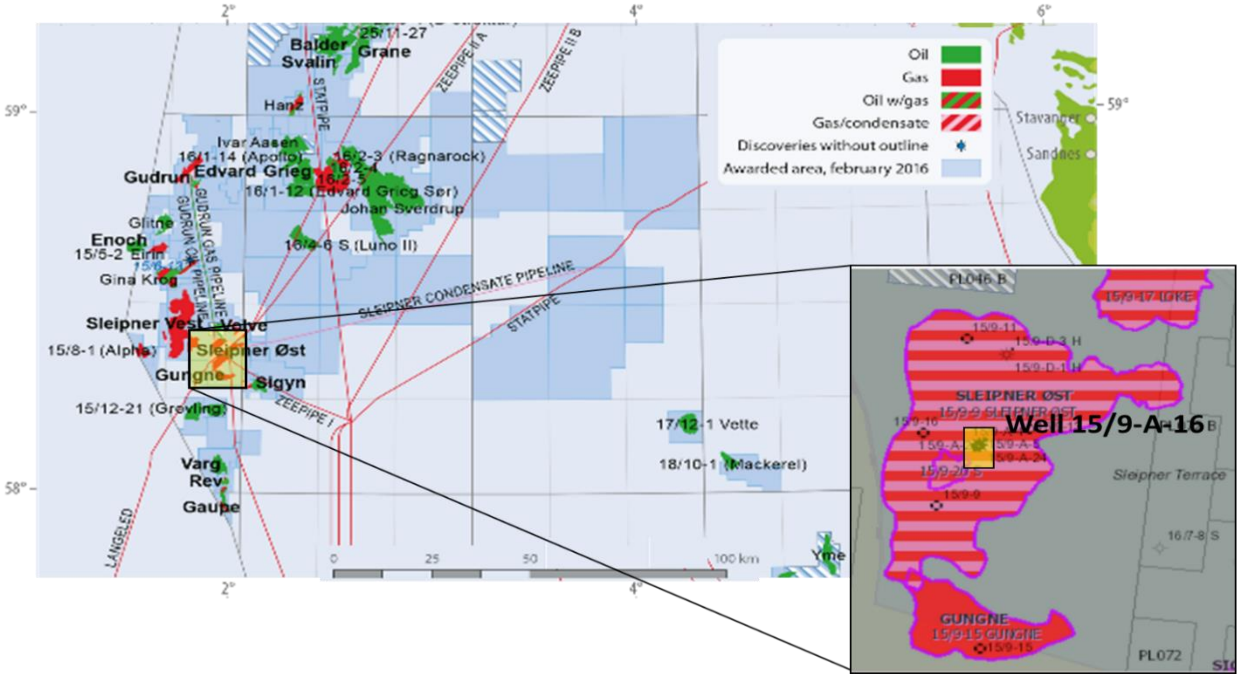

Figure 2.1: *Location of the Sleipner Field in the Norwegian North Sea. Sleipner East field is indicated by the yellow rectangle. A Zoom view with the location of the Injection Well 15/9-A-16 is also shown. Modified from The Norwegian Petroleum Directorate (NPD).*

- The middle upper Miocene presents mostly parallel reflectors and increasing downwards density, resistivity and compressional velocity. This unit is part of the basin-ward prograding sediment wedge, whose thickness is around 100 to 150m in the Sleipner area (Bøe and Zweigel, 2001).
- The Lower upper Miocene is also known as the shale drape that is overlaying the Utsira sandstone. The shale drape shows parallel seismic reflections in both the basin center and towards the basin margin. This unit has a thickness of 50m and is located above a sand wedge or above the top of Utsira, where this wedge is absent (Bøe and Zweigel, 2001).

According to Chadwick et al. (2004) the upper most unit (Upper Seal) is mostly composed by glacial-marine shales and tills of Quaternary.

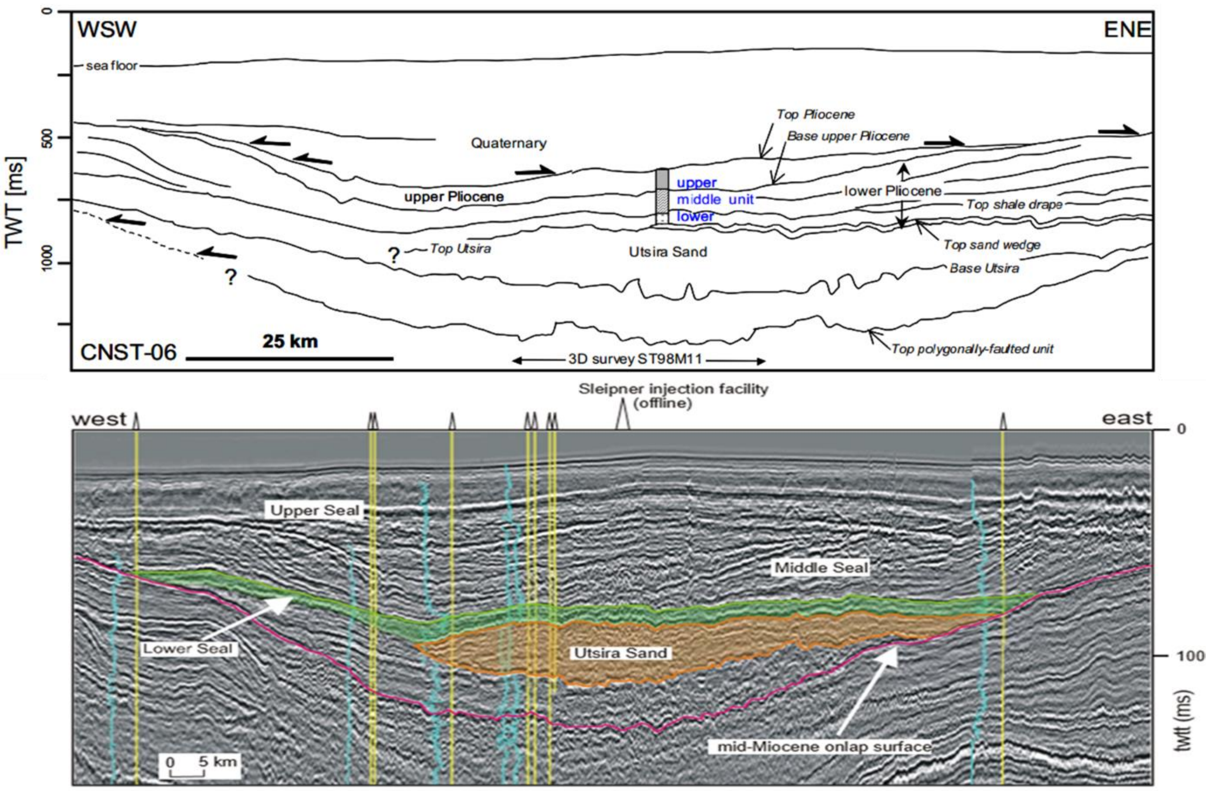

Figure 2.2: *West - East regional seismic line (TWT) through the North Sea. Top: geological section across the Sleipner area based on the seismic line CNST82-06, from (Zweigel et al., 2000). Bottom: seismic section, illustrating the stratigraphy and structural configuration of the Utsira Formation and its cap-rock shale. Sleipner injection well location is also shown. From (Chadwick et al., 2002)*

Regarding the mineralogy composition of the Nordland Group several studies reveals that the samples are clay silts or silty clays rich with an average composition of quartz (30%), mica (30%), kaolinite (14%), chlorite (1%), potassium feldspar (5%), smectite (4%), calcite (4%), albite (2%), pyrite (1%) and gypsum (1%). From XRD results it was determined that this unit shale has a capillary pressure entry of about 2 and 5.5MPa., therefore is able to trap a CO_2 column height between 637 and 1833m approximately. According to these results it has been stablished that the leakage of CO_2 through the pore network is quite unlikely (Kemp et al., 2001).

Furthermore, the porosity measurement of several samples from wells located in the UK side of the Nordland Group show a very poorly porous system with limited volume of micro porosity. This micro pores only represent a few percent of the total rock volume and they are also poorly connected to each other. This result supports the unlikely leakage of the CO_2 via pore network.

However, other mechanisms should be taken into account, for instance fractures within the cap-rock (Kemp et al., 2001).

2.2 Utsira formation

The Utsira formation is defined as the lower part of the Nordland Group, which is characterized as a thick sandy unit at the base and a shale unit above. In the Sleipner area only the sandy unit is present that is referred as Utsira sand (Lothe and Zweigel, 1999).

The Utsira formation is a late Cenozoic post-rift succession of the North Sea, whose extension area is more than 26000km^2. Its eastern and western limits have been described as stratigraphic onlaps. This formation varies its grain size, being finer towards the South-West, away from the Norwegian continental margin. Northwards, the Utsira sandstone presents very complex depositional patterns, with some isolated depocenters and some areas of non-deposition (Chadwick et al., 2004).

The top of the Utsira sandstone shows a distinctive horizon that is described by a gradual upward increasing of the gamma rays values, since it delineates the transition from the sandy units to a shale units of the Nordland Group (Lothe and Zweigel, 1999).It varies gently in depth from 550 to 1500m, showing a general dip towards the South and South West. Near the Sleipner field, it is found mainly around a depth of 800 and 900m (Chadwick et al., 2004).

In contrast, the base of the formation presents an abrupt change of the gamma ray values decreasing upwards. This trend indicates the separation between the sand body and the underlaying shales of the Hordaland Group. The depth registered for the base of the Utsira Formation varies from 1020 to 1112m. In the same way, this shows a preferential dipping direction towards the South. In addition, the base topography is considered much more complex than the top, since it has been affected by mud diapirism. The mud diapirs have been interpreted as the result of reverse faulting that has not affected its upper part and most importantly, the cap-rock shale (Lothe and Zweigel, 1999).The thickness of the Utsira formation varies along with the localized depocenter or depression of its base. As a general trend this unit is thickening towards West (Lothe and Zweigel, 1999). For instance, towards the south the maximum thickness is around 300m (near Sleipner) and further North, it is around 200m (Chadwick et al., 2004).

From well log information, the gamma ray and resistivity shows a blocky pattern with low gamma ray values and several peaks and intervals of high readings. These have been interpreted as mica, clays and some glauconitic presence in the sandstone. The thinner intra-reservoir clays layers, have thickness that typically range from less than 1 up to 3m (Zweigel et al., 2004). In general, these peaks also correspond to high resistivity peaks that are seen in the upper and lower shales from the Nordland and Hordaland Group, respectively (Figure 2.3). Moreover, it is possible to see a thick mudstone layer of about 5-6m thick just beneath the top of the Utsira Formation. This mudstone layer separates the main part of the sandstone from an eastward thickening sand wedge (Zweigel et al., 2004).

The depositional environment for this formation is still field of research, since several authors have proposed different models. Some of these model are presented as follow, the tidal sand ridges complex by Rundberg (1989), the geostrophic-induced contourites by Galloway (1997) and turbidites by Gregersen et al. (1997). The latter suggestion correlates quite well with the result from core analysis studies, since those pointed out that there is almost not sign of planar structures rather chaotic deposition process as turbidites prevail (Lothe and Zweigel, 1999).

When it comes to the evaluation of the physical properties of this reservoir, it is well-know that the Utsira sand has a favorable porosity and permeability which make it suitable as a large scale multisite disposal. The reservoir characteristic information is taken from core analysis and cuttings. These reveal that grains size is in general fine and uncemented, with presence of some medium to coarse grains. The grains are mainly composed of quartz. Nevertheless, other minerals are also present in the rock, such as feldspar, shell fragments (calcite), mica, and albite, among others. Regarding the reservoir quality based on porosity and permeability measurements, the former shows values between 31 and 42%. These are also supported by laboratory measurements and log data, whose ranges go from 35 to 42,5% and 35 to 40%, respectively. The measured permeability range is between 1-3 Darcy (Chadwick et al., 2004).

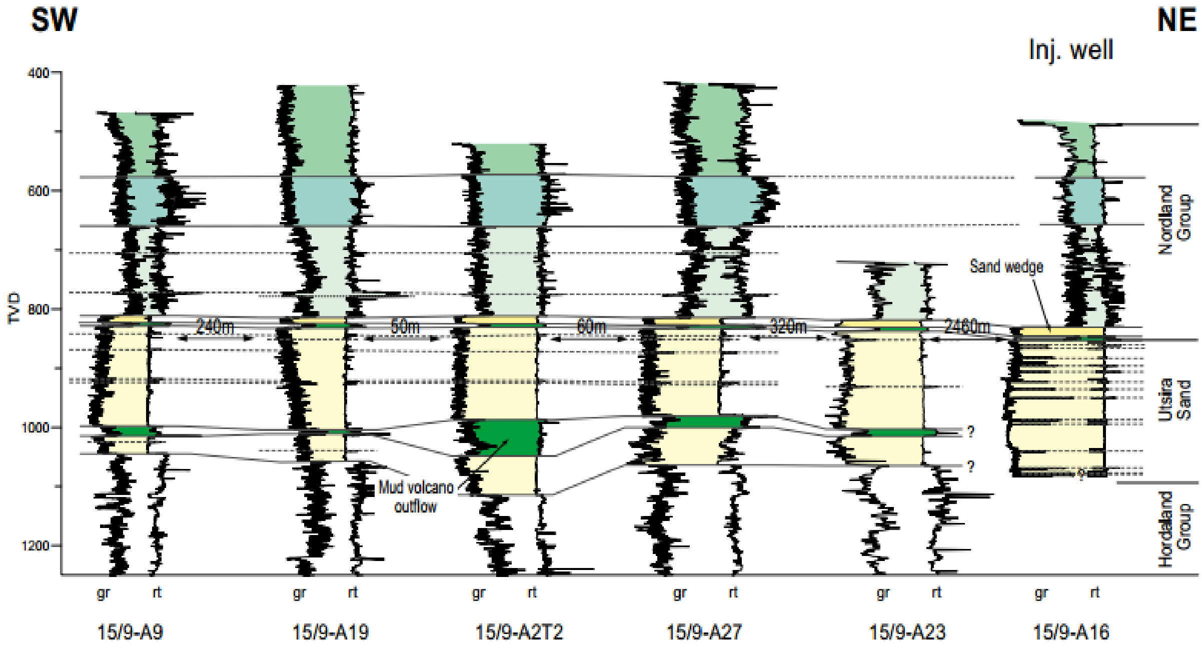

Figure 2.3: *Well cross-section near the Sleipner injection facility, whose orientation is southwest-northeast.The thin interlayer shales into the Utsira sandstone can be correlated locally. A thick shale unit below the Utsira Formation varies drastically in thickness corresponding to the interpretation of mud volcano outflows. The distance among wells is indicated at 850m true vertical depth (TVD). From (Lothe and Zweigel, 1999).*

Chapter 3 Seismic Attenuation–Wave Propagation Theory

This Chapter presents a brief description of some theoretical fundaments that support the work. It starts from some insight regarding attenuation, how this phenomenon has been modelled and incorporated through the wave propagation. Then different mechanisms that can cause attenuation mainly at mesoscale are mentioned. Finally, the governing wave equation for a poroelastic medium presented in Biot’s theory, along with some rock physics models that take into account mesoscale heterogeneities are described.

3.1 Seismic viscoelastic attenuation

The seismic waves’ amplitude decrease rapidly when its distance from the source point increases. Knowing the way this amplitude decay occurs, how fast and how this dependent on frequency is quite important in order to have some insight regarding the subsurface structure. In addition, they will have an impact on the amplitude based interpretation from a quantitative point of view (Cormier, 2011).

There are three main mechanisms responsible for the amplitude attenuation, such as geometrical spreading, intrinsic attenuation and scattering. The geometrical spreading can be defined as the energy density reduction that occurs as a wave front expanses. For a homogenous and isotropic medium the geometrical spreading is simply proportional to the distance travelled by the body wave from the source to the receiver. However, in a more realistic model it is possible to assume strong variation of the rock properties with depth and less variation laterally, even though, these variation are considered the geometrical spreading can be computed in a simple way via ray tracing theory (Cormier, 2011).

Intrinsic attenuation refers to the energy lost due to heat and internal friction when a seismic wave travels to the medium. The intrinsic attenuation has different mechanism depending on the scale at which this is evaluated. For instance, the microscopic mechanisms have been described in several ways, as viscous and resistive properties of atoms in crystalline lattices, movement of fluids between grain boundaries and cracks and frictional sliding cracks (Cormier, 2011).

The scattering attenuation is described by the scattered elastic energy which is redistributed into different direction away from the receiver. Scattering phenomenon occurs when a wave front reach wavelength scale heterogeneities in the medium, producing reflection, refractions and conversion of the elastic energy. These irregularities are defined by discontinuities or rapid variation of the medium properties velocity and density (Cormier, 2011).

The earth is far from being a perfectly elastic medium, since the amplitude loss of a wave that travels through it, decays no only due to geometrical spreading or reflection and transmission of the energy at the interface, meaning that the wave can propagate infinitely. In contrast, the wave energy will be continuously diminishing due to the conversion of the elastic energy into heat because of the friction. As a consequence, an amplitude reduction and phase shift will occurs (Cormier, 2011).

3.1.1 Attenuation coefficient α.

When the internal configuration of the material particles depends on the stress applied is called anelastic material. This is the result of stress–strain applied by a wave propagating through the medium and irreversible deformations of the crystal defect structure occurs. In order to describe this phenomenon, the attenuation coefficient α and the quality factor Q are introduced as dimensionless quantities (Aki and Richards, 1980).

The absorption of wave energy is constant per cycle, so its decay can be described by an exponential function of the distance travelled. For a plane wave in a homogenous medium, the absorption is given by Equation (3-1), where A and A_0 is the amplitude of the wave at given distance and the initial amplitude, respectively, x is the distance and α is the attenuation coefficient (Sundvor, 1989)

$$A(x) = A_0 e^{-\alpha x} \ . \tag{3-1}$$

By rearranging Equation (3-1), it is clear that the attenuation coefficient depends on the medium properties

$$\alpha = -\left[\frac{\ln(A(x)/A_0)}{x} \right]. \tag{3-2}$$

3.1.2 Quality Factor Q

There are several expressions that describe the quality factor mostly depending on the parameters that are used to introduce the attenuation. However, its meaning is the same as the measure of how dissipative a material is.The larger the Q, the smaller attenuation will be and vice versa (Mavko et al., 1998). The attenuation is always accompanied by dispersion effects that are mainly related to the differences in the travel velocity for each individual frequency component of the wavefront. Dispersion must be taken into account along with attenuation, since the phase shift in the wave due to this phenomenon guarantees a causal arrival of the signal in the context of the linear theory (Futterman, 1981).

Linear theories are based on the fact that the amplitude dependence of the propagation velocity and Q at strains less than 10^{-6}, has not been observed yet, therefore this strongly suggests that the material response is mostly due to linear effects. In other words, the sum of strain that results from the application of each stress function individually is equivalent to the strain from a superposition of two stress functions (Kjartansson, 1979).

The quality factor can be expressed as the maximum energy stored during a cycle divided by the energy lost during a cycle or the amplitude displacement loss after a cycle (Kjartansson, 1979). Equation (3-3) where W denotes the original displacement and ΔW indicates the displacement change

$$Q = \frac{\Delta W}{2\pi W} . \tag{3-3}$$

The quality factor can be also expressed in terms of the attenuation coefficient α, where V is the phase velocity and f is frequency, as shown in Equation (3-4). Finally, it is possible to associate the quality factor with the phase angle *(δ)* between stress and strain as in (3-5) (Mavko et al., 1998).

$$Q \approx \frac{\alpha V}{\pi f} , \tag{3-4}$$

$$Q \approx \tan \delta . \tag{3-5}$$

Even though it is well know that the attenuation is a frequency dependent phenomenon that mainly results in the absorption and change in the shape of the wavefronts, several studies have shown that it is possible to model an attenuation factor frequency independent or nearly frequency independent within a specific frequency range (Kjartansson, 1979). One of the simplest attenuation theory is the Band limited Near-Constant Q (NCQ), developed by Kolsky (1956) and constant Q factor developed by (Kjartansson, 1979). Both theories are based on a linear viscoelasticity, causality and dissipative material.

For the Kolsky's model the wave dispersion is defined by the phase velocity presented in (3-6)

$$V_{(f,Q)} = V_0\left(1+\frac{1}{\pi Q}\ln\left(\frac{\omega}{\omega_0}\right)\right), \tag{3-6}$$

where the phase velocity depends on both frequency and quality factor, V_0 is the phase velocity at given reference frequency ω_0 and ω will vary along with the whole frequency band. Futterman (1981) shows that the selection of the reference frequency is free, as long as the phenomenological criterion that it must be small in compassion with the lower frequency evaluated is fulfilled (Futterman, 1981).

3.2 Zero Offset reflectivity in a stack of periodic layers

Ursin and Stovas (2002) and Stovas and Ursin (2003) derivated via numerical models the reflection and transmission response (R/T) for stack of periodic layers at zero offset. They concluded that these responses are highly dependent on the configuration of the layers, for instance the number of layers and their thickness. Later on, Stovas and Ursin (2007) analyzed the propagation of acoustic waves through a periodic layer medium by an eigenvalue decomposition of the propagator matrix. They found out that there are two parameters that mainly control the wave propagation such as the reflection coefficient and the ratio of one way travel time of the two parts of the cycling layered medium.

There are three regimes that can be recognized and analyzed in both the frequency and time domain. In a low frequency regime the periodic structure behaves as effective medium, the second regime is considered as transition zone and the third one at high frequency can be described by the time-average velocity. (Stovas and Ursin, 2007). This was also shown by Stovas and Roganov (2010) and Dupuy and Stovas (2016) by introducing additional effects as intrinsic attenuation due to mesoscale heterogeneities with different rock physics models, for instance standard linear solid from Carcione (2007) and Pride et al. (2005) poroelastic model, respectively. For both simulations the attenuation peak is located at higher frequency than the seismic bandwidth.

3.2.1 Multi-layer reflection and transmission response

The simulation of the reflection and transmission response for an acoustic P-wave the propagation matrix is computed for one cycle of two layers and is given by Dupuy and Stovas (2016) as

$$S_k(\omega) = \frac{1}{1-r^2(\omega)}\begin{pmatrix} e^{i\theta_1} & 0 \\ 0 & e^{-i\theta_1}\end{pmatrix}\begin{pmatrix} 1 & r(\omega) \\ r(\omega) & 1\end{pmatrix}\begin{pmatrix} e^{i\theta_2(\omega)} & 0 \\ 0 & e^{-i\theta_2(\omega)}\end{pmatrix}\begin{pmatrix} 1 & -r(\omega) \\ -r(\omega) & 1\end{pmatrix}. \tag{3-7}$$

The normal incident reflection coefficients at the interfaces and their corresponding phase factors are presented in Equations (3-8) and (3-9), respectively

$$r(\omega)=\frac{\rho_2 V_{P2}(\omega)-\rho_1 V_{P1}}{\rho_2 V_{P2}(\omega)+\rho_1 V_{P1}}, \tag{3-8}$$

$$\theta_1=\frac{2\pi f d_1}{V_{P1}}=2\pi f t_1 \text{ and } \theta_2(\omega)=\frac{2\pi f d_2}{V_{P2}(\omega)}=2\pi f t_2(\omega). \tag{3-9}$$

The parameters related to layer 2 are frequency dependent, because of the intrinsic attenuation. The wave propagation travel-time of each layer are represented by t_1 and $t_2(\omega)$ and they are expressed as $t_k=d_k/V_k$ being ω and f the pulsation and the frequency, correspondingly. Finally the propagation matrix elements are given in Equation (3-10)

$$\begin{aligned}
S_k(\omega)&=\begin{pmatrix} a_k(\omega) & b_k(\omega) \\ c_k(\omega) & d_k(\omega)\end{pmatrix},\\
a_k(\omega)&=\frac{1}{t_1 t_2(\omega)}\left(e^{i(\theta_1+\theta_2(\omega))}\left(1-r^2(\omega)e^{-2i\theta_2(\omega)}\right)\right),\\
b_k(\omega)&=\frac{1}{t_1 t_2(\omega)}\left(-re^{i(\theta_1+\theta_2(\omega))}+r(\omega)e^{i(\theta_1-\theta_2(\omega))}\right),\\
c_k(\omega)&=\frac{1}{t_1 t_2(\omega)}\left(re^{i(\theta_1-\theta_2(\omega))}-r(\omega)e^{i(\theta_1+\theta_2(\omega))}\right),\\
d_k(\omega)&=\frac{1}{t_1 t_2(\omega)}\left(e^{-i(\theta_1+\theta_2(\omega))}\left(1-r^2(\omega)e^{2i\theta_2(\omega)}\right)\right).
\end{aligned} \tag{3-10}$$

Due to the periodicity of the layers the final response from several cycles can be easily computed by multiplying the propagation matrix for one single cycle by itself *m* times, where *m* is the total number of cycles

$$S_m(\omega)=\prod_{k=1}^{m}S_k(\omega)=\begin{pmatrix} a_k(\omega) & b_k(\omega) \\ c_k(\omega) & d_k(\omega)\end{pmatrix}. \tag{3-11}$$

The last step involves the computation of the R/T response in frequency domain by using the mathematical expression given in Equation (3-12)

$$t_D(\omega) = \frac{1}{d_m(\omega)}, \qquad r_D(\omega) = \frac{b_m(\omega)}{d_m(\omega)}. \tag{3-12}$$

The energy loss of the wave can be estimated by

$$E = 1 - \left|t_D(\omega)\right|^2 - \left|r_D(\omega)\right|^2. \tag{3-13}$$

3.3 Full Waveform propagation into a poroelastic medium

Firstly, some differences between a viscoelastic and poroelastic medium must be pointed out. Viscoelastic medium takes into account the attenuation effects due to all possible mechanism in an implicit way, through the inclusion of rate or history (memory variables). This stress–strain history is introduced by time derivatives, e.g Maxwell, Voigt and Standard linear solid models. In addition, the elastic energy partition will produce only four wave modes, for instance an incident P-wave will turn into P and PS reflected and transmitted (Mavko et al., 1998).

In contrast, when it comes to poroelastic medium the attenuation mechanism is considered in an explicit manner, which means that the physical process is somehow defined. There are several mechanisms as fluid flow effects, dissipation due to relative motion between the frame and the fluids, partial saturation effects such as gas pocket embedded in more viscous fluid. In this case, an additional wave known as low P-wave or Biot-wave describes the differential motion due to the interaction between the frame and the fluid phase (Mavko et al., 1998).

The approach that is implemented in this work to compute the full waveform propagation response from a point source through a layered medium is performed by combining the generalized reflection and transmission matrix method developed by Kennett (1983) with the discrete wavenumber technique (Bouchon, 1981). This solution was already performed by Garambois and Dietrich (2002) for simulation of the couple seismic and electromagnetic waves propagating into a porous media based on the previous work of Pride (1994). A brief description of this numerical development that is only focused on the seismic waves couple P-SV is presented herein, therefore the full wave equations are not accounting for the electromagnetic field.

Pride (1994) derived in the frequency domain the dynamic equations controlling the couple seismic electromagnetic wave propagation through a porous medium (Garambois and Dietrich, 2002). For a stratified medium Haartsen and Pride (1997) expressed this as system of first order ordinary partial equations.

$$\frac{\partial}{\partial z}\mathbf{B} = \mathbf{A}\mathbf{B} + \mathbf{F}, \tag{3-14}$$

where **B** is the displacement-stress vector, **F** is the source point vector and ***A*** matrix is defined hereafter. In general, the transformation to reach system (3-14) follows the cylindrical wave decomposition in the frequency-wave number domain and a subsequence decomposition of each wave field into vertical and horizontal components. The **B** vector accounts for the set couples of the propagation of fast P-waves *(Pf)*. Biot slow P-wave *(Ps)* and S-wave polarized in the vertical plane of propagation *(SV)*, see Equation (3-15) where the ***u*** is the macroscopy average displacement of the solid grains, ***w*** is the Darcy displacement, τ is the stress tensor and ***P*** is the fluid pressure. This parameters are explained in more detail hereafter (Garambois and Dietrich, 2002)

$$\mathbf{B}^{PSV} = \left[u_1, u_z, w_z, \tau_{1,} \tau_{zz}, P\right]. \tag{3-15}$$

The wave fields as displacement and stress can be decomposed into upwoing and downgoing wave contributions. This allows to connect the displacement–stress vector **B** to a wave vector **V** that contains upward and downward complex potentials of all wave types. This relation and vector **V** are given in Equations (3-16) and (3-17), where the subscripts U and D stand for upward and downward, respectively (Garambois and Dietrich, 2002)

$$\mathbf{B} = \mathbf{D}\mathbf{V}, \tag{3-16}$$

$$\mathbf{V}^{PSV} = \left[V_U^{Pf}, V_U^{Ps}, V_U^{SV}, V_D^{Pf}, V_D^{Ps}, V_D^{SV}\right]. \tag{3-17}$$

Matrix **D** is defined by the eigenvectors of the matrix **A**, these values were computed by Haartsen and Pride (1997) for the isotropic homogenous poroelastic medium. For the case of PSV the dimensions of the matrix **D** is 4x4. Following the same formulations described by Kennett and Kerry (1979) the matrix **D** can be expressed as it is shown in (3-18), where $\mathbf{M}_U$ and $\mathbf{M}_D$ are submatrices that transform the upgoing and downgoing wave potentials into displacements and $\mathbf{N}_U$, $\mathbf{N}_D$ do the same for the stresses (Garambois and Dietrich, 2002)

$$\mathbf{D} = \begin{pmatrix} \mathbf{M}_U & \mathbf{M}_D \\ \mathbf{N}_U & \mathbf{N}_D \end{pmatrix}. \tag{3-18}$$

The reflection and transmission coefficients are computed by using the method presented by Kennett and Kerry (1979). From Equation (3-17) it is possible to see that an incident wave at the interface between two porous media generates three reflected and three transmitted waves. This means that for a poroelastic medium we have an additional conversion of the energy that does not occur either in an elastic or viscoelastic medium. The boundary conditions must be set as:

$$\mathbf{B}(z^-) = \mathbf{B}(z^+). \tag{3-19}$$

Then the propagator matrix **Q** is presented and introduced in Equation (3-20). The inverse of **D** is computed numerically. Then the partitioned of **Q** is given by Equation (3-21)

$$\begin{aligned} \mathbf{V}_-(z^-) &= \mathbf{Q}(z^+, z^-)\mathbf{V}_+(z^+), \\ \mathbf{Q}(z^+, z^-) &= \mathbf{D}_-^{-1}(z^-)\mathbf{D}_+(z^+), \end{aligned} \tag{3-20}$$

$$\mathbf{Q}(z^+, z^-) = \begin{pmatrix} \mathbf{Q}_{UU} & \mathbf{Q}_{UD} \\ \mathbf{Q}_{DU} & \mathbf{Q}_{DD} \end{pmatrix}. \tag{3-21}$$

Finally, the reflection and transmission coefficients in a PSV system are represented by matrices (3x3), for example the $\mathbf{R}_D$ matrix is given by Equation (3-22)

$$\mathbf{R}_D = \begin{pmatrix} r_D^{PfPf} & r_D^{PfPs} & r_D^{PfSV} \\ r_D^{PsPf} & r_D^{PsPs} & r_D^{PsSV} \\ r_D^{SVPf} & r_D^{SVPs} & r_D^{SVSV} \end{pmatrix}. \tag{3-22}$$

Generalizing the reflection and transmission matrix the expression for a receiver above the source point can be written as

$$\mathbf{W} = \left(\mathbf{C}_\mathbf{U}^\mathbf{R} + \mathbf{C}_\mathbf{D}^\mathbf{R}\mathbf{R}_\mathbf{U}^\mathbf{FR}\right)\left(\mathbf{I} - \mathbf{R}_\mathbf{D}^\mathbf{RS}\mathbf{R}_\mathbf{U}^\mathbf{FR}\right)^{\mathbf{-1}} \mathbf{T}_\mathbf{U}^\mathbf{RS} \left[\mathbf{I} - \mathbf{R}_\mathbf{D}^\mathbf{SL}\mathbf{R}_\mathbf{U}^\mathbf{FS}\right]^{-1} \left(\mathbf{R}_\mathbf{D}^\mathbf{SL} \sum\nolimits_\mathbf{D} - \sum\nolimits_\mathbf{U}\right), \tag{3-23}$$

where **W** is the wave fields composing the displacement-stresses. The $\mathbf{R}_\mathbf{U}^\mathbf{FR}, \mathbf{R}_\mathbf{D}^\mathbf{RS}, \mathbf{R}_\mathbf{U}^\mathbf{FR}, \mathbf{R}_\mathbf{D}^\mathbf{SL}$ and $\mathbf{T}_\mathbf{U}^\mathbf{RS}$ are the coefficient matrices of the reflection and transmission. In this case, *F* indicates the free surface, *R* the receiver level, *S* the source level and *L* the lower half-space. All these coefficients are recursively constructed for a stack of uniform layers from the reflection and transmission matrices at each interface. $\mathbf{C}_\mathbf{U}^\mathbf{R}$ and $\mathbf{C}_\mathbf{U}^\mathbf{R}$ are matrices that convert the downgoing and upgoing wave amplitudes into their corresponding wave field at the receiver location. Lastly, $\mathbf{R}_\mathbf{D}^\mathbf{SL} \sum_\mathbf{D} - \sum_\mathbf{U}$ describes the total energy of the upgoing wave emitted from the source. This computations have to be performed for each wave component, for instance for each frequency and each horizontal wave number (Garambois and Dietrich, 2002).

All the computations are being carried out in the frequency and wave number domain (ω, k). The wave fields can be transformed to the time distance domain by using the Fourier and Hankel transforms of the plane wave response. Firstly, the integral over the horizontal wave number is performed by using the discrete wave number method introduced by Bouchon (1981). Secondly, the integral over the frequency is calculated by using a discrete Fourier transform with a complex frequencies (Bouchon, 1979). Finally, the wave fields that were computed in cylindrical coordinates are transformed to Cartesian coordinates (Garambois and Dietrich, 2002).

3.4 Poroelastodynamic

The governing wave equations for a poroelastic medium (anelastic) are seen as rearrangement of Biot's (1956). Pride (2005) assumed an exponential function $e^{-i\omega t}$, where t is time and ω is angular frequency obtaining the expression in Equation (3-24). A poroelastic medium account for the wave propagation of 3 types of waves. The fast and slow compressional wave and the shear waves. The slow P-wave is called Biot-wave, which is strongly diffusive and attenuated at low frequency (Dupuy and Stovas, 2013)

$$\begin{aligned}
&\nabla\tau = -\omega^2\left(\rho\mathbf{u} + \rho_f\mathbf{w}\right),\\
&\tau = \left[K_U\nabla\cdot\mathbf{u} + C\nabla\cdot\mathbf{w}\right]\mathbf{I} + G\left[\nabla\mathbf{u} + \left(\nabla\mathbf{u}\right)^T - 2/3\left(\nabla\cdot\left(\mathbf{uI}\right)\right)\right],\\
&-P = C\nabla\cdot\mathbf{u} + M\nabla\cdot\mathbf{w},\\
&-\nabla P = -\omega^2\rho_f\mathbf{u} + \omega^2\tilde{\rho}\mathbf{w}.
\end{aligned} \tag{3-24}$$

where **u** is the average displacement of the solid grains, **w** is the relative fluid-to-solid displacement. It is possible to define $\mathbf{u_s}$, $\mathbf{u_f}$ as the average displacement of solid grains and fluid phases through, average volume, and the porous space, respectively. Therefore $\mathbf{u_s}=\mathbf{u}$ and $\mathbf{w}=\phi(\mathbf{u_s}-\mathbf{u_f})$, where ϕ is porosity. τ is the bulk stress tensor defined in Equation (3-25), where τ_s and τ_f are the tensors in the grain and the fluid, correspondingly. ***P*** is the fluid pressure and ρ is the bulk density of the material, which depends on the fluid density, solid density (ρ_s) and the porosity being an arithmetic mean expressed by Equation (3-26)

$$\tau = \phi\tau_f + \left(1-\phi\right)\tau_s, \tag{3-25}$$

$$\rho = (1-\phi)\,\rho_s + \phi\rho_f\,. \tag{3-26}$$

The theory behind the presented Equation (3-24), is based on the assumption that a porous material is uniform within a certain scale of measurement, which is between the grain scale and the wavelength scale (mesoscale). What is known as a macroscopy flow that is well explained by the Biot's theory, in which the differential pressure in the fluids created by the pass of P-wave through a porous material, is equilibrated within a wave period (wavelength scale). Nevertheless, it does not generate enough attenuation to explain some laboratory measurements and field results (Pride, 2005).

Due to that, Pride (2005) suggests some possible explanations for these observations, such as the existence of a mesoscopic heterogeneities. The origin of these heterogeneities might be related to either lithological variations (double porosity) or different geometrical distribution of the fluid phases (patchy saturation). In the same manner as the squirt flow effect, the equilibration of the pressure gradient when a plane wave travels through a porous material, takes longer for the compliant parts than the stiffer parts of the material, creating what is known as local flow. That seems to be able to explain attenuation in the seismic range (Pride, 2005). A particular characteristic of these mesoscopic mechanisms, is that turns the elastic moduli of the standard Biot's theory into complex and frequency dependent quantities.

The application of the Biot's theory considering the mesoscopic scale heterogeneities, implies the understanding and definition of some parameters. One needs to keep in mind the three inertial terms such as: the fluid density, the mean density and the flow resistance term, they are related to the dynamic loss of energy due to the fluid flow (ρ_f, ρ, $\tilde{\rho}(\omega)$, respectively). Additionally, there are four mechanical parameters composed by three incompressibilities: the bulk modulus K_U, the Biot's modulus C, the fluid storage parameter M. They are complex variables and frequency dependent.

For instances, K_U is the undrained bulk modulus and it is defined when the fluid is not allow to either enter or leave the porous space in the sample during deformation. C is the Biot's modulus that represent the fluid/solid coupling. The moduli M measures how much fluid can be collected in the pores in presence of fluid pressure changes (Dupuy and Stovas, 2013, Pride, 2005). Lastly,

B represent the change of pore pressure because of the change in the total vertical stress, and it is called as the Skempton's coefficient.

Due to the complexity nature and frequency dependent of the four mechanical parameters, it is not possible to implement Gassmann theory directly. This is mainly, because his theory is valid under certain conditions and within a low frequency range. K_U and B become real and frequency independent variables under the Gassmann theory assumptions (Pride, 2005). Therefore, it is possible to homogenize the medium and then apply the Biot-Gassmann fluid substitution theory, where the modulus K_U, C, M are expressed in terms of K_D, K_S, K_f and ϕ (3-27). These parameters can be adapted to various models such as saturated, partially saturated or double porosity media (Dupuy and Stovas, 2013)

$$\begin{aligned} K_U &= \frac{\phi K_D + \left(1-\left(1+\phi\right)K_D/K_S\right)K_f}{\phi\left(1+\Delta\right)}, \\ C &= \frac{\left(1-K_D/K_S\right)K_f}{\phi\left(1+\Delta\right)}, \\ M &= \frac{K_f}{\phi\left(1+\Delta\right)}, \\ \Delta &= \frac{1-\phi K_f}{\phi K_S}\left(1-\frac{K_D}{\left(1-\phi\right)K_S}\right). \end{aligned} \tag{3-27}$$

Independently of the model used, the Gassmann relations are only valid for a rock that host a single fluid and is monomineralic. Therefore, disregarding the type of fluid distribution in the porous medium and mineral composition of the grains, an effective medium is needed to apply the generalized Biot-Gassmann theory (Dupuy et al., 2016).

3.4.1 Uniform saturation distribution

In order to simulate a uniform fluid distribution, some averaging process are proposed to compute the effective fluid bulk modulus K_f , effective fluid density ρ_f and viscosity. The first one is estimated through the equation proposed by Brie et al. (1995), which considers the huge difference between the fluid bulk modulus of water and gas, see Equation (3-28). An important feature of this, is its ability to describe by the exponent e different fluid distribution models. For example, when e=1 the upper bound (Voigt, 1889) is represented, whereas when e=40 the lower bound (Reuss, 1929) is obtained (Brie et al., 1995). The former suggests a patchy mixing fluid distribution, without contemplating the physical mechanisms as it is done in White's patchy model. The lower bound, stand for a uniform distribution (well-mixed at the finest scale). In this case, the exponent in Equation (3-28) is set equal 5 as proposed by Carcione et al. (2006).

Moreover, the effective fluid density is expressed as a weighted average using the volume fraction of each fluid proposed by Domenico (1976) and given in Equation (3-29), where *V* stands for the volume fraction and the sub-scripts *brine* and *CO₂* indicate liquid and gas, respectively

$$K_f = \left(K_{fbrine} - K_{fCO_2}\right) V_{brine}^{e} + K_{fCO_2}, \tag{3-28}$$

$$\rho_f = \sum_i V_i \rho_{fi}. \tag{3-29}$$

The relation proposed by Teja and Rice (1981), is used to obtain the effective fluid viscosity of the water and CO_2 mixed. This relation is given by Equation (3-30), where η is viscosity

$$\eta = \eta_{CO_2} \left(\frac{\eta_{brine}}{\eta_{CO_2}} \right)^{\left(1 - V_{CO_2}\right)}. \tag{3-30}$$

Finally, the wave attenuation in this fluid distribution model is the Biot global fluid flow, which is explained by the Darcy's law via the complex frequency dependent dynamic permeability $k(\omega)$ (Johnson et al., 1987). The viscosity η and the hydraulic permeability k_0 are related through the Darcy law. This complex permeability is written as

$$k(\omega) = \frac{k_0}{\sqrt{1 - \frac{1}{2} i \frac{\omega}{\omega_c}} - i \frac{\omega}{\omega_c}}, \tag{3-31}$$

where the relaxation frequency ω_c indicates the frequency limit at which viscous losses are dominant, beyond that the inertial effects take place (Dupuy et al., 2016). This characteristic frequency is expressed in terms of the Archie's law, where *m* is the cementation exponent that links the geometrical complexity of a porous medium with the distribution of the space and tortuosity (Adler et al., 1992, Brown, 1980)

$$\omega_c = 2\pi f_c = \frac{\eta}{\rho_f k_0 \phi^{-m}}. \tag{3-32}$$

The flow resistance term $\tilde{\rho}(\omega)$ is a complex and frequency dependent variable given by (3-33), where *i* is the complex number and is directly involved in a poroelastodynamic system (Equation 3-24)

$$\tilde{\rho}(\omega) = \frac{i\eta}{\omega k(\omega)}. \tag{3-33}$$

3.4.2 Patchy fluid distribution (White's model)

White (1975) proposed a patchy fluid distribution model with the aim of explaining the physical mechanisms behind the fluid flow induced by the seismic wave. He attributed the generation of the fluid flow induced by difference in pressure gradients. This variations are the result of having a partially saturated rock with inhomogeneities, since the pressure gradient is higher near the gas pockets with respect to other parts of the rock. Subsequently, a considerable loss of energy is then revealed as compressional wave attenuation in the seismic bandwidth (White, 1975). This theory was later modified by Dutta and Seriff (1979). Figure 3.1 depicts White's model using spherical gas pockets embedded in a cubical array. Some assumption are made for the model: *i)* the rock frame is considered to be uniform, *ii)* the entire volume outside the spherical pockets is saturated with liquid. The average bulk modulus calculations are carried out by assuming that the volume is a concentric sphere, as it is illustrated in the right hand side of the Figure 3.1, where the volume of the outer sphere is equal to the volume of the original cube (White, 1975).

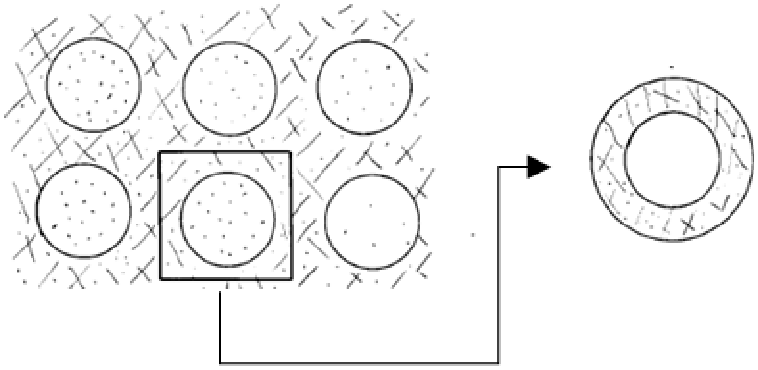

Figure 3.1: *Patchy fluid distribution model of porous rock with mixture of gas and brine. Gas phase is represented by spherical pockets. The typical volume considered in the calculation is the pair of concentric spheres shown in the right hand side (modified from (White, 1975)).*

Pride et al. (2004) described the motion of the two fluids into the pore space and their interaction with the solid phase, based on White's model and using double porosity theoretical framework. He also proposed a way to compute the effective medium parameters, even though, in this case they are frequency dependent to be able to use the Biot-Gassmann theory. This adaptation is presented below for the bulk-drained, Skempton and bulk undrained modulus ($K_D(\omega)$, $B(\omega)$, $K_U(\omega)$), respectively

$$\frac{1}{K_D(\omega)} = a_{11} - \frac{a_{13}^2}{a_{33}-\gamma(\omega)}, \tag{3-34}$$

$$B(\omega) = \frac{-a_{12}\left(a_{33}-\gamma(\omega)\right) + a_{13}\left(a_{23}+\gamma(\omega)\right)}{\left(a_{22}-\gamma(\omega)\right)\left(a_{33}-\gamma(\omega)\right) - \left(a_{23}+\gamma(\omega)\right)^2},$$

$$K_U(\omega) = \left(\frac{1}{K_D(\omega)} + B(\omega)\left(a_{12} - \frac{a_{13}\left(a_{23}+\gamma(\omega)\right)}{a_{33}-\gamma(\omega)}\right)\right)^{-1}. \tag{3-35}$$

From the (3-34) and (3-35), the storage coefficient M (ω) and Biot's modulus C (ω) are given by (3-36), where α is the Biot-Willis constant and K_{D0} is the bulk drained modulus obtained by harmonic average.

$$C(\omega) = B(\omega)K_U(\omega),\ M(\omega) = B(\omega)\frac{K_U(\omega)}{\alpha},\ \alpha = 1 - K_{Do}/K_S \tag{3-36}$$

The mechanical property matrix elements are defined by constant values $a_{ij}\left(i, j \in (1,3)\right)$ as expressed in Equation (3-37). In this case V_1 and V_2 correspond to the volume fraction of each fluid being the V_1 the more viscous (water). B_1 and B_2 are the Skempton moduli. The shear modulus G is frequency independent and equal to the drained shear modulus G_D. at the seismic frequency range

$$a_{11} = \frac{1}{K_{Do}},\ a_{22} = \left(-\beta + V_1/B_1\right)\frac{\alpha}{K_{Do}},\ a_{33} = \left(-\beta + V_2/B_2\right)\frac{\alpha}{K_{Do}}, \tag{3-37}$$

$$a_{12} = -\frac{V_1\alpha}{K_{Do}},\ a_{13} = -\frac{V_2\alpha}{K_{Do}},\ a_{23} = \frac{\beta\alpha}{K_{Do}}.$$

A new parameter β was introduced by Pride et al. (2004) to consider undrained patches and be able to apply elasticity law to the composite material, where K_H is the elastic modulus of the composite. They are expressed by Equation (3-38) and Equation(3-39), respectively

$$\beta = \left(\frac{V_1 V_2}{B_1 B_2} \right) \frac{V_1 B_1 + V_2 B_2 - 1/\alpha + K_{Do}/K_H}{1 - \left(1/\alpha - K_{Do}/K_H \right)\left(V_1/B_1 - V_2/B_2 \right)}, \tag{3-38}$$

$$K_H = 1 \Bigg/ \left[\frac{V_1}{K_{Do}/\left(1 - \alpha B_1\right) + 4G/3} + \frac{V_2}{K_{Do}/\left(1 - \alpha B_2\right) + 4G/3} \right]. \tag{3-39}$$

For this model, an additional parameter called the internal transport coefficient $\gamma(\omega)$ is introduced. It depends on of γ_p and ω_p and they are presented in Equation (3-40) and Equation (3-41), respectively

$$\gamma(\omega) = \gamma_p \sqrt{1 - \frac{i\omega}{\omega_p}}, \tag{3-40}$$

$$\gamma_p = \frac{V_1 k_0}{\eta_1 L_1^2}, \ \omega_p = \frac{K_{D0} B_1 k_0 V_1^2 \left(V/S\right)^2}{\eta_1 \alpha L_1^4} \left(1 + \sqrt{\frac{\eta_2 B_2}{\eta_1 B_1}} \right)^2 . \tag{3-41}$$

γ_p and ω_p, are the described by some geometrical parameters: L_1 and V/S. They are defined only for specific range of saturation for both fluid phases. *S* is the contact surface between fluids, *V* is the volume and *L* is the distance in the phase 1. The phase 1 must have the lowest mobility *(* k_0/η *)*. In order to obtain an analytical solution Pride et al. (2004) proposed that the spherical patches (radius *a*) are disconnected, therefore the following conditions are true:

- If *V2<<V1* where phase 2 is the less viscous fluid, represented by spheres of radius *a*, embedded into the spheres of radius *R*. The geometrical parameters are: $V/S = R^3/3a^2 = aV_2/3$ and $L_1^2 = 9V_2^{-2/3}a^2\left(1 - 7V_2^{1/3}/6\right)/14$. Since the phase 2 is considered to be immobile with respect to the solid matrix, due to its amount is quite low, hence the inertial terms are expressed only as a function of the phase 1 as: $\rho_f = \rho_1$ and $\tilde{\rho} = i\eta_1/\omega k_0$

- If *V1<<V2* in this case the less viscous phase is dominant, therefore the geometrical parameters are $V/S = aV_1/3$ and $L_1^2 = a^2/15$ and the inertial terms are now defined only as function of phase 2 as: $\rho_f = \rho_2$ and $\tilde{\rho} = i\eta_2/\omega k_0$

3.4.3 Effective viscoelastic properties

Finally, the effective seismic properties such as: velocities and quality factors for both compressional and shear waves can be computed. S_P, S_{Biot} and S_s represent the complex slowness for P fast, P slow and S-wave, respectively. From these two quantities it is possible to compute the effective phase velocities as given in Equation (3-43), by taking the real part of their corresponding slowness. The quality factors are function of the real and imaginary part of the slowness as is shown in Equation (3-44) (Dupuy et al., 2016)

$$S_{P,Biot}^2 = \pm\frac{\gamma(\omega)}{2} + \frac{1}{2}\sqrt{\gamma^2(\omega) - \frac{4\left(\rho\tilde{\rho}(\omega)\rho_f^2\right)}{HM - C^2}}, \qquad S_s^2 = \frac{\rho - \rho_f^2/\tilde{\rho}(\omega)}{G}, \tag{3-42}$$

$$V_{P,Biot}(\omega) = \frac{1}{\mathrm{R}_e\left(S_{P,Biot}(\omega)\right)},\ V_S(\omega) = \frac{1}{\mathrm{R}_e\left(S_S(\omega)\right)}, \tag{3-43}$$

$$Q_{P,Biot,S}(\omega) = \frac{\mathrm{Re}\left(S_{P,Biot,S}^2(\omega)\right)}{\mathrm{Im}\left(S_{P,Biot,S}^2(\omega)\right)}. \tag{3-44}$$

From (3-42), an auxiliary parameter $\gamma(\omega)$ needs to be defined to calculate the wave slowness, where *H* is the P-wave modulus, and this one will be frequency dependent or not depending on the fluid distribution model. Both are given in Equation (3-45) and Equation(3-46), correspondingly

$$\gamma(\omega) = \frac{\rho M + \tilde{\rho}(\omega)H - 2\rho_f C}{HM - C^2}, \tag{3-45}$$

$$H = K_U + \frac{4}{3}G. \tag{3-46}$$

Chapter 4 AVO Theory

This Chapter is meant as an introduction of some concepts related to quantitative seismic interpretation emphasizing the Amplitude Versus Offset principles. A brief explanation of the exact solution for the reflection and transmission scattered matrix (Zoeppritz equations) and its most common approximations are presented. In addition, a new modelled based AVO approximation and inversion scheme (OptAVO) developed in SINTEF Petroleum Research is also described.

The seismic interpretation discipline can be divided into major groups, what is known as qualitative interpretation and quantitative interpretation (QI). From qualitative interpretation the main aim is tracking reflectors in travel time and space. The seismic reflectors represent geological events at specific period of time, hence their proper interpretation allows the definition of the reservoir structure and delineation. The well understanding of the amplitudes variations due to fluid presences or geological contrast between geological layers is not emphasized (Avseth et al., 2005).

On the other hand, the QI fully addresses the analysis and understanding of the amplitude variations. Thusly, this allows to confirm the hydrocarbon presence and gives a better comprehension during the prospect evaluation and reservoir characterization phase. Several techniques have been implemented as part of QI analysis such as: post-stack amplitude analysis (bright/dim spot), Amplitude versus Offset or Amplitude versus Angle (AVO/AVA), acoustic and elastic inversion and forward seismic modeling (Avseth et al., 2005).

Seismic amplitudes can be describe as the response cause by elastic contrast between two layers. Therefore a lot of additional information can be extracted from it, as long as, the amplitude analysis is being carried out carefully and correctly. Some of this additional information is related to the reservoir properties itself, for instance lithology, porosity, fluid type, saturations and pore pressure (Avseth et al., 2005).

It is important to notice, that the success of this amplitude variation analysis is highly affected by the quality of the data and type of processing that has been performed. For this type of analysis it is widely used the concept of *True Amplitude Processing*. This refers mainly to the attempt to process the data in such a way that all factors which affect the amplitude that are not associated to geological features must be removed. For instance, all those that are related to the survey equipment; variability of the sensitivity in the source and receivers, coupling and directivity of the array (Simm et al., 2014).

In addition, there are some other effects that are related to the nature of the subsurface, but they are not of relevant interest, thus it is preferable to remove them from the data during processing. Some of them are geometrical spreading, scattering, diffractions, multiples, dispersion, reflector rugosity and curvature, and in general superimposed noise, attenuation and anisotropy. The last two effects, could give us extra information as long as, their origin were better understood. Figure 4.1 shows a schematic representation of all the effects that alters the seismic wave amplitude during its travel through the earth from the source to the receiver. As a result of this true amplitude processing, the variations in amplitude that is being seen in the data can be interpreted as a change in fluids, lithology, porosity, pressure and saturations, at least with a higher degree of confidence (Simm et al., 2014).

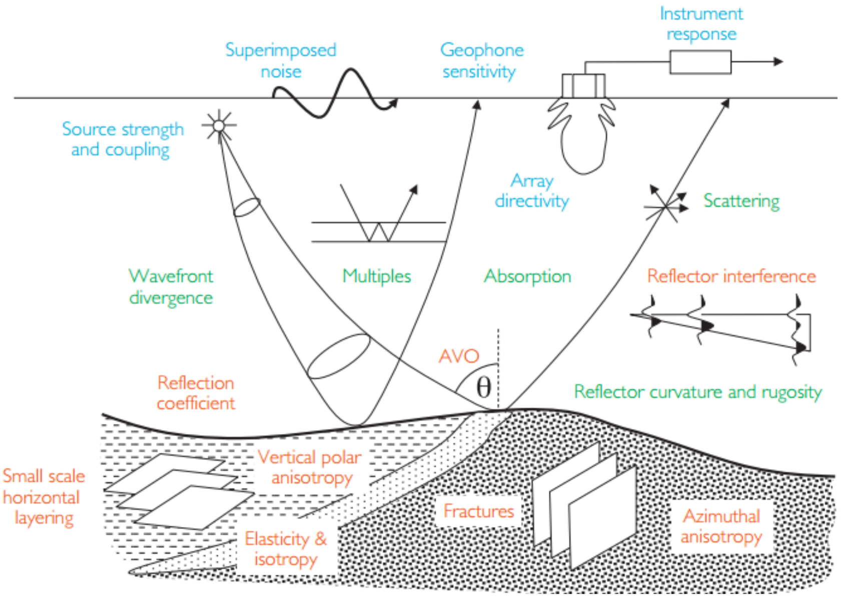

Figure 4.1: *Factors affecting wave amplitude during its travel time from the source to the receiver (modified from Sheriff, 1975). From (Simm et al., 2014).*

4.1 AVO/AVA

Feng and Bancroft (2006) defined the Amplitude Variation with Offset (AVO) as the variation in seismic amplitude with shot-receiver distance in a pre-stack seismic data. This technique is based upon the assumption of a plane wave travelling through an elastic medium. Every time the wave hits and interface between two layers with different elastic properties, the energy is partitioned at both side of the boundary as it is illustrated in Figure 4.2.

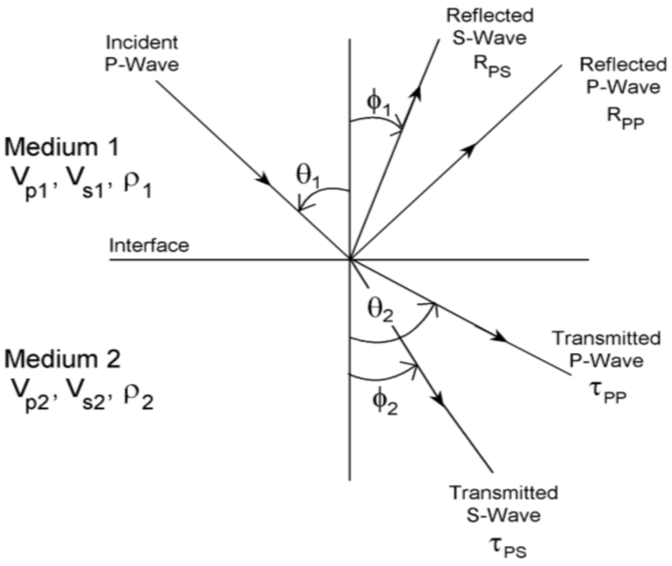

Figure 4.2: *Reflection and transmission at the interface between two half-space with elastic contrast for an incident P plane wave. It can be noticed that there is a partitioning of the energy at the interface, part of it is being reflected as P-wave with the same incident angle, whose reflection coefficient is denoted as Rpp, there is also part of the energy that is being transmitted through the second medium with a transmitted coefficient of Tpp). In addition, there is a conversion mode of the P incident wave into a S-wave, which is reflected Rps and transmitted Tps, correspondingly. From Russell and Hampson (2004).*

4.2 Reflection and Transmission Coefficients

The plane wave theory has been widely used in order to investigate elastic wave behaviour when waves are being propagated into the Earth. This theory was fully developed by Knot (1899) with his generalization of the medium taking into account fully variation in the elastic moduli and densities of the medium by using potential fields (Aki and Richards, 1980). Later on, Zoeppritz came out with a solution to compute the reflected energy when an incident plane wave strikes a plane reflector (Russell and Hampson, 2004).

Reflection and transmission coefficients of P-SV waves across a solid-solid interface are represented by the scattering matrix, which is shown in Equation (4-1). The acute and grave accents are used in order to indicate whether the wave is upcoming or downgoing, respectively. This can be obtained by using the appropriate boundary conditions stablishing continuity of the x- and z-components of the displacement and stresses. The scattering matrix can be described by each of its columns, which represent the four waves scattered by specific wave type when hitting the interface as it shown in Figure 4.3

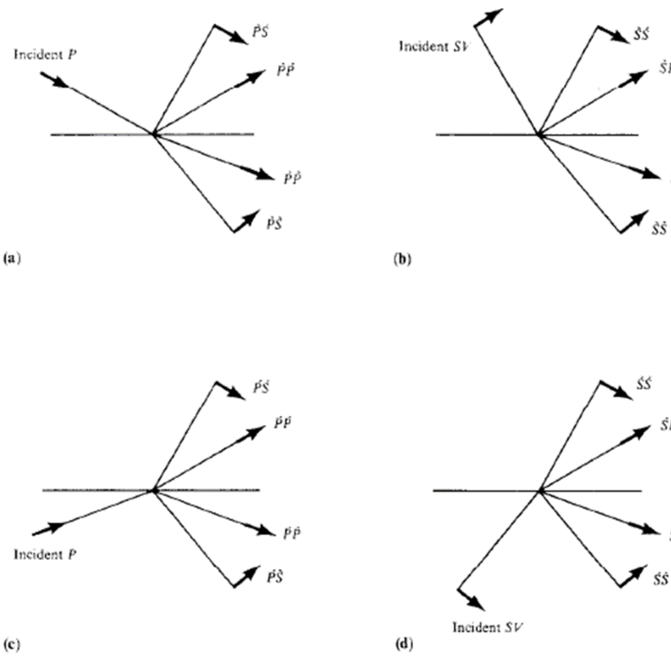

Figure 4.3: *Representation of the sixteen possible reflection/transmission coefficients arising from a welded interface between two solid layer materials, when a P-SV waves hit the interface.The short arrows indicate the direction of the particle motion, (Aki and Richards, 1980).*

$$\begin{pmatrix} \overset{\backslash}{P}\overset{/}{P} & \overset{\backslash}{S}\overset{/}{P} & \overset{/}{P}\overset{/}{P} & \overset{/}{S}\overset{/}{P} \\ \overset{\backslash}{P}\overset{/}{S} & \overset{\backslash}{S}\overset{/}{S} & \overset{/}{P}\overset{/}{S} & \overset{/}{S}\overset{/}{S} \\ \overset{\backslash}{P}\overset{\backslash}{P} & \overset{\backslash}{P}\overset{\backslash}{P} & \overset{/}{P}\overset{\backslash}{P} & \overset{/}{S}\overset{\backslash}{P} \\ \overset{\backslash}{P}\overset{\backslash}{S} & \overset{\backslash}{S}\overset{\backslash}{S} & \overset{/}{P}\overset{\backslash}{S} & \overset{/}{S}\overset{\backslash}{S} \end{pmatrix}. \tag{4-1}$$

As a result, system of four equations with four variables must be solved. In order to achieve that, some assumptions are made, such as the four possible incident wave are present having same constant horizontal slowness *(p),* whose displacement amplitude is given by $\overset{\backslash}{P}_1, \overset{\backslash}{S}_1, \overset{/}{P}_2, \overset{/}{S}_2$. This particular case is illustrated in Figure 4.5, where the subscripts indicates the medium where the waves are being propagated, for instance subscript 1 stands for the layer above the interface and 2 for the layer below. After some simplification assuming that the corresponding displacement amplitudes for the scattered waves are: $\overset{/}{P}_1, \overset{/}{S}_1, \overset{\backslash}{P}_2, \overset{\backslash}{S}_2$. Considering the boundary conditions as continuity of the displacement and traction $u_x, u_{y,} \tau_{xx}, \tau_{zz}$, four equations are obtained. Rearranging these equations in a way that all the scattered waves are in the left hand side and the incident waves in the right hand side, the expression given by (4-2)

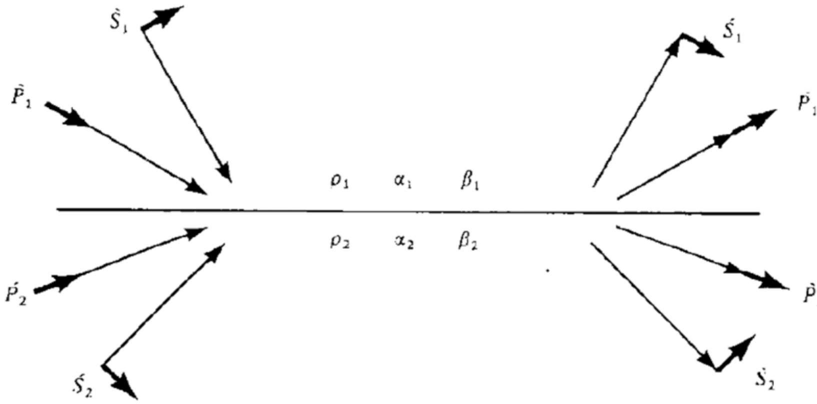

Figure 4.4: *System of incident and scattered plane P-SV waves, from which the scattering matrix can be easily computed. The short arrows indicate the direction of the particle motion while long arrows show the direction of the wave propagation (Aki and Richards, 1980).*

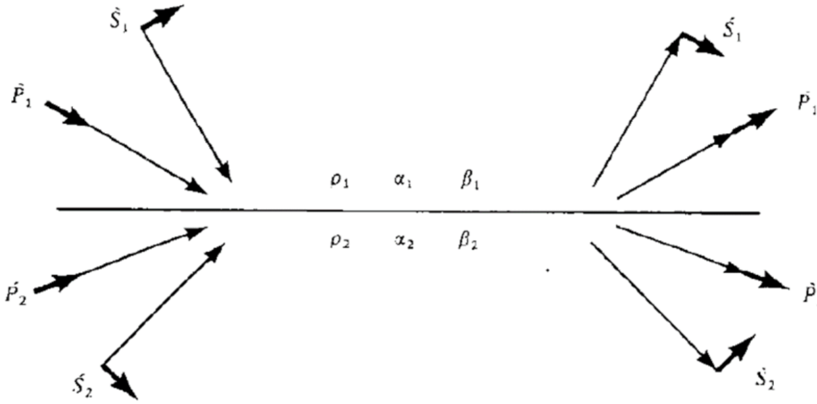

Figure 4.5: *System of incident and scattered plane P-SV waves, from which the scattering matrix can be easily computed. The short arrows indicate the direction of the particle motion while long arrows show the direction of the wave propagation (Aki and Richards, 1980).*

$$\mathbf{M}\begin{pmatrix} \acute{P}_1 \\ \acute{S}_1 \\ \grave{P}_2 \\ \grave{S}_2 \end{pmatrix} = \mathbf{N}\begin{pmatrix} \grave{P}_1 \\ \grave{S}_1 \\ \acute{P}_2 \\ \acute{S}_2 \end{pmatrix}, \tag{4-2}$$

where the **M** and **N** are the coefficient matrices presented in Equations (4-3) and (4-4), where α and β are the P and S wave velocities, respectively, ρ is the density of the medium, i_1 and i_2

indicate the P wave incident and transmitted angle, whereas j_1 and j_2 are the S wave reflected and transmitted angles, respectively

$$\mathbf{M}=\begin{pmatrix} -\alpha_1 p & -\cos j_1 & \alpha_2 p & \cos j_2 \\ \cos i_1 & -\beta_1 p & \cos i_2 & -\beta_2 p \\ 2\rho_1\beta_1^2 p\cos i_1 & \rho_1\beta_1\left(1-2\beta_1^2 p^2\right) & 2\rho_2\beta_2^2 p\cos i_2 & \rho_2\beta_2\left(1-2\beta_2^2 p^2\right) \\ -\rho_1\alpha_1\left(1-2\beta_1^2 p^2\right) & 2\rho_1\beta_1^2 p\cos j_1 & \rho_2\alpha_2\left(1-2\beta_2^2 p^2\right) & -2\rho_2\beta_2^2 p\cos j_2 \end{pmatrix}, \tag{4-3}$$

$$\mathbf{N}=\begin{pmatrix} \alpha_1 p & \cos j_1 & -\alpha_2 p & -\cos j_2 \\ \cos i_1 & -\beta_1 p & \cos i_2 & -\beta_2 p \\ 2\rho_1\beta_1^2 p\cos i_1 & \rho_1\beta_1\left(1-2\beta_1^2 p^2\right) & 2\rho_2\beta_2^2 p\cos i_2 & \rho_2\beta_2\left(1-2\beta_2^2 p^2\right) \\ \rho_1\alpha_1\left(1-2\beta_1^2 p^2\right) & -2\rho_1\beta_1^2 p\cos j_1 & -\rho_2\alpha_2\left(1-2\beta_2^2 p^2\right) & 2\rho_2\beta_2^2 p\cos j_2 \end{pmatrix}. \tag{4-4}$$

For the special case when $\grave{P}_1 = 1,$ and $\grave{S}_1 = \acute{P}_2 = \acute{S}_2 = 0,$ the first column of the scattered matrix becomes simple as $\left(\acute{P}_1, \acute{S}_1, \grave{P}_2, \grave{S}_2\right)^T$, for instance the first column of $\mathbf{M}^{-1}\mathbf{N}$. In the same way, for the other columns similar results can be obtained, therefore the whole matrix is given by (4-5)

$$\begin{pmatrix} \grave{P}\acute{P} & \grave{S}\acute{P} & \acute{P}\acute{P} & \acute{S}\acute{P} \\ \grave{P}\acute{S} & \grave{S}\acute{S} & \acute{P}\acute{S} & \acute{S}\acute{S} \\ \grave{P}\grave{P} & \grave{P}\grave{P} & \acute{P}\grave{P} & \acute{S}\grave{P} \\ \grave{P}\grave{S} & \grave{S}\grave{S} & \acute{P}\grave{S} & \acute{S}\grave{S} \end{pmatrix} = \mathbf{M}^{-1}\mathbf{N}. \tag{4-5}$$

So simple expressions can be used to compute each element of the scattering matrix, which have a repeated use of the seismic properties variables and cosine-dependent terms given in Equations (4-6) and (4-7)

$$a=\rho_2\left(1-2\beta_2^2 p^2\right)-\rho_1\left(1-2\beta_1^2 p^2\right),\ b=\rho_2\left(1-2\beta_2^2 p^2\right)+2\rho_1\beta_1^2 p^2, \tag{4-6}$$

$$c=\rho_1\left(1-2\beta_1^2 p^2\right)+2\rho_2\beta_2^2 p^2,\ d=2\left(\rho_2\beta_2^2-\rho_1\beta_1^2\right),$$

$$E=b\frac{\cos i_1}{\alpha_1}+c\frac{\cos i_2}{\alpha_2},\ \ F=b\frac{\cos j_1}{\beta_1}+c\frac{\cos j_2}{\beta_2},$$

$$G = a - d\,\frac{\cos i_1}{\alpha_1}\frac{\cos j_2}{\beta_2},\;\; H = a - d\,\frac{\cos i_2}{\alpha_2}\frac{\cos j_1}{\beta_1}, \tag{4-7}$$

$$D = EF + GHp^2 = (\det \mathbf{M}) \big/ \left(\alpha_1\alpha_2\beta_1\beta_2\right).$$

Since the scope of this work is focused on the first column of the scattering matrix, which represent the reflection and transmission coefficients for an incident down-going P wave, their corresponding formulas are presented in Equation (4-8)

$$\begin{aligned}
\grave{P}\acute{P} &= \left[\left(b\,\frac{\cos i_1}{\alpha_1} - c\,\frac{\cos i_2}{\alpha_2}\right)F - \left(a + d\,\frac{\cos i_1}{\alpha_1}\frac{\cos j_2}{\beta_2}\right)Hp^2\right] \Big/ D,\\
\grave{P}\acute{S} &= -2\,\frac{\cos i_1}{\alpha_1}\left(ab + cd\,\frac{\cos i_2}{\alpha_2}\frac{\cos j_2}{\beta_2}\right)p\alpha_1 \big/ \left(\beta_1 D\right),\\
\grave{P}\grave{P} &= 2\rho_1\,\frac{\cos i_1}{\alpha_1}F\alpha_1 \big/ \left(\alpha_2 D\right),\\
\grave{P}\grave{S} &= 2\rho_1\,\frac{\cos i_1}{\alpha_1}Hp\alpha_1 \big/ \left(\beta_2 D\right).
\end{aligned} \tag{4-8}$$

The Zoeppritz equations gives us an exact solution for the reflection and transmission coefficients at different incident angles, however, its results are not easy to interpret or associated directly with any physical insight. These equations can be successfully modified by simpler expressions that, at the same time bring a direct link between the reflectivity and the seismic properties of the medium (Castagna and Backus, 1993). Several of the well-known approximations are discussed in the next section.

4.3 Linear Approximations of Zoeppritz equations

The Zoeppritz equations approximations are based upon some suppositions as the contrast between the elastic parameters of the layer below and above the interface is weak, as well as, the range of the incident angle is no larger than 35 degrees approximately (small angles). The main advantages of all these approximation is the intuitive interpretation that can be made out of them and are linear equations easy to solve and invert to obtain rock properties. The pioneer in presenting an approximation of the Zoeppritz equations was Bortfeld (1961), showing the link of amplitude variation with offset in terms of rock properties. However, in his development, there was not an explicit indication of how reflections coefficients vary with offset or angle, therefore this approximation was not considered for a practical point of view. Later on, Aki and Richards (1980), Shuey (1983), Smith and Gidlow (1987) and others shows different approximations which are widely used nowadays (Feng and Bancroft, 2006).

The approximations presented herein are those included into the Optimal AVO inversion scheme developed by SINTEF and those are used to compute reflectivity property sections from the AVO attributes.

4.3.1 Aki Richards approximation

Aki and Richards (1980) approximation shows the variation in the reflection coefficients in terms of incident angle by using three terms. The first terms refers to the relative contrast in P-wave velocity, the second in S-wave velocity and third one in density. This can be written as follow:

$$Rpp(\theta) \cong \frac{1}{2}\left(1-4p^2V_s^2\right)\frac{\Delta\rho}{\rho} + \frac{1}{2\cos^2\theta}\frac{\Delta V_p}{V_p} - 4p^2V_s^2\frac{\Delta V_s}{V_s}, \tag{4-9}$$

where:

$$p = \frac{\sin\theta}{V_p}, \qquad \theta = (\theta_2 + \theta_1)/2,$$

$$\Delta\rho = \rho_2 - \rho_{1,} \qquad \rho = (\rho_2 + \rho_1)/2,$$

$$\Delta V_p = V_{p2} - V_{p1,} \qquad V_p = (V_{p2} + V_{p1})/2,$$

$$\Delta V_p = V_{s2} - V_{s1,} \qquad V_s = (V_{s2} + V_{s1})/2.$$

The variables in the Equation (4-9) are described as follow: p corresponds to the ray parameter, θ_1 and θ_2 are the incident and the transmission angle respectively, V_p, V_s and ρ are the compressional velocity, shear velocity and density of the layers. The subscripts 1 and 2 indicate the elastic properties of the layer above and below the interface, respectively (Castagna and Backus, 1993).

Later on, this have been reformulated by several authors depending on their purpose. For example, for interpretation purposes, the rearrangement done by Wiggins et al. (1983) (Simm et al., 2014)

$$R(\theta) = A + B\sin^2\theta + C\sin^2\theta\tan^2\theta, \tag{4-10}$$

where:

$$A = R_0 = \frac{1}{2}\left(\frac{\Delta V_P}{V_P} + \frac{\Delta\rho}{\rho}\right),$$

$$B = G = \frac{1}{2}\frac{\Delta V_P}{V_P} - 4\left(\frac{\mathrm{V_S}}{\mathrm{V_P}}\right)^2\left(\frac{\Delta V_P}{V_S}\right) - 2\left(\frac{V_S}{V_P}\right)^2\left(\frac{\Delta\rho}{\rho}\right),$$

$$C = A_3 = \frac{1}{2}\left(\frac{\Delta V_P}{V_P}\right).$$

For this arrangement, the variables remains the same as in Equation (4-9). The coefficients A, B and C in the equation refers to Intercept (R_0) or zero angle reflection coefficient (acoustic impedance contrast). B is known as a gradient or slope (G), which introduces the effect in shear velocities with angle variations in addition to compressional and density properties. C (A_3) is defined as the curvature of the amplitude response near the critical angle. Figure 4.6 illustrates the meaning of the tree coefficients in the Aki and Richards's approximation. In general, for seismic interpretation the range of angles is limited and not larger than 30 - 40 degrees, so the higher order terms are neglected (Simm et al., 2014).

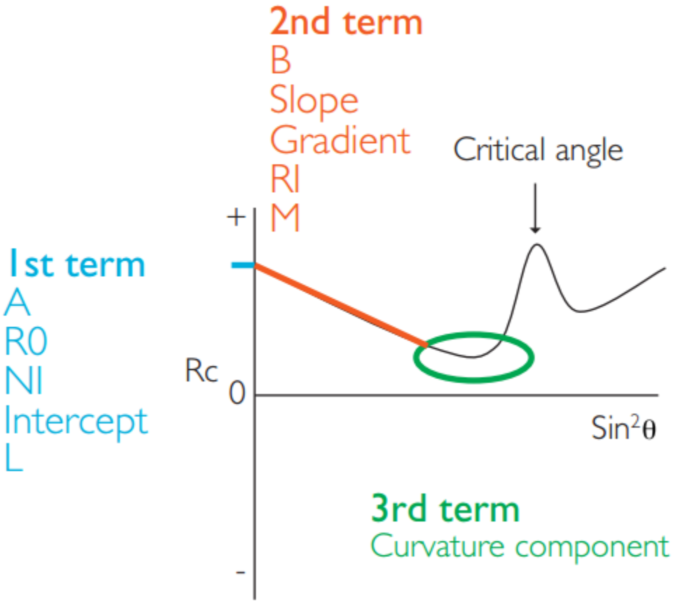

Figure 4.6: *Three components of the Aki and Richards (1980) approximation of the Zoeppritz equations. From Simm et al. (2014).*

4.3.2 Smith and Gidlow approximation

Smith and Gidlow (1987) came up with another approximation based on Aki and Richards's formulation, in order to perform a weight stack on the correct seismic gathers to obtain information about the rock properties. Firstly, they rearrange the Aki and Richards's equation obtaining the expression given in (4-11). In this case V_P and V_S are denoted as α and β (Feng and Bancroft, 2006)

$$R(\theta)=\left[\frac{1}{2}\left(\frac{\Delta\alpha}{\alpha}+\frac{\Delta\rho}{\rho}\right)\right]-2\frac{\beta^2}{\alpha^2}\left[2\frac{\Delta\beta}{\beta}+\frac{\Delta\rho}{\rho}\right]\sin^2\theta+\frac{1}{2}\frac{\Delta\alpha}{\alpha}\tan^2\theta. \tag{4-11}$$

From this equation an additional simplification was performed by using Gardner's relationship (4-12) to remove the dependency on density

$$\rho=a\alpha^{1/4}, \tag{4-12}$$

after differentiating, it gives

$$\frac{\Delta\rho}{\rho}=\frac{a}{4}\frac{\Delta\alpha}{\alpha}, \tag{4-13}$$

substituting Equation (4-13) into Equation (4-11) gives

$$R(\theta)=c\frac{\Delta\alpha}{\alpha}+d\frac{\Delta\beta}{\beta}, \tag{4-14}$$

$$\text{where } c=\frac{5}{8}-\frac{1}{2}\frac{\beta^2}{\alpha^2}\sin^2\theta+\tan^2\theta \text{ and } d=-4\frac{\beta^2}{\alpha^2}\sin^2\theta.$$

Solving Equation (4-14) by generalized linear inversion (GLI) via least squares in order to derive weights that can be applied in the seismic gathers to obtain estimates for $\Delta\alpha/\alpha$ and $\Delta\beta/\beta$. These quantities are defined as the fractional ratios of P- and S-wave velocities, respectively. Moreover, Smith and Gidlow derived other kind of weighted stacks, but related to a different rock properties such as: "Pseudo-Poisson's ratio reflectivity" and "Fluid Factor" (Feng and Bancroft, 2006).

In the same way, Goodway et al. (1997) showed a different way to estimate the P- and S-wave reflectivity variation as function of incident angle, expressing the Aki and Richards's equation in terms of P- and S-wave impedance relative changes ($\Delta I_P/I_P$ and $\Delta I_S/I_S$) as it shown in (4-15)

$$R(\theta)=\left[\frac{1}{2}\left(1+\tan^2\theta\right)\right]\frac{\Delta I_P}{I_P}-4\frac{\beta^2}{\alpha^2}\frac{\Delta I_S}{I_S}\sin^2\theta+\left[2\frac{\beta^2}{\alpha^2}\sin^2\theta-\frac{1}{2}\tan^2\theta\right]\frac{\Delta\rho}{\rho}. \tag{4-15}$$

From the previous equations and assuming that $\beta/\alpha=2$ in addition to the fact that the validity of this approximation is for small angles then $\tan\theta\approx\sin\theta$, hence the third term depending on the density vanishes given the following expression

$$R(\theta)=\left(1+\tan^2\theta\right)R_p-\left(2\sin^2\theta\right)R_s. \tag{4-16}$$

Goodway et al. (1997) also proposed the estimation of two additional AVO attributes in terms of Lame's constants scaled by density $\lambda\rho$ and $\mu\rho$. Those corresponds to the product of density and the elastic properties incompressibility and rigidity, respectively. He showed this with the aim of improving the petrophysical discrimination

$$\begin{aligned} \lambda\rho &= I_P^2 - 2I_S^2, \\ \mu\rho &= I_S^2. \end{aligned} \tag{4-17}$$

4.4 OptAVO

The Optimal AVO tool (OptAVO) was developed in SINTEF Petroleum Research by Causse et al. (2007). This tool overcomes the limitation faced by the standard linearized approximations, which are usually only valid for weak property contrasts along the interface, and they lose accuracy near the critical angle. These limitations might add significant errors in the estimation of the seismic parameters changes across the reflectors during the AVO analysis. The OptAVO tool is a model based approach that allows to compute AVO linear functions and attributes with a higher degree of accuracy. A general form of the linear AVO function can be seen as:

$$R(\theta) \approx C_1 f_1(\theta) + C_2 f_2(\theta) + C_3 f_3(\theta) + \cdots. \tag{4-18}$$

By comparing one of the Zoeppritz approximation and the equation proposed by Causse et al. (2007a), for instance (4-10) and (4-18), one can see that the basis functions C_1, C_2 and C_3 in the former equation corresponds to 1, $\sin^2(\theta)$ and $\sin^2(\theta)\tan^2(\theta)$ respectively. These trigonometric functions are then replaced by what it is called the optimal basis functions$f_i(\theta)$ (Causse et al., 2007a).

The model-driven AVO tool, estimates the optimal basis functions from rock physics models and well log data available. They are the input to the prior model, which is simulated via Zoeppritz equations in order to obtain a realistic distribution of the reference curves (N reflectors AVO models) at M different incident angles (Causse et al., 2007a). In addition, the basis functions$f_i(\theta)$ are calculated in such a way that they optimally describe each of the AVO modeled curves. In order to obtain the basis functions, singular value decomposition method (SVD) is applied to the **R** matrix, which contains the reference curves and whose dimension is *MxN*. The mathematical expression of this application is shown in Equation (4-19), where matrices **V**, **D** have the same dimension *NxN*, and **F** is have *MxN* matrix, correspondingly. **V** is orthogonal, **D** is diagonal and the columns of **F** are orthonormal. The column k of **F** is denoted by fk, hence Equation (4-19) can be expressed in an easier way as presented by Equation (4-20)

$$\mathbf{R} = \mathbf{FDV} = \mathbf{FW}, \tag{4-19}$$

$$R_j(\theta_i) = w_1 f_1(\theta_i) + w_2 f_2(\theta_i) + w_3 f_3(\theta_i) + \cdots + w_N f_N(\theta_i). \tag{4-20}$$

The AVO modeled curves can be easily expressed in the same form as Equation (4-20), where w_i refers to the weights or optimal AVO attributes. The largest weights are associated to the first functions, therefore this implies that f_1 will have the most contribution into the AVO reference curve distribution and f_2 the second most significant contribution and so on.

Even though, this optimized attributes do not have an obvious physical meaning, they can be used directly for fluid and lithology discrimination. It is important to mention that these attributes are related to the conventional attributes such as: intercept R_0, gradient G and curvature A_3, hence the OptAVO attributes can be transformed into a more accurate estimation of the conventional ones. This is done via establishing relations between the optimized and usual attributes since the reference curves are known. Hence their functions $R_j(\theta_i)$ can be expressed in the form (4-10) by using the analytical coefficients R_{0j}, G_j and A_{3j} ending up with the following expression

$$R_j(\theta) \approx R_{0,j} + G_j \sin^2(\theta) + A_{3,j} \sin^2(\theta) \tan^2(\theta). \tag{4-21}$$

Similarly, inverting Equation (4-19) gives an expression of the basis functions as linear combination of the reference modelled functions, indicating h_{jk} line j, column k of the matrix $\mathbf{H=W^{-1}=VD^{-1}}$ then system (4-22) is obtained. Then inserting Equation (4-22) in (4-21) provides analytical conventional AVO approximation of the basis function which can be introduced into Equation (4-10) as shown in Equation (4-23). Finally, back projection of the optimal attributes into more accurate estimates of the R_0, G and A_3 (Causse et al., 2007a).

$$f_k(\theta) = \sum_{j=1}^{N} h_{jk} R_j(\theta) \tag{4-22}$$

$$R_j(\theta) \approx \tilde{R}_0 + \tilde{G} \sin^2(\theta) + \tilde{A}_3 \sin^2(\theta) \tan^2(\theta), \text{ with}$$

$$\tilde{R}_0 = \sum_{j=1}^{N} R_{0,j} \sum_{k=1}^{L} h_{jk} C_k ,$$
$$\tilde{G} = \sum_{j=1}^{N} G_j \sum_{k=1}^{L} h_{jk} C_k , \quad \text{and} \tag{4-23}$$
$$\tilde{A}_3 = \sum_{j=1}^{N} A_{3,j} \sum_{k=1}^{L} h_{jk} C_k .$$

4.4.1. AVO classification scheme

The optimal AVO analysis proposed by Causse et al. (2007b) also includes a classification procedure. Several strategies were investigated in order to select the most suitable one. It allows to allocate a specific point *M* (measured attribute) into a corresponding class in the multi-attribute space, based on the shortest distance. The way this distance is determined in terms of the attributes relative importance has to be considered cautiously, since this will affect the discrimination between different classes and its sensitivity to noise (Causse et al., 2007b).

The distance definition is known as Mahalanobi distance. The inputs are the mean and covariance of the different attributes. Therefore it takes into account variances and correlations between the different attributes separately for each class. In addition, it is assumed that the input data follow a Gaussian distribution (Avseth et al., 2005). The expression for this distance, is given in Equation (4-24), where the $\mathbf{c} = [C_1, C_2, ...]$, $\boldsymbol{\mu}_\mathbf{i}$ are column vectors representing *M* at the centre of the ellipse for each class *i* in a optimize attribute space, correspondingly and $\sum_i^{-1}$ represents the covariance matrix for a given class *i*. The introduction of the inverse of the covariance matrix is capable to balance the relative contribution of the coefficients for the classification. In order to reduce the sensitivity to noise in the data, the covariance matrices for each class is modified by increasing the squared distance l^2 and L^2 of the minor and major axis of the confidence ellipse by σ_w^2 (white noise variance).

$$d_{Mi}^2 = \left(\mathbf{c} - \boldsymbol{\mu}_\mathbf{i}\right)^T \sum\nolimits_i^{-1} (\mathbf{c} - \boldsymbol{\mu}_\mathbf{i}) \tag{4-24}$$

Figure 4.7 illustrates the classification scheme by using two different classes whose covariance matrix representation is given by the confidence ellipses. Figure 4.7 a shows the approach if a simple Euclidean distance is implemented, from which is possible to see that the ellipse is more elongated along C_1 attribute direction than C_2. This is due to the fact that C_1 has higher weight in the SVD. This will lead to wrong classification because of the largest effective importance of C_1 over C_2. On the other hand, by using Mahalanobi distance as it was pointed out earlier, it is possible to give balance on the relative importance of the coefficients and at the same time minimizing the sensitivity to noise (see Figure 4.7 b).

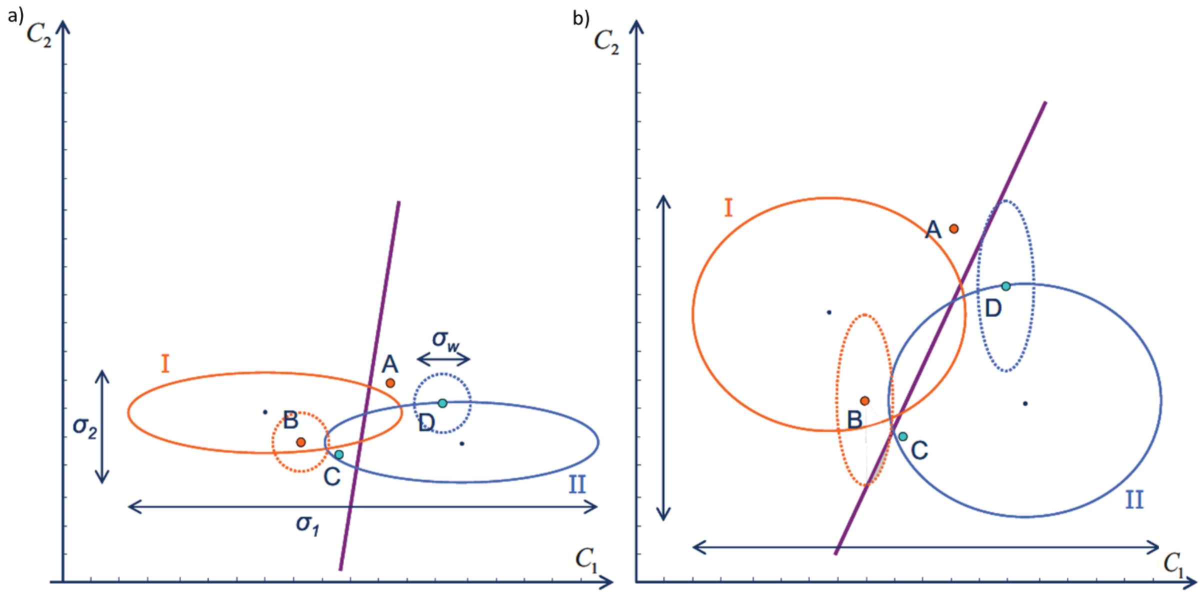

Figure 4.7: *Illustration of the classification scheme for different distance definition, which highlighted the trade-off between discrimination and robustness for noise. a) C_1-C_2 cross-plot with confidence ellipses for two classes, where point A and B are closer to the class I ellipse and point C and D are closer to the class II. The random noise is indicated by the circles around B and D, this noise has a variance σ_w, which would move B and D around these circles. If a normal distance is used as classification criteria the areas of the plot that are allocated to each class are separated by the straight line (wrong classification for C and A). b) Effect of elongation of the ellipse in the C_2 axis as a result of the balance on the relative importance of the coefficient. Consequently the noise is now represented by ellipses rather than circles. However, a good balance has been achieved and the points are properly classified. Figure modified from Causse et al. (2007b).*

Additionally to the noise stabilization, the reliability of the classification must be considered. There are three possible type of situation in which no class at all is defined: *i)* when points are too close or are exactly on the edge of two different classes, *ii)* when the distance to nearest class is too large, and *iii)* when the mismatch between the approximate and observed AVO curve is too large (Causse et al., 2007b).

4.5 Offset – Incident Angle domain relation

Zoeppritz equations and all of their approximations are function of the incident angle, however, the seismic data is recorded in terms of offset. These two domains are roughly similar, their relation is not linear and this must be considered into the processing and analysis schemes. Figure 4.8 illustrates the difference between common offset and common angle gathers, from where it is possible to see that in the offset domain the angle decreases with depth, whereas in the angle domain the angles remains constant with depth (Russell and Hampson, 2004).

The transformation from constant offset traces to constant angle traces is established via full ray tracing procedure. However, a good approximation can be estimated by using straight rays. The multi-layer medium involves the ray parameter *p* and the total traveltime *t*. This approximation is given by Equation (4-25)

$$\sin\theta = \frac{xV_{INT}}{tV_{RMS}^2}, \tag{4-25}$$

where x is a given offset, V_{INT} is the interval velocity for a particular layer, V_{RMS} is the RMS velocity down to the layer.

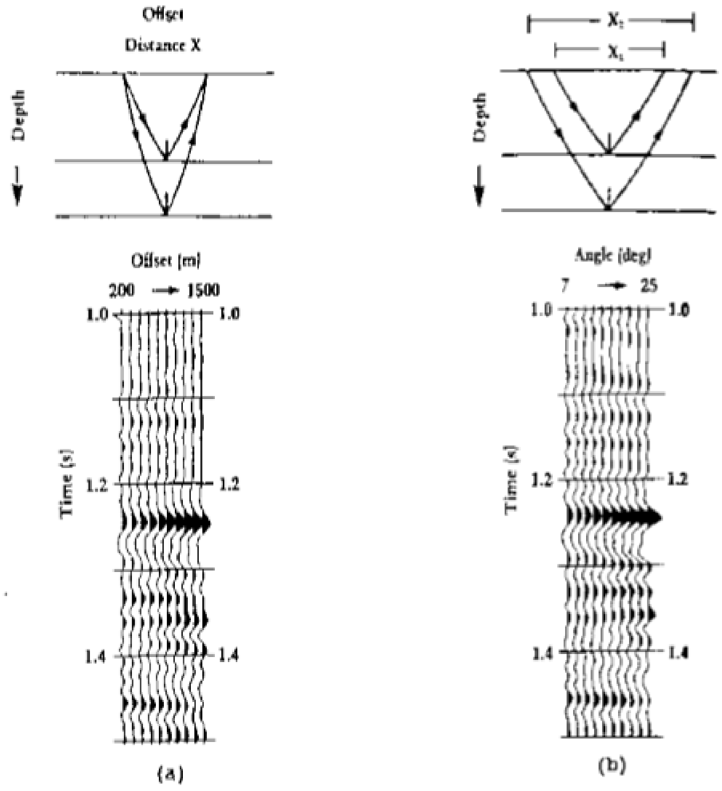

Figure 4.8: *Offset and Angle relation. a) ray geometry (top) AVO response (bottom). b) ray geometry (top) and equivalent response in angle domain AVA (bottom). From Russell and Hampson (2004).*

Chapter 5 Methodology

This chapter presents all the procedures and considerations in order to evaluate and understand the effects of attenuation on seismic amplitude through modelling. In addition, the real data application of an elastic AVO inversion is presented in the Utsira formation, in order to obtain estimation of the CO_2 that has been accumulated into the reservoir.

The modelling itself is divided in the two main groups: synthetic modelling and more realistic models. The former is mainly dealing with simplified models with the aim of having a better understanding how the attenuation can affect the seismic response, in terms of amplitude and phase distortion. The latter, shows more realistic models that are a closer representation of the Utsira sandstone in the Sleipner Field. In this case, the combination of tuning and attenuation effects are counteracting each other. It is important to take into consideration which effect is dominant in the response, since this will directly influence the AVO analysis.

Firstly, estimations of the reflection and transmission coefficients (R/T) as a function of incident angle are investigated for a purely elastic medium and viscoelastic medium. When it comes to elastic medium, all the layers are elastic (elastic-elastic contrast). For the viscoelastic or poroelastic case, they correspond to elastic/viscoelastic or elastic/poroelastic interfaces, which means that the shales are always consider purely elastic and the sands will be either viscoelastic or poroelastic. Secondly, a full wavefront propagation for elastic, viscoelastic and poroelastic media is performed to obtain their corresponding seismograms, from which is possible to extract and compare individual traces. Finally, real data application of Optimal AVO inversion (OptAVO, SINTEF Petroleum Research tool) is presented for two seismic sections at and near the injection point in the well 15/9-16A.

5.1 Attenuation modelling

5.1.1 Reflection and transmission coefficient estimation

In order to have a better understanding about how the anelasticity effects can affect the seismic response in terms of amplitude, a simple model of two half-spaces and one interface is simulated. This single interface is the boundary between a purely elastic cap-rock shale and a partially saturated poroelastic sandstone (brine – CO_2). Four different scenarios were tested, varying the water saturation S_w between 5, 20, 80 and 95%.

The poroelastic medium is simulated using the Biot's poroelasticity theory (1956), presented in Chapter 3. In the same way, the intrinsic anelasticity was introduced by using a patchy saturation model and the effective fluid medium model described in Chapter 3. The effective seismic properties for the poroelastic sandstones are computed at 30Hz, which corresponds to the dominant frequency in the seismic data of the Sleipner field. The seismic properties for the cap-rock shale (Nordland Group) are estimated from well log data, specifically the injection well 15/9-16-A.

From the well data, only compressional sonic, density and gamma ray logs are available to identify and compute the seismic properties V_P, V_S and ρ. The shear wave sonic log it is not available, therefore V_S is computed from the compressional sonic log by using Vernik's empirical relation (Mavko et al., 1988). Table 5-1 presents the seismic parameters of the cap-rock shale extracted from the well.

Table 5-1: Seismic parameters of the cap-rock shale estimated from well 15/9-16-A (Nordland Group).

	Seismic Property	Value
Shale	V_p (m/s)	2375,2
	V_s (m/s)	969,18
	ρ (kg/m^3)	2130,1

As it was mentioned early the computation of the seismic properties is based on appropriate rock physics models. For this particular case, the patchy fluid distribution is used. The input parameters to perform a rock physics forward model and obtain the seismic properties can be defined in terms of the fluid phase and the solid phase of rock. The former accounts for all the fluids which are occupying the pore space of the rock. These are described by their bulk modulus, density and viscosity. Regarding the solid phase of the rock, this one can be subdivided by the composition of the grain minerals and the structure of the rock frame. The characteristic of the grain minerals that compose the rock are defined by the bulk and shear modulus and the solid density of the rock. These parameters are computed taking into account the volume fraction of each mineral using Hashin and Shtrikman bounds (1963), for both the elastic moduli and the weighted average formula for the density. The rock frame is described by the undrained bulk and shear moduli, porosity, hydraulic permeability and cementation factor. Table 5-2 and Table 5-3 summarized the input parameters for the forward modelling and the estimated seismic properties and corresponding quality factor for the partially saturated sands.

Table 5-2: Properties of the solid and rock framework for the Utsira sandstone and properties of fluids phases.

Properties	**Parameter**	**Value**
Grain (solid mineral)	*Ks (GPa)*	39.29
	Gs (GPa)	44.8
	ρs (kg/m3)	2663.5
Frame	*KD (GPa)*	2.56
	GD (GPa)	0.85
	k0 (m2)	2 10-12
	Porosity ϕ	0.37
	m	1
Brine	*Kf1 (GPa)*	2.31
	ηf1 (Pa,s)	0.00069
	ρf1 (kg/m3)	1030
CO2	*Kf2 (GPa)*	0.08
	ηf2 (Pa,s)	0.00006
	ρf2 (kg/m3)	700
Sw	*V1*	1 , 0.95, 0.8, 0.2
Patches size (only for White model)	*a (cm)*	1

Table 5-3: Seismic Effective properties for Patchy and Uniform fluid saturation models.

CO_2-brine Sand	**S_w %**	**V_P (m/s)**	**V_S(m/s)**	**Density (kg/m^3)**	**Q_P**	**Q_S**	**Frequency (Hz)**
Patchy Model by White (1975)	95	1682	643.45	2053	7368.18	3541.86	30
	80	1487	646.15	2035.9	1806.02	3511.3	30
	20	1412.3	658.29	1961.4	903.52	637.08	30
	20	1450	684.5	1961.4	20	15	3000
	5	1412.9	661.39	1943.1	855.3	631.13	30
Uniform Model by Brie et al. (1981)	95	1933.64	643.45	2053	209667.10	3237.62	30
	80	1650.4	646.33	2034.7	40374.16	2458.80	30
	20	1404.95	658.3	1961.4	1135.62	867.18	30
	20	1430	673.8	1961.4	27.9	22.2	2500
	5	1411.26	661.39	1943.1	904.38	680.75	30

Once the seismic properties triplet are calculated assuming perfectly elastic shale and poroelastic sandstone, the reflection and transmission coefficients as a function of incident angle are computed using Zoeppritz exact solution (Chapter 4, Equation (4-8)). The incorporation of the attenuation is done through the introduction of the complex slowness (see Equation (3-42)) and keeping real values for the ray parameter p. The same computation is carried out for a pure elastic case, when the shale and the sandstone reservoir are both elastic. In this case, no complex reflection and transmission coefficients are computed. The complexity of these coefficients is mainly due to the anelasticity effects (velocity dispersion and attenuation). The quality factor Q is the main contributor of the coefficient's imaginary part at the pre-critical incident angle. The same estimation is done at 3000Hz only for the 20% S_w case and patchy model, since according to previous studies the highest attenuation and dispersion effects for this model are seen at this frequency and S_w range, where the Qp and Qs factors are considered low enough (20 and 15, respectively). Refers to Appendix A, Figure Figure A-1.

For this specific case no critical angle exists, since V_P of the layer below the interface is always less than V_P of the layer above. So the conditions according to the Snell's law to generate a refracted wave at critical angel is not met.

The real and imaginary parts of the reflection and transmission coefficients are estimated and plotted. In the same way, a direct comparison of the absolute value of the corresponding reflection and transmission coefficient for the elastic and anelastic case are plotted and compared.

5.1.2 Full waveform propagation simulation

The aim of this section is to evaluate the combining effect of layering and intrinsic attenuation due to mesoscale heterogeneities. In this case, the evaluation account for the full waveforms, which means that all type of possible waves (direct, surface, refracted), fast compressional wave, slow compressional wave known as Biot- P wave, conversion modes (vertically polarized shear wave SV) and multiple reflections are taking into account. The Biot-P wave is only computed in the poroelastic case. In previous work (Torres, 2016) this evaluation was done only considering incident and reflected P and S-wave individually, since it was a zero offset simulation.

There are some differences between the zero offset simulation and the full waveform simulation which can be summarized as follow: *i)* the input layer thickness can vary, however, the input model is still 1D (no lateral variations), *ii)* the computation of the seismic parameters for all the layers are based on Biot's poroelasticity theory for the poroelastic case, *iii)* acquisition geometry must be set, for instance receivers and source number, receiver distance and position, source type, minimum and maximum offset, *iv)* imaginary component of the angular frequency is included into the computations to dampen time aliasing. It also shifts the integration path singularities from the real *k*-axis to the complex one (wave number), *v)* the propagation matrix and the reflection and transmission coefficients are computed based on Kennett and Kerry formulation as it was presented in Chapter 3. Another important fact within the computation is that the geometrical spreading effect inherent to the wave propagation is taken into account.

The full waveform simulation is carried out for elastic, viscoelastic and poroelastic cases. The former needs only the specification of the seismic properties V_P, V_S and ρ of each layer. The viscoelastic case needs in addition the P- and S-wave quality factors, those are constant and frequency independent quantities (computation based on NCQ theory). In contrast, the poroelastic case requires the knowledge of rock physics parameters for each layer and the slowness and quality factor are frequency dependent and complex values. Due to that, these parameters for the elastic cap-rock shale and intra-shale layers in the Utsira reservoir must be determined.

For simplicity, it is assumed that the cap-rock shale and the intra-shale layers both have the same rock properties. These parameters are obtained from previous rock physics inversion models (Yan, 2016). Table 5-4 and Table 5-5 present the shale input parameters and its corresponding seismic parameter estimation, respectively. The latter, differs slightly from the values extracted from the well and previously presented in Table 5-1. However, these differences are inside the estimated uncertainty range and previous publications (Ravazzoli and Gómez, 2014, Carcione et al 2006). The cap-rock shale is modelled from the surface up to the top of Utsira sand. Therefore, the three consecutive seals are assumed to have the same rock properties (no variations with temperature and effective pressure are considered).

Table 5-4: Poroelastic properties of the Nordland Group shales and its saturated fluid.

Properties	Parameter	Value
Grain (solid mineral)	Ks (GPa)	22.6
	Gs (GPa)	1.2
	ρs (kg/m3)	2390
	KD (GPa)	2.26
	GD (GPa)	1.67
Frame	$k0$ (m2)	1.40 10-17
	Porosity ϕ	0.16
	m	1
	$Kf1$ (GPa)	2.31
Brine	$\eta f1$ (Pa,s)	0.00069
	$\rho f1$ (kg/m3)	1030

Table 5-5: Seismic properties of the cap-rock shale estimated by rock physics forward modeling.

	Seismic Property	Value
	V_p (m/s)	2391.8
Shale	V_s (m/s)	876.77
	ρ (kg/m^3)	2171.9

Additionally, the injection well is used to define the configuration for the stack of periodic layers present at the Utsira formation in the Sleipner field. Figure A-2 in Appendix A, illustrate this patterns indicating the top of each of the intra shale layers that have been interpreted in the area. Table A-1 in Appendix A summarizes the total number of layer (18 layers) with their respective top and bottom depths. The acquisition geometry is selected based on the real acquisition parameters which are shown in Table 5-6, Figure 5.1 illustrates the geometry setup for the simulations.

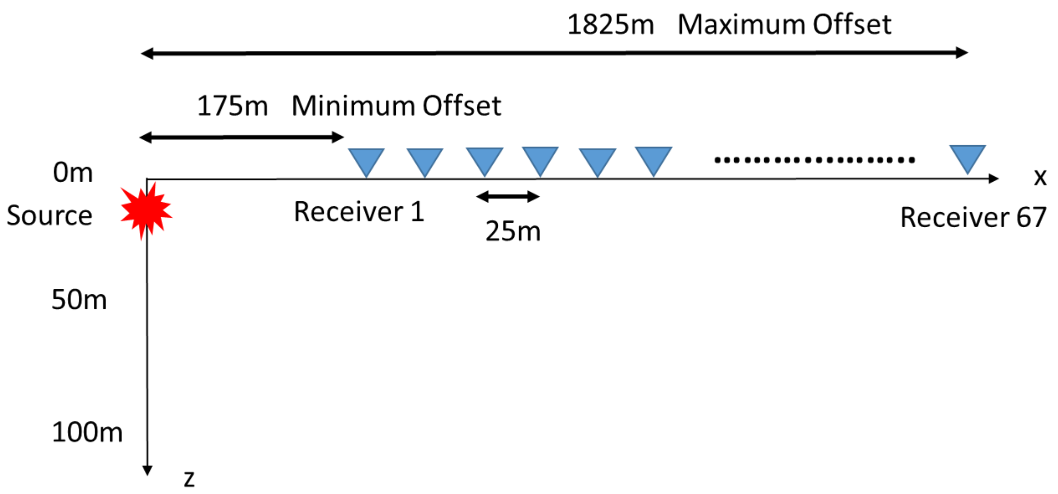

***Figure 5.1**: Sketch of the source and receivers geometry for the full waveform propagation simulations.*

5.1.3 Wave propagation in elastic and viscoelastic media

First of all, a simple model case is carried out in order to have a better understanding of the possible viscoelasticity effects into the wave propagation. In order to do this, an elastic model and a viscoelastic model are compared. The input parameters are the same as presented in Table 5-5. It is important to notice that the viscoelasticity is introduced by using a constant value of the quality factor. The complex phase velocities are computed by using the theory of Band-limited Near-Constant Q (linear independent in the frequency band) given in Equation (3-6).

The P-wave velocity model is given in Figure 5.2. Three layer model composite of a thick shale overburden (830m), an elastic/viscoelastic brine-CO_2 sandstone (about 200m thick) which is overlaying a shale is generated. Both shales are modeled as elastic layers with the same seismic properties. The water layer in this case is not included into the model, hence the simulation of the seismic acquisition can be seen as if the source and receivers are deployed at the seabed.

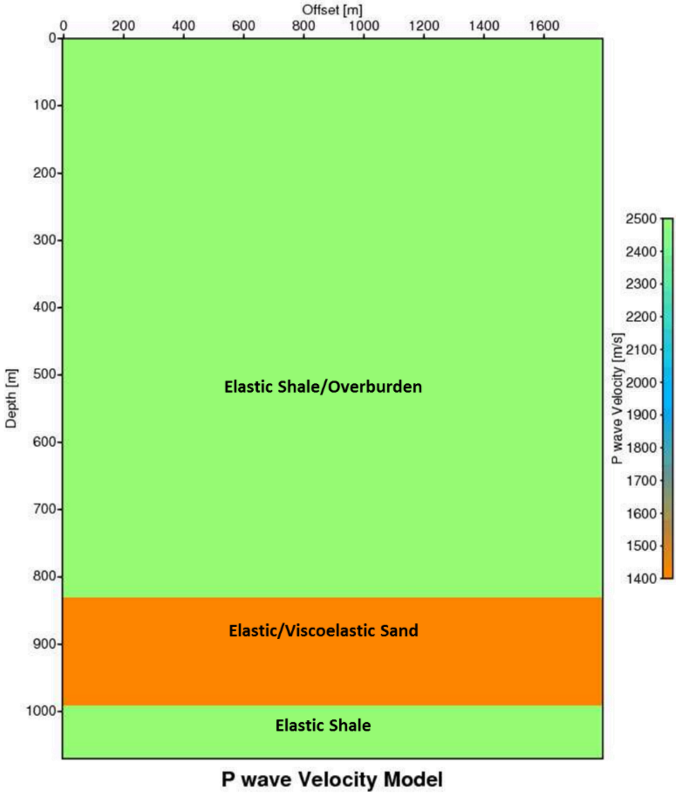

Figure 5.2: *P-wave Velocity model in Depth domain. From top to bottom 830.5m thick elastic shale (overburden), 200m thick elastic/viscoelastic sands (partially saturated with* CO_2 *and brine,* S_w*=20%) and elastic shale with the same properties as the overburden. The velocities for each layer are 2391.8m/s, 1405m/s and 2391.8m/s, respectively.*

The seismic properties of the sandstone are computed for a uniform fluid distribution, described using the effective average of the fluid properties at 20% S_w using Brie's equation. The test is done for the effective seismic properties computed at 30 and 2500Hz, corresponding to the viscoelastic model 1 and 2, respectively. The former being the dominant frequency of the seismic data and the second one is the attenuation frequency peak for the given fluid distribution case (See Appendix A, Figure A-1). For all simulations, the direct wave has been suppressed from the seismograms, since the main focus is on the reflected waves.

Moreover, the relation between the offset and incident angle is computed using Equation (4-25). In this way, it is possible to analyze the behavior of the magnitude and phase of the reflection coefficients and correlate it with the synthetic seismograms in order to discriminate the amplitude effects due to acoustic impedance contrast (reflectivity) and attenuation (see Figure 5.3). It is worth noting that the offset angle conversion was only performed for the PP waves, however, the difference between PP and PS are quite small at short offsets. Therefore, this relation is considered as reference for the PS case.

Figure 5.3: *Offset versus incident angle for the top and bottom PP reflection of the reservoir sand.*

Comparison of the elastic and viscoelastic seismogram are presented in the Chapter 6. In addition, extraction and comparison of near and far traces is done in order to associate the effects of the attenuation in terms of offset or incident angle.

5.1.4 Partial stack for enhancing attenuation effects

The main goal is the enhancement of the attenuation effects in the synthetic model. The AVO analysis of a 3D seismic cube involves some pre-conditioning process of the gathers. Beside the appropriate filtering, AVO friendly spectral balancing and geometrical spreading corrections what is called super gather, Ostrander gather or COS (common offset stack) is also performed. This step is part of the standard subroutines used in several seismic interpretation softwares. The common offset stack concept is to stack traces which are within a specific range of offset. This can be seen as a box whose dimensions are defined by an offset and CDP range. This concept is illustrated by Figure 5.4 (Russell and Hampson, 2004).

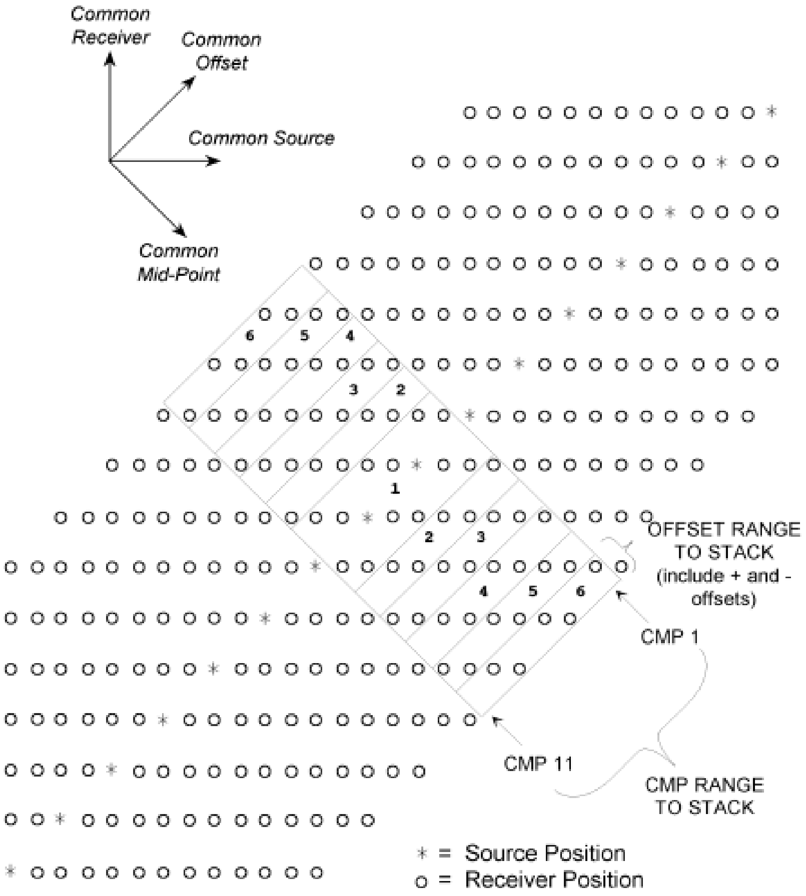

***Figure 5.4**: Acquisition layout illustrating all types of sorting data and pointed out the Common offset stack concept. Figure from Russell and Hampson (2004).*

The major advantage of the COS is to enhance the signal to noise ratio of the gather while, the offset domain is still preserved. As a result, any AVO anomaly can be seen more easily. However, some undesirable effects can be introduced to the data due to the inappropriate selection of the CMP and offset range. For instance, the selection of too many traces for both cases might cause structural smearing or amplitude distortions (Russell and Hampson, 2004).

For the reasons exposed above partial staking method is employed to boost the possible differences between the elastic and viscoelastic seismograms at different offset ranges. A brief description of the method is presented hereafter.

Firstly, it is assumed that the earth model is composed by homogeneous, isotropic and horizontal layers as it is shown in Figure 5.2. Therefore, the acquisition geometry for a single shot can be reproduced several times, which represents the total number of shots. Once all these parameters are defined the synthetic data of one single shot (2D line, single cable streamer) is repeated and all the corresponding headers are generated using Seismic Unix platform. The acquisition parameters and headers are given in Table 5-6 and Table 5-7. Figure 5.5 also depicts the acquisition geometry layout by indicating the x coordinate position of source and receivers (sx and gx headers, respectively), which simulates the movement of the vessel along the gx direction.

Table 5-6: Seismic acquisition parameters.

Acquisition Parameters	
Number of Shots	170
Cable Length	1650
Source Depth	0.1m
Number of Channels	67
Channel Separation	25m
Shot Separation	25m
Sample Interval	2.44ms
Record Length	2500ms
CMP spacing	12.5m
Minimum Offset	175m
Maximum Offset	1825m
Number of CDP	405

Table 5-7: Synthetic seismic data headers (*suheaders*).

fdlr (field record number)	Tracl (trace sequence number within a line)	sx (source x coordinate)	sy (source y coordinate)	gx (x group coordinate)	gy (y group coordinate)	sdepth (source depth)	offset (distance between source and group point)	cdp (cdp ensemble number)
1	1	0	10	175	0	0.1	175	67
1	2	0	10	200	0	0.1	200	66
1	3	0	10	225	0	0.1	225	65
1	4	0	10	250	0	0.1	250	64
⋮	⋮	⋮	⋮	⋮	⋮	⋮	⋮	⋮
170	65	4225	10	6000	0	0.1	1775	341
170	66	4225	10	6025	0	0.1	1800	340
170	67	4225	10	6050	0	0.1	1825	339

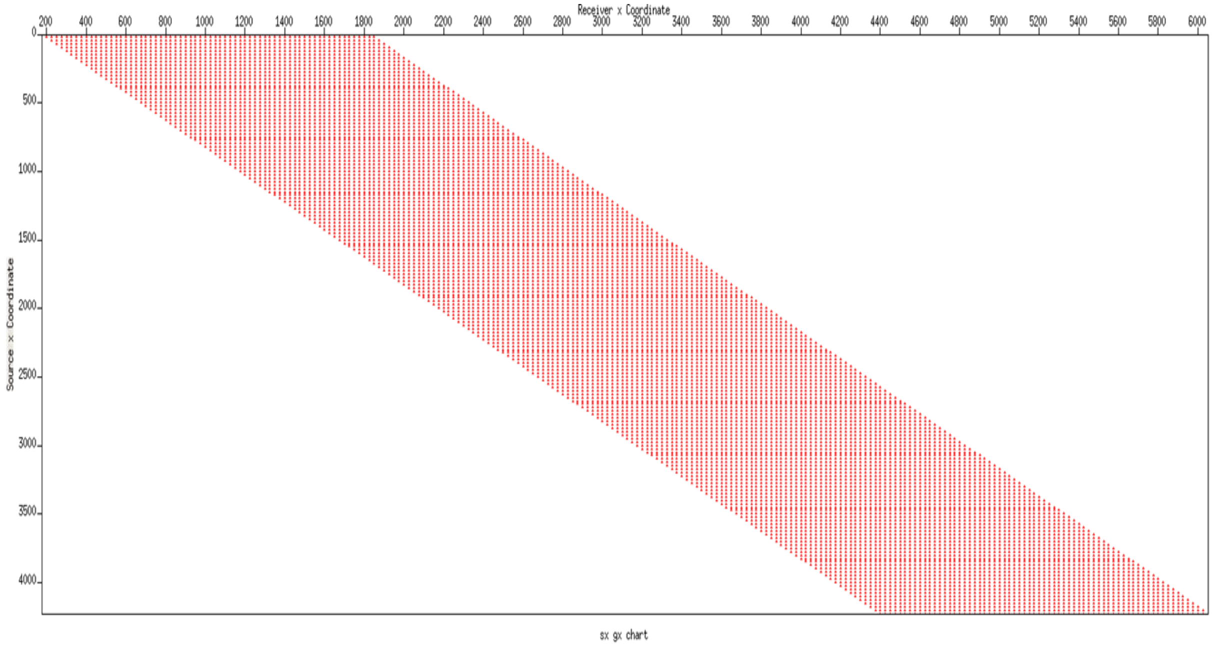

Figure 5.5: *Acquisition layout for the synthetic seismic data (2D seismic line by deploying several receivers in the seabed along the x direction). Source x coordinate is representing Y axis and the group x coordinates is representing the X axis.*

A quick inspection of the headers and shot gathers is done by using *surange* for the former and *suximage* or *suxwigb* functions for the latter. *Surange* function shows the range value of each header, those are shown in Table 5-8. In the same way, the other two functions allow to visualize the data in either variable density or wiggle form, respectively. This is very useful tool as quick quality control (see Figure 5.6). The shot gathers are then sorted in the common mid-point or common reflection point domain (CDP/CRP). It is important to notice that, since the model is based on horizontal layers these two concepts are exactly the same.

After sorting the data by CDP-offset a simple gain function is applied with the aim of improving quality of the semblance plot calculation and perform more accurate velocity picking. However, for this specific case any further processing is being applied to remove multiples or other type of unwanted waves. For example, converted P-SV waves. Hence, once the gain function is introduced by *sugain* specifying a simple relation that multiplies the data by t^2, it is possible to see that most of the noise has been boosted (see Figure 5.7).

Table 5-8: Header's value ranges obtained by *surange* function in Seismic Unix.

Header Value Range	Min.	Max.
tracl	1	67
fdlr	1	170
cdp	1	405
offset	175m	1825m
sx	0m	4225m
sy	10m	10m
gx	175m	6050m
gy	0m	0m
sdepth	0.1m	0.1m
ns	1026	1026
dt	2440µs	2440 µs
Total number of traces	11390	11390

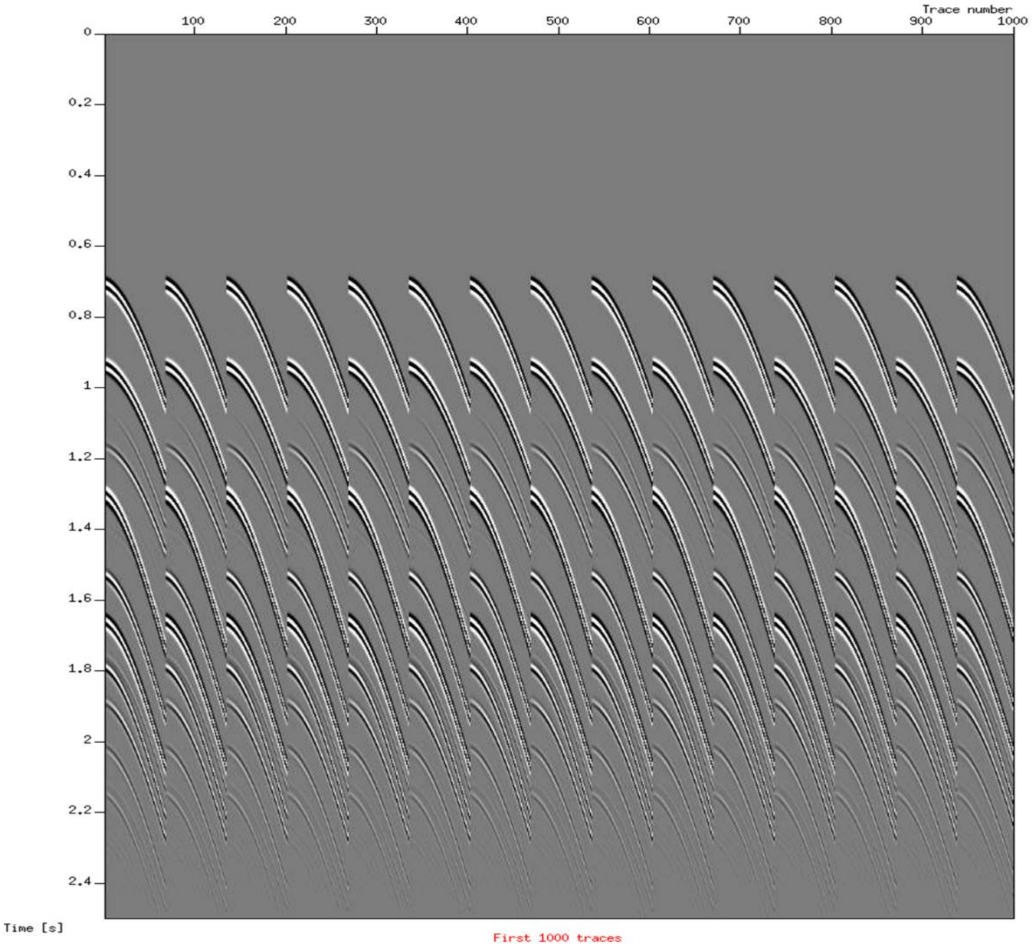

Figure 5.6: *Common Shot Gathers display. Visualization of the synthetic data as a first quality control. The first 1000 traces are shown by using suximage function in Seismic Unix.*

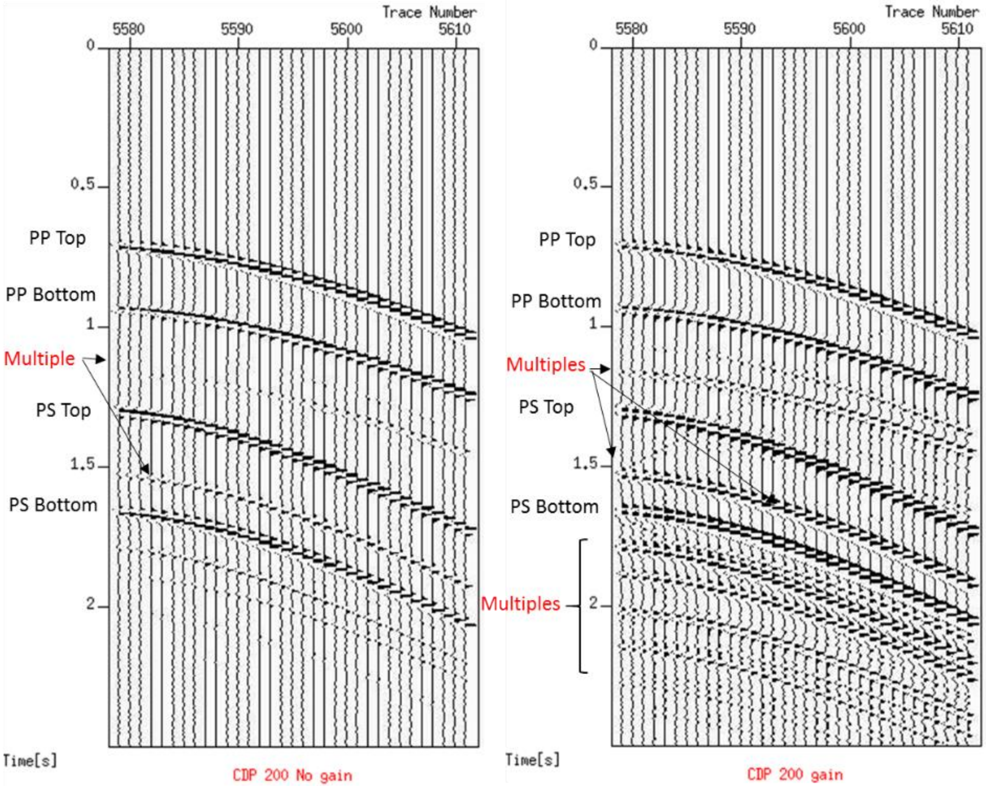

Figure 5.7: *CDP 200 comparison before and after amplitude gain. CDP 200 no gain (left). CDP 200 after gain (right). The identification of some important reflection from the top and base of the sand layer are highlighted, as well as, some possible multiple reflections.*

Since the velocity model only varies with depth a single velocity function is applied for the all the CDP gathers. Figure 5.8 shows a CDP gather before and after NMO correction with their corresponding velocity function obtained from the velocity picking in the semblance plot. A NMO mute is applied after the correction to suppress the stretching effect of the far offset traces. As it shows by Figure 5.8, only the PP reflections are properly corrected.

Finally, the partial stacks are generated by specifying the offset ranges. At this stage, the offsets are grouped in a way that all the stacks have the same size and trace number (22 traces). The near offset is defined from 175 to 725m, the mid offset from 725 to 1275m and the far offset are all the traces that fall in the range from 1275 to 1825m. The same procedure is carried out for both, elastic and viscoelastic cases. After, obtaining the partial stacks, the difference between them is computed. The partial stack and their differences can be displayed for comparison purpose.

Once the synthetic traces are computed those are loaded into Matlab, in order to extract a single trace and perform trace to trace comparison. The result are presented in the Chapter 6.

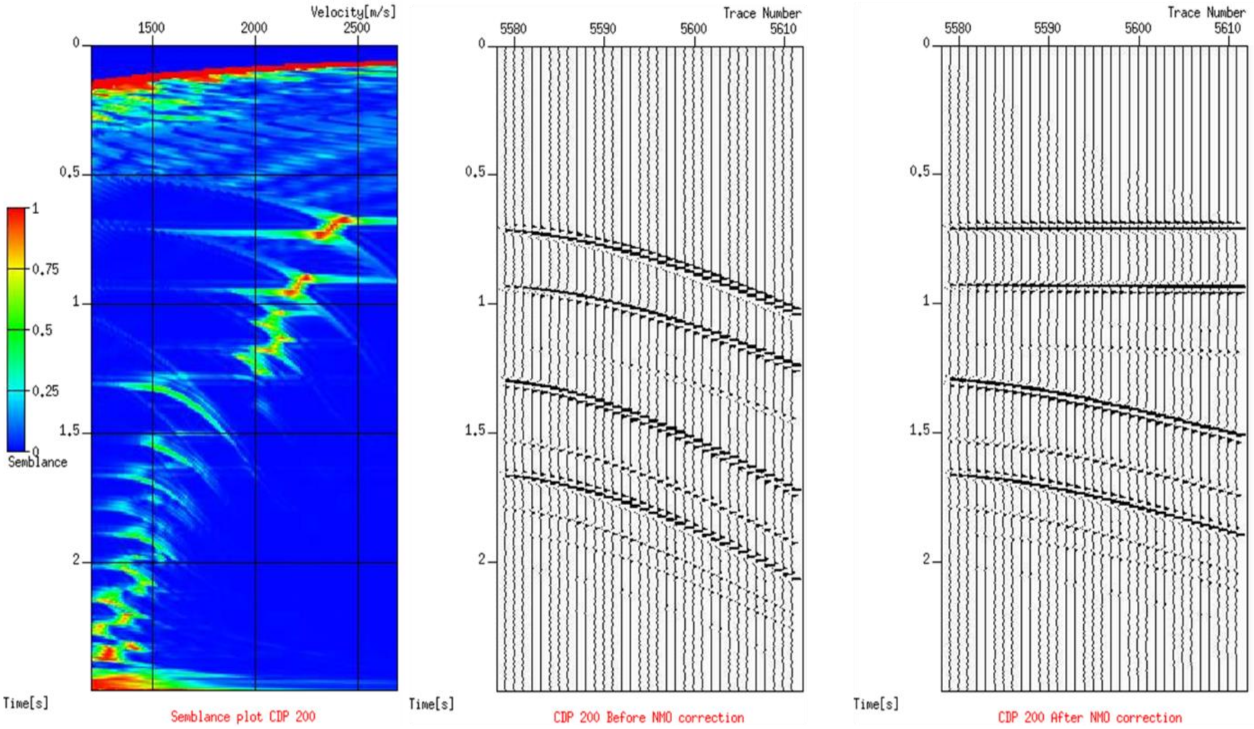

Figure 5.8: *Velocity analysis and NMO correction. Semblance velocity analysis (left). CDP gather 200 before NMO correction (middle). CDP gather 200 after NMO correction. The NMO correction is only applied for the PP reflections that correspond to the top and bottom of the sand layer.*

5.2 Realistic Cases

5.2.1 Zero offset simulation

A zero offset wave propagation simulation is performed in order to evaluate the effects of intrinsic attenuation and layering in a periodically stack of layers as it seen in the Utsira formation. In this case, the main focus is to evaluate the response in frequency domain to compare with further analysis from the full waveform propagation. A very simple model of constant thickness layers, which consist of 9 shales and 9 sands for a total of 18 layers was generated. The layer thicknesses is defined as d_1 and d_2 for shale and sand whose corresponding values are equal to 11.47 and 2m. This gives as a result a net-to-gross ratio (N/G) of 0.85. The total thickness of the model is 122m.

All the thin shales layers are considered elastic, whereas the sandstones are poroelastic media partially saturated with CO_2. The shale layers properties are P-wave velocity (V_{P1}) and density (ρ_1). In contrast, the sandstone velocity is frequency dependent and complex being denoted as V_{P2} (ω) and its density as ρ_2. The properties of the elastic shales and poroelastic sandstones are given in Table 5-1 and Table 5-2, respectively. The effective values of the seismic properties for the poroelastic sandstones are computed for Brie's model at 30Hz, which is the central frequency of the seismic data in Sleipner field. Both elastic and poroelastic approximation of the R/T responses are computed for P-waves using Equation (3-12) at different S_w values (20, 80, and 95%) in order to simulate different acoustic impedance contrasts. Figure 5.9 illustrates the acquisition and the layers configuration used for the simulation.

In addition, the energy loss for the wave propagating through the medium was computed using Equation (3-13).

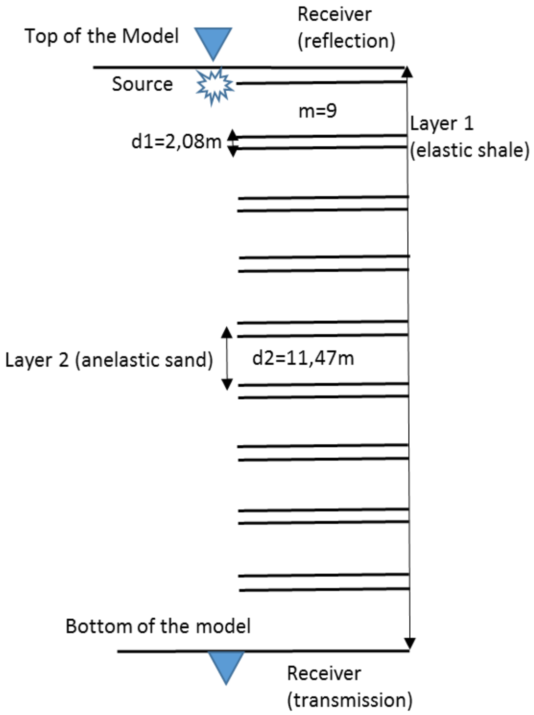

Figure 5.9: *Acquisition layout and geometry of the stack of periodic layers simulating the thin inter-layer shales and thick sandstones sequence with m= 9 number of cycles.*

5.2.2 Full waveform propagation

The same methodology as that presented in the Section 5.1 is applied for a more realistic cases, which resemble the staking patterns of the Utsira sandstone. At this stage, all sandstone layers are simulated with the same water saturation from top to bottom. The main idea is to understand the layering effect and how this is affecting by different CO_2-brine concentrations. Secondly, a more real case is carried out, in which the sand layers vary their CO_2-brine saturation according to reservoir models (Savioli et al., 2016). Figure A-3 in Appendix A, illustrates the most likely S_w levels for each sand layers around the injection well. It is worth noting that this reservoir simulation was done mimicking the CO_2 and brine simultaneous flow after 7 years of injection, therefore this model is taken only as reference.

According to this model the CO_2 saturation varies from top to bottom indicating higher concentrations near the injection point and at the uppermost layers of the Utsira sandstone. The average thickness for the CO_2 accumulations in its highest concentration (60-80%) is about 5 to 15m approximately. This has been previously reported by Chadwick et al. (2010). Just below larger accumulations the CO_2 saturation decreases gradually reaching 20 and 10% .The same pattern is shown for all the nine layers. Table A-2 in Appendix A, summarized the configuration of each layer and their corresponding CO_2 saturation. Figure 5.10 shows the P-wave velocity model built according to this criteria.

For the simulation with constant saturations, three different values are used: 20, 80 and 95%. Elastic, viscoelastic and poroelastic cases are computed. Special attention to the 20% S_w case is made, since this is the CO_2 concentration level that shows higher attenuation and dispersion effects. Figure A-4 in Appendix A, shows the P-wave velocity model for each case. Therefore one additional simulation is run, increasing the permeability of the Utsira sandstone from 2 to 200 Darcy. This nonrealistic value is used with the purpose of shifting the attenuation peak from 2500 down to 30Hz, in order to get Q values as those as Carcione's model. This is based on the Archie's law where the angular frequency ω_c is inversely proportional to the hydraulic permeability that is described in Chapter 3 by equation (3-32). The input parameters for the elastic, viscoelastic and poroelastic cases are the same as presented in Table 5-3 and Table 5-2.

Different comparison among elastic, viscoelastic and poroelastic cases are performed for trace 5 and trace 65. Results of this analysis are presented in the Chapter 6. The other two water saturation (80 and 95%) simulations are compared only for the elastic and poroelastic cases. In addition, the poroelastic cases, are compared among water saturation variations for near, mid and far traces. This is done to consider the AVO response.

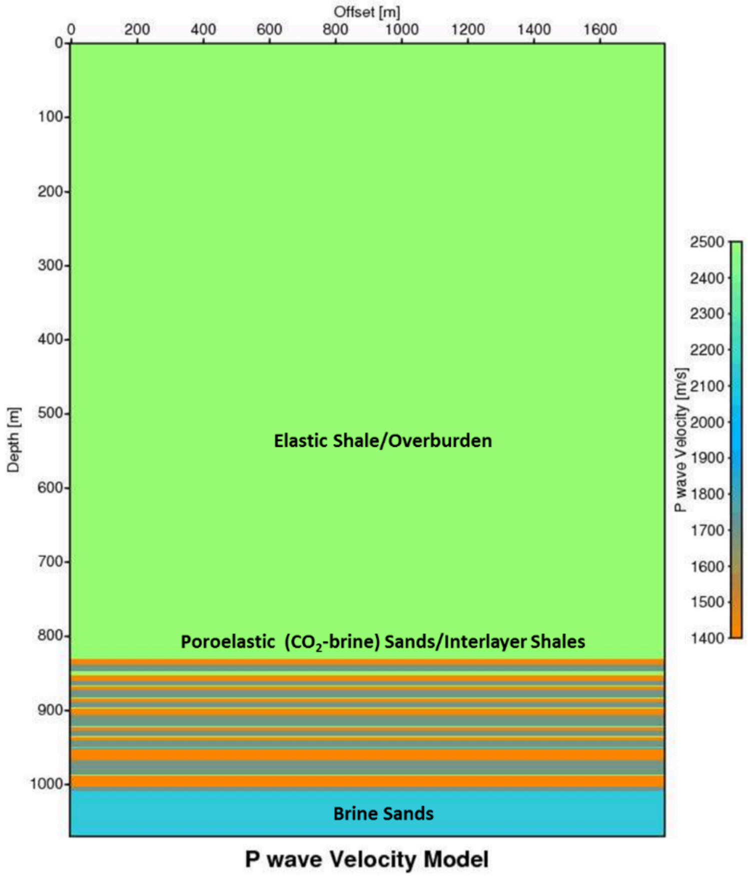

Figure 5.10: *P-wave velocity model based on reservoir simulations (Savioli et al., 2016) and thickness definitions by OptAVO tool (Chadwick et al. (2010). The overburden and interlayer shales have the same velocity of 2391.8m/s. Poroelastic sand present a saturation gradient from 80 to 20% with corresponding velocities of 1404.5 and 1650.4m/s and at the bottom of the model (1070m depth) brine sands with P-wave velocity of 2050m/s.*

5.3 Real data applications AVO inversion

This subchapter presents the methods to carry out OptAVO inversion by using the internal AVO tool developed by SINTEF Petroleum Research. The AVO inversion is performed for 2D seismic sections extracted from a 3D PSTM (Pre Stack Time Migrated) cube. This seismic vintage in the Sleipner field was acquired and processed in 2008. It corresponds to a 12 years after starting the injection process in 1996. The procedures are described herein.

5.3.1 Seismic and well data availability

The seismic cube for 2008 vintage has been provided by courtesy of Statoil S.A. The 2D seismic sections extracted are located at the injection point and 542m away of it, at the end of the injection well trajectory (well 15/9-16/A). These lines were selected since from the former it is possible see the upwards migration of the CO_2 plume and the latter can be comparable with future Full Waveform Inversion (FWI) results. Figure 5.11 shows the location of the 2 seismic lines 1838 and 1880, respectively. A brief description of the processing sequence applied to the data is summarized in Table B-1 (see Appendix B).

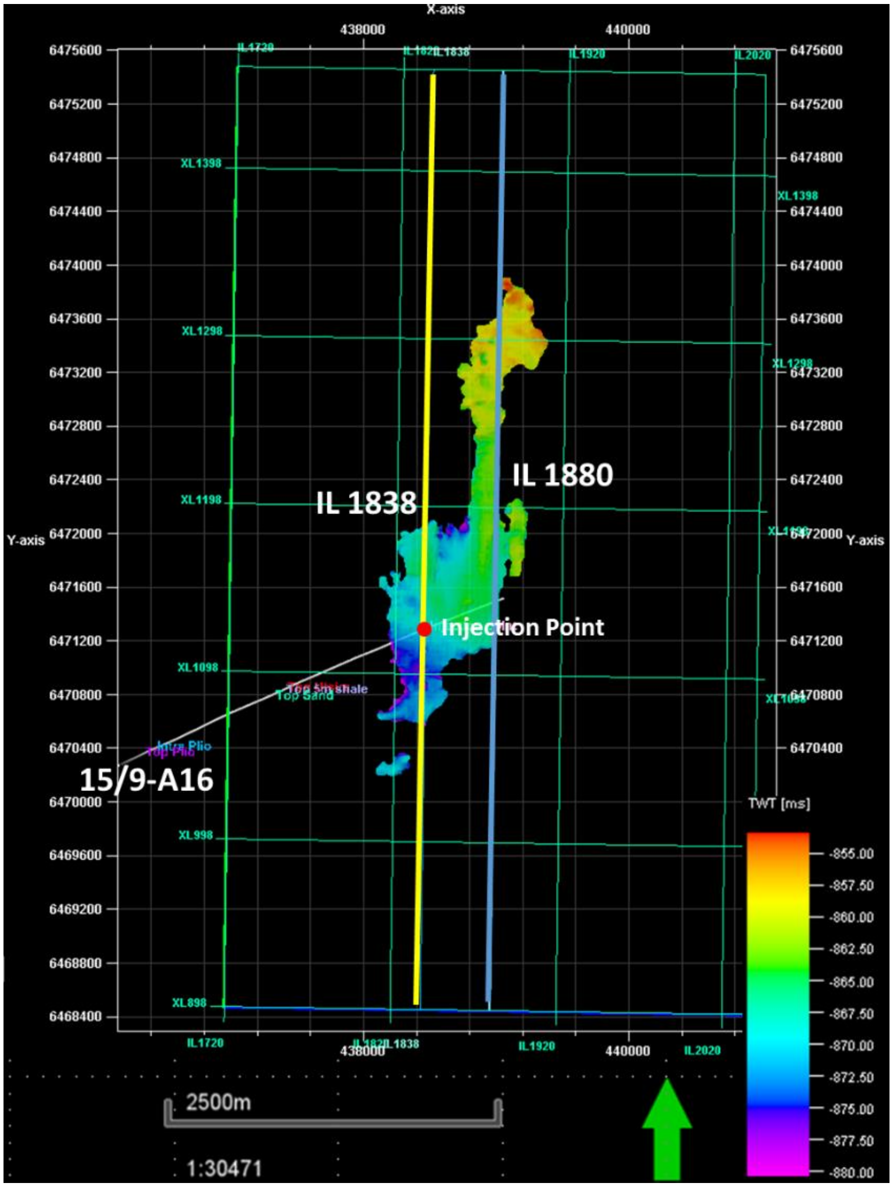

Figure 5.11: *Base map showing the injection well trajectory (well 15/9-A16) and the location of the injection point (red dot). The seismic survey grid is shown in green and two seismic sections corresponding to Inline 1838 and Inline 1880 are denoting by yellow and blue lines respectively. The head of the borehole and its vertical section are outside of the seismic survey, Inline 1838 is intersecting the injection point and Inline 1880 is at the toe of the well trajectory. The topmost CO_2 layer interpretation is also shown with its corresponding colorbar in TWT (ms).*

In order to perform a reliable AVO characterization, it is fundamental to have a good CDP gathers quality. A quick quality control of the preconditioning of the gather before AVO analysis of the data is done, where extraction of a CDP range (7 CDP) is visualized in Seismic Unix. The selection of the CDP ranges is divided by three extraction windows as follow, one at the left hand side of the CO_2 plume, one at the plume and one at the right hand side of the plume, which are indicated as a), b) and c) zones, respectively, (see Figure 5.12).

It is important to note that some residual move-out is still present in the data, for instance in Figure 5.13 a. At the top reservoir, around 0.86s the gathers show stretching effects at far offsets due to some inaccurate velocities (overcorrections). In addition, possible anisotropy effects can introduce inaccuracy in the velocity estimation since the travel-time curve is no longer hyperbolic. Moreover, coherent noise might have not been completely removed. However, the data at the top of the sand and 5m thick shale look pretty flat (0.86 and 0.9s approximately). Similarly, inside the CO_2 plume the quality of the gathers is reasonably good, and it is noticeable the difference regarding the reflectivity and visibility of additional reflectors just below the top of the Utsira sandstone, that are completely absent outside the CO_2 plume a) and c). These observations must be considered during the analysis of the data. The same data quality control is carried out for the Inline 1880 (Figure B-1 and Figure B-2 in Appendix B).

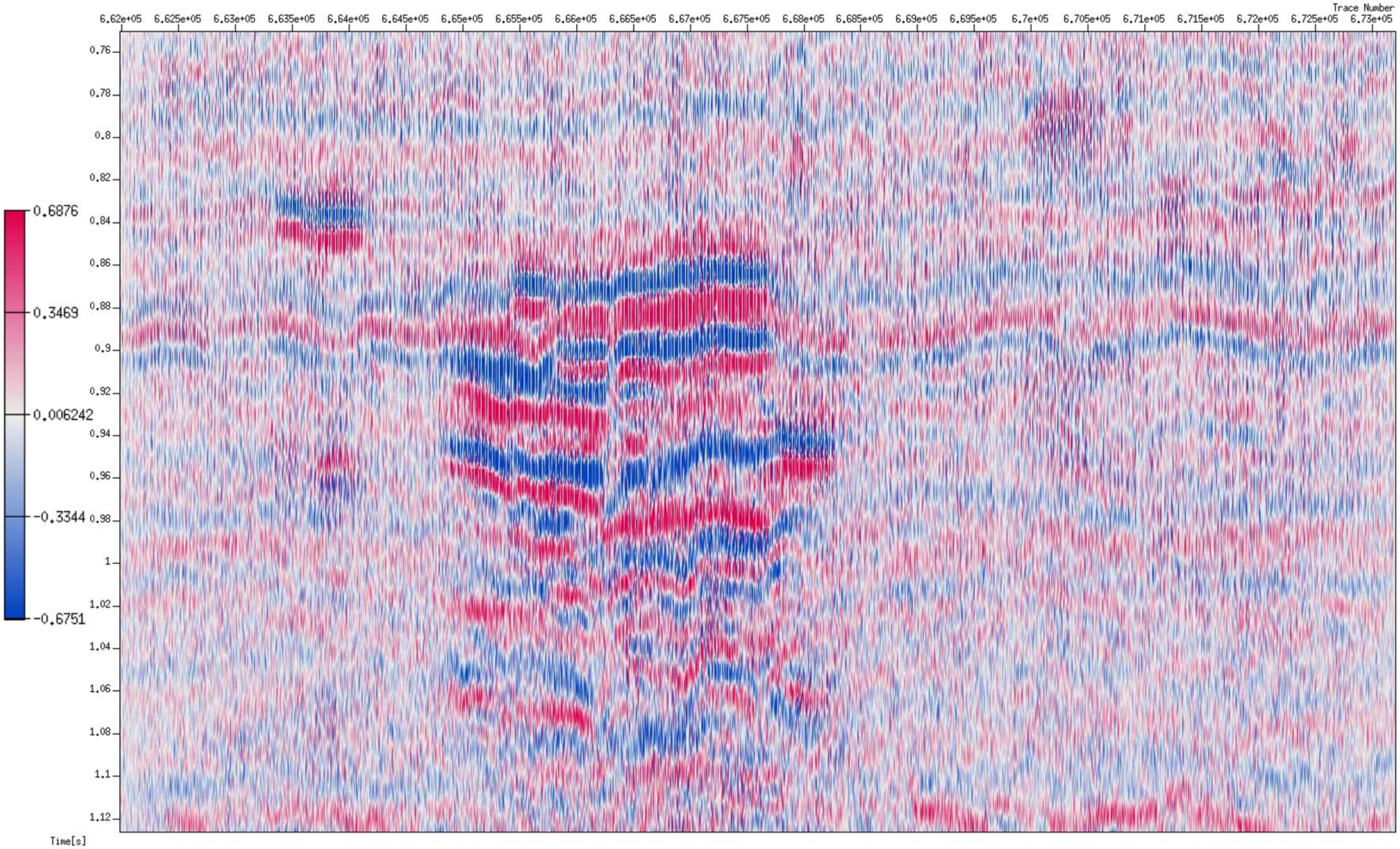

Figure 5.12: *PSTM CDP gathers extracted from Inline 1838 within the time window from 0.750s to 1.125s and CDP range from 898 to 1458 (total of 561 CDP).*

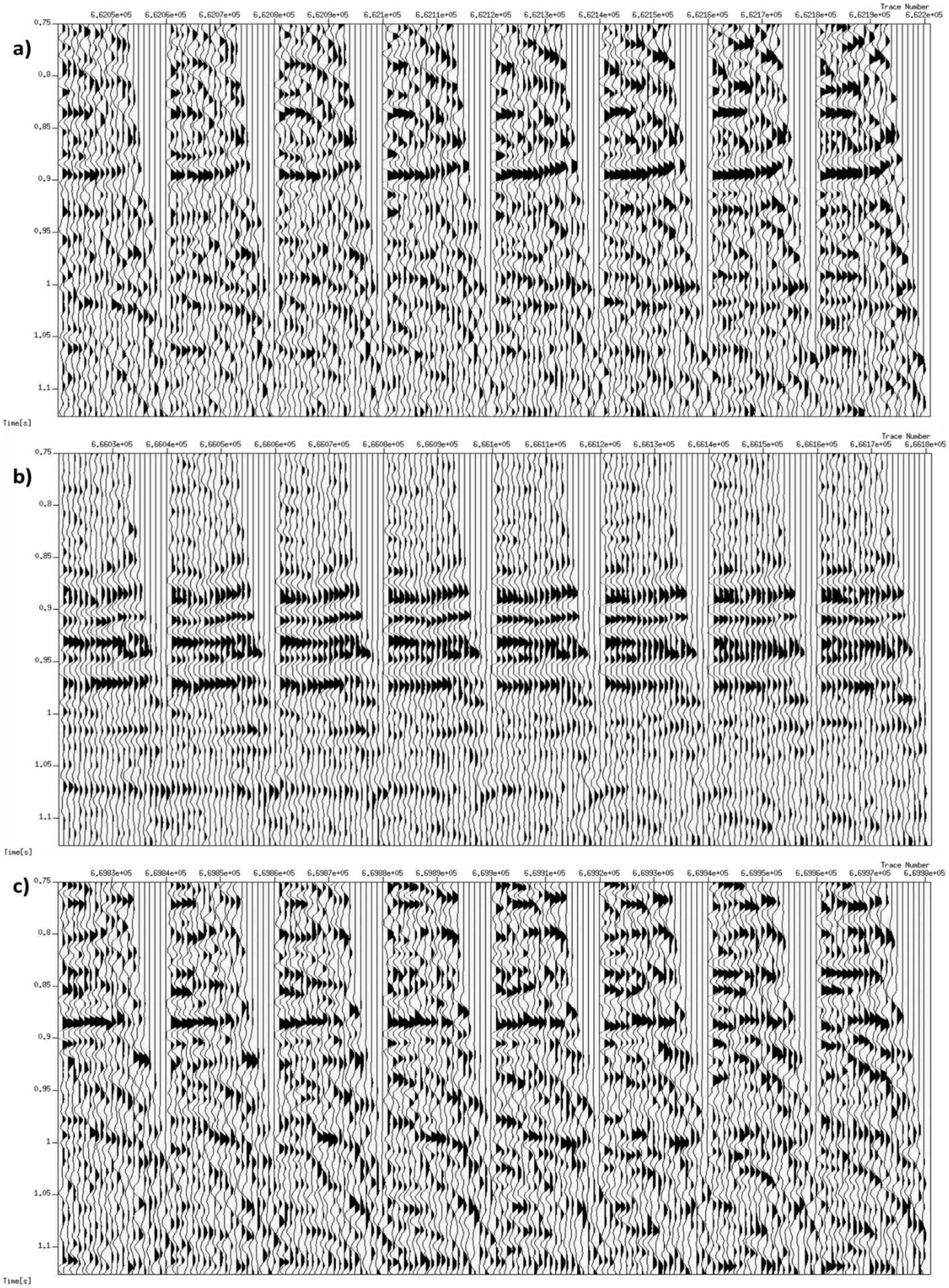

Figure 5.13: *PSTM CDP gathers extraction in wiggle display from the Inline 1838. a) CDP gather range 901-908 at the left hand side of the plume, b) CDP gather range 1100-1107 inside the CO_2 plume, c) CDP gather range 1290-1297 at the right hand side of the pume as indicated in Figure 5.12.*

The OptAVO tool, has some specific requirements that must be fulfilled in order to use it. The number of traces per CDP must be regular, the number of time samples and depth samples from the wells should be equal. As it was mentioned earlier, the optimal AVO inversion is mainly model driven approach, which implies a strong dependency of the well input parameters to model the AVO reference curves. The well information available is only a few meters above the reservoir sand, it does not reach the base of the sandstone (694 – 1070m) and it is away from the 2D section for about 2800m approximately. Therefore, the seismic lines must be also limited to its equivalent range in time e.g. 750 – 1125ms. Inside this time range it is possible to capture the CO_2 plume development from the injection point to the uppermost layer where the CO_2 is expected to be in its highest concentration trapped by the overlaying shale drape or cap-rock (Nordland Group Shale).

For the reasons exposed above, the Inlines 1838 and 1880 have been cropped within CDP and time interval ranges. Total number of CDP extracted is 561, whose CDP number goes from 898 to 1458. Each CDP has 20 traces that gives a total of processed traces equal to 11220, whose offset range is from 287 to 1712m. The offset increases by 75m. The time range is from 750 to 1125ms. Table 5-9 summarized the header ranges for the data (Inline 1838). The same information for the Inline 1880 is given in Table B-2 (Appendix B).

Table 5-9: Header ranges for Inline 1838 extracted from a PSTM vintage 2008.

Header Value Range	Min.	Max.
tracl	661981	673200
cdp	898	1458
offset	287m	1712m
sx	438424.55m	438528.76m
sy	6468452.75m	6475451.98m
gx	1838m	1838m
gy	898m	1458m
ns	189	189
dt	2000µs	2000 µs
Total number of traces	11220	11220

Regarding the well information, it is the same as the one used in the synthetics cases for the attenuation modelling. In addition to P-, S-wave velocity logs and density one additional estimation is computed in order to obtain a porosity log. The porosity log is computed from density via density-porosity relations. The main goal is to generate synthetic well logs that simulate the seismic properties after CO_2 injection, since this information is not available. This fluid substitution is carried out using the Biot's theory in combination with average approach to homogenize the fluid phase, for instance Brie's Equation (3-28). Its flexibility in allowing us to reproduce a wide range of possible mixing laws by changing the e exponent to be equal to 1, 5 and 40.

Firstly, the data is read from Seismic Unix into the OptAVO code in Matlab. This first step captures all relevant information from the seismic headers, such as: sample rate, trace length, number of CDP, number of trace per CDP, number of offset and minimum and maximum offset among others. The ray parameter is computed and a simple angle-offset conversion is performed based on a plane-layer ray tracing in a smooth depth –velocity model function as input. This approach is for PP reflections only. Since the ray tracing needs as input a single velocity function, this one is taken from the interval velocity model converted to depth outside the CO_2 plume. A map with the angle versus offset relation is shown in

Figure 5.14, from where it is clear that the incident angles decrease with time/depth. In the same way, at the same time/depth level, the incident angle increases with offset. Around the target level, from the top of the Utsira sandstone and the injection point (0.865 – 1.045s), the maximum angle range is approximately from 30 up to 45 degrees from the deepest to the shallowest point around the CO_2 plume.

The next step is called lithology definition. The lithology definition is the extraction of the well information and definition of the lithofacies based on previous knowledge of the area, wells and rock physics models. This is considered as quite important stage, since the geological model is the input for the generation of the reference reflectivity models and subsequence AVO reference curves. The well logs are upscaled from 2.1cm to 0.5m in order to be comparable to seismic and have the same number of samples as every trace in the seismic section. The input information from the well is depth, gamma ray, P-wave sonic and density. The shear wave velocity is computed using Vernik’s empirical relation (Mavko et al., 1998) and the total porosity log is also computed and used as an input to the synthetic generation of the well after CO_2 injection.

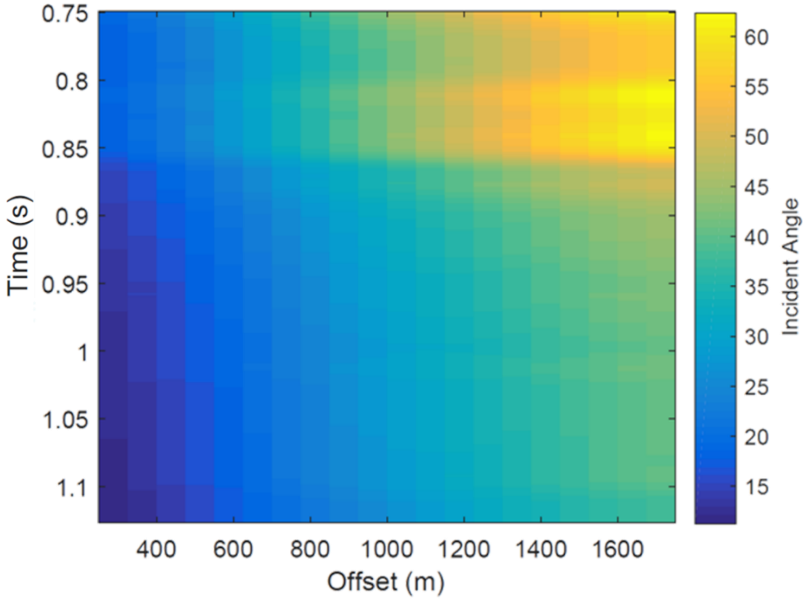

Figure 5.14:*Offset – Incident Angle relation as funtion of time/depth. The colorbar represent the incident angles.*

The poroelastic properties of the cap-rock shale, inter shale layers and the sandstone reservoir are kept constant as reported in Table 5-2 and Table 5-4. This implies that no changes in the rock frame are taken into account in terms of temperature and effective pressure, at least between 694 – 1070m deep. The same assumptions are made for the fluid properties. The CO_2 around this range of depth is considered in its supercritical point. Therefore, their CO_2 values are computed at 8MPa and around 28°C (effective pressure and temperature) using Erik Lindeberg's CO2Therm tool that solves the equation of the state given by Span and Wagner (1996).The brine properties have been defined based on several authors (Furre et al., 2015, Gasda et al., 2012, Ghaderi and Landrø, 2009), also considering its dependency on temperature, pressure and salinity.

The synthetic well logs are computed for different CO_2 saturation, for instance 0, 10, 20, 30 and 80%. The former is done with the purpose of testing the rock physics forward modelling. Figure 5.15 shows the synthetic results for 100% water saturation compared with the real data. It is noticeable that the shale estimation properties difference are much larger than in the sandstone intervals, this might be related to the high uncertainty in the definition of the shale parameters itself. Similarly, it seems that the estimated shear wave velocity presents a considerable difference compare with the estimations results from Vernik's relation. However, by computing the difference between synthetic result and real data are around +-150 up to 200m/s within the shale intervals. On the other hand, for P-wave velocities, the difference are slightly higher being around -100 to 300m/s.

Even though, the difference in the seismic properties for the shale are not reproduced with high level of confidence, the sands properties which are of interest for the fluid substitution simulation are quite well estimated or at least they show less variations. The difference between the synthetic brine sand and the information recorded in the field is much less being approximately between+-100m/s for P-wave and S-wave. Finally, no difference are recorded for the density log, since this is perfectly overlapping on top of the recorded field data (see Figure 5.15). The difference results are shown in Figure 5.16.

Additionally, it is important to keep in mind that the shear wave velocity was not recorded from the field. It was obtained via empirical relations from the compressional wave. This means that there is an added uncertainty in its values.

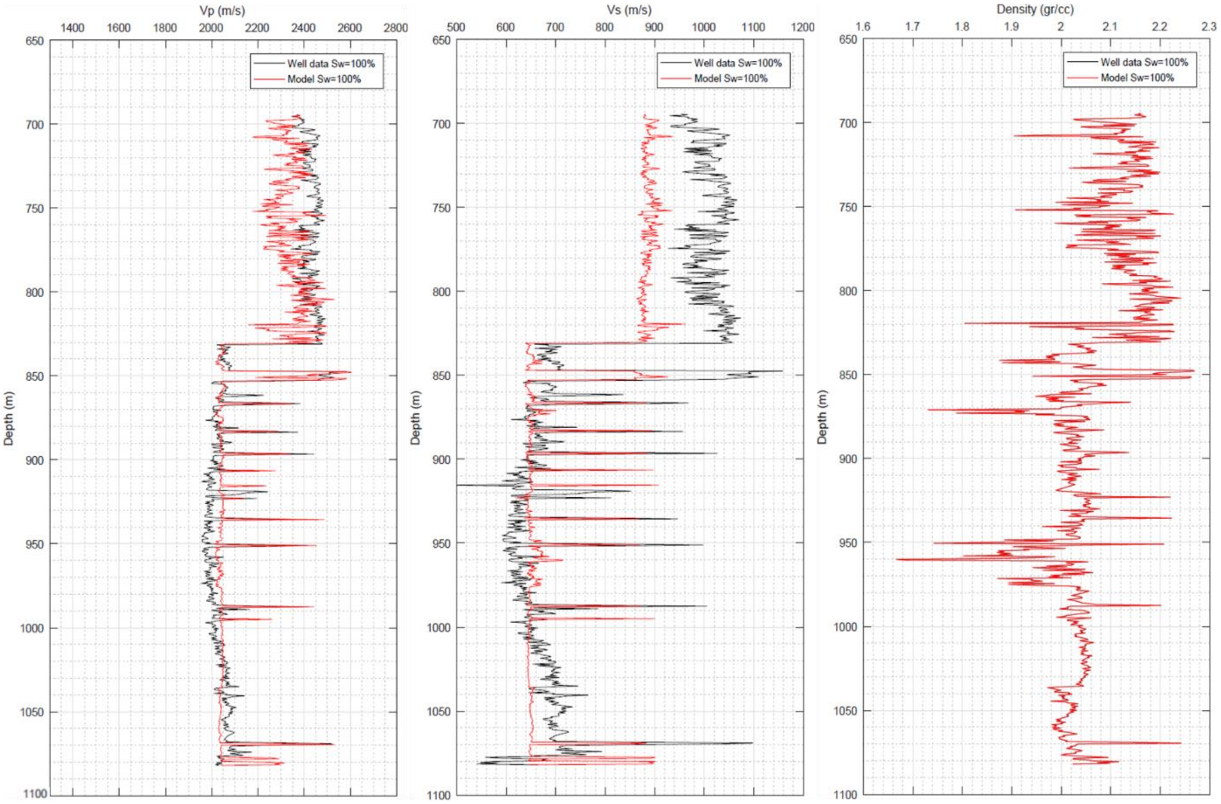

Figure 5.15: *Original Well logs (black) compared with synthetic logs generated via rock-physics forward modelling (red) displayed in true vertical depth (TVD) before* CO_2 *injection. From left to right P-wave velocity, S-wave velocity and density.*

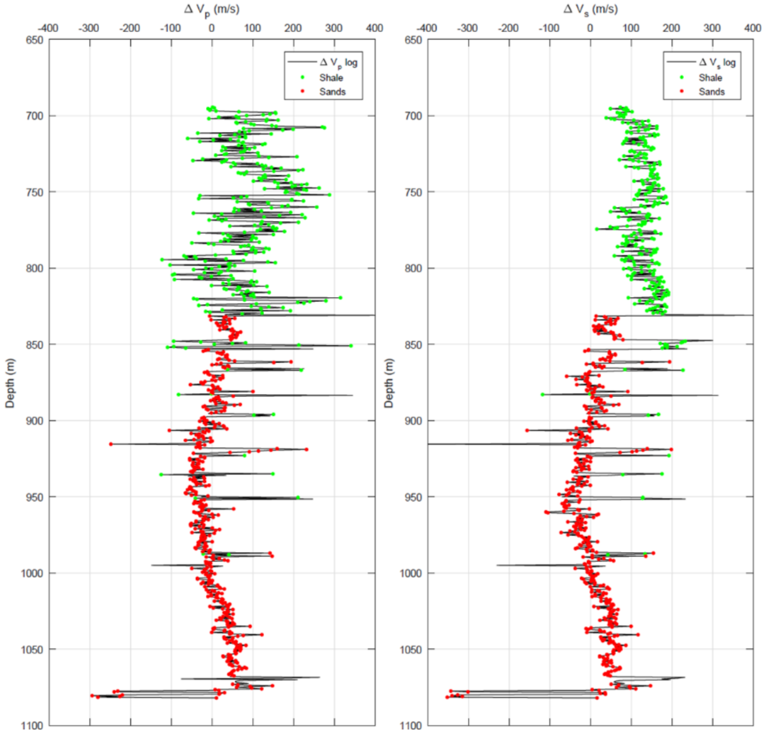

Figure 5.16: *Well logs difference between original and synthetic data before $C0_2$ injection. Shale and sandstones intervals are indicated by green and red dots, respectively. P-wave velocity (left) and S-wave velocity (right).*

5.3.2 Lithofacies and AVO reflection models definition

The lithofacies are then defined along the well, indicating their corresponding depth. In this case 5 different facies are selected: shales (cap-rock and interlayer shales), brine sands, CO_2 brine sands with 20, 70, 80 and 90% water saturation. Regarding the partially saturated sandstones, since there is not precise information about the thickness of these accumulations, the highest CO_2 saturation is expected to be in the upper most part of each sand layers with an average thickness of about 4 and 10m approximately (Chadwick et al., 2010). From this point to the bottom of each layer is assumed higher water saturation levels, for example 80 and 100% inside and outside the plume, respectively. This simplified model is based on Savioli et al. (2016) reservoir simulation results. Even though this model is used as starting point, all the possible CO_2 saturations and classes are generated and evaluated for each depth along the section.

From these facies definitions, it is possible to compute the depth trends and obtain mean values, as well as, the standard deviation of each seismic properties (See Figure B-3 in Appendix B). From these values, the cross correlation matrices, which determine the grade of variability and dependency of the three parameters are also computed. Several cross-plots of the seismic properties are generated to evaluate the AVO feasibility, e.g. V_P-ρ, V_S-V_P, Acoustic Impedance-V_P-V_S ratio, V_S-ρ and $\lambda\rho$-$\mu\rho$ (see Chapter 6).

The next step involves the generation of the reflectivity models and AVO reference curves. The former is needed to define the AVO classes. Several reflectivity realistic scenarios at each interface (for each depth/time level along the section) are generated based on the model. For instance, shale above brine sands that can be found along the section outside the CO_2 plume. Another possibility could be shale above 80% CO_2 – brine sand inside the plume. Figure 5.17 shows the AVO reflector classes that are being considered as input of the geological model. For example, the first row and first column represent the shale/shale reflector class, the second column is shale/brine sands, the third is shale/sand CO_2=80% and so on. In this case, since the main goal is to have an estimation of the CO_2 saturation in the Utsira formation most of the classes are represented by shale on top of sandstone with different values of S_w.

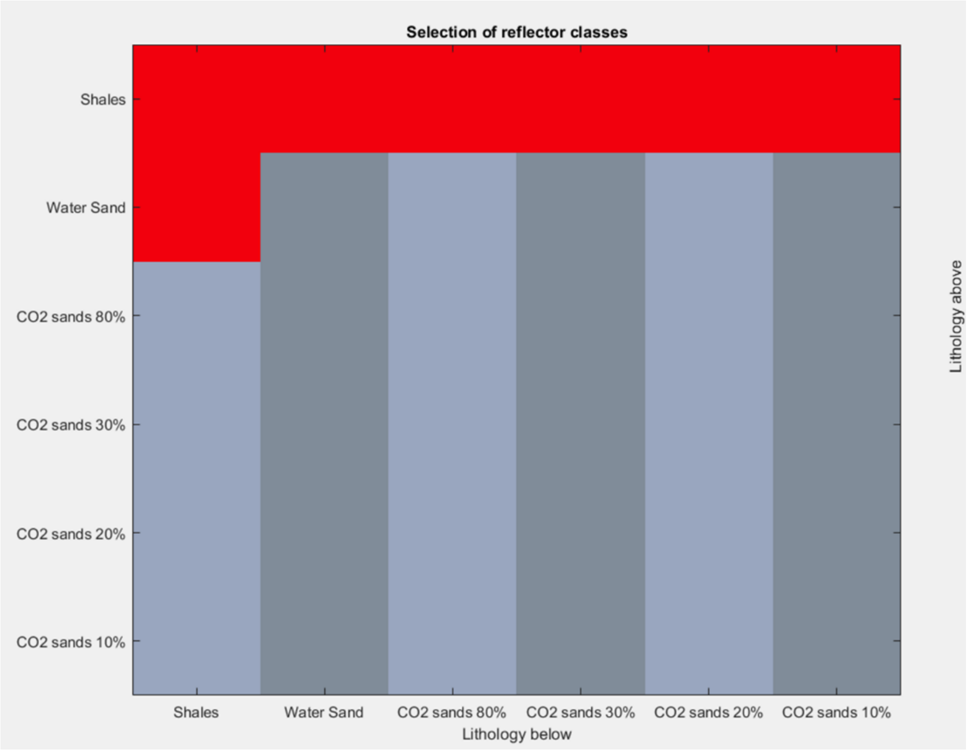

Figure 5.17: *Reflector classes selection board. On the right hand side the lithology above the interface is indicated and the bottom part the lithology below the interface is indicate. The red squares represent the selected reflector classes.*

Since this is mainly a statistical approach, user defines number of random models. In this case, 100 realization are considered per class. Afterwards, the AVO reference curves are calculated at the specified depth using Zoeppritz reflectivity equations (elastic, homogenous and isotropic medium). The number of coefficients for the conventional and optimal AVO functions computation is set to 3 with a maximum incident angle of 35 degrees (see Figure 5.18).

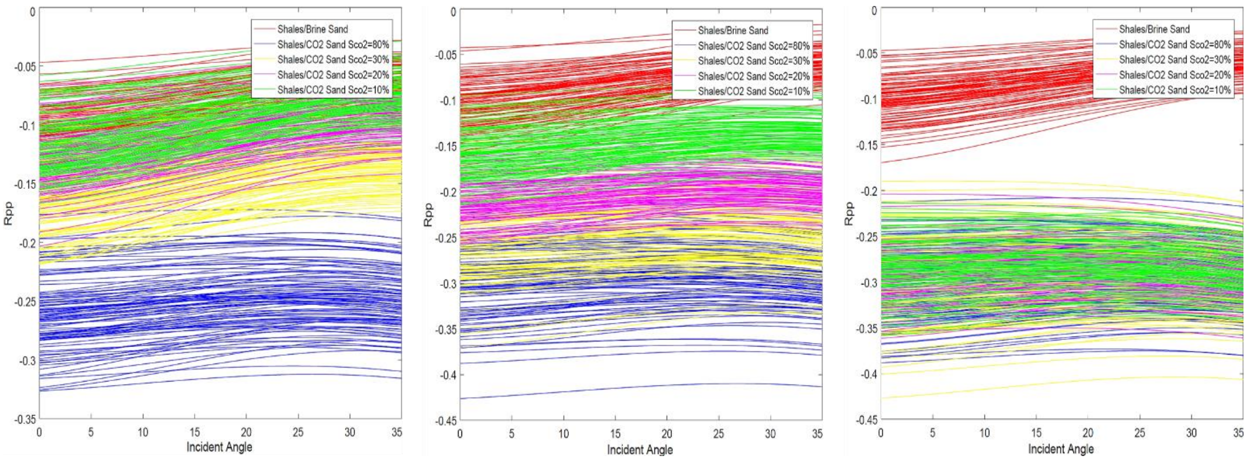

Figure 5.18: *Reference curves for different reflector classes computed with a fluid distribution using Brie's equation with exponent e=1, 5 and 40 (left, middle and right panel, respectively).*

5.3.3 Optimal AVO basis function and coefficients.

Depth dependent optimal basis functions and its corresponding coefficients are computed for each reference curve via SVD as was exposed in Chapter 4 (see Equations (4-19) and (4-20)). Conversion matrix is also computed, based on the analytical AVO coefficients computed by Aki and Richards's approximation. That allows to transform the optimal AVO attributes into the conventional ones to facilitate the interpretation and be able to associate these attributes to relative seismic property contrasts or reflectivity.

5.3.4 AVO inversion and classification

A least square inversion is performed to the data in order to obtain AVO attributes sections by fitting the pre-stack amplitude from the seismic at each position along the section with the linear approximation in the Equation (4-18). At this stage, a statistical constrain can be implemented by removing outliers through the selection of the standard deviation as a parameter to identify them. These outliers can be seen as the sample whose basis function produce data that differs significantly from the real seismic. Figure 5.19 shows C_1 attribute section and the relative error associated, after removing outliers with standard deviation factor larger than 1.5.

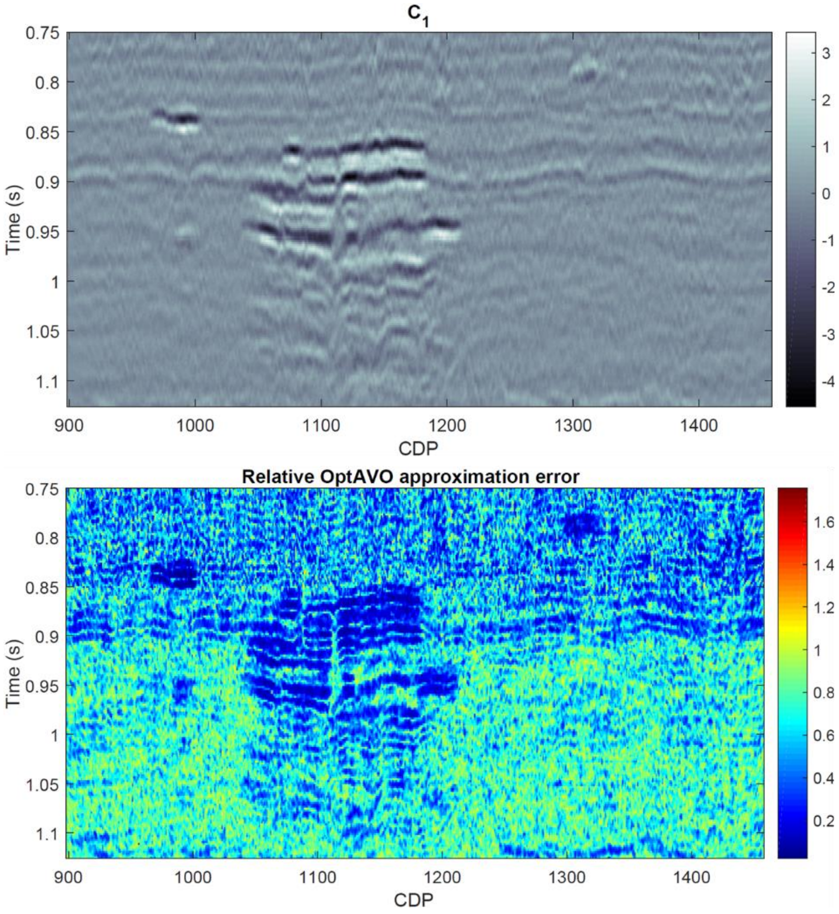
C_1

Relative OptAVO approximation error

Figure 5.19: *Optimal* C_1 *attribute section (top) and the relative approximation error (bottom).*

The attributes sections are also calibrated. This calibration procedure is equivalent to the scaling process to maintain the relative amplitudes. Thus, a specific time window and CDP range is chosen where one or more dominant classes (lithologies) are likely to be present. In this case, a window from 0.75 and 0.8s and CDP 900-950 group outside of the plume is used for calibration with two different test: only shale/shale and then shale/shale, shale/brine and brine sand/shale as the expected classes. The outcome from this, is the application of a scaling factor for each of the attribute sections separately, in a way that the variance within the selected area fits with the variance of the reference attribute in the same depth interval for the expected classes in the calibration window (Causse et al., 2007b).

In addition, the optimal AVO tool allows us to apply a classification scheme to the calibrated attributes. The result, is a colour class section where each colour represents the most probable class at each point along the section (Causse et al., 2007b). In order to do that, the mean and covariance matrices of the distribution of different reflector classes must be computed. Both the mean and covariance define each reflector class in the multi-attribute domain. Hence, they can be used as a tool for classification. In this way, the most probable class is found for each location in the multi-attribute space. It is possible to assign several reflector classes to the same single class, for example shale/brine sands and brine sand/shales can form a single class for the final classification.

Moreover, it is possible to obtain classification sections with their corresponding quality control to evaluate the accuracy of this procedure. By doing this, those three cases mentioned in the Chapter 4, where the possibility of no classification is considered are taken into account. Three different parameters are defined for the quality control such as epsilon, maximum distance and error. The former marks the points that are close to the border between two different classes in the attribute domain. The maximum distance defines the points that are far away from the class centers. Therefore, if a point is at a distance larger that the selected distance it will not belong to that specific class. Finally, the latter accounts for the definition of points whose reference curve does not fit well with the real data such as the reference approximation error and the norm of the measured reflectivity from the data is larger than the maximum error specified.

5.3.5 Elastic reflectivity sections

The inverted optimal AVO reflectivity attributes (C_1, C_2 and C_3) can be transformed using the conversion matrix to the conventional AVO attributes (R_0, G and A_3). Therefrom via other rearrangement of Equation (4-10), it is possible to obtain reflectivity sections in terms of relative changes in the elastic properties. For example, acoustic impedance, shear impedance and density reflectivity. The computation of the elastic reflectivity is performed by applying specific AVO approximation equation. In this case, Smith and Gidlow (1987) and Goodway et al. (1997) are used. They parametrized their approach in terms of P-wave impedance, S-wave impedance and density (Equation (4-15)).

Chapter 6 Results and Discussion

This chapter presents the results obtained for each stage of the project with their respective analysis. Firstly, the comparison between purely elastic and viscoelastic layers reflection and transmission coefficients are presented as function of incident angle. Followed by the description of the synthetic simulation of the wave propagation in a layered poroelastic medium (anelasticity effects). Finally, the real data application results obtained from the AVO elastic inversion in the Sleipner is also shown.

6.1 Reflection and transmission coefficients in a viscoelastic medium

Figure 6.1 depicts the absolute value of the R/T coefficients for 20% S_w measured at 30Hz. This shows an overlapping between coefficients computed along an interface for perfectly elastic layers in solid black lines and their corresponding values for an interface between an elastic and viscoelastic layer. This trend is present for PP and PS reflection, as well as, their corresponding transmissions. It is important to notice that the viscoelasticity turns the coefficients from real to complex values at the pre-critical angle. The imaginary part of the coefficients can be mainly attributable to the attenuation effects. As it has been shown by Moradi and Innanen (2015), the imaginary part is controlled by the relative contrast in both elastic and anelastic properties (quality factors). Even though, the viscoelasticity is controlling the imaginary part minor effects are also seen in the real part. Indeed, the absolute value of the coefficients is build up from their real and imaginary part.

In addition, Figure 6.1 shows the difference between the absolute value of the coefficients for an elastic and viscoelastic cases. It is clear that the differences are quite small and they do not have any impact on the shape of the curves. Regarding the reflectivity and transmissivity of an incident P wave (Rpp and Tpp), they are considerably smaller than those for an incident P wave and reflected and transmitted converted S wave (Rps and Tps). In general, Tpp difference remains constant for all incident angles decreasing steadily around 65 degrees. On the other hand, Rpp shows that at 40 degrees there is not different between elastic and viscoelastic reflection coefficients, while at larger angles (41 – 70 degrees) the difference are slightly smaller than at near angles (0 – 40 degrees) with the maximum value at zero offset. There is also a change of sign in the difference results. In contrast, the converted S wave for both reflection and transmission have more or less the same behavior with higher difference values.

Similar behavior for both reflection and transmission coefficients is seen at higher water saturation. However, there is a particular trend for the Rpp and Tpp difference at 80%, because they show the higher difference at zero offset with a gradual reduction as the incident angle increases.

Moreover, as expected it is possible to see that with increments of the water saturation the absolute reflections coefficients difference are getting closer to zero, since the seismic properties of the shale and sand layers are more similar (less acoustic impedance contrast). Besides, the quality factor for both P- and S-waves also tend to increase, which decreases the attenuation effects. At 80% water saturation the Rpp and Tpp differences show the larges values with a distinctive trend towards lower values with increasing incident angles. On the other hand, Rps and Tps show the same behavior as for 20 and 95% water saturation. Rpp and Tpp at 95% water saturation again present the same behavior as for 20% with a substantial reduction of the difference values. This is a clear evidence that the attenuation effects are lower at higher S_w levels.

The same result are obtained when the simulation is carried out by using Brie’s model (see Appendix A, Figure A-5.*)*

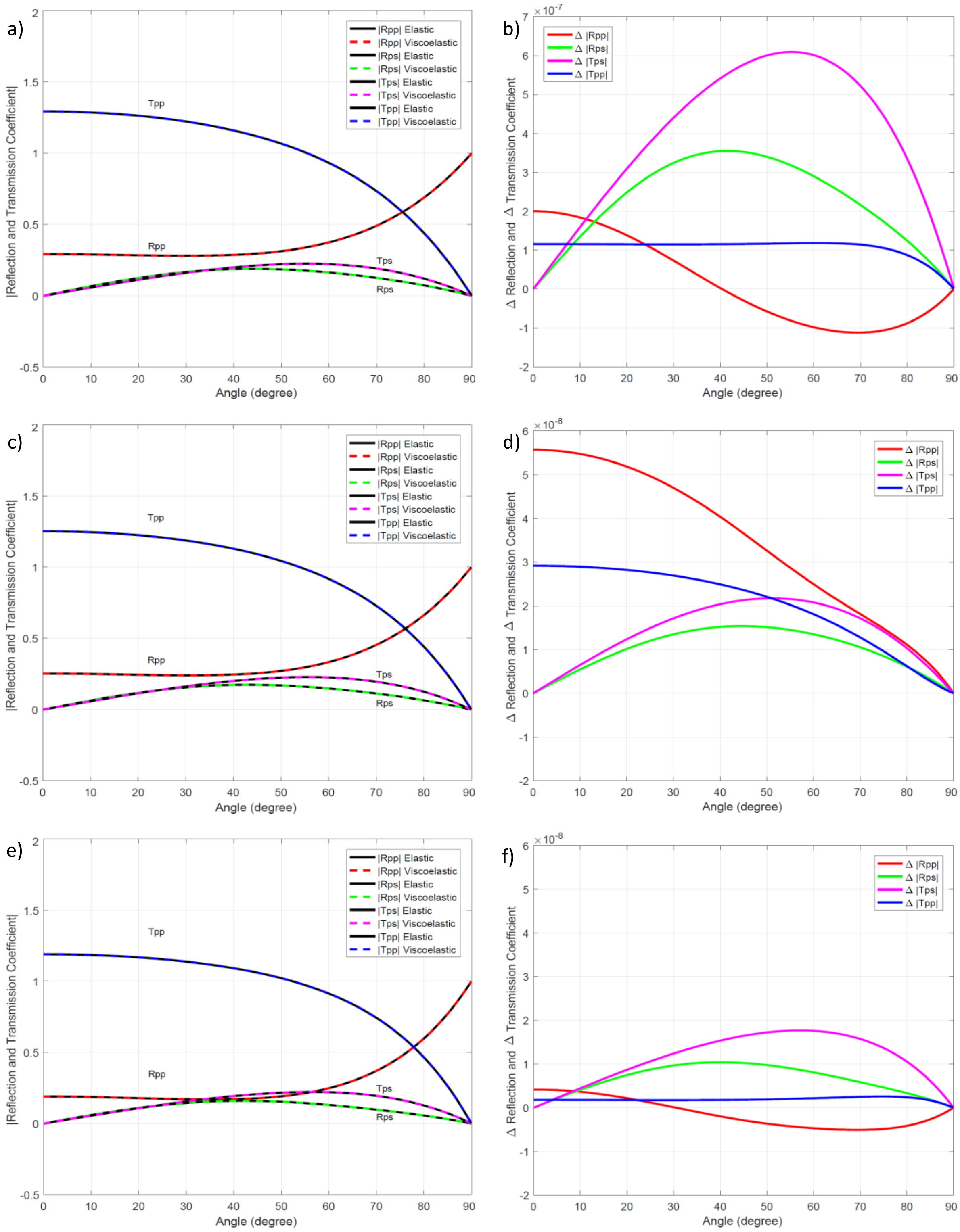

***Figure 6.1:** Reflection and Transmission coefficient absolute values and their corresponding difference between elastic and viscoelastic case. a), c) and e) the absolute value of reflection and transmission coefficients from an incident P wave being reflected and transmitted at the interface of elastic shale/elastic sand (solid black) and elastic shale/viscoelastic sand (dashed red, blue, green and magenta) as function of incident angle for different water saturation levels 20, 80 and 95%, respectively. b), d) and f) absolute difference between the reflection and transmission coefficients elastic and viscoelastic cases for 20, 80 and 95% Sw.*

Figure 6.2 shows the real and imaginary part of the reflection coefficients Rpp at 20% water saturation, from whence it is noticeable that the real part for elastic and viscoelastic medium are perfectly on top of each other. The imaginary part which is controlled by the attenuation effects is considerably low. Its values are in the order of 10^{-4} to 10^{-5}. Therefore, their contribution can be neglected at least for a single interface case.

These results are in agreement with several previous studies when it has been shown that quality factor larger than 100 are not able to introduce attenuation effects within the seismic bandwidth. As it was presented earlier the quality factor for P- and S-waves at 20% S_w measured at 30Hz is around 904 and 637, respectively. Taking into account that most of the attenuation is carried by the imaginary part of the coefficients influencing the amplitude and introducing a phase shift of the wave. For all the cases it was proved that the magnitude of the imaginary coefficients is quite low and it can be considered as elastic.

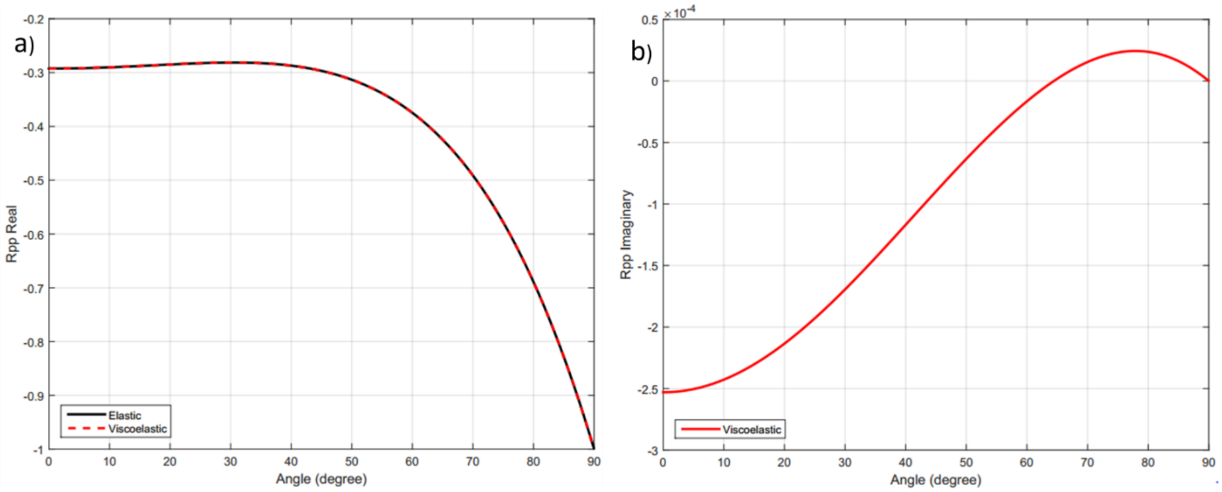

Figure 6.2: *Reflection coefficients for incident and reflected P-wave (Rpp) at the interface between two half-space. Elastic shale above the interface and elastic/viscoelastic partially saturated sandstone (20% S_w) below the interface (black and red, respectively). The seismic effective properties are computed at 30Hz. a) real part of the reflection coefficients, b) imaginary part of the reflection coefficient (viscoelastic).*

The results obtained when the effective seismic parameters are computed at 3000Hz for a sandstone with 20% water saturation are presented in Figure 6.3. The comparison between the real part of the Rpp for the elastic an viscoelastic cases is shown with their respective differences. The difference is visible, but its value is just in the order of 10^{-3}. Similarly to the previous results the behaviour of the difference shows the same trend; the largest at zero offset and getting smaller and smaller with increasing incident angle. When it comes to the evaluation of the imaginary part of the reflection coefficients for the viscoelastic case, very low values are obtained, being around -0.001 to -0.012. Therefore, it is important to point out that although the quality factor is about 20, the difference between the elastic and viscoelastic reflection coefficients is quite small and it does not have any significant impact, at least for this specific model. This is in agreement with Behura and Tsvankin (2009), who showed that moderate attenuation values (quality factor between 20 and 50), does not produce any difference between the reflection coefficients for the elastic and viscoelastic case. They showed that even though with a quality factor equal to 10 the difference is not significant. Only when the attenuation is extremely strong (quality factor very low, for instance 2.5 or 5, which is not realistic for deep sediments), a considerable difference is seen between elastic and viscoelastic reflection coefficients.

In a similar way, Behura and Tsvankin (2009) computed the reflection coefficients by linearizing the exact plane wave, where the model parameters simulate a purely elastic shale and attenuate oil sand. Their findings are in agreement with the obtained results. The largest difference between the elastic and viscoelastic cases, when a strong attenuation is induced, are seen at zero offset, and gradually decreases with incident angle. Additionally, Ursin and Stovas (2002) pointed out through their numerical simulations that the imaginary part of the R/T coefficients is quite low, even though the relative contrast between the quality factors are not small. Hence, the effects of attenuation in the R/T coefficient is very difficult to observe.

From these results, it is possible to see that for a simple case of a single interface between two layers, being elastic/elastic and elastic/viscoelastic contrast, the reflection and transmission coefficients show the same behaviour. This is seen for all the saturation cases, even for the saturation that shows the highest attenuation levels (20%) at 3000Hz, whose quality factor is equal to 20. Although the attenuation is considerable high, it seems that for this specific case the reflection and transmission coefficients are not affected by viscoelasticity effects.

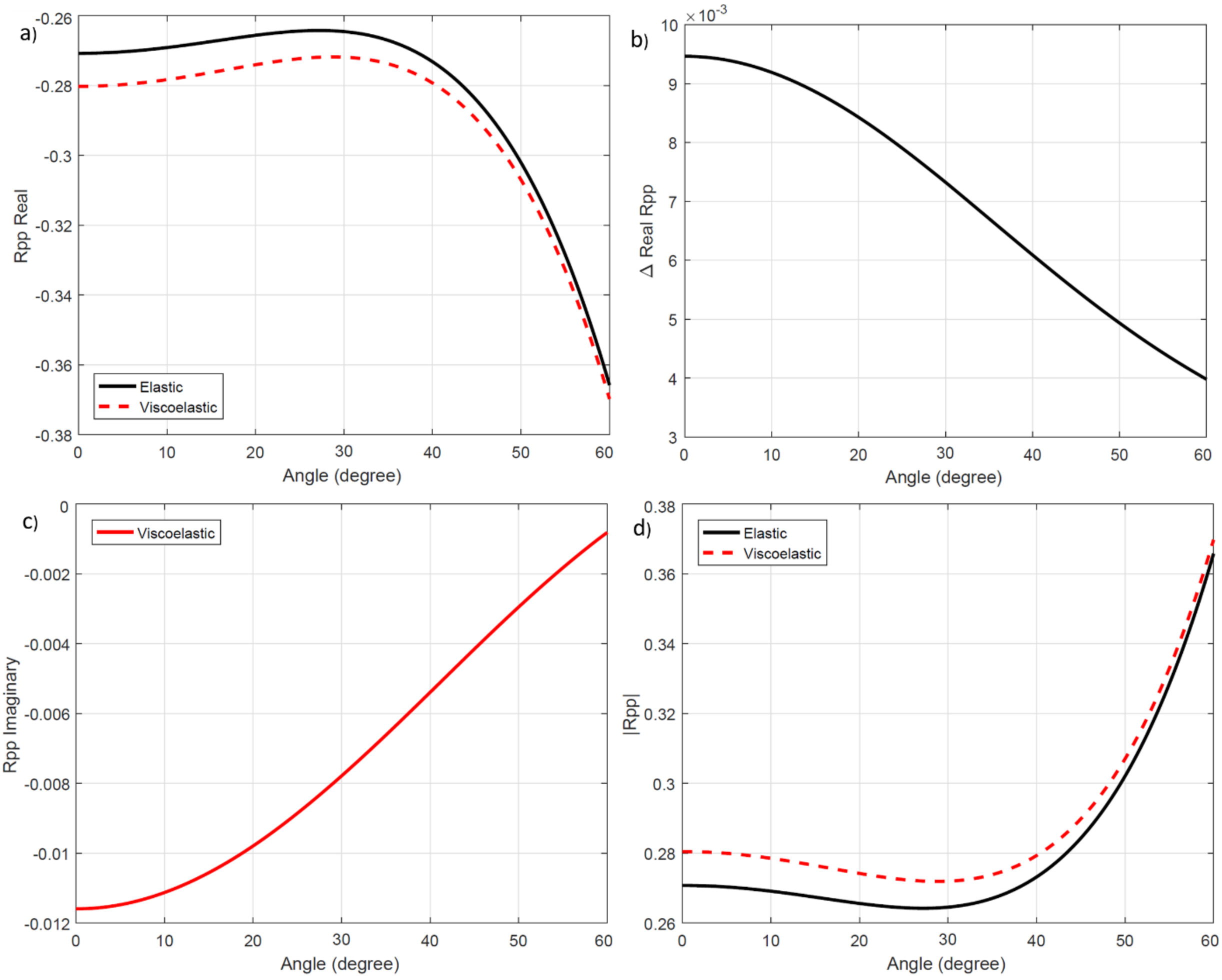

Figure 6.3: *Reflection coefficients for an incident and reflected P-wave (Rpp) at the interface between two half-spaces, the seismic properties are computed at 3000Hz for a 20%* S_w *(attenuation peak). Elastic (black) and viscoelastic (red) cases are compared. a) real Rpp comparison, b) real Rpp difference, c) imaginary Rpp for the viscoelastic case and d) Rpp absolute values comparison.*

6.2 Full waveform propagation for elastic/viscoelastic models

This section presents the results of a synthetic earth model consistent of three horizontal and homogenous layers. This considers the elastic case of the reservoir sand as a reference and the viscoelastic as the attenuated model.

6.2.1 Synthetic models

The previous results are limited by the fact that the wave only propagates through the elastic medium (cap-rock shale) and the viscoelasticity is only take into account when the wave hits the interface. For this reason, a conceptual model is tested, in order to evaluate the attenuation effect when the wave is travelling through the viscoelastic layer itself.

According to the conceptual model previously presented in Figure 5.2, two main PP reflections are expected to be identified in the traces. First, the reflection from the top of the reservoir and second the reflection from its bottom are easily recognized. Similarly, later strong arrivals corresponding to PS reflections are also expected along with internal multiples. Figure 6.4 depict the comparisons between the synthetic seismogram obtained when a wave propagates through a perfectly elastic medium and two viscoelastic media (viscoelastic models 1 and 2). Additionally, Figure 6.5 and Figure 6.6 show the magnitude and phase of the reflection coefficients for the PP and PS wave at the top and bottom of the reservoir, respectively. From the previous analysis it was noticed that the reflection and transmission coefficients for elastic and viscoelastic cases do not differ from one another. Therefore the results presented corresponds to the viscoelastic model 1.

From Figure 6.4 it is clear that a perfectly elastic model seems to behave in the same way as viscoelastic model 1, where the quality factor values for P- and S-waves are 1135 and 876, respectively. On the other hand, the viscoelastic model 2 shows noticeable difference respect to the elastic and viscoelastic model 1. Figure 6.4 c and d show that amplitude differences are for the PP and PS reflection at the bottom of the reservoir, as well as, in the multiple reflections. In contrary, the direct wave and the PP and PS reflections from the top of the reservoir do not show any significant amplitude damping effect. These results are consistent and expected, since the overburden shale is perfectly elastic for all the models. Therefore, when the wave travels through it, no attenuation and dispersion effects occurs. In the case of the viscoelastic model 2, the quality factor values are low enough to introduce the viscoelasticity effects into the wave propagation.

From the synthetic seismogram plots, it is very difficult to say whether or not, phase change are occurring. Also, it is important to keep in mind that, there is an offset range limitations, since the maximum offset of the simulated data is only 1800m. The phase shift effects might be likely to occur at longer offset.

As it was mentioned earlier the offset to incident angle conversion was done, in order to correlate the reflection coefficients response with the synthetic seismograms. Figure 6.5 illustrates how the Rpp and Rps change in magnitude and phase with incident angle at the top of the reservoir sand. In this case, no critical angle exists. According to the offset and incident angle relation, the maximum offset of 1800m corresponds to 47.67 degrees, whereas the minimum offset of 175m is equivalent to 6 degrees. From the synthetic seismogram, one can see that the PP reflection amplitudes are quite weak at near offset. However, they show a steady increase at around 600 up to 900m, from where their amplitudes increase rapidly. These results are pretty consistent with what it is seen from Figure 6.4 c, since 600m offset corresponds to

20 degrees in angle, which is the point where the reflection coefficient magnitude increases and is being more pronounced at around 28 degrees and further angles.

When it comes to PS reflection, although the increments in amplitude occurs at shorter offset in comparison with PP, their maximum magnitude is smaller. For instance, the amplitude rise is visible from 400m (14.5 degrees approximately). It is worth noting that in the case of the PS reflection at 1400m, it is possible to see its maximum reflection coefficient magnitude. At offsets from 0 to 250m, the amplitude is very low, since there is not PS wave at zero offset.

Regarding possible phase changes, it is observed from Figure 6.5 that for this interface any change is expected, even at far angles for both PP and PS reflections.

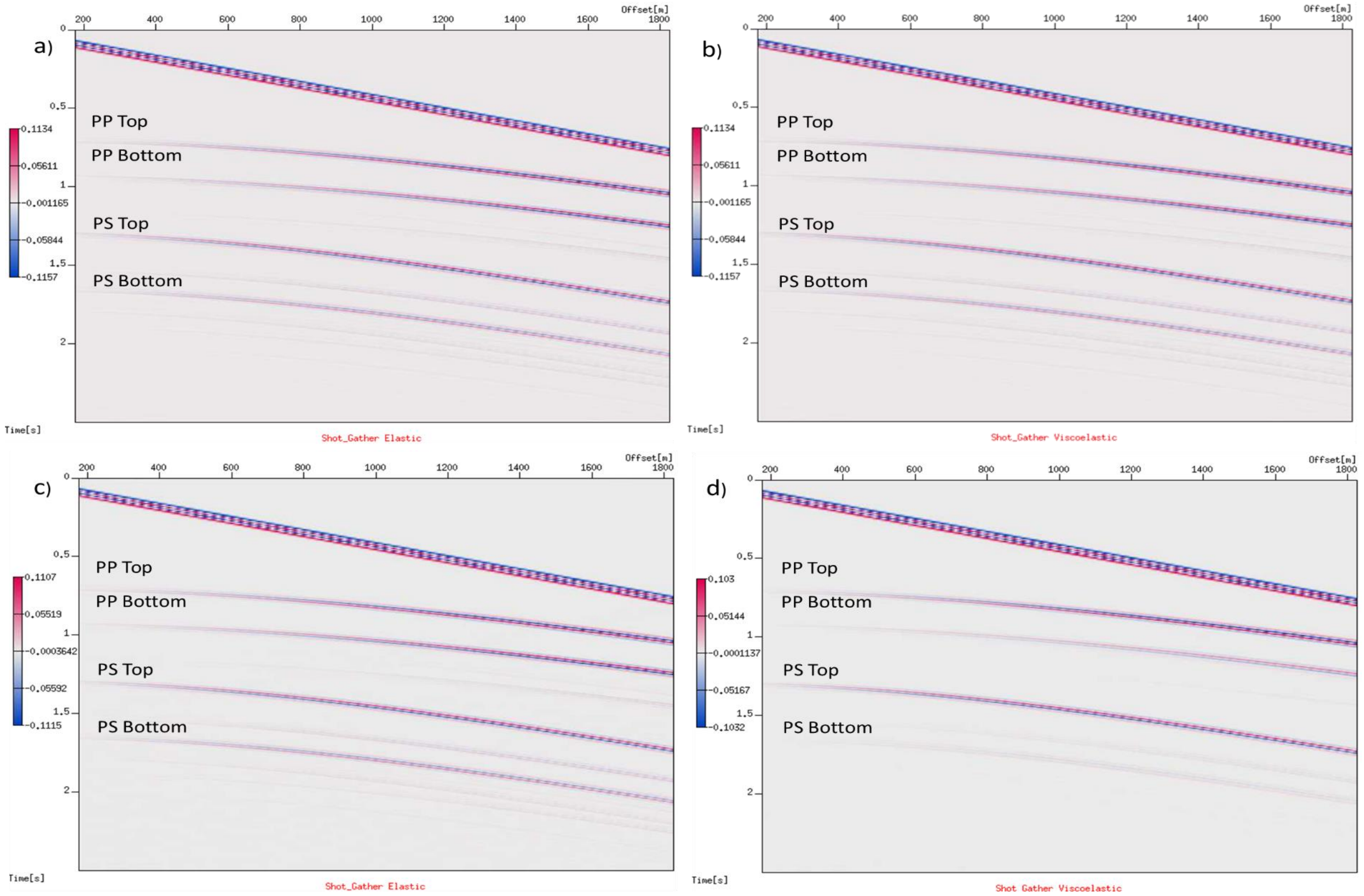

Figure 6.4: *Synthetic Seismogram (shot gather) for elastic/elastic and elastic/viscoelastic cases. a) elastic seismogram, b) viscoelastic seismogram with model 1 (Qp=1135 and Qs=876). c) elastic seismogram, d) viscoelastic seismogram with model 2 (Qp=27 and Qs=22).*

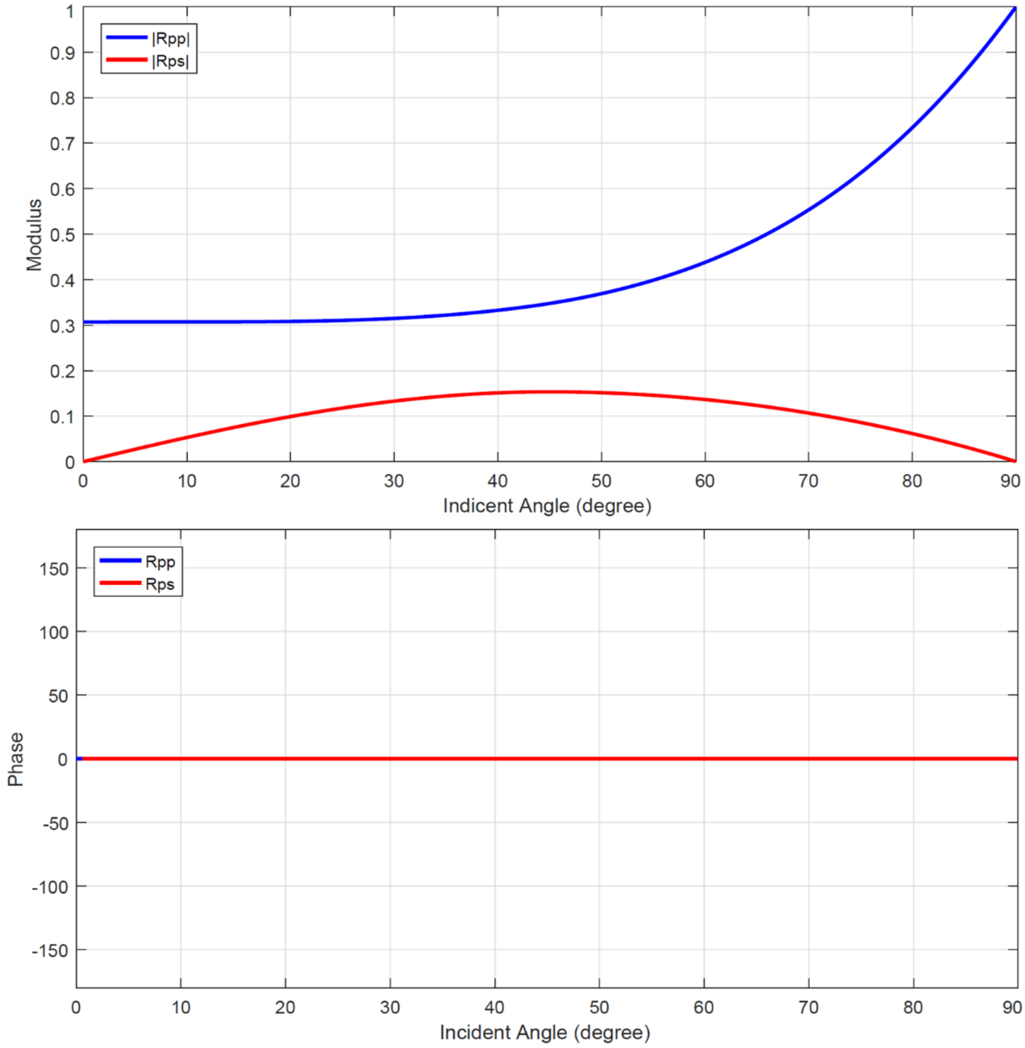

Figure 6.5: *Reflection coefficients magnitude and phase, estimated at the top of the reservoir for the PP- and PS-wave propagating into the elastic overburden. Reflection coefficients magnitude as a function of incident angle (top), Reflection coefficients phase as function of incident angle (bottom).*

The same analysis is carried out for the reflections at the bottom of the reservoir. At this point, it is more likely to see changes related to the viscoelasticity effects, since the wave has propagated into the viscoelastic layer. According to the relation offset - incident angle, we have that the minimum and maximum offset of 175 and 1800m correspond to 3.17 and 25.26 degrees, respectively. In this case, the limitation in longer offset has a higher impact than in the shallower reflector. However, this also avoid the recording of refracted waves, since the critical angle of 36.5 degrees is beyond the maximum angle that can be analyzed.

The PP reflection amplitudes at the bottom of the reservoir start increasing at 800m offset (13.6 degrees), the same behavior is seen for the magnitude of the Rpp. Moreover, the PS reflection from the seismogram shows in general weaker amplitudes than for the top of the reservoir, which is expected, since the local maximum in Rps magnitude is almost twice less than the absolute maximum seen for the top of the layer (0.1 and 1.75, correspondingly). However, a similar trend is seen, in which the amplitude increases from 650m offset reaching a local maximum between 1250 and 1800m. Due to the lack of offset, it is not possible to see the decreasing and increasing effect towards a local minimum at the critical angle and towards the absolute maximum of 0.3 at about 55 degrees, respectively.

Although the amplitudes and reflection coefficients have the same behavior, it is worth noting that the reduction in amplitude for both PP and PS reflections at the bottom of the layer might be related to attenuation effects. Since Rpp values at far offsets (1400-1800m) for the top and base of the layer are quite similar (0.34-0.37 and 35-0.38, respectively). However, the amplitude is highly attenuated for the latter.

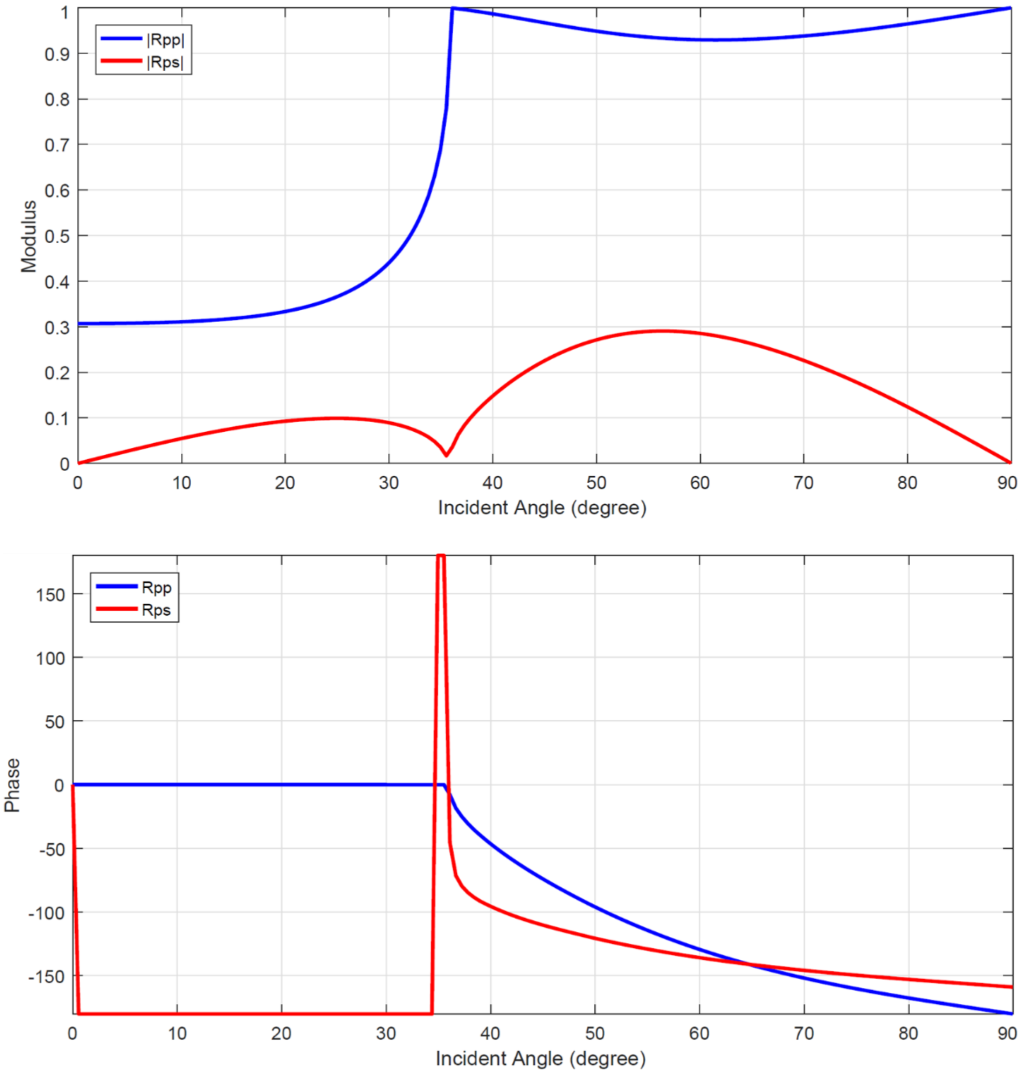

Figure 6.6: *Reflection coefficients magnitude and phase, estimated at the bottom of the reservoir for the PP- and PS-wave propagating into the viscoelastic reservoir sand. Reflection coefficients magnitude as a function of incident angle (top), Reflection coefficients phase as function of incident angle (bottom).*

The phase changes are also limited to the offset ranges. It is worth noting that the phase change seen for the PP and PS reflection coefficients is mainly driven by the acoustic impedance contrast instead of any possible viscoelastic effects, since these changes are occurring beyond the critical angle. Even for the purely elastic case, the reflection and transmission coefficients are complex numbers. Therefore, the imaginary part is responsible for the phase shift of the signal. Before reaching the critical angle, PP has zero phase, whereas PS shows a 180 degrees phase.

The analysis on the individual traces is given in Figure 6.7, which illustrates the response for near and far offset traces extracted from a seismogram. From Figure 6.7, it is clear that the attenuation effect is almost negligible for the viscoelastic model 1, whose quality factors are higher than 100 for both P- and S-wave. In contrast, the attenuation effect become considerable for the viscoelastic model 2, when quality factors are low enough. For instances, all the extracted viscoelastic traces (5 and 65) after the PP and PS reflections from the top of the reservoir show a significant damping of their amplitude (more than a half). It is also noticeable, the early arrivals of the events in comparison with the elastic responses. It is worth notice that regardless the value of the quality factor the first reflection which corresponds to the top of the reservoir does not show any visible difference between the elastic and viscoelastic models. This might be related to the fact that the wave has only propagated within the elastic medium that is the same for all models (see Figure 6.1). The difference arises at the reflection from the bottom of the reservoir, because the wave has already travelled through the attenuated medium (partially saturated sand) as it was shown in the synthetic seismograms (Figure 6.4).

One can also observe from Figure 6.7 , that PS attenuation effect seems to be slightly larger than PP reflection from the bottom of the reservoir. This might be related to the fact that the quality factor for the S-wave is lower than the P-wave. Hence, the converted wave will show more attenuation. Moreover, the multiple reflections show the strongest attenuation effects, since the reflection and transmission coefficients in general are characterized by values lower than one. Because of that, the higher order, multiple reflections will damp the amplitude at every reverberation losing energy gradually, in addition to the fact that longer pathways are travelled.

The attenuation effects were introduced by incorporating the quality factor, which turns constant and real phase velocities into frequency dependent and complex velocities. This frequency dependent velocity, is directly related to phase velocity dispersion. Having this in mind, one can distinguish the different effects seen in the trace response.

Firstly, both elastic and viscoelastic models deal with a partially saturated sand, whose thickness is 200m. Hence it is possible to disregard tuning effects. Secondly, the attenuation and dispersion are considered together, which is a key factor to understand the obtained results. When the viscoelasticity is incorporated, the velocity depends on frequency. Considering that the wave propagation is done in the frequency domain, all the reflection and transmission coefficients (propagation matrix) are also computed for each frequency within the whole frequency band. One might expect that the viscoelastic case presents slightly higher velocities than the elastic one ending up with a reduction of the acoustic impedance contrast of the layers. Lower acoustic impedance contrast gives lower reflection amplitude.

Although the Amplitude versus Offset (AVO) effect for the CO_2-brine sand is quite large, it is possible to identify the attenuation effects at different offset traces. For instance, the far offset trace for the elastic case shows a much larger amplitude than the near offset trace (0.15 instead of 0.0055 correspondingly). Although the viscoelastic model 2 shows the same AVO behaviour, the amplitude magnitude for both far and near traces compared to the elastic case is quite lower (0.056 and 0.0025, respectively). Thus, this must be taken into account when it comes to the AVO analysis.

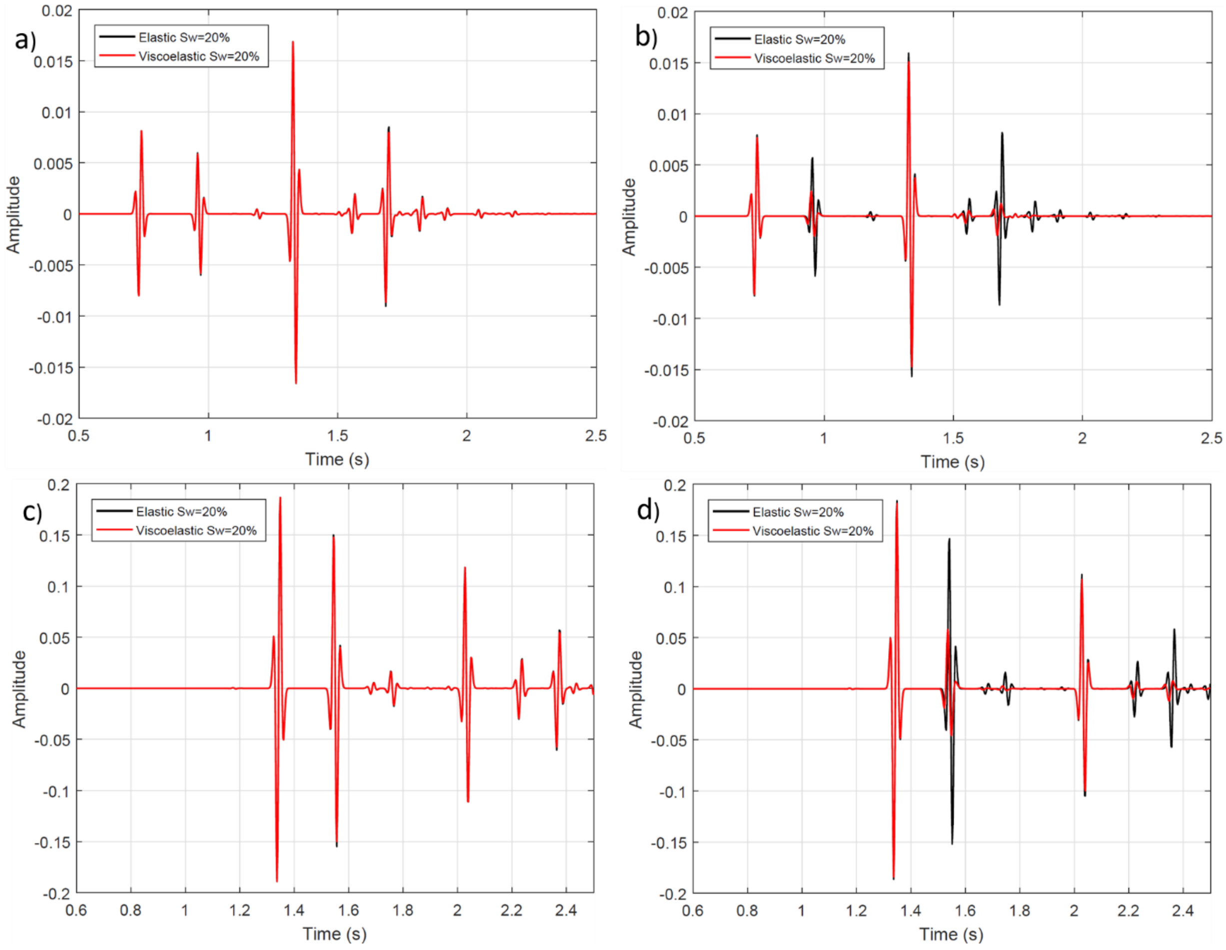

Figure 6.7: *Traces from the seismogram at different offsets for elastic (reference model) and viscoelastic (attenuated model). The reference model is constructed considering all the layers as purely elastic. There are two viscoelastic modes: i) model 1 is constructed based on Qp=1135 and Qs=867 values computed at 30Hz and ii) model 2 is based on Qp=27 and Qs=22 computed at 2500Hz for the Utsira sand rock properties. a) and c) show elastic/viscoelastic model 1 and b) and d) show elastic/viscoelastic model 2. The top panels (a, b) illustrate near offset trace (trace 5) and bottom panels (c, d) show far trace (trace 65).*

6.2.2 Stacked traces comparison

So far, wavelet response comparison between elastic and viscoelastic sand reservoir has been limited to single traces. The following results show the partial stack as an attempt to evaluate, the possible attenuation effect introduced by the viscoelastic models 1 and 2. It is important to notice that this comparison is only focused on the PP reflections for the top and bottom of the sand.

Figure 6.8 shows the partial stack result for elastic and viscoelastic case model 2. First, the AVO effect is quite noticeable from both top and bottom of the reservoir. As it was presented in the previous section the amplitude response is increasing with incident angle and longer offsets, which in the case of the top reflector is getting more negative. In contrary, the bottom reflector increases its amplitude getting more positive. This behaviour is seen for both elastic and viscoelastic cases. Second, there is an amplitude damping at the bottom of the reservoir, which is associated to attenuation effects. Although the far offset traces should show stronger attenuation due to the fact that the wave is traveling longer distance within the viscoelastic layer, they still show larger amplitudes than the near traces. This is because the acoustic impedance contrast or AVO behaviour is dominant over attenuation. It is worth noting that the difference between mid and far offset stacks is quite hard to see. This is mainly related to the limitation in offset; if there were longer offset this distinction would be clearer. On the other hand, the comparison between the elastic case and viscoelastic case model 1 does not show any difference. This is a clear indication that model 1 behaves as an elastic model.

When it comes to the individual trace comparison one can clearly see that differences between elastic and viscoelastic model 1 are in the order of 0.0002 and 0.0005 for the near and far trace, respectively. While for the viscoelastic model 2 the differences are about 0.005 and 0.014, correspondingly. This means that the magnitude’s difference for model 2 is ten times higher than for model 1. Even though the AVO effects dominates in all the cases, the far offset traces show larger differences than the near traces probably indicating that those are being more attenuated.

Unfortunately the staking process in this particular case is not helpful to enhance difference between elastic and viscoelastic models (see Figure 6.9). However, it is quite useful to show the AVO dominant effect.

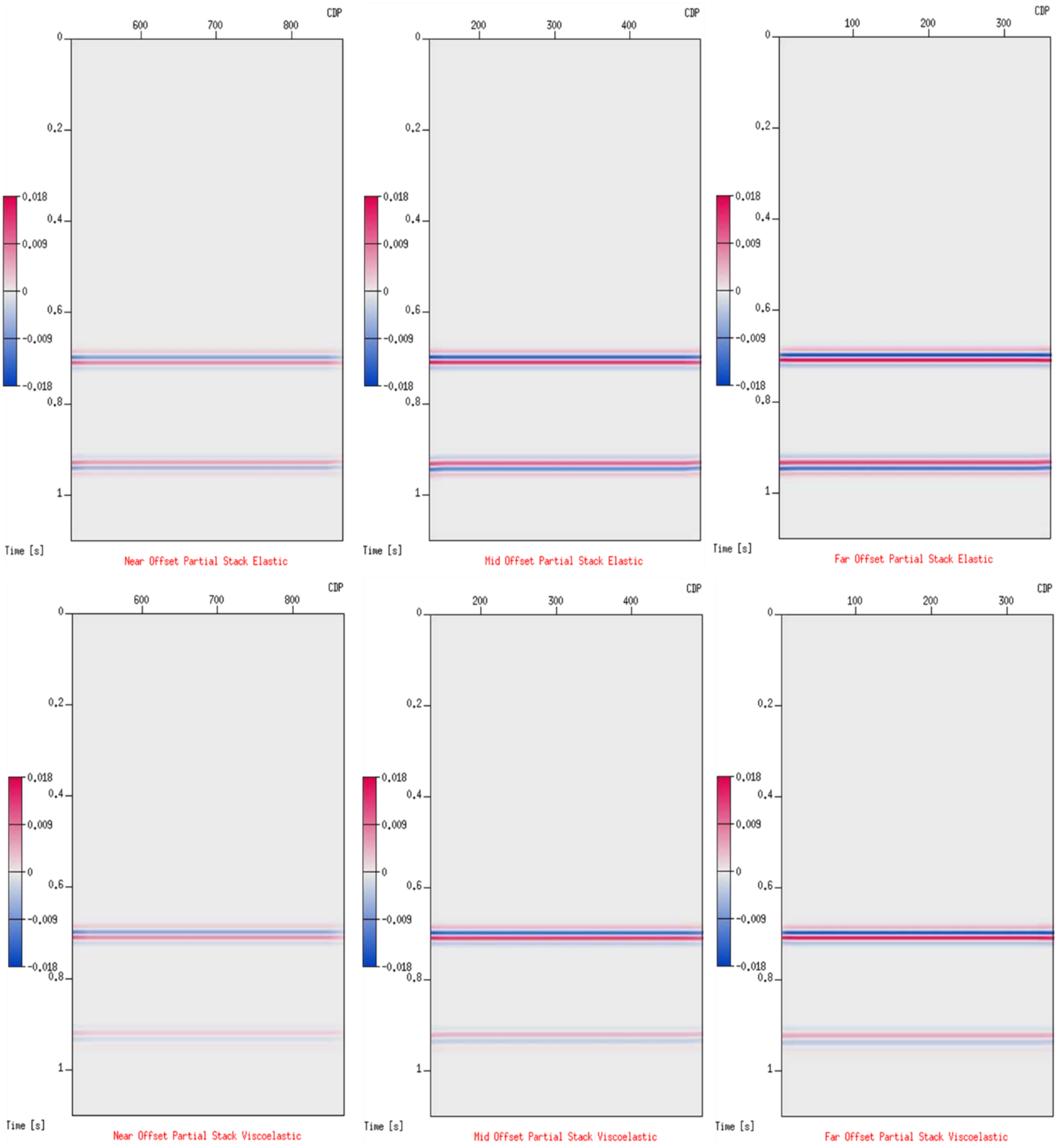

Figure 6.8: *Partial Stack for elastic/elastic (top panel) and elastic/viscoelastic medium model 2 (bottom panel). From left to right near (175m-725m), mid (725m-2175m) and far (2175m-1825m) offset stacks.*

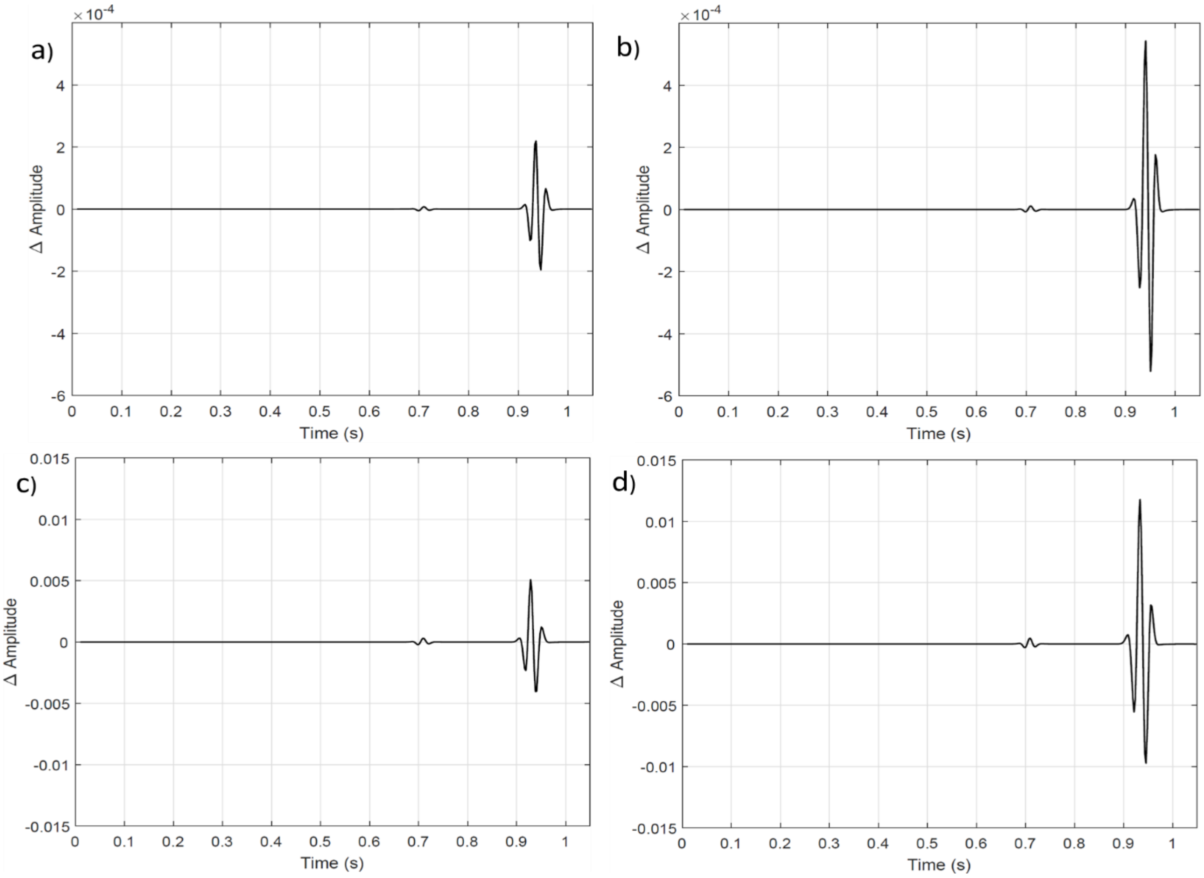

Figure 6.9: *Trace difference for elastic/viscoelastic model 1 (top) and elastic/viscoelastic model 2 (bottom). a) and c) show a trace extracted from the near offset partial stack, b) and d) show a trace extracted from the far partial stack.*

6.3 Realistic models

After analysing conceptual models of attenuation, more realistic models of the Utsira sandstone configuration are compared. Notice that in average the total thickness of the reservoir around the injection well 15/9-16A is 200m as it was simulated in the simple case. However, the Utsira sandstone is not a homogenous sand, it has at least 8 well defined thin inter-layer shales. It was shown by Torres (2016) that a constant thickness layer simulation of the Utsira formation (stack of periodic layers) by nine 2m thick shales and nine 11,4m thick sands at 30Hz dominant frequency is not enough to reach an effective medium. A higher number of layers, for instance 32 or more layers, are needed. In such a case, the reflection of each interface and possible interbedded multiples will be present in the response.

6.3.1 Zero offset R/T response in frequency domain

The R/T responses in frequency domain were computed for different water saturation, which correspond to different reflection coefficients and therefore acoustic impedance contrast. Figure 6.10 shows the results obtained for each saturation. From the upper panel it is possible to see the responses and the energy loss in a wider frequency range, whereas the bottom panels shows the same results only constrained into the seismic bandwidth (0 – 100Hz). One can see the different behaviour of the R/T response for each reflection case. It is noticeable the increment in the energy loss with increasing frequencies. Similarly, the lower water saturation shows a considerable damping of the energy even within the seismic frequency range, while at 80 and 95% the energy loss is quite low at both low and high frequencies. In the case of 95% water saturation it can be considered almost negligible.

In addition, it is possible to see that the larger the reflection coefficient, the larger and more often the transition zones will develop. This transition zones are associated to the stop band or blocky regime, as described by Stovas and Ursin (2007) and Stovas and Roganov (2010). They are shown as periodically repetitions that alternates between propagation regimes. The results are in agreement with what was found in these previous studies, since this transitions zones get larger due to increments in the acoustic impedance contrast. It is also noticeable that the reflection and transmission responses for elastic and viscoelastic cases are exactly the same for the highest water saturation levels. At 80% S_w very slight differences are seen with increasing frequencies. On the other hand, at 20% S_w the difference between the elastic and viscoelastic responses seems to be considerable, even at low frequencies. Another interesting feature in the frequency domain is that after the stop band, the energy loss always increases considerably.

One should expect similar results in time domain. It is worth noting that these result are in a good agreement with the previous observations regarding the attenuation effects as function of water saturation, since they indicate that the greater the S_w the lower the attenuation, as it was seen in the reflection and transmission coefficient analysis with incident angle.

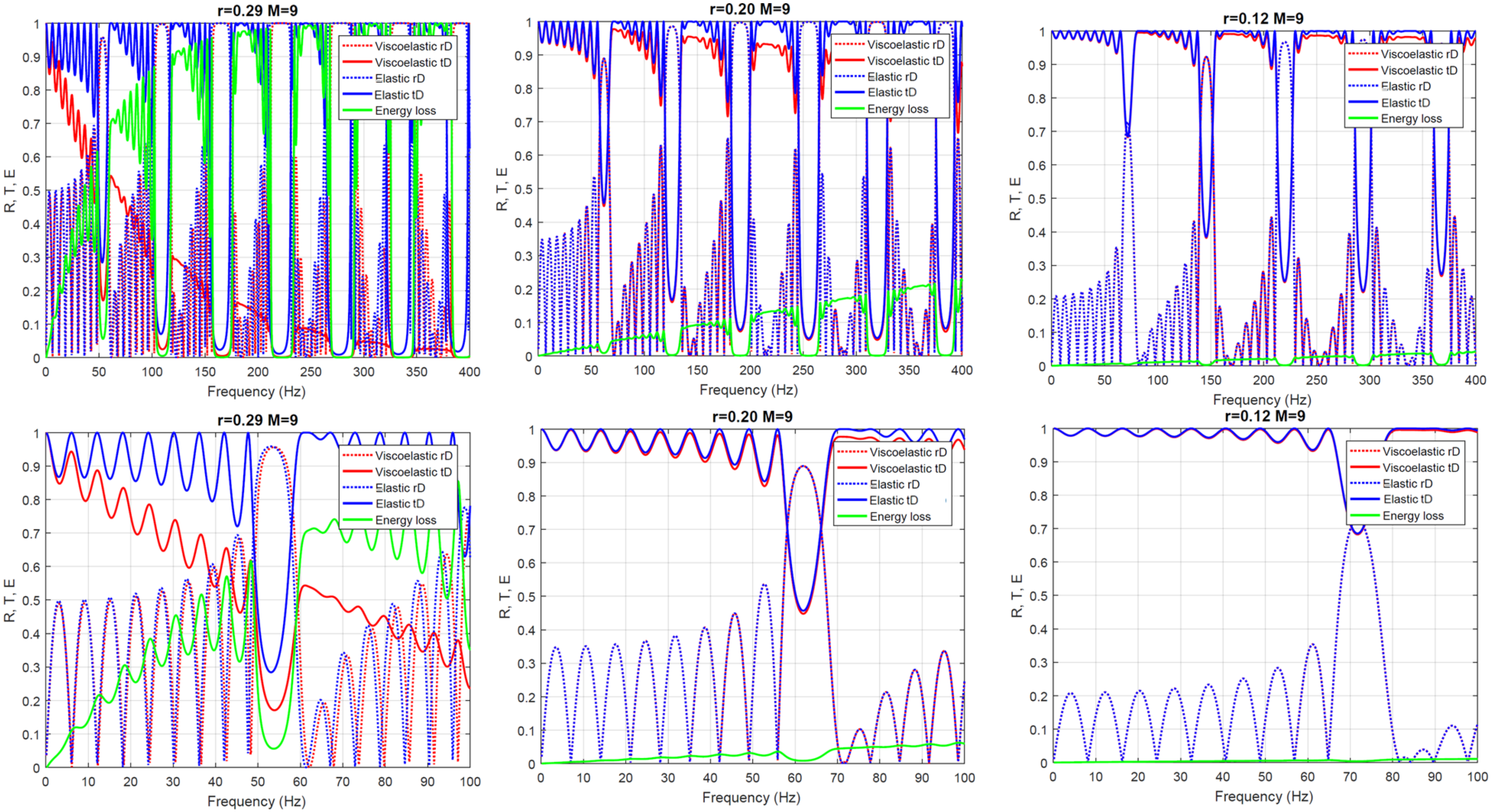

Figure 6.10: *Reflection and transmission responses at normal incident angle in frequency domain with their corresponding energy loss for different water saturations. a) and d) R/T responses for 9 number of cycles at 20%* S_w *which corresponds to a reflection coefficient of r=0.29. b) and e) R/T responses for 9 number of cycles at 80%* S_w *which corresponds to a reflection coefficient of r=0.20. c) and f) R/T responses for 9 number of cycles at 95%* S_w *which corresponds to a reflection coefficient of r=0.12. Reflection response is indicated in blue, transmission in red and energy loss in green, the distinction between elastic/elastic and elastic/anelastic contrast is denoted as solid and dot lines, respectively.*

6.3.2 Constant Sw for all the layers

As it was mentioned, more emphasis has been put in the model with 20% water saturation and additional simulations are compared. Figure 6.11 shows the comparison between an elastic and two poroelastic models. The poroelastic models differs in the value of the hydraulic permeability for the Utsira formation. Model 1 has 2 Darcy permeability and model 2 has 200 Darcy permeability. The permeability values for the model 2 are used with the purpose of inducing attenuation within the seismic frequency band, as a Carcione's model (low Qp and Qs values).

One can see that for both near and far offset traces the attenuation effects when the permeability is 2 Darcy are too low, since the elastic and poroelastic cases present exactly the same response with just a very gentle variations at the latter arrivals (most likely multiple reflections). On the other hand, for the model 2 with 200 Darcy, the attenuation effect is quite large. However, the first arrivals for both PP and PS reflections show the same behaviour, no difference are seen. The seismic response differs significantly only for the latter arrivals. For example, in the trace 5 (near offset) at approximately 0.75 and 1.35s after the first PP and PS arrivals, one can see these attenuation effects more pronounced. The same behaviour is clear in the trace 65 (far offset) but at latter times, for example, at 1.37 and 2.075s approximately.

Figure 6.13 illustrates the comparison between the elastic/elastic and elastic/poroelastic cases for the PP and PS reflections trends individually. In general, the primary reflections shows slightly higher amplitude response for the poroelastic case than the elastic one, this might be related to some inaccuracy during the normalization process of the traces. It is important to notice that no significant phase shift is visible for the PP reflections. However, the PS reflections shows very little shift between the elastic and poroelastic cases. This might be associated to the fact that the quality factor for the S-wave is always lower than for the P-wave, therefore larger attenuation effects could be expected. The same patterns are presented for the far offset traces (see Appendix A, Figure A-6).

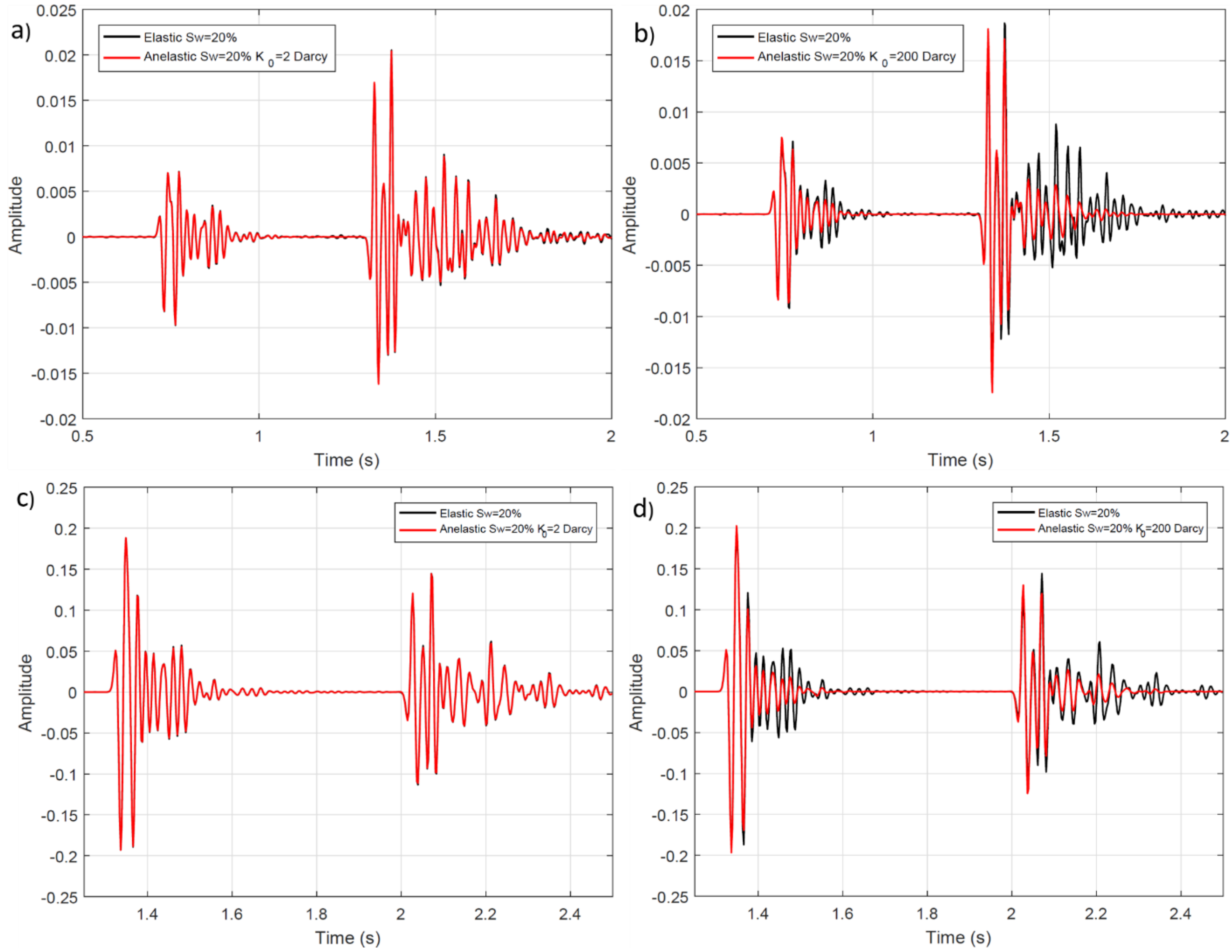

Figure 6.11: *Near and far traces (trace 5 and 65) comparisons between elastic and anelastic response for stack of periodic layers at 20% Sw, top and bottom panels, respectively. a) and c) elastic/anelastic comparison by using the Utsira formation poroelastic properties. c) and d) elastic/anelastic comparison by increasing the reservoir permeability to shift the attenuation peak from 2500Hz down to 30Hz (seismic dominant frequency).Elastic and anelastic are indicated by black and red colors, respectively.*

The results obtained are in agreement with some previous analysis regarding the evaluation of the combining effect of layering medium and attenuation (Stovas and Roganov, 2010, Stovas and Ursin, 2007). They showed that the difference between elastic/elastic, elastic/anelastic and anelastic/anelastic are mostly seen in the multiple reflections, almost at end of the reflection response. One can justify this by the fact that the energy loss of the signal is directly proportional to the pathway traveled by the wave. Therefore, multiple reflections or reverberations within a specific layers will produce additional partition of the signal, along with reflection coefficients with higher order. Even though, their analysis is limited to zero offset, it is pretty consistent with the results obtained for variable incident angle responses.

Similarly, they indicated that reflection and transmission responses in the frequency domain have a distinctive patters depending on the regime. For instance, three different situations are indicated: *i)* time average medium, *ii)* blocky regime, *iii)* effective medium. The first one and last one have similar behavior in time and frequency domain, in contrast the blocky regime does not show any response after the first arrivals (Stovas and Roganov, 2010, Stovas and Ursin, 2007).

According to the results obtaining in the previous section, there were not a significant difference in the R/T responses between the elastic/elastic and elastic/anelastic cases except for 20% S_w. However, it seems that the response in frequency domain can be different from the time domain as it was also presented by Stovas and Roganov (2010). They showed that, there was a quite large difference for various number of cycles between the reflection and transmission responses in the frequency domain. Also they noticed increments in the energy loss. On the other hand, the time domain response shows weak attenuation effects that are more pronounced only for the multiple reflections at the tail of the signal. It is important to point out, that their simulations were carried out with a quality factor equal to 20 at 200Hz. In this case, similar results are seen at least for 20% S_w, where no significant attenuation can be identified in the poroelastic model 1 (2 Darcy permeability). This might be also associated with the high quality factor values obtained for this specific model (Q_p=1135).

In addition, the viscoelastic approach by using 2 different models was also tested for stack of periodic layers as it was mentioned in Chapter 5. From Figure 6.12 trace 5 (near trace) is illustrated for both elastic/elastic and elastic/viscoelastic cases. The signal shows the same response as for the conceptual model. This is a clear indication that the value of the quality factor is a key to introduce the attenuation effects. Once again, this results are pretty consistent with those obtained by (Ursin and Stovas, 2002, Behura and Tsvankin, 2009), where they pointed out the value range in which the quality factor introduces efficiently the energy loss.

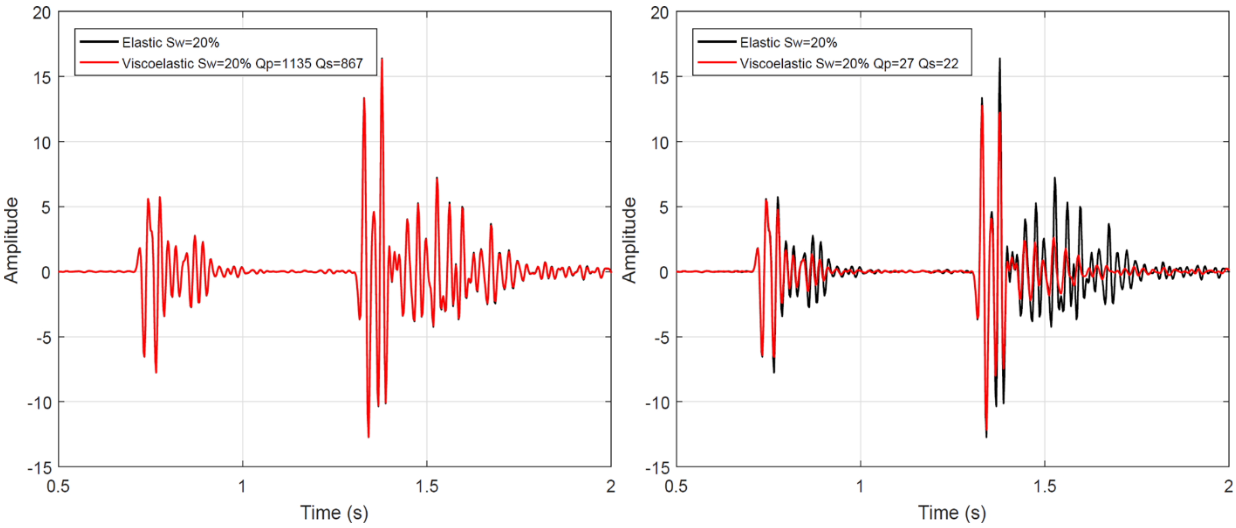

***Figure 6.12**: Near trace (trace 5) comparison between elastic and viscoelastic response for Utsira reservoir (stack of periodic layers) at 20% Sw. Elastic/viscoelastic the viscoelasticity is determined by introducing Qp=1135 and Qs=867 quality factors measured at 30Hz (right). Elastic/viscoelastic the viscoelasticity is determined by introducing Qp=27 and Qs=22 quality factors measured at 2500Hz (left).*

Another interesting comparison was carried out between the elastic/elastic, elastic/viscoelastic and elastic/poroelastic cases. One can see from Figure 6.14 that disregarding whether the quality factor values are frequency independent or not their magnitude itself is what controls the attenuation effects. By using the appropriate poroelastic parameters to get the same quality factor at given frequency (30Hz), it is possible to see that the response of viscoelastic (frequency independent Q and frequency dependent phase velocity) and poroelastic (frequency dependent Q and phase velocity plus additional conversion of the energy due to slow P-wave) is pretty much the same. However, the latter shows slightly higher attenuation, which is more emphasized in the PS reflection trends.

Moreover, from the right panel of the Figure 6.14 it is obvious that the elastic, viscoelastic model 1 (high Q values) and poroelastic model 1 (permeability 2 Darcy) are almost equivalent to each other. Similarly, viscoelastic model 2 (low Q values) and poroelastic model 2 (permeability 200 Darcy) resemble one another. This means, that for the specific poroelastic model of the Utsira formation by assuming a fluid phase average approach with Biot-Gassmann theory, the mesoscale heterogeneities do not have any significant impact in the amplitude response of the signal. But if a model as Carcione et al. (2006) is implemented strong attenuation will occur.

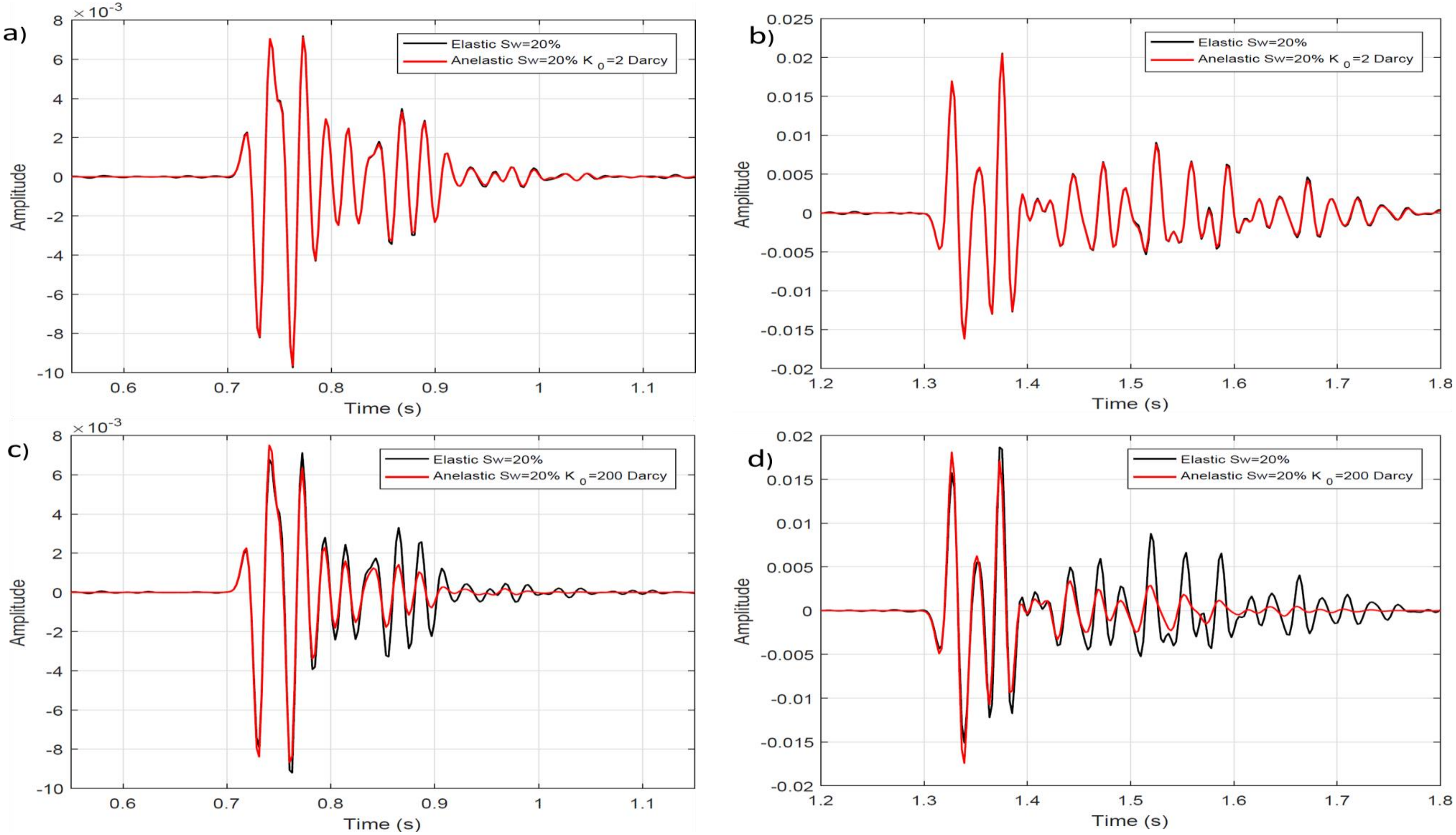

Figure 6.13: *Near Trace comparison (trace 5) after the first PP reflection arrival and the first PS reflection arrival. Stack of periodic layers at 20% Sw. a) and c) reflection response after the first PP arrival elastic/anelastic for the Utsira sand poroelastic properties and 200 Darcy permeability (shifted attenuation peak). b) and d) reflection response after the first PS arrival elastic/anelastic for the Utsira sand poroelastic properties and 200 Darcy permeability (shifted attenuation peak).*

In this specific case, the frequency range should be in the order of the kHz for the intrinsic attenuation to have an important effect. This results agree with what was found by analyzing the reflection and transmission coefficients of a single interface.

These results are not in agreement with previous simulation of the Utsira aquifer made by Carcione et al. (2006) and Rubino et al. (2011). In contrary, they showed that the attenuation peak is reached within the seismic frequency band at 80% and 90% S_w, correspondingly. This implies a quality factor value of 20 and 15 for P- and S-wave velocities, respectively. The main difference is associated to the way the intrinsic attenuation is considered. First of all, Carcione's model used poro-viscoelastic approach, this mean that by using Zener (standard solid model) in combination with the White model to account for the mesoscale heterogeneities, it is possible to boost the intrinsic attenuation and make it considerable in the seismic frequency limit. Moreover, some poroelastic input parameters also differs. He has pointed out, that it might be possible that by using only poroelastic models, it is not enough to obtain strong attenuation effects at least within the seismic bandwidth.

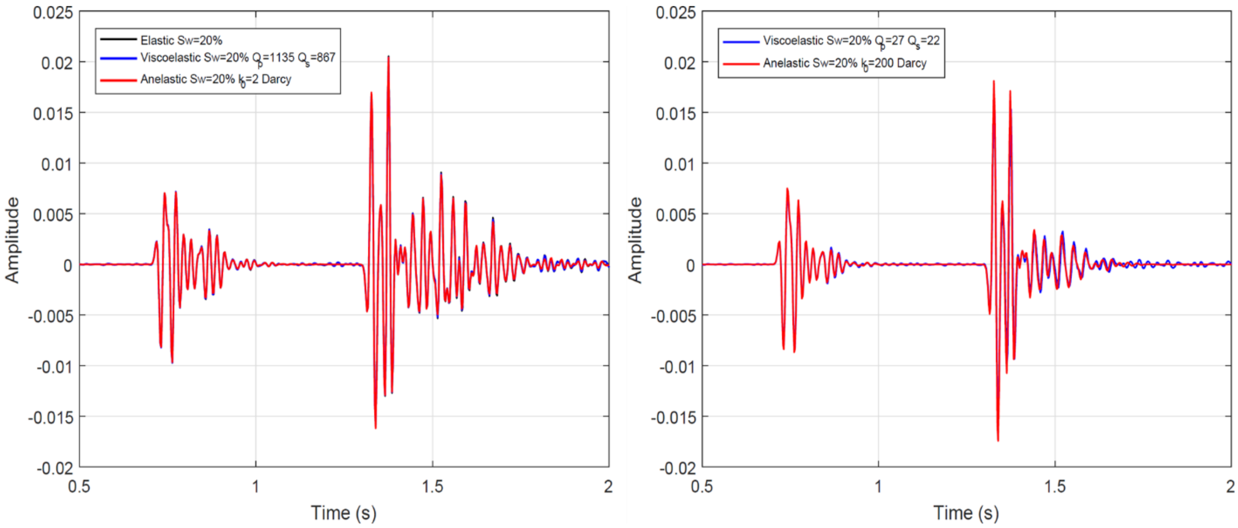

Figure 6.14: *Near trace (trace 5) comparison response for elastic/viscoelastic/poroelastic for the Utsira sand reservoir at 20% Sw. Elastic sand (black), viscoelasticity introduced by Qp=1135 and Qs=867 (blue) and poroelastic sand with permeability of 2 Darcy (red) all are equivalent to effective seismic properties measured at 30Hz, right panel. Viscoelastic sand with Qp=27 and Qs=22 (blue) and poroelastic sand with permeability of 200 Darcy, for an equivalent attenuation peak shift from 2500Hz to 30Hz, left panel.*

6.3.3 Evaluation of the seismic response with Sw variations.

By increasing the water saturation even less attenuation effect is seen in the response. This is also an expected results, since from previous analysis it was shown that the attenuation for both P- and S-wave are higher at lower S_w. At higher water saturation, the amplitude reduction was quite significant but this is seen for the elastic and anelastic case. Due to the increasing water concentration levels, the effective P-wave velocity and density of the sandstone tend to increase as well. Hence, they become closer to the shale properties and reduce the acoustic impedance contrast along with the reflection response.

After showing that the elastic/elastic and elastic/anelastic response are pretty much the same, the variation in amplitude with offset as a function of water saturation is investigated. Figure 6.15 shows the results of extracting a near, mid and far traces from the seismogram at 20, 80 and 95% S_w, from whence it is obvious that the AVO effects seems to be stronger than any possible attenuation effect.

One can see two distinctive trends. First, the near and mid offset traces show lower amplitude than the far offset trace. This is indicated by the amplitude scale. Second, the variation in water saturation is not associated to any possible intrinsic attenuation effect due to partial saturation. Although the highest attenuation should be present at 20% S_w, the higher amplitude of the signal is seen instead. This is mainly driven by the acoustic impedance contrast between the shale and sand layers. As it was mentioned earlier, the acoustic impedance contrast diminishes with increments in water saturation, ending up with lower reflection coefficients and diming the amplitude. The larger differences are seen between 20 and 95% S_w. Moreover, these differences are quite noticeable for the PP reflection but they are less prominent for the PS reflections, due to the lack of shear wave‘s sensitivity to fluids. In Appendix A, Figure A-8 is a zoom version of the PP reflection from where it is possible to see clearly the different response in terms of amplitude in addition to phase shift and change in the wavelet shape itself. However, all these effects are driven by the acoustic impedance contrast between the layers.

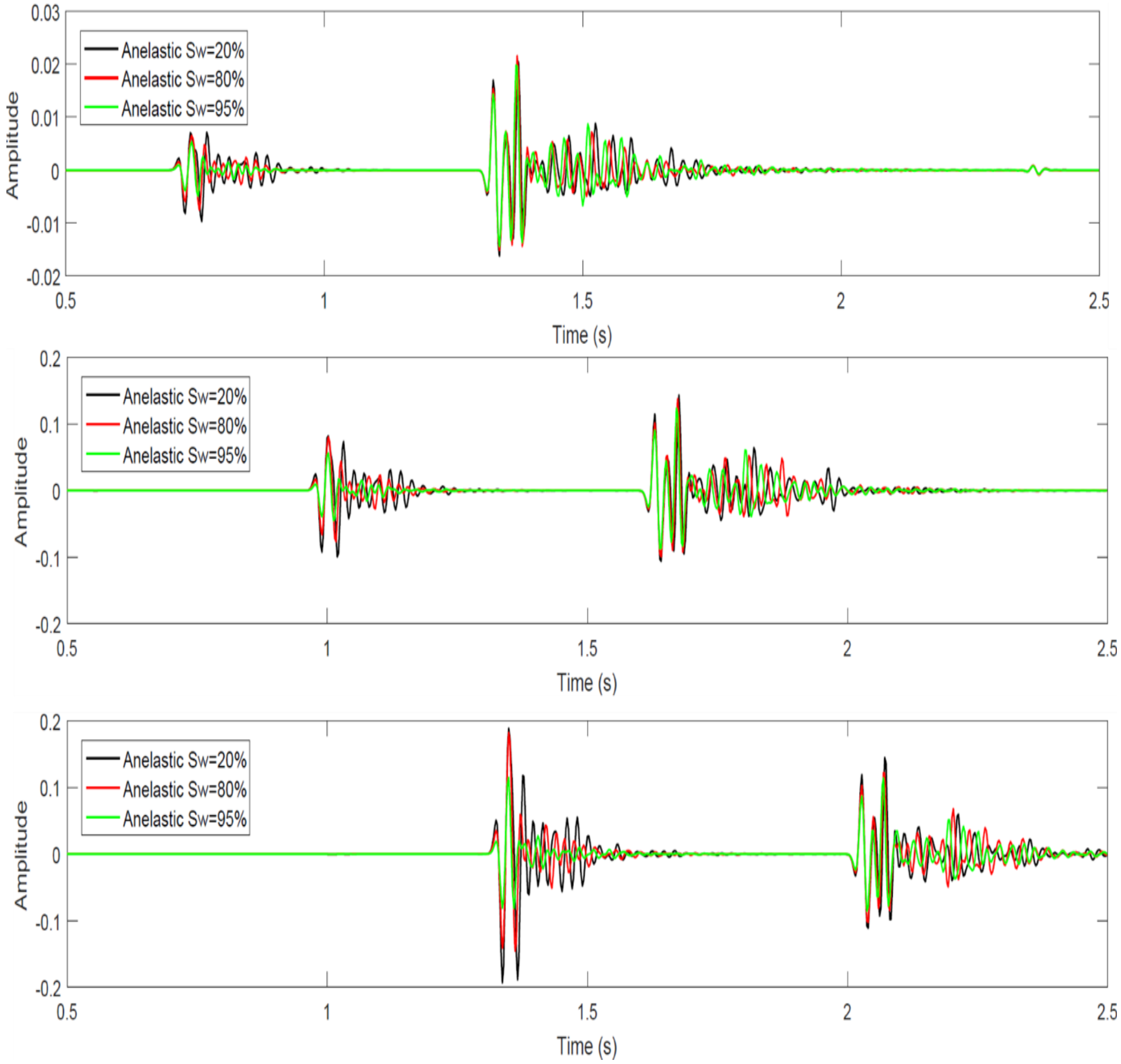

Figure 6.15: *Trace comparison at 20, 80 and 95% S_w (black, red and green colors respectively). Near trace (top). Mid trace (middle). Far trace (bottom).*

6.3.4 Seismic response for various S_w at different depth levels

Figure 6.16 illustrates that the closest model to the possible distribution of CO_2 in the Utsira formation does not differ from the previous simulations. In the same manner, no attenuation effects are seen, therefore is it reasonable and still valid to use an elastic solution of the plane wave reflection and transmission coefficients as the Zoeppritz equations to perform an AVO study, since the intrinsic attenuation for the given model might not represent any source of errors for a quantitative amplitude analysis.

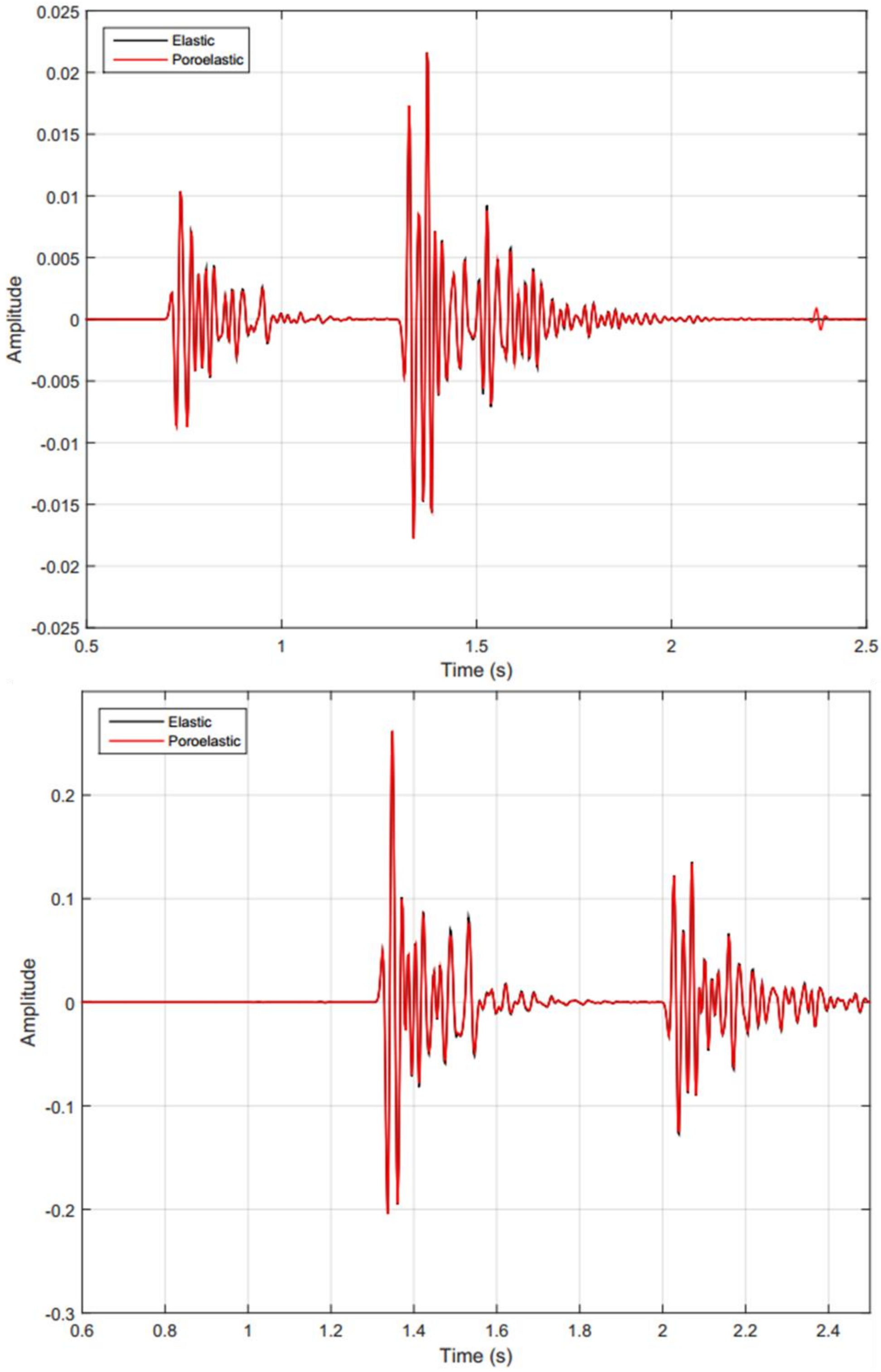

Figure 6.16: *Synthetic Seismogram comparison elastic/elastic and elastic/poroelastic for Utsira formation by using different Sw saturation levels according to Savioli et al. (2016) reservoir simulation model. Top panel near trace (5) and bottom panel far trace (65).*

6.4 AVO Real data applications

The following subsection presents the results obtained from the Optimal AVO technique applied to real data. The main purpose of this section is to show how different fluid distributions inside the pore space can change the AVO feasibility and seismic detectability.

As it was mention in Chapter 5, the AVO analysis was carried out in two seismic section (Inline 1838 and Inline 1880) extracted from a 3D PSTM cube. In general, the result for each of them are quite similar, therefore in most of the cases only the results for one line are presented.

6.4.1 AVO feasibility and seismic detectability

Before applying any AVO analysis to the data, it is quite important to know whether or not the tool is capable of distinguishing among fluid and lithological changes in the specific area of study. As it was pointed out by Avseth et al. (2005), the feasibility of the technique and good comprehension of the geological settings is a key factor.

As part of the AVO assessment, several seismic properties cross-plots obtained from well information and rock physics models are analysed. Figure 6.17 shows Acoustic impedance (AI) vs V_P-V_S ratio and $\lambda\rho$-$\mu\rho$ cross-plots. The former is quite useful and can be directly associated to rock properties and fluid via rock physics templates (Avseth et al., 2005). From whence, it is possible to identify different geological trends. It is worth noting that the differences among the panels are associated to the type of fluid distribution that is being modelled. The top panels represent the upper bound patchy mixing (Voigt average), middle panel are for an intermediate fluid mixture and the lower panels show the lower bound uniform mixing (Reuss average).

In all the three cases, it is noticeable that the lithological discrimination is done properly, since the shales are completely detectable and separated from the sandstones. For instance, shale is the lithology with the highest acoustic impedance values, this is also reflected in the $\lambda\rho$-$\mu\rho$ cross-plot where they reach the highest values due to the relation of these quantities to P- and S-impedances (see Equation (4-17)). One can see that the AI values for shales are well defined, being around 4700 and 5600m gr/s cm^3 approximately. Similarly, their V_P-V_S ratio shows a narrow range of values from 2.25 up to 2.5, which is in agreement for a shale with porosity rage of 16-20%. When the Brie exponent e is equal to 1 or 5 the V_P/V_S alone is not a good lithology discriminator, because the sandstone with very high CO_2 saturation (80%) and the sandstone with lower saturations (around 30 and 20%) are located within the same range as the shales.

This clear discrimination between shales and sandstones under this specific geological settings is expected, since at the depth of the target (750-1000m), the Nordland group shales are considered as a hard response rock, because they exhibit larger rock frame properties, less porosity and larger compaction, density and P- and S-wave velocities than the underlying Utsira sandstone. In contrast, the latter is a weak sand with very high porosity, permeability and poorly consolidated. One can see that μρ is almost a pure lithological indicator, even though the bulk density is affected by the fluids, this relation is linear and proportional to the S_w. At the same time, the sensitivity to fluids is controlled by the porosity. It is important to keep in mind the mineralogical components of the shale, since they control the shear or rigidity modulus of the solid frame. The Norland group shales are silty quartz rich, hence, they are considered as hard rock (Avseth et al., 2005). The typical range for the shale in terms of μρ is from 4 to $6x10^6$(m gr/s $cm^3)^2$. The same occurs with λρ properties since the Lamé parameter is related to the P-wave velocity modulus including incompressibility as fluid indicator and rigidity for lithology. In this case, shales are fully saturated by brine and in general the mineralogy composition and compaction of the shale is much higher than the sandstone with a range between 1.5 to $2x10^7$(m gr/s $cm^3)^2$.

When it comes to the analysis of the sandstones, even though these are well separated from the shales, the capability to discriminate among the same lithology in terms of CO_2 saturation could be a very challenging task, depending on the fluid distribution. Figure 6.17 shows how some specific CO_2 concentrations could be easier to be identified than others. The same patterns are shown for each of the cases in the AI-V_P/V_S and λρ-μρ. The AI impedance range for the brine sandstone is well defined from 3700 to 4500m/s x gr/cm^3. In the same way, their V_P/V_S is the highest, even higher than for shales (from 2.7 to 3.3 approximately). This response allows to have a proper discrimination between brine sand shales. However, when the fluid distribution is gradually changed from the patchy (upper bound) to uniform (lower bound) mixing, it is possible to see that the lower CO_2 saturation clusters (10, 20 and 30%) are well discriminated. They are clustered together towards the higher CO_2 saturations, and therefore totally isolate from the brine sands (see, Figure 6.17 a-b, c-d and e-f, respectively).

For example in Figure 6.17 a-b, the lower CO_2 saturation shows slightly lower AI values than the brine (3500-4300m/s x gr/cm^3). However, their V_P/V_S values fall in the same range, hence limiting the discrimination capability. It is important to notice that 10% CO_2 case is overlapping the brine sands. On the other hand, the sandstone with high CO_2 concentration is located in the left hand side of the plot, being characterized by lowest AI and lower V_P-V_S ratio, from 2000 to 3250m/s x gr/cm^3 and 2.3 to 2.5, correspondingly. As it was mentioned earlier in the patchy case this highly CO_2 saturated sandstone have the same values of V_P/V_S than the shales.

Therefore, the AI is playing the most important role to discriminate. Due to the lack of sensitivity to fluids of μρ parameter all sandstones have the same value range from 1 to $2x10^6$(m gr/s $cm^3)^2$ .and their fluid discrimination is only indicated by the λρ parameter which increases with S_w from 0.4 up to $1.5x10^7$(m gr/s $cm^3)^2$.

From Figure 6.17 c-d, one can see that the acoustic impedance among the sandstones with 80, 30 and 20% CO_2 shows a large overlapping range and V_P/V_S is much better discriminator in this case. Only sandstones with 10% CO_2 are discriminated by both AI and V_P/V_S values from brine sands and shales. Lastly, Figure 6.17 e-f show that all sandstones partially saturated with CO_2 regardless their saturation are grouped together. This indicates that under this fluid distribution assumption it is only possible to distinguish between the brine sands, shales and CO_2 partially saturated sandstones, but when it comes to quantitative estimation of gas saturation, it is unlikely to obtain reliable results.

All these trends are closely related to the P-wave behaviour in terms of water saturation, since shear wave velocity is not affected directly by fluid changes. Density effects are responsible for its linear proportional behaviour with S_w instead. These changes can be seen as gradually and completely independent on fluid distribution. However, P-wave velocity relation with water saturation has more complex behaviour and it strongly depends upon the distribution of the fluid phases into the pore space (see Figure B-4 in Appendix B). The patchy mixing law from Voigt average implies that just a slight change in velocity of 50 or 100m/s might be caused by an injection of 10 up to 30% CO_2, this could easily fall into a realistic uncertainty range. Therefore, it would be difficult to have a reliable quantification of the fluids within a low CO_2 concentration range. Only those areas with higher saturation could be estimate with higher degree of certainty. The opposite applies for Reuss average where just a small amount of CO_2 will drop drastically the compressional velocity to constant level among a wide range of saturations (10-100%). Moreover, using e= 5 a higher possibilities to discriminate among CO_2 saturations are present.

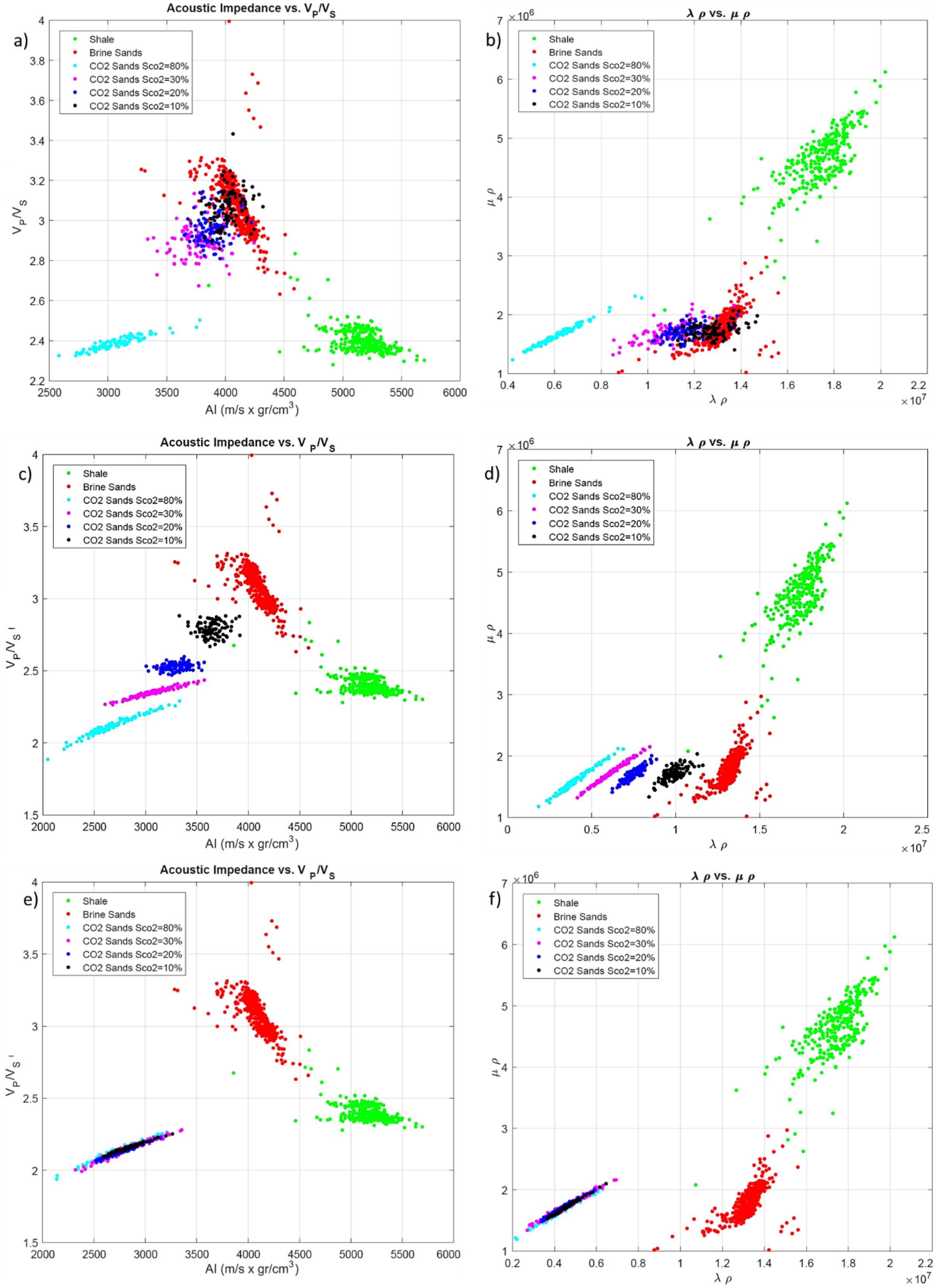

Figure 6.17: *Acoustic Impedance vs Vp-Vs ration and λρ vs μρ cross-plot for different fluid distributions simulated by Brie's equation. a) and b) corresponds to e exponent equal 1 (patchy mixing law upper bound Voigt average), c) and d) e exponent equal 5, e) and f) e exponent equal 40 (uniform saturation lower bound Reuss average).*

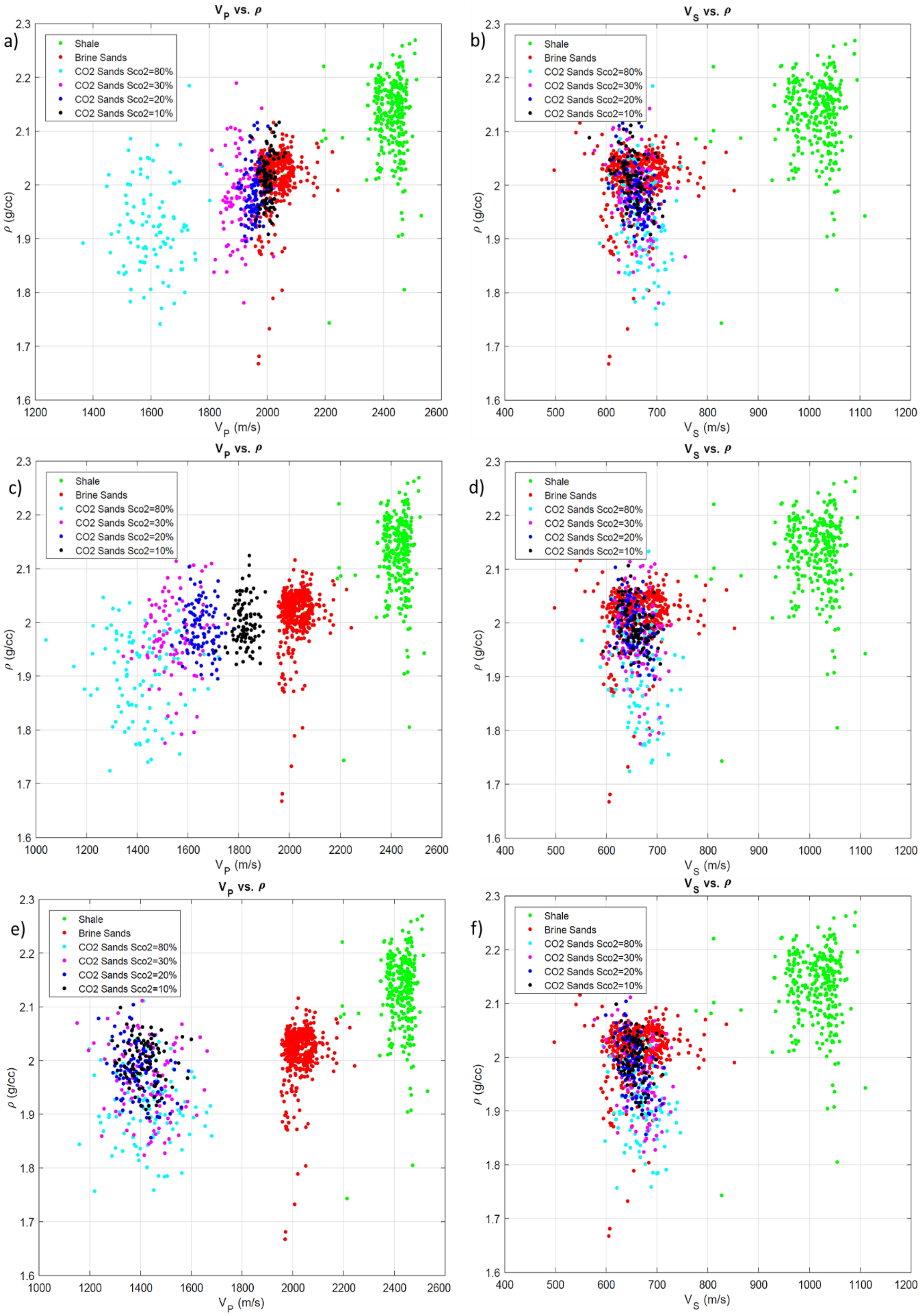

Figure 6.18: *V_P vs ρ and V_S versus ρ cross-plot for different fluid distributions simulated by Brie's equation. a) and b) corresponds to e exponent equal 1 (patchy mixing law upper bound Voigt average), c) and d) e exponent equal 5, e) and f) e exponent equal* 40 *(uniform saturation lower bound Reuss average).*

In the conventional context of rock properties evaluation at usual depths of about 2500 or 3000m, one can expect that shales should have higher V_P/V_S and maybe lower AI than brine sands, as long as, the sandstone shows moderate porosity and compaction. In this case, shales have the higher AI and lower V_P/V_S in comparison with brine sands. This is clear indication that lithology effects are playing a quite important role by changing the usual seismic property trend. However, there is a good agreement with the rock physics templates (RPT) in the sense that the increments of V_P/V_S and lower AI are associated to higher porosity and poor consolidation of the rock as it is the case of Utsira. In addition, the fluid effects exhibit the expected reduction of the both V_P/V_S and AI which locates all the partially CO_2 sandstones to the lower left corner of the plot. These results can be comparable with those obtained by Bachrach and Avseth (2008). They showed that shallow sandstone, (Utsira is around 800-1000m depth) that are poorly consolidated and whose friction between the grain contacts is almost negligible, present a drastic response in V_P -V_S ratio, which is higher than shales.

Figure 6.18 shows the cross-plots of V_P-density and V_S-density for the three different fluid distributions. It is clear that density and shear velocity changes due to fluid effects are not enough for discrimination. Density can be only used as a weak lithology discriminator, whereas the shear velocity properly separates shales from sandstones. On the other hand, compressional velocity allows to distinguish lithology and fluids content because of its dependency on the bulk modulus. However, the quantitative discrimination based on velocity is constrained by the way in which the fluids phases are distributed.

6.4.2 AVO Calibration

The calibration process as part of the workflow it is highly important and considered as a crucial step, since it has a considerable effect on computed attributes and classification results (Causse et al,. 2007b). It seems that the calibration process is quite sensitive to the selected classes (lithofacies). For instance, the outcome from the selection only of shales/shales is giving the most sensible results in accordance with the previous studies and the known information of the area (see Figure 6.24). In addition to that, the quality control of the classification results inside the plume is quite acceptable.

On the other hand, the results given by the second selection showed in Figure 6.19 (shales/shales, brine sands/shales and shales/brine sands) indicate that the shales reflectivity is almost inexistent. This means that the background reflectivity is controlled only by the reflectivity contrast between brine sands/shales and shales/brine sands. Moreover, the estimations of CO_2 for the same fluid distribution in this case (e=5) is completely different that one obtained with the first selection. For example, all CO_2 layers show 80% saturation with some minor accumulation of 30%. The reliability of this outcome is quite low, since after the quality control most of the points fall into the no defined class (null values) in white colour. This might be a clear indication of the unreliability of the obtained result under this class selection. A reason for this high discrepancies could be associated to the fact that grouping the contrasts between brine sands/shales (weak reflectivity) as equal to shales/shales (almost no reflectivity), the strong lithology effect due to the contrast between a hard consolidated shale and soft unconsolidated sandstone is completely removed. Therefore, any strong reflectivity anomaly might be directly associated with the highest CO_2 saturation, since those must have the strongest AVO effect.

Moreover, from the Optimal AVO attributes cross-plot analysis, it is clear the scattering of the seismic data. It might be possible that random noise from residual move-out, non-hyperbolic move-out, coherent noise and multiples is still present in the data. However, it was shown that when the calibration is performed with only shales/shales class, the result has less uncertainty and the scattering of the seismic data is reduced. As was pointed out by Causse et al. (2007b) and Traub (2008), further investigations must be done related to the calibration stage within the AVO workflow, since it seems to be very sensitivity to the lithofacie selection and could strongly mislead interpretation and conclusion.

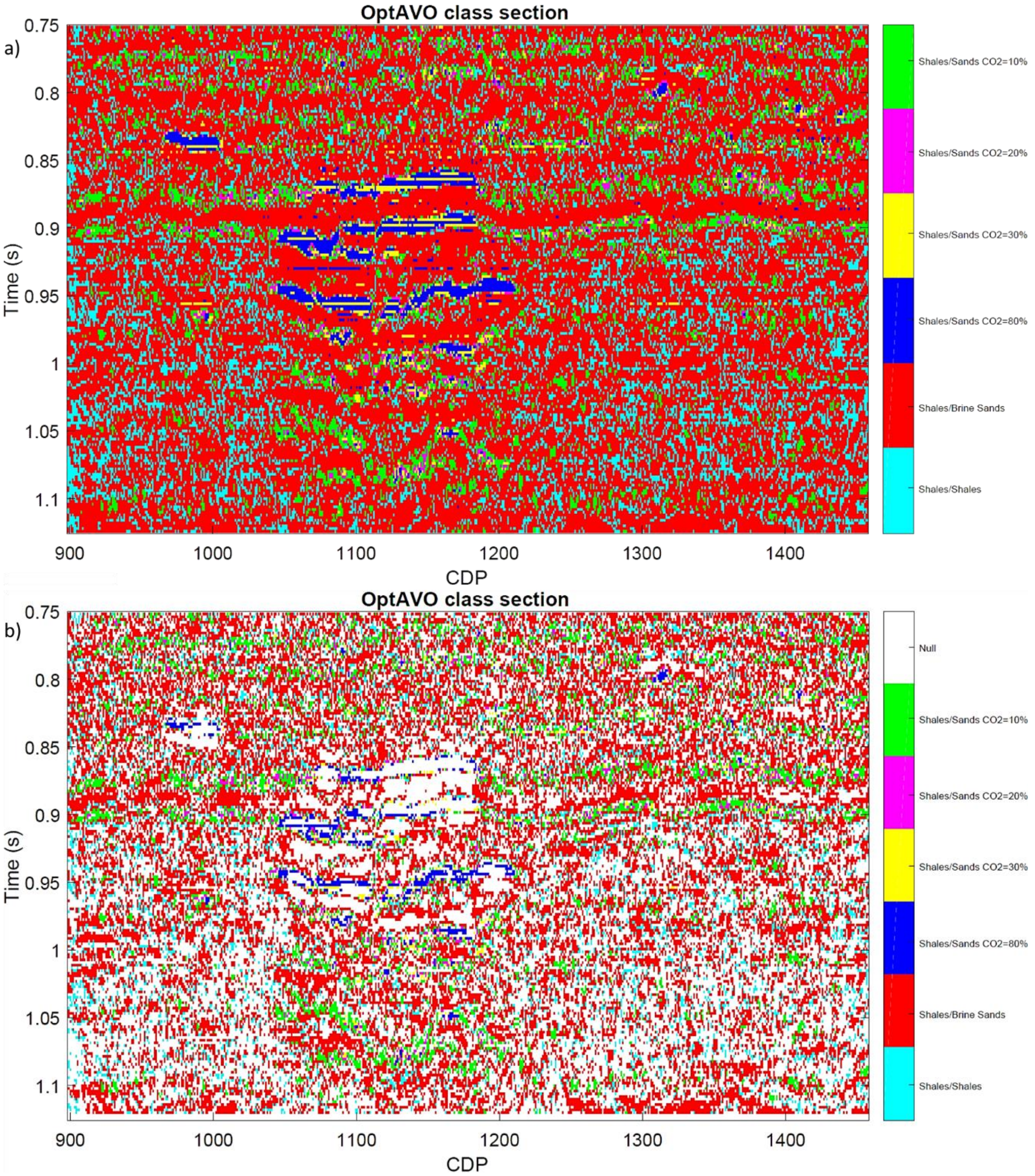

Figure 6.19: *AVO classification section and cross-plot attributes results with calibration window including shales/shales, brine sands/shales and shales/brine sands. a) Classification section, b) classification section after quality control. Color code denotes the different AVO reference classes (lithofacies interface).*

6.4.3 AVO Attribute cross-plots

Several AVO attribute cross-plots are presented in this section. First, the optimal AVO attributes C_1, C_2 and C_3 are used for discrimination. Also the same attributes obtained from seismic within a time window inside and outside the CO_2 plume are presented and compared. The range of CDP and the position of the gathers are the same as zone a) and b) shown in Figure

5.12 and Figure 6.24 as part of the QC and classification section results, respectively. The same plots are shown for the conventional AVO attributes R_o, G and A_3.

Figure 6.20 and Figure 6.21 depict the different simulated classes and the result of the seismic inversion. It is clear from both figures that regardless of the attribute type the discrimination in terms of CO_2 saturation is quite challenging. All clusters representing each individual class have large overlapping are with each other. It is difficult to say if the seismic amplitudes corresponds to sandstone with 10, 20 or 30% CO_2 saturation. C_1-C_2 and C_1-C_3 seems to be the better attributes to discriminate some of the sandstones, whereas C_2-C_3 does not separated properly the different lithologies. For instance all classes are on top of each other. On the other hand, from a qualitative point of view the results are quite satisfactory, since the information taken outside the plume does not show any anomalous reflectivity character. They are mostly on top of shale/shale, brine/shale and shale/brine classes that are considered as part of the background trend with quite low reflectivity. From the results inside the plume is it clear that the seismic data points are widely spread, moving towards the partially saturated sandstones in the C_1-C_3 and all the conventional AVO cross-plot.

The intercept and gradient cross-plot reveals that all the partially saturated sandstones have the same AVO class IV. This AVO class was introduced by Castanga and Swam (1997) and is characterized by sands whose reflection coefficients become less negative with increasing offset. This type of AVO does occur when a soft sand with gas, is underneath of a stiff shale. In this particular case, the previous conditions are met, since the Utsira sandstone is highly unconsolidated and the overlying shales are reported as silt rich lithology.

From Figure 6.21, it seems that R_0-A_3 indicates that several points belong to higher CO_2 saturation (80%), whereas the other plots show that almost none of the seismic samples fall into this category. This inconsistencies might be associated to seismic data noise and uncertainties.

Figure 6.22 and Figure 6.23 illustrate the AVO attribute results when e exponent is equal to 5. As expected the discrimination among the partially saturated sandstones is larger. However, it is still limited by the range of variability of the seismic properties within each class. In general, the behavior of the different cross-plots is the same. In the optimal AVO attribute space, the better discriminator attribute pairs are C_1 and C_2 and C_1 and C_3, whereas in the conventional space all the cross-plots are equally capable to separate the different classes.

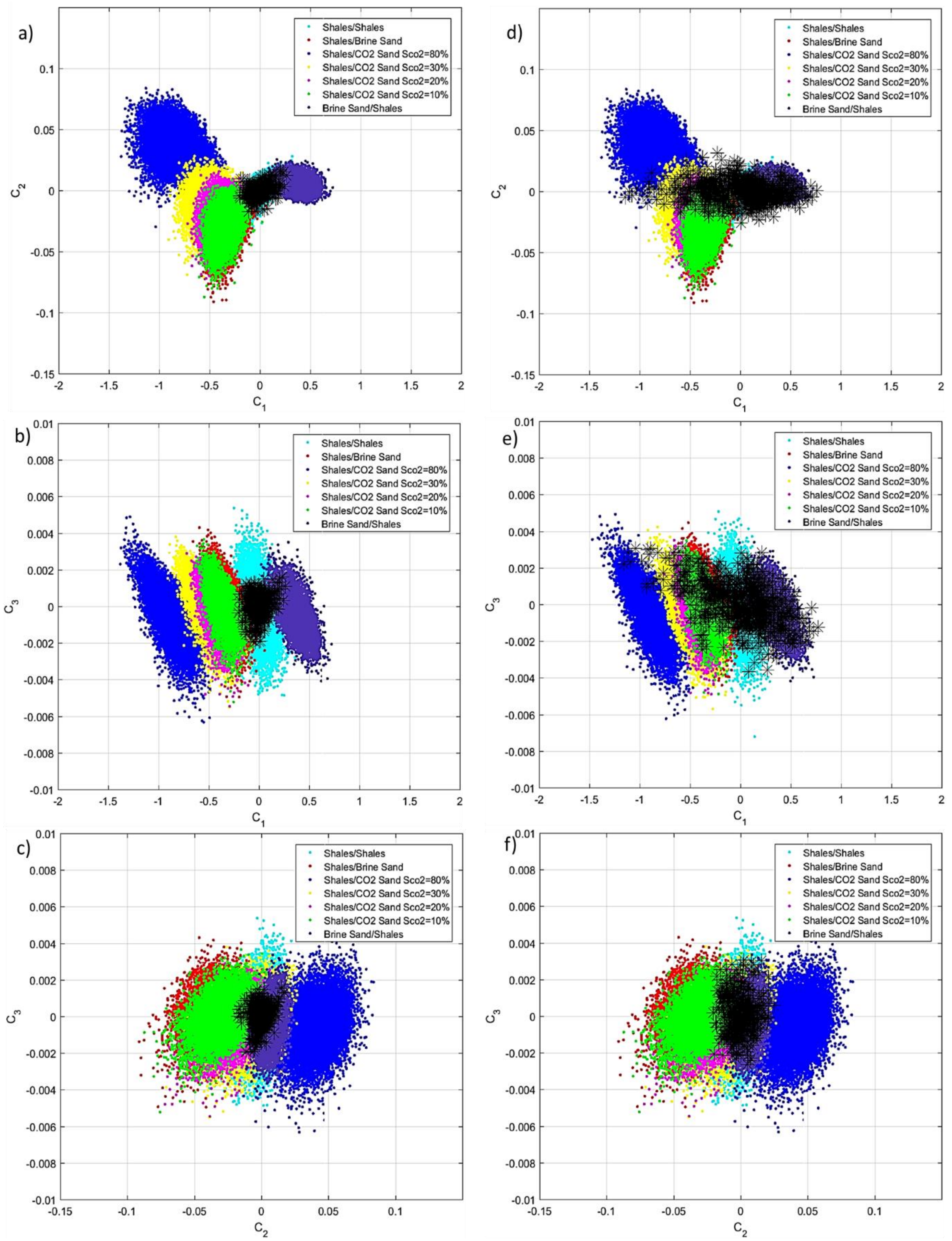

Figure 6.20: *Optima AVO cross-plot for Inline 1838 within a time window from 0.85 to 0.96s inside and outside the CO_2 plume for Brie e exponent equal 1. a)-c) C_1, C_2 and C_3 cross-plot of CDP gathers outside the plume (900-910). d)-f) C_1, C_2 and C_3 cross-plot of CDP gathers inside the CO_2 plume (1100-1110).*

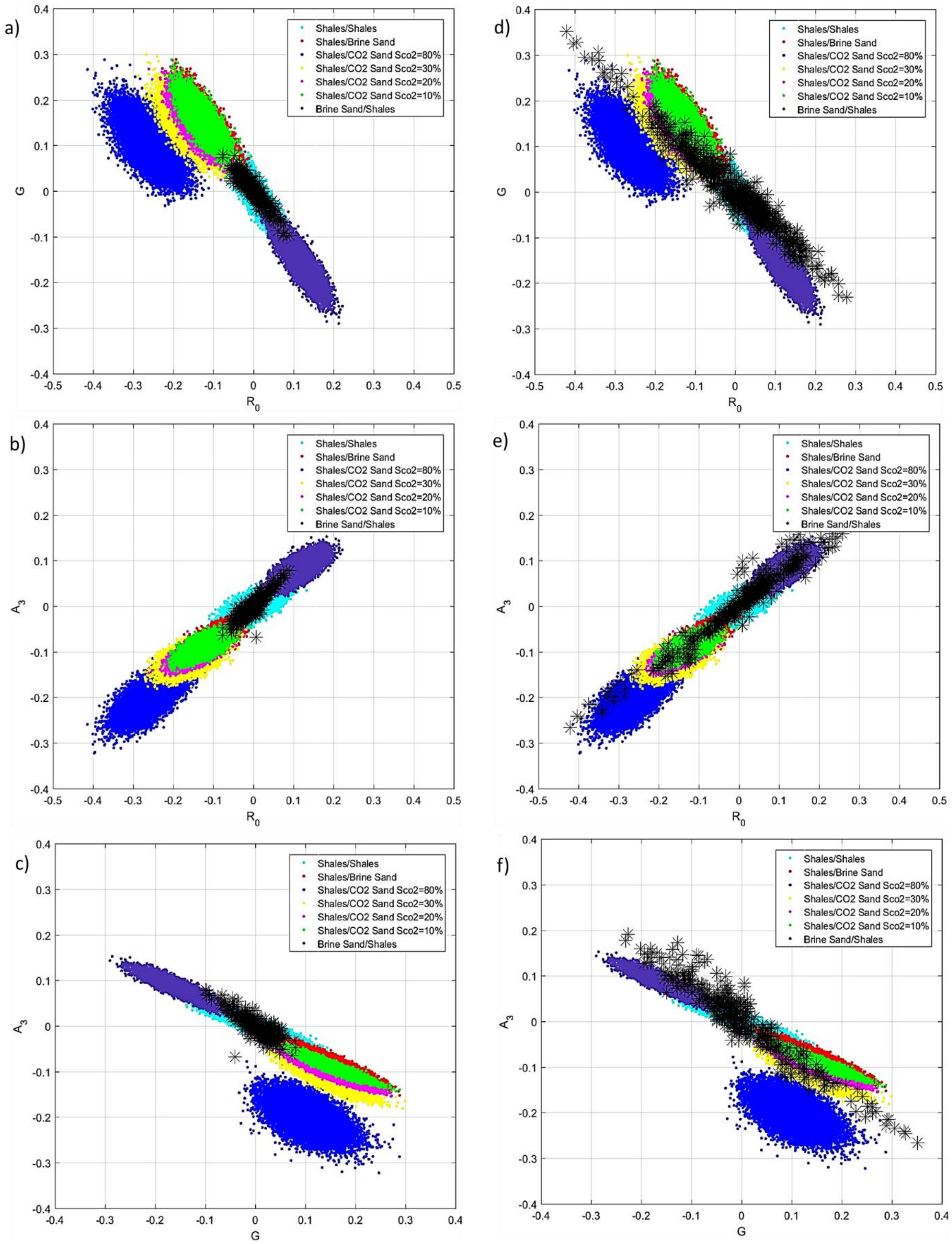

__Figure 6.21:__ Convention AVO attributes estimated from C_1, C_2 and C_3 cross-plot for Inline 1838 within a time window from 0.85 to 0.96s inside and outside the CO_2 plume for Brie e exponent equal 1. a)-c) R_0, G and A_3 cross-plot of CDP gathers outside the plume (900-910). d)-f) R_0, G and A_3 cross-plot of CDP gathers inside the CO_2 plume (1100-1110).

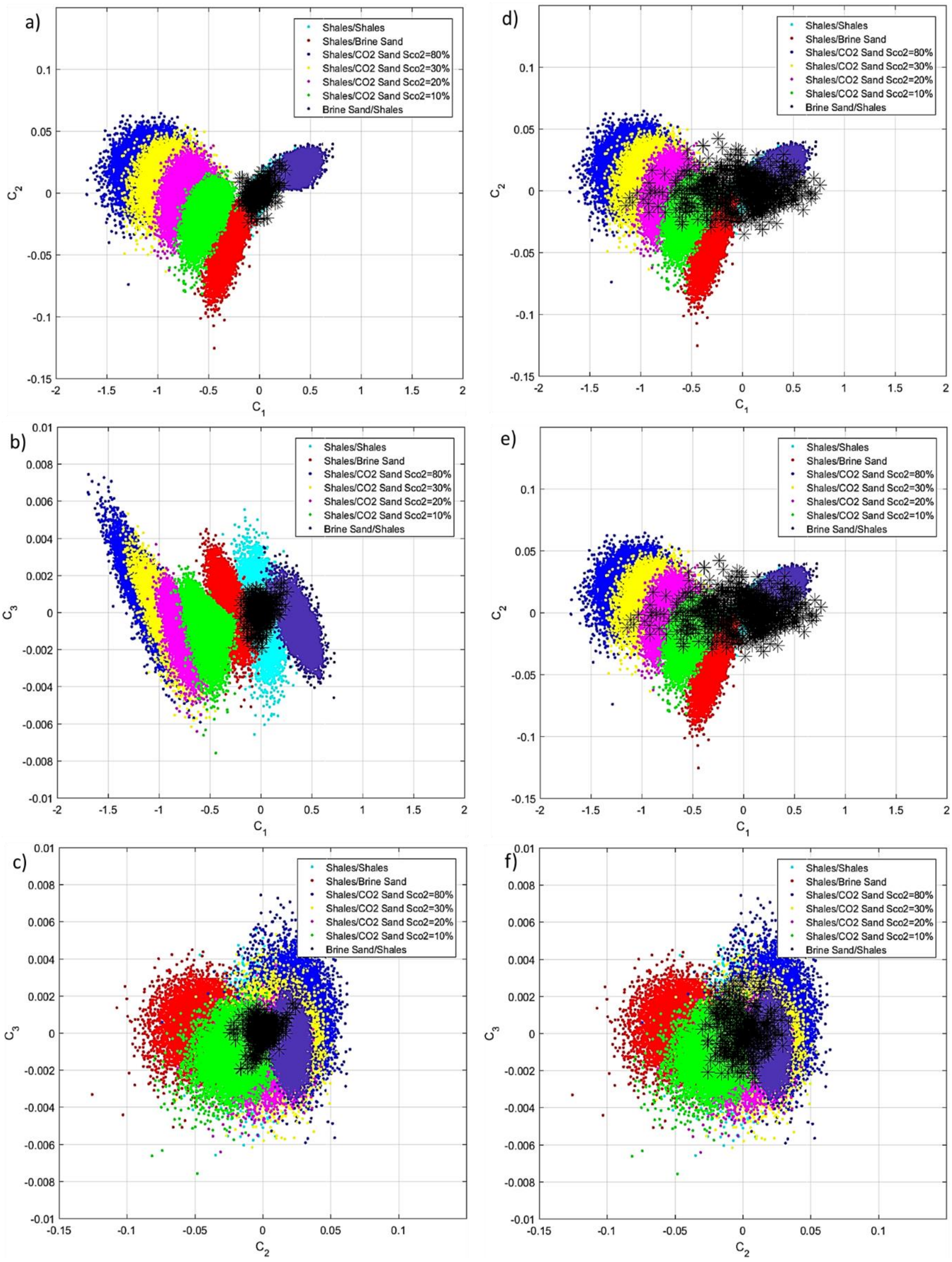

Figure 6.22: *Optima AVO cross-plot for Inline 1838 within a time window from 0.85 to 0.96s inside and outside the CO$_2$ plume for Brie e exponent equal 5. a)-c) C$_1$, C$_2$ and C$_3$ cross-plot of CDP gathers outside the plume (900-910). d)-f) C$_1$, C$_2$ and C$_3$ cross-plot of CDP gathers inside the CO$_2$ plume (1100-1110).*

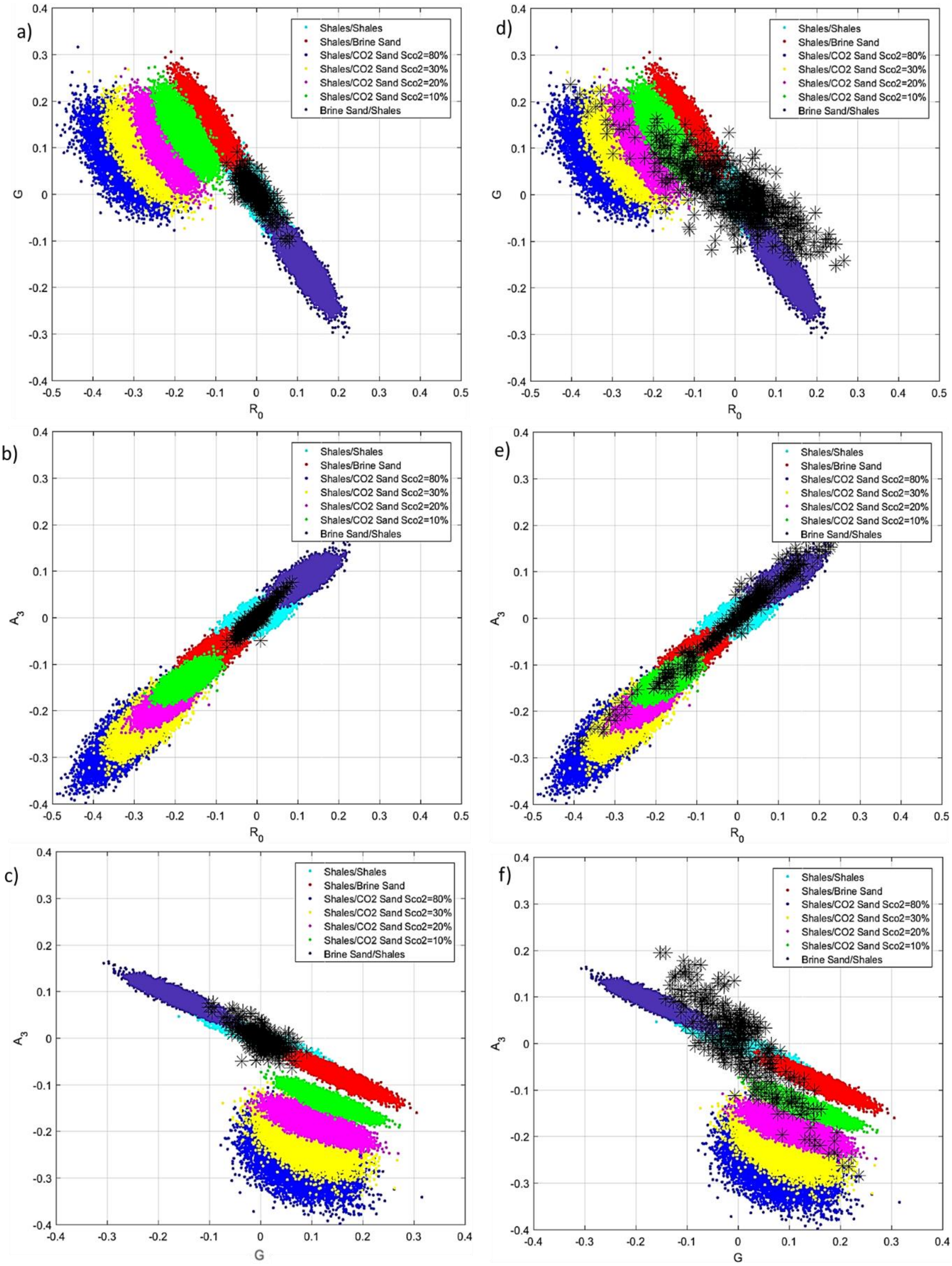

Figure 6.23: *Convention AVO attributes estimated from C_1, C_2 and C_3 cross-plot for Inline 1838 within a time window from 0.85 to 0.96s inside and outside the CO_2 plume for Brie e exponent equal 5. a)-c) R_0, G and A_3 cross-plot of CDP gathers outside the plume (900-910). d)-f) R_0, G and A_3 cross-plot of CDP gathers inside the CO_2 plume.*

Regarding the most probable CO_2 saturation in the sandstone according to these results, one can expect quite low values. From R_0-G it is clear that the cluster of points are around the background trend. At the same time, they are shifted from right to left falling into lower CO_2 saturation classes, the most populated one is 10% which at the same time is strongly overlapping by 20 and 30%. Just a few point are located further left and up being inside the boundary between 30 and 80%. Moreover, from intercept and curvature is clear that a quite large amount of seismic points belong to the lowest CO_2 saturation class. Similarly, several are falling into 20, 30 and 80%, respectively. It is important to point out that the in the gradient vs. curvature plot a good discrimination of the 10% CO_2 sand from the brine sands and others with higher saturation is quite good. This might suggest with higher level of certainty that for this type of fluid distribution the majority of the seismic amplitudes seems to respond to the lowest CO_2 concentration. Moreover, the 80% class is wide spread behind the other saturations.

Results obtained using uniform mixing law (lower bound, Reuss average), present similar behavior in all the cases inside and outside the plume. However, as it was shown in the previous section, only a very small percentage of CO_2 is enough to reduce drastically the compressional wave velocity, in such a manner that the brine sands are completely separated from the partially saturated ones. Thusly, the AVO attributes are not able to detect the difference between different classes; all cross-plots show the partially saturated sandstone together and separate from the background trend (see Figure B-5 and Figure B-6 in Appendix B).

Similar results were obtained for Inline 1880. The main difference between these two lines is mostly related to the sparsity of the seismic data points. For a specific attribute cross-plot, it is possible to detect higher or lower levels of scattering where some of the points might not belong to any modelled classes. This is normal behavior because the real seismic data suffer from a wide combination of effects that might not be directly associated to the rock properties. Those must be properly addressed during the processing but it is not always the case. In addition, the simulated classes are based on well log data and rock physics models and there is always uncertainty associated to it. Several assumptions are made in order to simplify the models such as isotropic, horizontal layers, perfectly elastic layers among others that can be a potential source of error.

It is worth noting that the well information is recorded in a completely different frequency range (in the order of kHz), whilst the frequency content of the seismic is usually between 5 and 100Hz. The well is able to detect very small differences in a few centimeters but the seismic looks at the average values in the range of several meters. For all these reasons there will be always a bias between both type of measurements and only general trends are interpreted, in addition to dispersion effects.

6.4.4 AVO lithofacies classification

As part of the AVO analysis and attribute estimations 2D sections with their respective lithofacies classification are also obtained via statistical approach as was presented in Chapter 4. From the previous results we might expect considerable differences between sections depending on how the fluid phases are disseminated into the porous medium. Figure 6.24, Figure 6.25 and Figure 6.26 show the distribution of each classes along the seismic section with the corresponding quality control, for Brie model with e exponent equal to 1, 5 and 40, respectively.

In general, it is possible to see at least 5 CO_2 layers interbedded by shales and brine sands. The patchy saturation shows the highest CO_2 concentration in the uppermost layers followed by 30% in most of the lower layers and 20% near the injection point (see Figure 6.24). These results are in a good agreement with previous results presented by Ghosh et al. (2015), who showed that it most likely to have patches of gas in the upper layers with 80% concentration. On the other hand, Brie model with exponent e equal to 5 shows a completely different scenario, suggesting that the most likely saturation of CO_2 in all the layers is about 10% with some higher accumulation of 80% at the shallower layers decreasing gradually from 30 to 10% (see Figure 6.25). The highest CO_2 levels are mostly associated with areas of higher amplitude anomalies. Finally, the uniform saturation model with e=40 indicates that all CO_2 layers have high saturation of 80% and minor concentrations of 30 (see Figure 6.26). Ghosh et al. (2015).suggest, that a finely uniform saturation of CO_2 and brine is expected, but in very low concentrations ranging from 40-20%.

Looking at the quality control sections it is clear that the Brie model with e exponent equal to 40 is giving the less reliable estimation of CO_2, since the amount of null data is larger than for the other two distributions. This is because of the lack of discrimination capability among the classes. From the previous results it was shown that the only property that allows to do that is the P-wave velocity and this one at the same time is strongly controlled by the fluid distribution. In contrast, for Brie model with e exponent equal to 1 and 5 the reliability of the estimates inside and outside the plume is much higher.

Similar results are found for Inline 1880, which is located further from the injection point (540m approximately). Considering that the stratigraphy of the area is not laterally variable, one can think that the extension of the plume follows some preferential directions (N-S) along the ridge (Chadwick et al., 2010) (see Figure 5.11, which shows the interpretation of uppermost CO_2 layer) leading by permeability patterns.

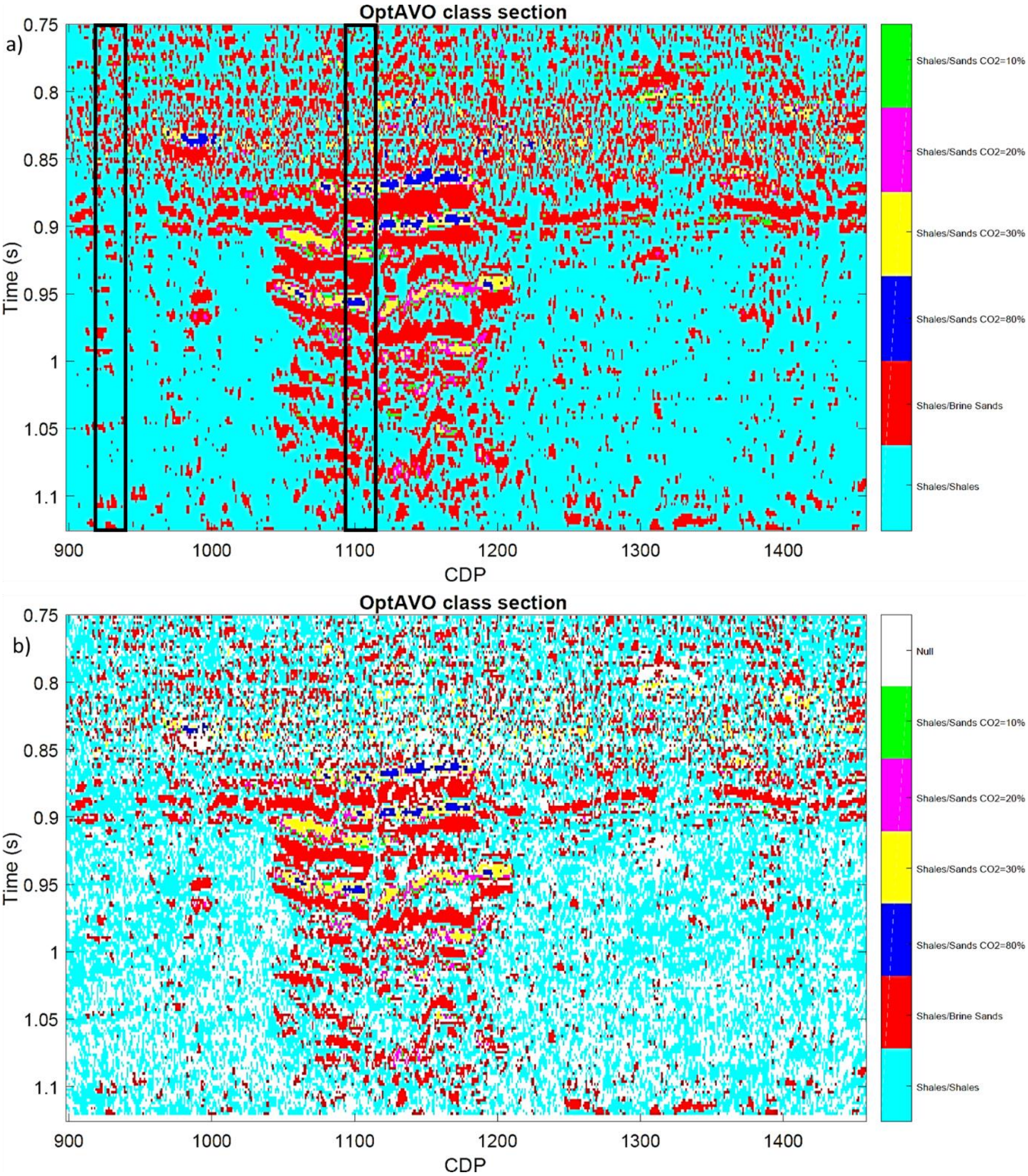

Figure 6.24: *Classification section of Inline 1838 with their corresponding QC for Brie model with e exponent equal to 1. a) initial classification b) and classification after quality control. Color code represents each of the classes and withe color represents null values. Black rectangles denote the CDP gathers selected inside and outside the plume for the AVO cross-plot analysis.*

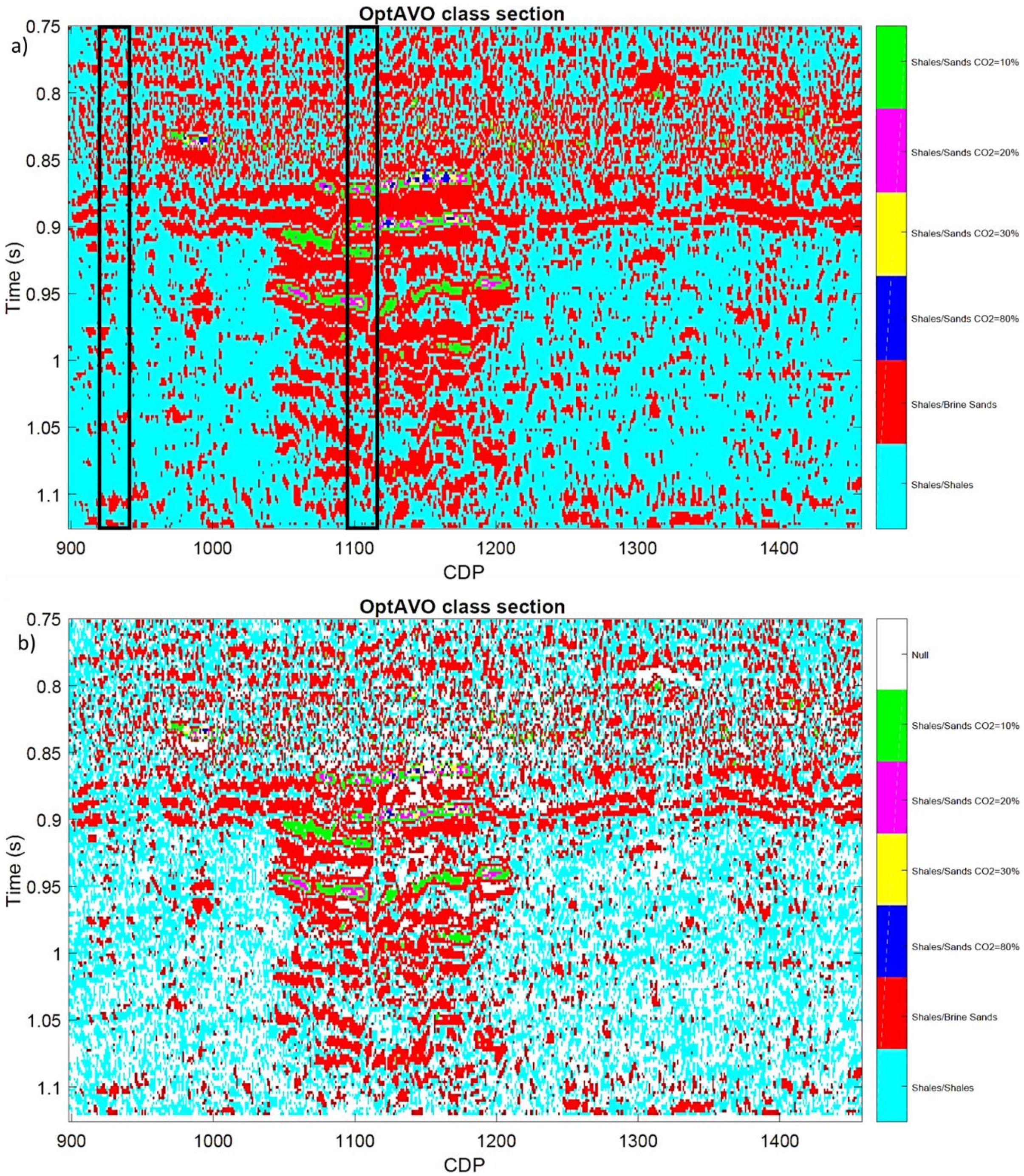

Figure 6.25: *Classification section of Inline 1838 with their corresponding QC for Brie model with e exponent equal to 5. a) initial classification b) and classification after quality control. Color code represents each of the classes and withe color represents null values. Black rectangles denote the CDP gathers selected inside and outside the plume for the AVO cross-plot analysis.*

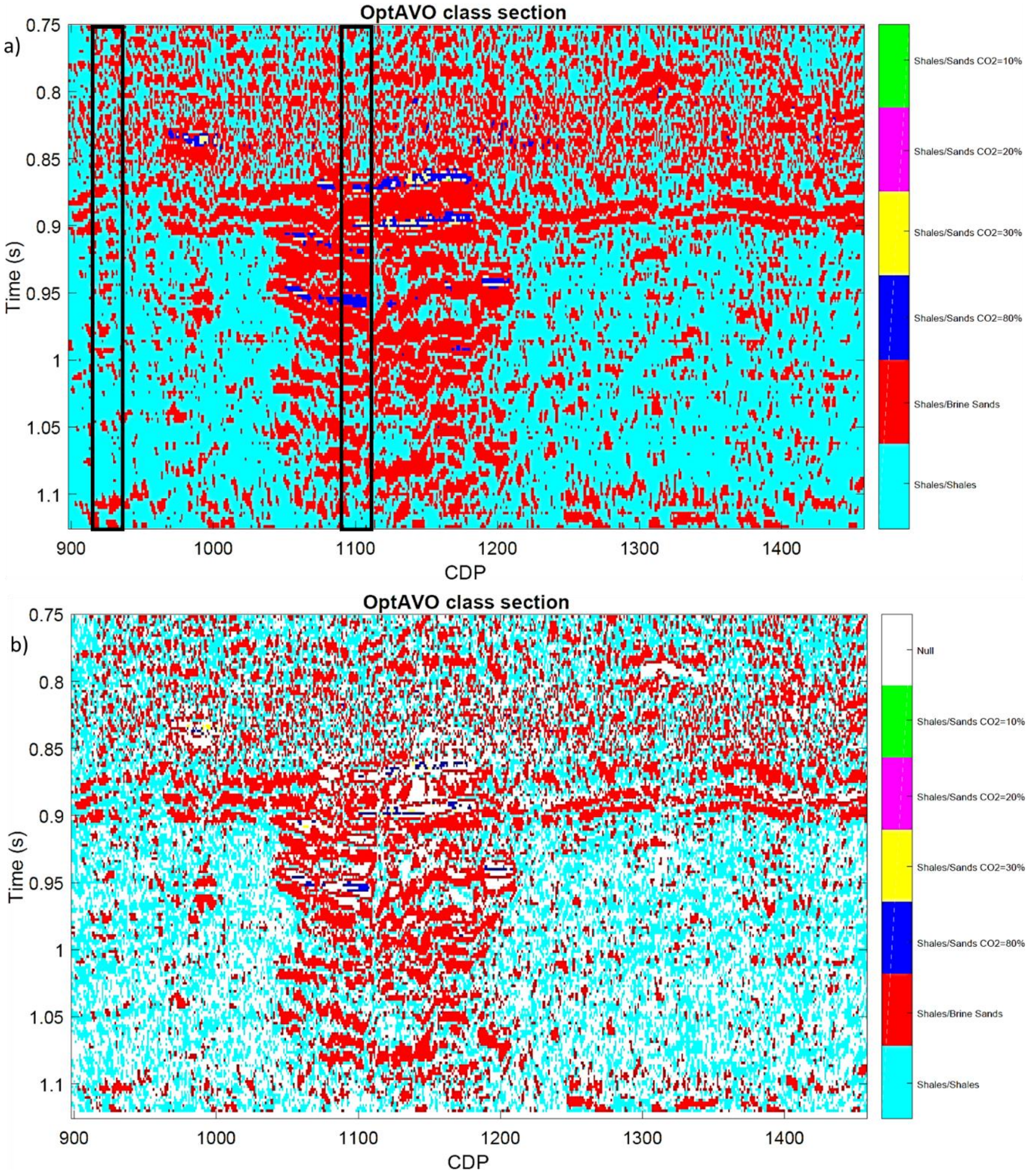

***Figure 6.26**: Classification section of Inline 1838 with their corresponding QC for Brie model with e exponent equal to 40. a) initial classification b) and classification after quality control. Color code represents each of the classes and withe color represents null values. Black rectangles denote the CDP gathers selected inside and outside the plume for the AVO cross-plot analysis.*

6.4.5 Elastic Reflectivity sections

Elastic reflectivity sections were generated from the estimates of the conventional AVO attributes via mathematical relations between the reflectivity AVO attributes and elastic properties (see Equations (4-10), (4-12) and (4-15)). P- and S-impedance reflectivities give a good qualitative insight about the CO_2 accumulation into the Utsira sandstone layers. Figure 6.27 and Figure 6.28 show both sections for Inline 1838 and Inline 1880 with the interpreted horizons. It is important to keep in mind that these results are relative contrasts between the interfaces. Therefore, can be only considered as qualitative indicators. Only those obtained with Brie model e exponent equal to 5 are shown, since all of them show the same patterns.

One can see from the impedance reflectivity that the CO_2 plume stands out from the background reflectivity trend. In this case, even the overburden has higher reflectivity than the Utsira formation outside the plume. This might be related to the poor consolidation of the reservoir leading to this low reflectivity. Although the reflection from the top of the sandstone and the cap-rock shale can be considered as weak, it is distinguishable and the reflectivity patterns (amplitude content, configuration of reflections, continuity) enhance the difference between these two lithofacies.

When it comes to the analysis of the data inside the plume, very distinctive patterns are seen. First, the reflectivity in magnitude increases for both negative values and positive values, revealing the difference in fluid content or lithology between each interfaces. The interlayer shales that were perfectly detected at the well log scale and no visible in the seismic data, now become visible. This is due to the CO_2 injection into the saline aquifer that starts to migrate upwards and accumulate partially inside the sandstone. The inter-layer shales act as weak barriers since the CO_2 can migrate upwards until it reaches the cap-rock seal of the Northland Group at the top of the Utsira formation.

From Figure 6.27, it is clear that at the top of the reservoir the area which is partially saturated with CO_2 has quite strong negative contrast (soft lithology) in comparison with the shales (hard lithology). Similarly, the strongest contrast is found in the upper layers and the reflectivity is getting weaker and weaker at the bottom. It is worth noting that there are some small accumulations that show the highest contrast values, so they might be associated with the largest saturations.

It is important to notice that the temporal thickness of the reflectors in the majority of the cases is much larger than the shale thickness reported from the wells. However, the seismic data is able to point out the higher contrast in elastic properties through amplitude anomalies. On the other hand, one need to keep in mind that for all the shale layers and some sand CO_2 layers, the tuning effect due to limitation in the vertical resolution is present in the response.

Although the shear wave impedance reflectivity contrast also suggests the same patterns, the reflectivity is not as strong as in the case of the P-impedance. This might be related to smaller sensitivity of the shear wave to fluids. In this case the introduction of the CO_2 in the system reduce the bulk density of the rock enhancing the density contrast between the shale and sandstones, (see Figure 6.29).

Inline 1880 shows a clear CO_2 plume development, which also presents a flatter reflectors in the uppermost top of the sandstone in comparison with Inline 1838. One additional CO_2 layer can be seen in this line. Likewise, the highest contrast are found in the shallower layers suggesting the largest gas accumulations as gas pocket or patches in agreement with the work presented by Ghosh et al. (2015). Similar trends are seen for the shear wave impedance. For both Inlines, the deeper layers show the push down effect due to the lower velocities that is accentuated near the injection point as was presented by Delépine et al. (2011).

The way the CO_2 is being distributed into the pore space, changes considerably the quantitative results. However, reflectivity sections show reasonable agreement from a qualitative point of view with both e=1 (patchy mixing) and e=5 (average mixing between patchy and uniform) models.

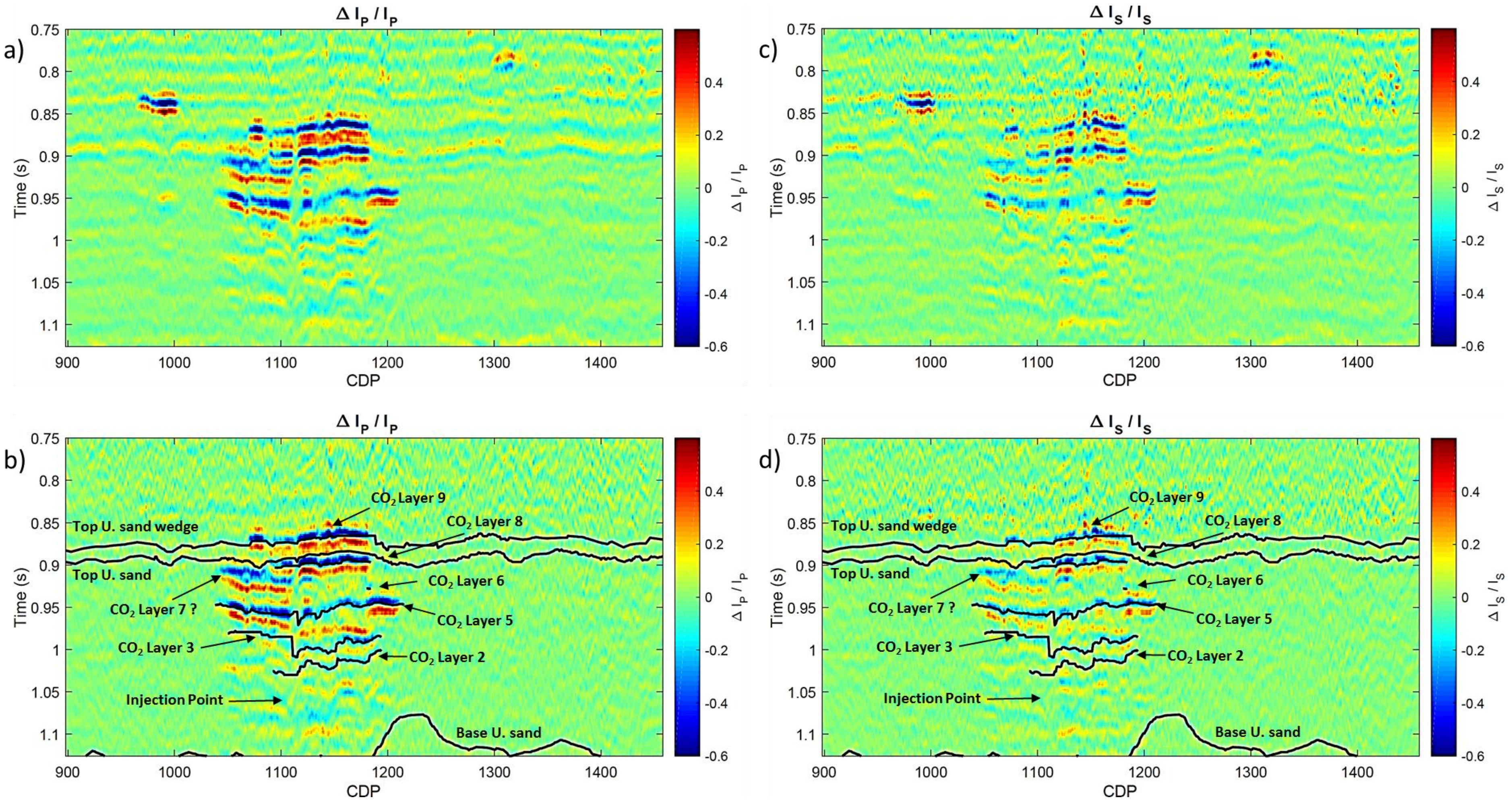

Figure 6.27: *Elastics Reflectivity sections of Inline 1838. a) and b) P wave impedance reflectivity, c) and d) S wave impedance reflectivity. The interpretation of key horizons and the position of the injection point are indicated in black.*

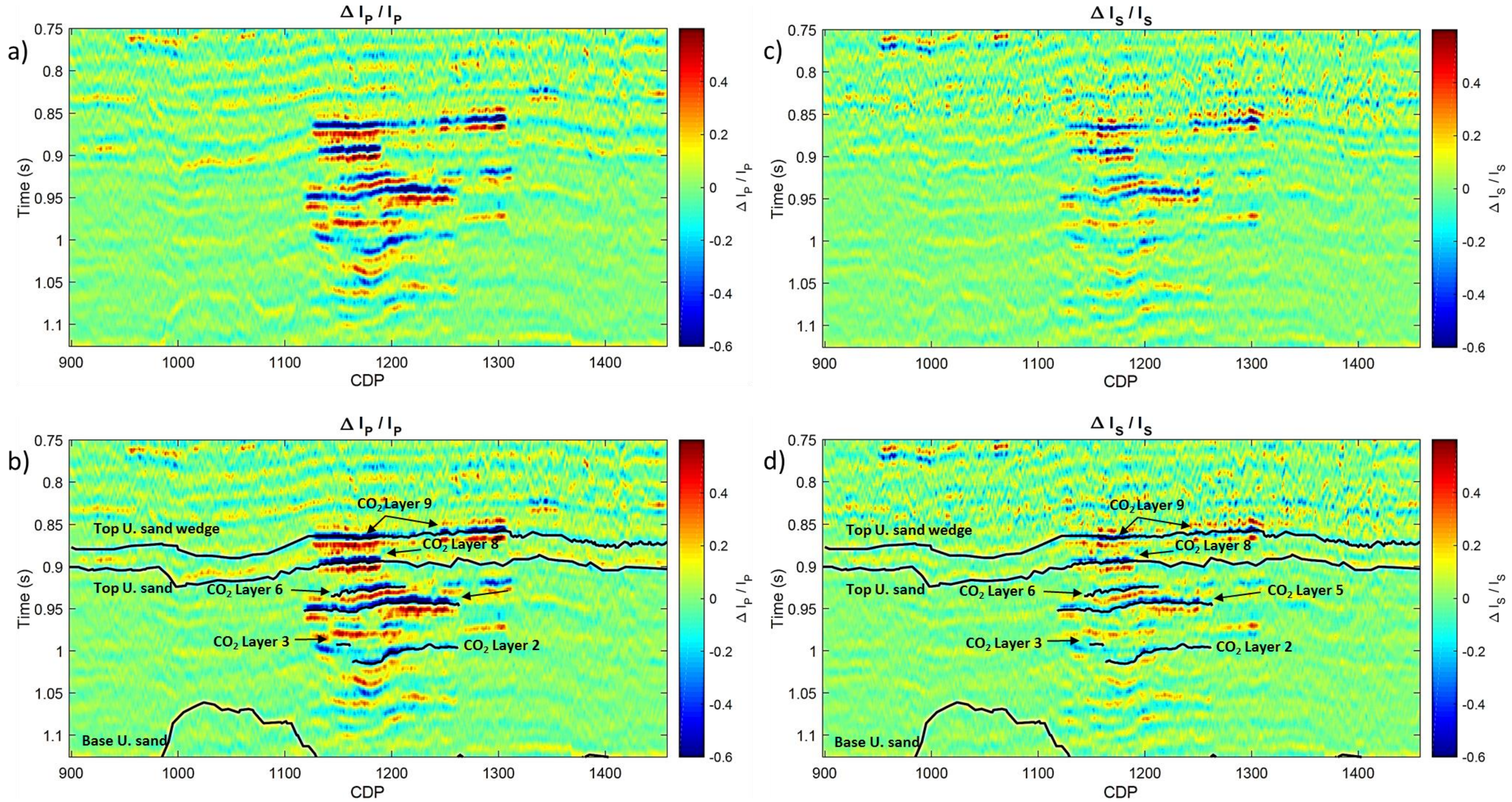

Figure 6.28: *Elastics Reflectivity sections of Inline 1880. a) and b) P wave impedance reflectivity, c) and d) S wave impedance reflectivity. The interpretation of key horizons and the position of the injection point are indicated in black.*

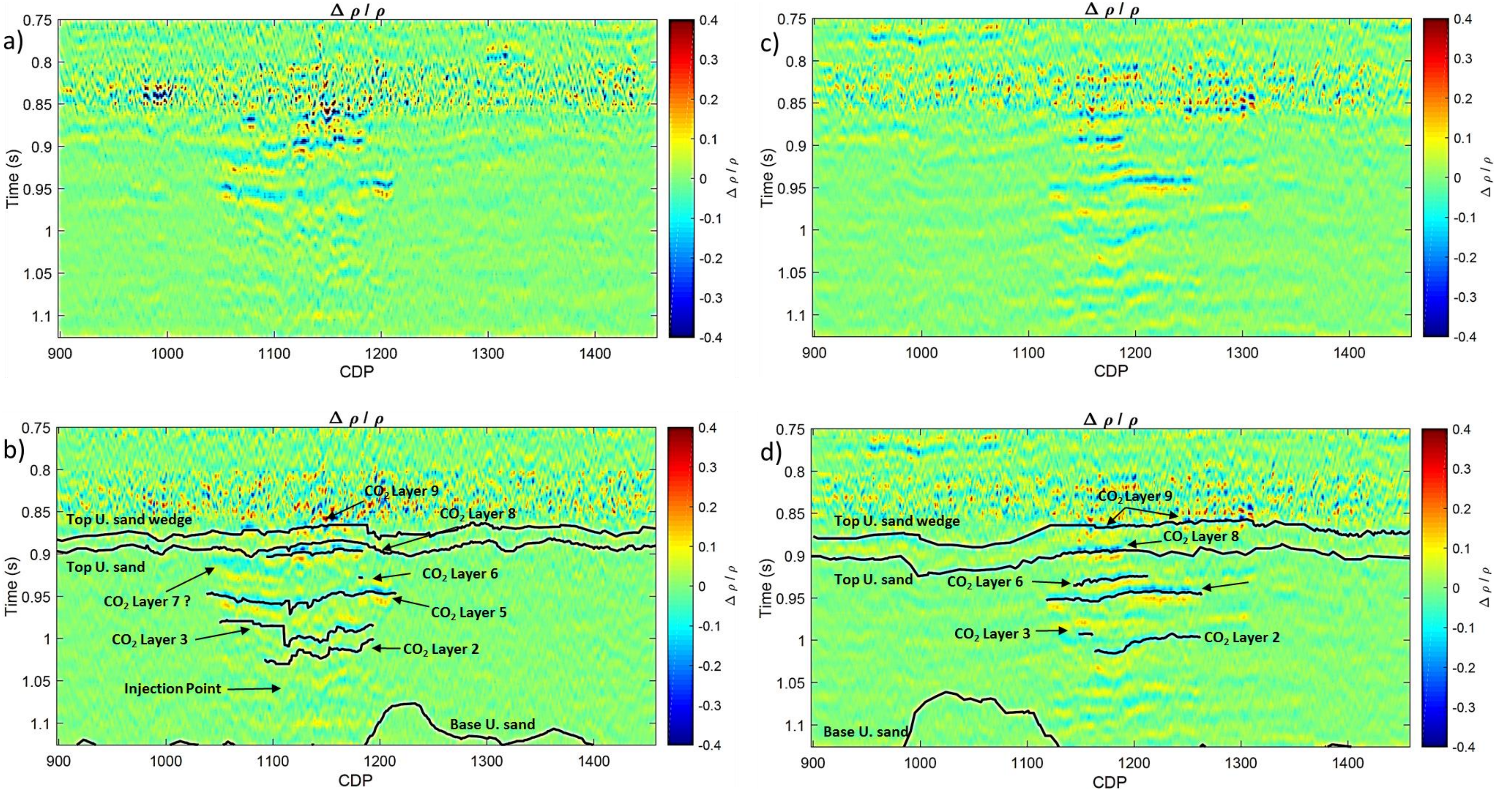

Figure 6.29**:** *Density reflectivity sections of Inline 1838 and Inline 1880. a) and b) Inline 1838, c) and d) Inline 1880. The interpretation of key horizons and the position of the injection point are indicated in black.*

Chapter 7 Conclusions

This work is composed by two main topics: attenuation modelling and AVO real data applications. The first one aims to investigate whether or not the intrinsic attenuation due to mesoscale heterogeneities and layering have a significant impact in the amplitudes and waveform phase. In addition, different water saturations, possible tuning and AVO effects were also considered. The second goal was to applied Optimal AVO techniques to real data of Sleipner field in order to estimate the CO_2 saturations.

The behavior of the reflection and transmission coefficients as function of incident angle for different S_w were evaluated for a single interface between elastic/elastic layers and between elastic/viscoelastic layers. From this, it was shown that there is no differences in terms of R/T coefficients between a perfectly elastic and viscoelastic medium for all the range of water saturations. Despite of a fact, that at 20% S_w the attenuation level is the highest at 3000Hz, it did not give any considerable difference. Therefore, it was thought that a single interface might not represent the total contribution of stack of periodic layers, since the wave is not being propagated through the attenuated medium.

Due to that, a synthetic model (3-layers model) was investigated with the aim to simulate the wave propagation through the attenuated medium. Two different viscoelastic scenarios were presented, which differ only in the value of the quality factor. For model 1 the quality factor was high (Qp=1135 and Qs=876 values obtained from a poroelastic simulation at 30Hz using Brie's model) and does not show any attenuation effect. In contrary, when the quality factor was low (Qp=27 and Qs=22) strong reduction of the amplitude was noticed. By comparing near and far traces it was possible to analyze the AVO effect due to the replacement of brine by CO_2. Although the AVO effect is quite strong, the damping in amplitude caused by the viscoelasticity was quite high (only model 2). This means that the attenuation effect was not cancelled by the AVO. The difference in amplitude at near and far traces between elastic and viscoelastic models were about twice. Therefore, this might have a considerable impact if it is not addressed properly.

From the partial stack volumes, the only conclusion was that the AVO response which is driven by the contrast between the elastic properties is an apparent dominant effect over the attenuation, since one might expect to have the largest attenuation in the far offset or far angles. However, the strongest damping is seen for the near offset traces. But this effect cannot be misinterpreted as attenuation, since in this case the near offset always showed lower reflection coefficients.

Afterwards, the staking layers were simulated to account for possible tuning effects and also to consider the total contribution of all possible reflected and transmitted waves. The zero offset simulation in frequency domain suggested that the attenuation is quite weak and the energy loss is almost negligible, at least for 80 and 95% $S_{w,}$ On the other hand, 20% S_w seemed to show attenuation. When it comes to the time domain response of the full waveform propagation for different water saturations (20, 80 and 95%), none of them showed any significant attenuation effects between elastic/elastic, elastic/viscoelastic and elastic/poroelastic. This was a clear indication that for this model the attenuation can be neglected. It was also shown that the quality factor is the main controller of the attenuation effects. The high quality factor values obtained from the simulations of Sleipner field do not affect the amplitude either the phase of the signal. Indeed, for this partially saturated sandstone using a poroelastic model with strong attenuation effects in the seismic frequency bandwidth, it would be necessary to increase up to unrealistic values the hydraulic permeability of the rock (200 Darcy. In summary, it is possible to apply a conventional AVO technique based on Zoeppritz elastic equations to the Sleipner case, since the poroelasticity based on the model tested in this study shows an elastic behavior of the medium.

Regarding the AVO technique applied to the 2008 seismic vintage, it was shown that quantitative estimation of the CO_2 accumulated into the reservoir is highly dependent on the fluid distribution type. This is not a surprising result since the seismic parameter that allow us to discriminate both, lithology and fluids is the P-wave velocity. The S-wave velocity and density are only able to proper distinguish between sandstone (soft lithology) and shales (hard lithology). Their sensitivity to fluids is quite low showing maximum difference of about 20m/s and 0.12gr/cc, respectively from 0 to 100% S_w. On the other hand, the P-wave velocity can show distinctive patterns with water saturation, depending upon how the fluid phases are being distributed into the medium. For this reason, the classification sections after AVO inversion showed a large discrepancy among the different fluid distribution models, since the capability of the AVO to detect different lithofacies with accuracy is also model dependent. In addition, the reliability of the classification results is strongly reduced when the e=40 model (uniform saturation) is used.

The ambiguity in the P- and S-wave impedance reflectivities associated with the type of distribution does not allow to get an accurate estimates of the CO_2 saturation. Therefore, more constrains in the initial model must be considered. On the other hand, the impedance reflectivity from a qualitative point of view is consistent to distinguish between the areas with higher, medium and lower CO_2 concentrations from those where no CO_2 presence is expected.

As future work, it is recommended to go beyond the AVO reflectivity results to obtain more quantitative analysis, for instances seismic inversion of the elastic reflectivity sections in order to get their corresponding elastic parameters. Although the possible results from absolute acoustic and shear impedances can give a better understanding and less uncertainty in the CO_2 estimations, other geophysical methods might be needed to reduce the ambiguities associated to the type of saturation distributions. For example, control source electromagnetics (CSEM). It is also advisable to carry out a more accurate sensitivity analysis regarding the proper selection of calibration parameters for the OptAVO tool, since they seem to have an important influence in the final results. It would be valuable to compare absolute elastic properties estimation obtained from AVO with other quantitative tools as rock physics inversion and FWI. Finally, the implementation of different attenuation models that can be able to represent a realistic fluid distribution and simultaneously introduce strong attenuation effects might be helpful to investigate and their influence in the CO_2 estimations.

References

ADLER, P. M., JACQUIN, C. G. & THOVERT, J. F. 1992. The formation factor of reconstructed porous media. *Water Resources Research,* 28**,** 1571-1576.

AKI, K. & RICHARDS, P. 1980. Quantative seismology: Theory and methods. *Freeman and Company,* 2.

AVSETH, P., MUKERJI, T. & MAVKO, G. 2005. Quantitative seismic interpretation: Applying rock physics tools to reduce interpretation risk: Cambridge.

BACHRACH, R. & AVSETH, P. 2008. Rock physics modeling of unconsolidated sands: Accounting for nonuniform contacts and heterogeneous stress fields in the effective media approximation with applications to hydrocarbon exploration. *Geophysics,* 73**,** E197-E209.

BEHURA, J. & TSVANKIN, I. 2009. Reflection coefficients in attenuative anisotropic media. *Geophysics,* 74**,** WB193-WB202.

BIOT, M. A. 1956a. Theory of propagation of elastic waves in a fluid-saturated porous solid. I. Low-frequency range. *The Journal of the acoustical Society of america,* 28**,** 168-178.

BIOT, M. A. 1956b. Theory of propagation of elastic waves in a fluid-saturated porous solid. II. Higher frequency range. *the Journal of the Acoustical Society of America,* 28**,** 179-191.

BIOT, M. A. 1962. Mechanics of deformation and acoustic propagation in porous media. *Journal of applied physics,* 33**,** 1482-1498.

BØE, R. & ZWEIGEL, P. 2001. C haracterisation of the Nordland Shale in the Sleipner area by XRD analysis-A contribution to the Saline Aquifer CO2 Storage (SACS) project. Confidential SINTEF Report 33.0764. 00/01/01.

BORTFELD, R. 1961. Approximations to the reflection and transmission coefficients of plane longitudinal and transverse waves. *Geophysical Prospecting,* 9**,** 485-502.

BOUCHON, M. 1979. Discrete wave number representation of elastic wave fields in three-space dimensions. *Journal of Geophysical Research: Solid Earth,* 84**,** 3609-3614.

BOUCHON, M. 1981. A simple method to calculate Green's functions for elastic layered media. *Bulletin of the Seismological Society of America,* 71**,** 959-971.

BRIE, A., PAMPURI, F., MARSALA, A. & MEAZZA, O. Shear sonic interpretation in gas-bearing sands. SPE Annual Technical Conference and Exhibition, 1995. Society of Petroleum Engineers.

BROWN, R. J. 1980. Connection between formation factor for electrical resistivity and fluid-solid coupling factor in Biot's equations for acoustic waves in fluid-filled porous media. *Geophysics,* 45**,** 1269-1275.

BROWN, S., BUSSOD, G. & HAGIN, P. 2007. AVO monitoring of CO 2 sequestration: A benchtop-modeling study. *The Leading Edge,* 26**,** 1576-1583.

CARCIONE, J. M. 2007. *Wave fields in real media: Wave propagation in anisotropic, anelastic, porous and electromagnetic media*, Elsevier.

CARCIONE, J. M., PICOTTI, S., GEI, D. & ROSSI, G. 2006. Physics and seismic modeling for monitoring CO 2 storage. *Pure and Applied Geophysics,* 163**,** 175-207.

CASTAGNA, J. P. & BACKUS, M. M. 1993. *Offset-dependent reflectivity—Theory and practice of AVO analysis*, Society of Exploration Geophysicists.

CASTAGNA, J. P. & SWAN, H. W. 1997. Principles of AVO crossplotting. *The leading edge,* 16**,** 337-344.

CAUSSE, E., RIEDE, M., VAN WIJNGAARDEN, A., BULAND, A., DUTZER, J. & FILLON, R. 2007a. Amplitude analysis with an optimal model-based linear AVO approximation: Part I—Theory. *Geophysics,* 72**,** C59-C69.

CAUSSE, E., RIEDE, M., VAN WIJNGAARDEN, A., BULAND, A., DUTZER, J. & FILLON, R. 2007b. Amplitude analysis with an optimal model-based linear AVO approximation: Part II—Field data example. *Geophysics,* 72**,** C71-C79.

CHADWICK, A., WILLIAMS, G., DELEPINE, N., CLOCHARD, V., LABAT, K., STURTON, S., BUDDENSIEK, M.-L., DILLEN, M., NICKEL, M. & LIMA, A. L. 2010. Quantitative analysis of time-lapse seismic monitoring data at the Sleipner CO 2 storage operation. *The Leading Edge,* 29**,** 170-177.

CHADWICK, R., ARTS, R. & EIKEN, O. 4D seismic quantification of a growing CO2 plume at Sleipner, North Sea. Geological Society, London, Petroleum Geology Conference series, 2005. Geological Society of London, 1385-1399.

CHADWICK, R., KIRBY, G., HOLLOWAY, S., GREGERSEN, U., JOHANNESSEN, P., ZWEIGEL, P. & ARTS, R. 2002. Saline Aquifer CO2 Storage (SACS2). Final report, geological characterisation of the Utsira Sand reservoir and caprocks (Work Area 1).

CHADWICK, R., ZWEIGEL, P., GREGERSEN, U., KIRBY, G., HOLLOWAY, S. & JOHANNESSEN, P. 2004. Geological reservoir characterization of a CO 2 storage site: the Utsira Sand, Sleipner, northern North Sea. *Energy,* 29**,** 1371-1381.

CLOCHARD, V., DELÉPINE, N., LABAT, K. & RICARTE, P. 2010. CO2 plume imaging using 3D pre-stack stratigraphic inversion: A case study on the Sleipner field. *First Break,* 28.

CORMIER, V. F. 2011. Seismic, viscoelastic attenuation. *Encyclopedia of Solid Earth Geophysics.* Springer.

DE BARROS, L. 2008. *Sensibilité et inversion des formes d'ondes sismiques en milieu poreux strati é.* Université Joseph Fourier, Grenoble.

DELÉPINE, N., CLOCHARD, V., LABAT, K. & RICARTE, P. 2011. Post-stack stratigraphic inversion workflow applied to carbon dioxide storage: application to the saline aquifer of Sleipner field. *Geophysical Prospecting,* 59**,** 132-144.

DOMENICO, S. 1976. Effect of brine-gas mixture on velocity in an unconsolidated sand reservoir. *Geophysics,* 41**,** 882-894.

DUPUY, B., GARAMBOIS, S. & VIRIEUX, J. 2016. Estimation of rock physics properties from seismic attributes—Part 1: Strategy and sensitivity analysis. *Geophysics,* 81**,** M35-M53.

DUPUY, B. & STOVAS, A. 2013. Influence of frequency and saturation on AVO attributes for patchy saturated rocks. *Geophysics,* 79**,** B19-B36.

DUPUY, B. & STOVAS, A. 2016. Effect of anelastic patchy saturated sand layers on the reflection and transmission responses of a periodically layered medium. *Geophysical Prospecting,* 64**,** 299-319.

DUTTA, N. & SERIFF, A. 1979. On White's model of attenuation in rocks with partial gas saturation. *Geophysics,* 44**,** 1806-1812.

FENG, H. & BANCROFT, J. C. 2006. AVO principles, processing and inversion. *CREWES Research Report***,** 18.

FURRE, A.-K., KIÆR, A. & EIKEN, O. 2015. CO2-induced seismic time shifts at Sleipner. *Interpretation,* 3**,** SS23-SS35.

FUTTERMAN, W. I. 1981. Dispersive body waves. *Seismic Wave Attenuation***,** 405.

GAO, L. & MOROZOV, I. 2011. AVO Analysis of 3-D/3-C Datasets from Weyburn CO2 Storage and Monitoring Project.

GARAMBOIS, S. & DIETRICH, M. 2002. Full waveform numerical simulations of seismoelectromagnetic wave conversions in fluid-saturated stratified porous media. *Journal of Geophysical Research: Solid Earth,* 107.

GASDA, S., NILSEN, H. & DAHLE, H. Upscaled models for CO2 migration in geological formations with structural heterogeneity. ECMOR XIII-13th European Conference on the Mathematics of Oil Recovery, 2012.

GERMÁN RUBINO, J. & VELIS, D. R. 2011. Seismic characterization of thin beds containing patchy carbon dioxide-brine distributions: A study based on numerical simulations. *Geophysics,* 76**,** R57-R67.

GHADERI, A. & LANDRØ, M. 2009. Estimation of thickness and velocity changes of injected carbon dioxide layers from prestack time-lapse seismic data. *Geophysics,* 74**,** O17-O28.

GHOSH, R., SEN, M. K. & VEDANTI, N. 2015. Quantitative interpretation of CO 2 plume from Sleipner (North Sea), using post-stack inversion and rock physics modeling. *International Journal of Greenhouse Gas Control,* 32**,** 147-158.

GOODWAY, B., CHEN, T. & DOWNTON, J. 1997. Improved AVO fluid detection and lithology discrimination using Lamé petrophysical parameters;"λρ","μρ", & "λ/μ fluid stack", from P and S inversions. *SEG Technical Program Expanded Abstracts 1997.* Society of Exploration Geophysicists.

GREGERSEN, U., MICHELSEN, O. & SØRENSEN, J. C. 1997. Stratigraphy and facies distribution of the Utsira Formation and the Pliocene sequences in the northern North Sea. *Marine and Petroleum geology,* 14**,** 893-914.

HAARTSEN, M. W. & PRIDE, S. R. 1997. Electroseismic waves from point sources in layered media. *Journal of Geophysical Research: Solid Earth,* 102**,** 24745-24769.

HASHIN, Z. & SHTRIKMAN, S. 1963. A variational approach to the theory of the elastic behaviour of multiphase materials. *Journal of the Mechanics and Physics of Solids,* 11**,** 127-140.

HOLLOWAY, S., CHADWICK, R., KIRBY, G., PEARCE, J., GREGERSEN, U., JOHANNESSEN, P., KRISTENSEN, L., ZWEIGEL, P., LOTHE, A. & ARTS, R. 2000. Saline Aquifer CO2 Storage (SACS)–Final report: Work Area 1 (Geology). *BGS report, 31pp., Commercial–in confidence*.

JOHNSON, D. L., KOPLIK, J. & DASHEN, R. 1987. Theory of dynamic permeability and tortuosity in fluid-saturated porous media. *Journal of fluid mechanics,* 176**,** 379-402.

KEMP, S., BOUCH, J. & MURPHY, H. 2001. Mineralogical characterisation of the Nordland Shale, UK Quadrant 16, northern North Sea. *British Geological Survey Commissioned Report CR/01/136*.

KENNETT, B. 1983. Seismic wave propagation in stratified media, Cambridge Univ. *Pres., Cambridge*.

KENNETT, B. & KERRY, N. 1979. Seismic waves in a stratified half space. *Geophysical Journal International,* 57**,** 557-583.

KJARTANSSON, E. 1979. Constant Q-wave propagation and attenuation. *Journal of Geophysical Research: Solid Earth,* 84**,** 4737-4748.

KNOT, C. 1899. Reflection and refraction of elastic waves with seismological application. *Philos. Mag,* 5**,** 64-97.

KOLSKY, H. 1956. LXXI. The propagation of stress pulses in viscoelastic solids. *Philosophical magazine,* 1**,** 693-710.

LANDRØ, M. 2001. Discrimination between pressure and fluid saturation changes from time-lapse seismic data. *Geophysics,* 66**,** 836-844.

LINDEBERG, E. 2013. Calculation of thermodynamic properties of CO2, CH4, H2O and their mixtures also including salt with the Excel macro ‘‘CO2 Thermodynamics’’. *SINTEF, Trondheim*.

LOTHE, A.E. & Zweigel, P. 1999. Saline Aquifer CO2 Storage (SACS). Informal annual report 1999 of SINTEF Petroleum Research’s results in work area 1 ‘Reservoir Geology’. *SINTEF Petroleum Research report* 23.4300.00/03/99, 54p. Restricted.

LUMLEY, D. E. 2001. Time-lapse seismic reservoir monitoring. *Geophysics,* 66**,** 50-53.

MAVKO, G., MUKERJI, T. & DVORKIN, J. 1998. Rock physics handbook: Tools for seismic interpretation in porous media. United Kingdom, Cambridge University Press.

MORADI, S. & INNANEN, K. A. 2015. Linearized AVO in viscoelastic media. *SEG Technical Program Expanded Abstracts 2015.* Society of Exploration Geophysicists.

PRIDE, S. 1994. Governing equations for the coupled electromagnetics and acoustics of porous media. *Physical Review B,* 50**,** 15678.

PRIDE, S. R. 2005. Relationships between seismic and hydrological properties. *Hydrogeophysics.* Springer.

PRIDE, S. R., BERRYMAN, J. G. & HARRIS, J. M. 2004. Seismic attenuation due to wave-induced flow. *Journal of Geophysical Research: Solid Earth,* 109.

RAVAZZOLI, C. L. & GÓMEZ, J. L. 2014. Seismic reflectivity in carbon dioxide accumulations: A review. *Carbon sequestration and valorization: InTech***,** 343-360.

REUSS, A. 1929. Berechnung der Flieggrenze yon Mischkristallen auf Grund der Plastizithtsbedingung fiir Einkristalle. *Z. Angew. Math. Mech,* 9.

RUBINO, J., VELIS, D. R. & SACCHI, M. D. 2011. Numerical analysis of wave-induced fluid flow effects on seismic data: Application to monitoring of CO2 storage at the Sleipner field. *Journal of Geophysical Research: Solid Earth,* 116.

RUNDBERG, Y. 1989. *Tertiary sedimentary history and basin evolution of the Norwegian North Sea between 60-62 N-An integrated approach. Dr. ing.* thesis, University of Trondheim, Norway, 308 pp,(reprinted in 1991 in Report 25 Institute for Geology and Rock Mechanics, University of Trondheim).

RUSSELL, B. & HAMPSON, D. 2004. AVO theory. *Hampson-Russell Software Services Ltd***,** 22-26.

SAVIOLI, G. B., SANTOS, J. E., CARCIONE, J. M. & GEI, D. 2016. A model for CO2 storage and seismic monitoring combining multiphase fluid flow and wave propagation simulators. The Sleipner-field case. *Computational Geosciences***,** 1-17.

SIMM, R., BACON, M. & BACON, M. 2014. *Seismic Amplitude: An interpreter's handbook*, Cambridge University Press.

SMITH, G. & GIDLOW, P. 1987. Weighted stacking for rock property estimation and detection of gas. *Geophysical Prospecting,* 35**,** 993-1014.

SPAN, R. & WAGNER, W. 1996. A new equation of state for carbon dioxide covering the fluid region from the triple-point temperature to 1100 K at pressures up to 800 MPa. *Journal of physical and chemical reference data,* 25**,** 1509-1596.

STOVAS, A. & ROGANOV, Y. 2010. Scattering versus intrinsic attenuation in periodically layered media. *Journal of Geophysics and Engineering,* 7**,** 135.

STOVAS, A. & URSIN, B. 2003. Reflection and transmission responses of layered transversely isotropic viscoelastic media. *Geophysical Prospecting,* 51**,** 447-477.

STOVAS, A. & URSIN, B. 2007. Equivalent time-average and effective medium for periodic layers. *Geophysical Prospecting,* 55**,** 871-882.

SUNDVOR, E. (1989). Tolkning av marinseismiske data. Del 1: Refleksjonsseismikk. Jordskjelvstasjonen. Universitetet i Bergen.

TEJA, A. & RICE, P. 1981. Generalized corresponding states method for the viscosities of liquid mixtures. *Industrial & Engineering Chemistry Fundamentals,* 20**,** 77-81.

TORRES, V. 2016. Sensitivity Analysis of AVO and stack of periodic layers responses in partially saturated (CO2 –Brine) sandstone at the Utsira Formation. *Project Report.* Trondheim: Norwegian University of Science and Technology.

TRAUB, B. 2008. CO2ReMoVe – WP 3.4: Sleipner AVO study on synthetic Sleipner data. *SINTEF Petroleum Research Report* 26.6139.00/03/08. Restricted.

URSIN, B. & STOVAS, A. 2002. Reflection and transmission responses of a layered isotropic viscoelastic medium. *Geophysics,* 67**,** 307-323.

VOIGT, W. 1889. Uber die Beziehung zwischen den beiden Elastizitätskonstanten isotroper Körper. Wied. *Ann. v38***,** 573-587.

WANG, Z., CATES, M. E. & LANGAN, R. T. 1998. Seismic monitoring of a CO2 flood in a carbonate reservoir: A rock physics study. *Geophysics,* 63**,** 1604-1617.

WHITE, J. 1975. Computed seismic speeds and attenuation in rocks with partial gas saturation. *Geophysics,* 40**,** 224-232.

WIGGINS, R., KENNY, G. & MCCLURE, C. 1983. A method for determining and displaying the shear-velocity reflectivities of a geologic formation: European Patent Application 0113944.

YAN, H. 2016. Rock Physics Inversion for CO2 Characterization at Sleipner: Sensitivity Tests and Baseline Application. *Project Report.* Trondheim: Norwegian University of Science and Technology.

ZWEIGEL, P., ARTS, R., LOTHE, A. E. & LINDEBERG, E. B. 2004. Reservoir geology of the Utsira Formation at the first industrial-scale underground CO2 storage site (Sleipner area, North Sea). *Geological Society, London, Special Publications,* 233**,** 165-180.

ZWEIGEL, P., HAMBORG, M., ARTS, R., LOTHE, A., SYLTA, Ø. & TØMMERÅS, A. Prediction of migration of CO2 injected into an underground depository: reservoir geology and migration modelling in the Sleipner case (North Sea). 5th International Conference on Greenhouse Gas Control Technologies, Cairns (Australia), 2000.

Appendix ASeismic Attenuation Modelling

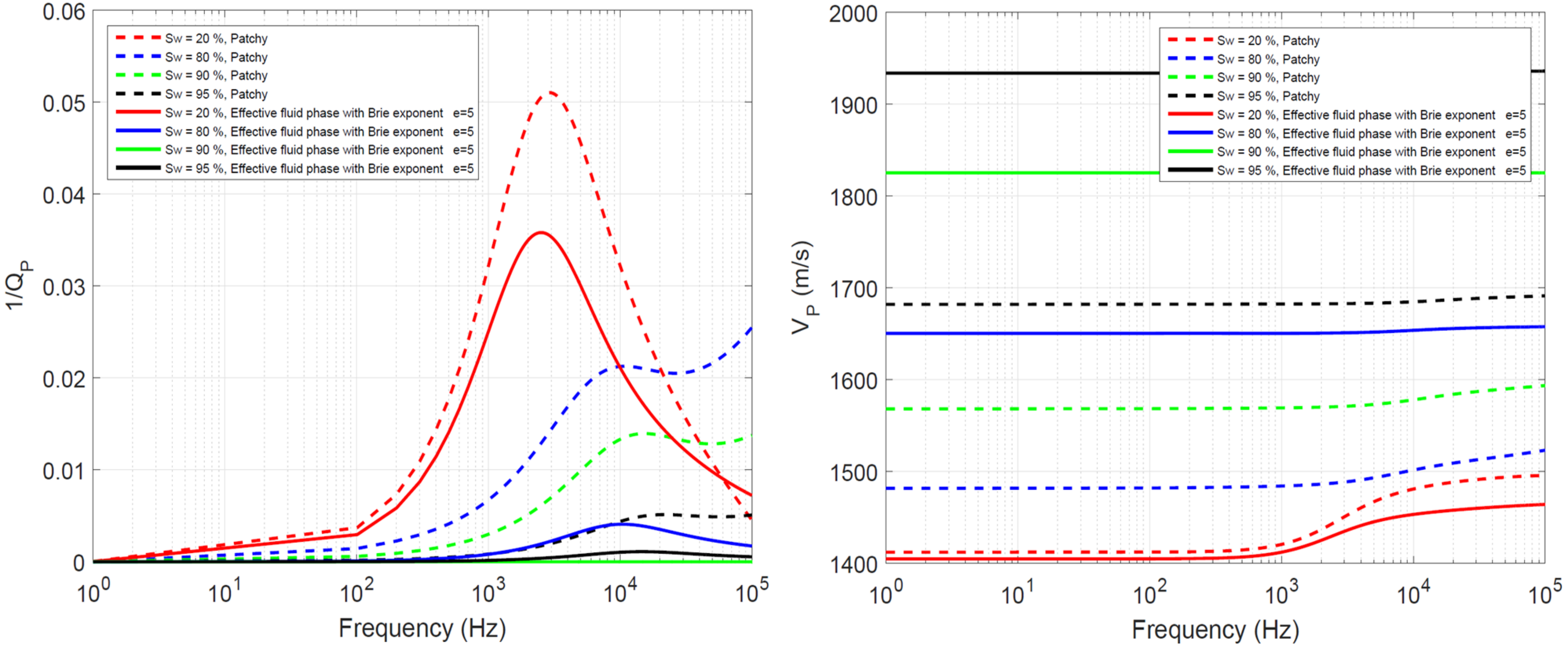

Figure A-1: *P wave attenuation and velocity dispersion as a function of frequency at 20, 80, 90 and 95% Sw for White's and Brie's model of fluid distribution. P wave attenuation (right) and velocity dispersion (left).*

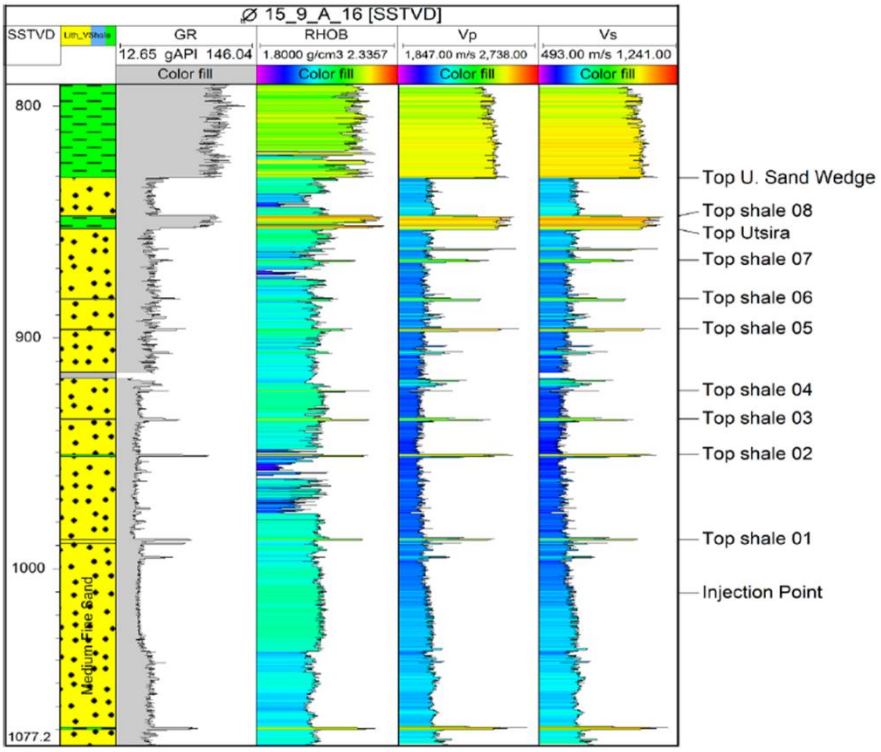

Figure A-2: *Well logs from the injection well 15/9-A-16. From left to right Lithology, Gamma Ray, density, V_p and Vs computed with Vernik's empirical relation and the top interpreted of interlayer shales and sand.*

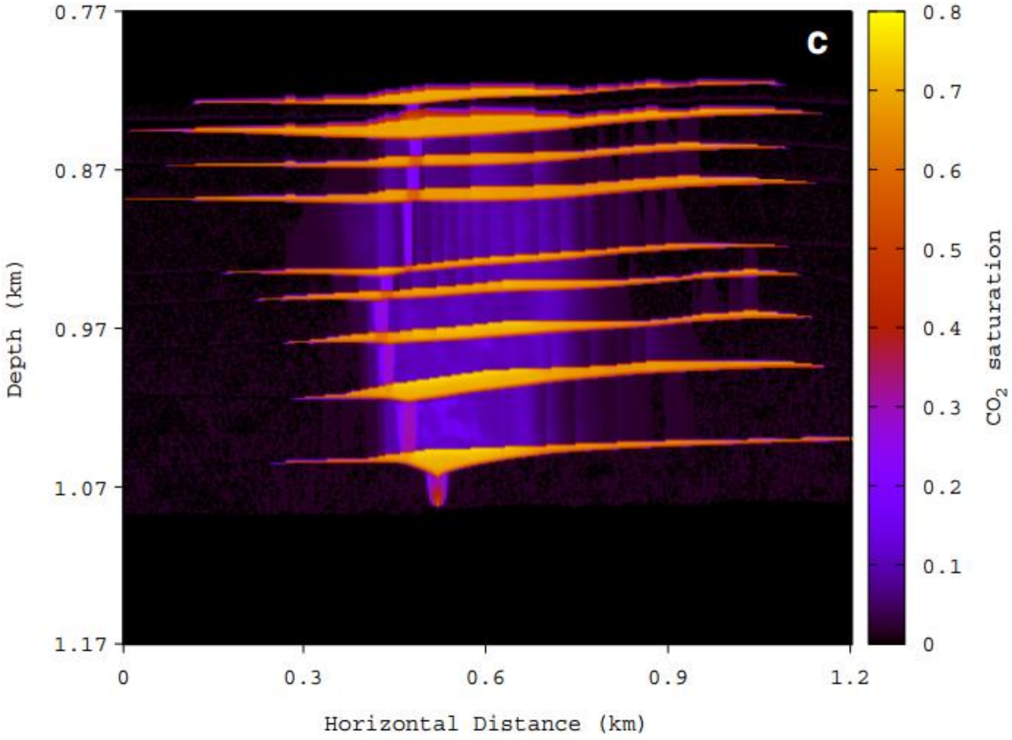

Figure A-3: *CO_2 saturation distribution after 7 years of injection (2003) as a result of the simultaneous CO_2 brine flow simulation with the Black-oil formulation for two phases in a porous media (Savioli et al., 2016).*

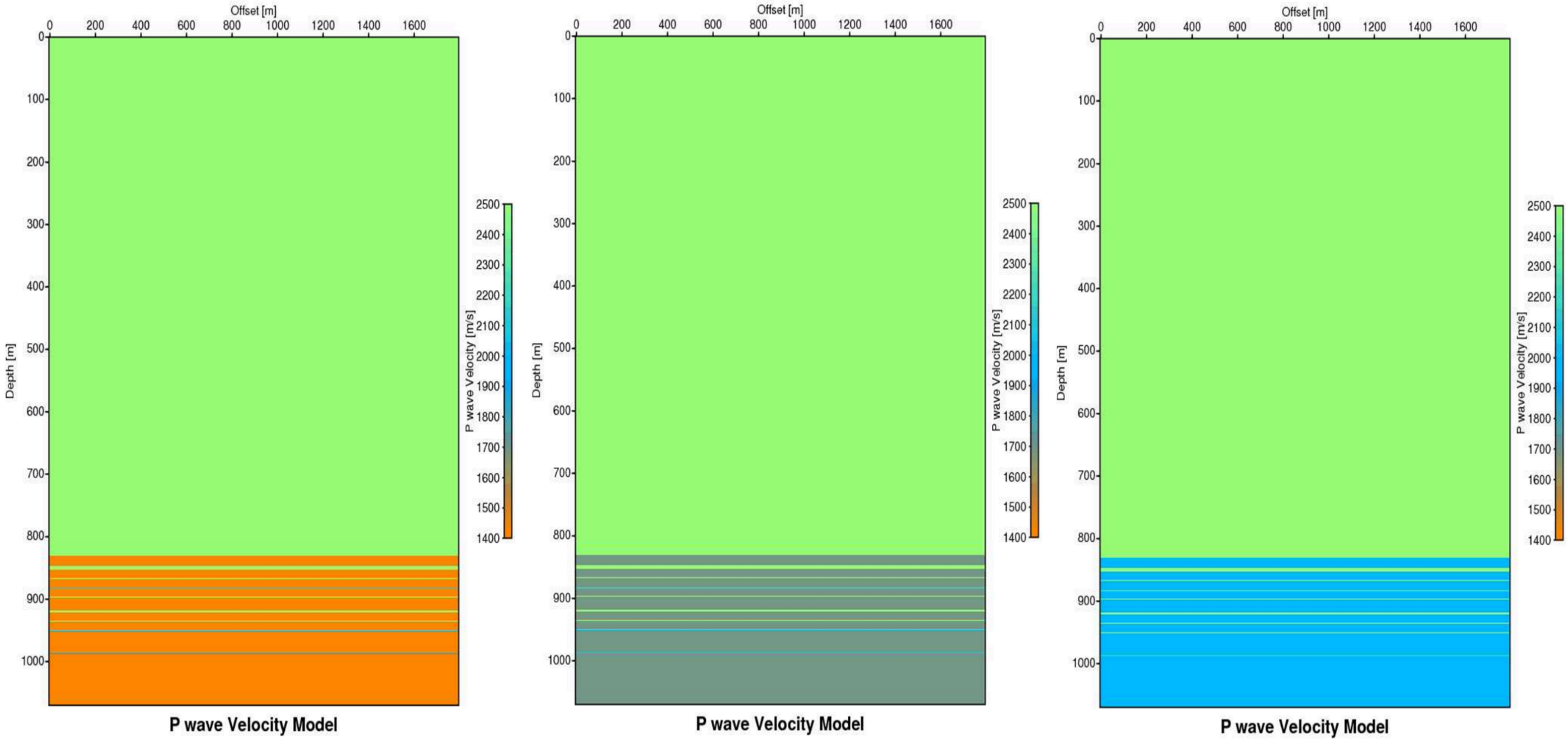

Figure A-4: *P wave velocity models for constant water saturation, from left to right 20, 80 and 95%. Overburden and interlayer shales have the same P wave velocity of 2391.8m/s, sandstone layers with 20%* S_w *have constant velocity of 1404.5m/s, 80% 1650.4m/s and sandstone with 95% water saturation present a constant velocity of 1933m/s.*

Table A-1: Utsira sandstone and its interlayer shale thickness interpreted above the injection point and extracted from 15/9-16A well.

Number of Layers	Lithology	Bottom Depth (m)	Thickness(m)
1	Overburden (Cap-rock Shale)	830.5	830.5
2	Sandstone	847.5	17
3	Inter-layer Shale	853	5.5
4	Sandstone	866	13
5	Inter-layer Shale	867.41	1.41
6	Sandstone	882.75	15.34
7	Inter-layer Shale	883.77	1.02
8	Sandstone	895.82	12.05
9	Inter-layer Shale	897.18	1.36
10	Sandstone	920	22.82
11	Inter-layer Shale	923.5	3.5
12	Sandstone	934.57	11.07
13	Inter-layer Shale	936.28	1.71
14	Sandstone	950.37	14.09
15	Inter-layer Shale	951.84	1.47
16	Sandstone	987.07	35.23
17	Inter-layer Shale	987.76	0.69
18	Sandstone	1070	82.24
	Injection point	1010.6	

Table A-2: Utsira sandstone with variable CO2 saturation and its interlayer shale thickness interpreted above the injection point and extracted from 15/9-16A well.

Number of Layers	**Lithology**	**Base Depth (m)**	**Sand interlayer For CO_2 Saturation (base of the layer)**	**Thickness of each layer**	**CO_2 %**
1	Overburden (Cap-rock Shale)	830.5	830.5	830.5	
			837.5	7	80
2	Sandstone	847.5	847.5	10	20
3	Inter-layer Shale	853	853	5.5	
			860	7	80
4	Sandstone	866	866	6	20
5	Inter-layer Shale	867.41	867.41	1.41	
			872.41	5	80
6	Sandstone	882.75	882.75	10.34	20
7	Inter-layer Shale	883.77	883.77	1.02	
			888.77	5	80
8	Sandstone	895.82	895.82	7.05	20
9	Inter-layer Shale	897.18	897.18	1.36	
			907.18	10	80
10	Sandstone	922	922	14.82	20
11	Inter-layer Shale	923.5	923.5	1.5	
			927.5	4	80
12	Sandstone	934.57	934.57	7.07	20
13	Inter-layer Shale	936.28	936.28	1.71	
			941.28	5	80
14	Sandstone	950.37	950.37	9.09	20
15	Inter-layer Shale	951.84	951.84	1.47	
			966.84	15	80
16	Sandstone	987.07	987.07	20.23	20
17	Inter-layer Shale	987.76	987.76	0.69	
			1002.76	15	80
			1008.6	5.84	20
18	Sandstone	1070	1070	61.4	0

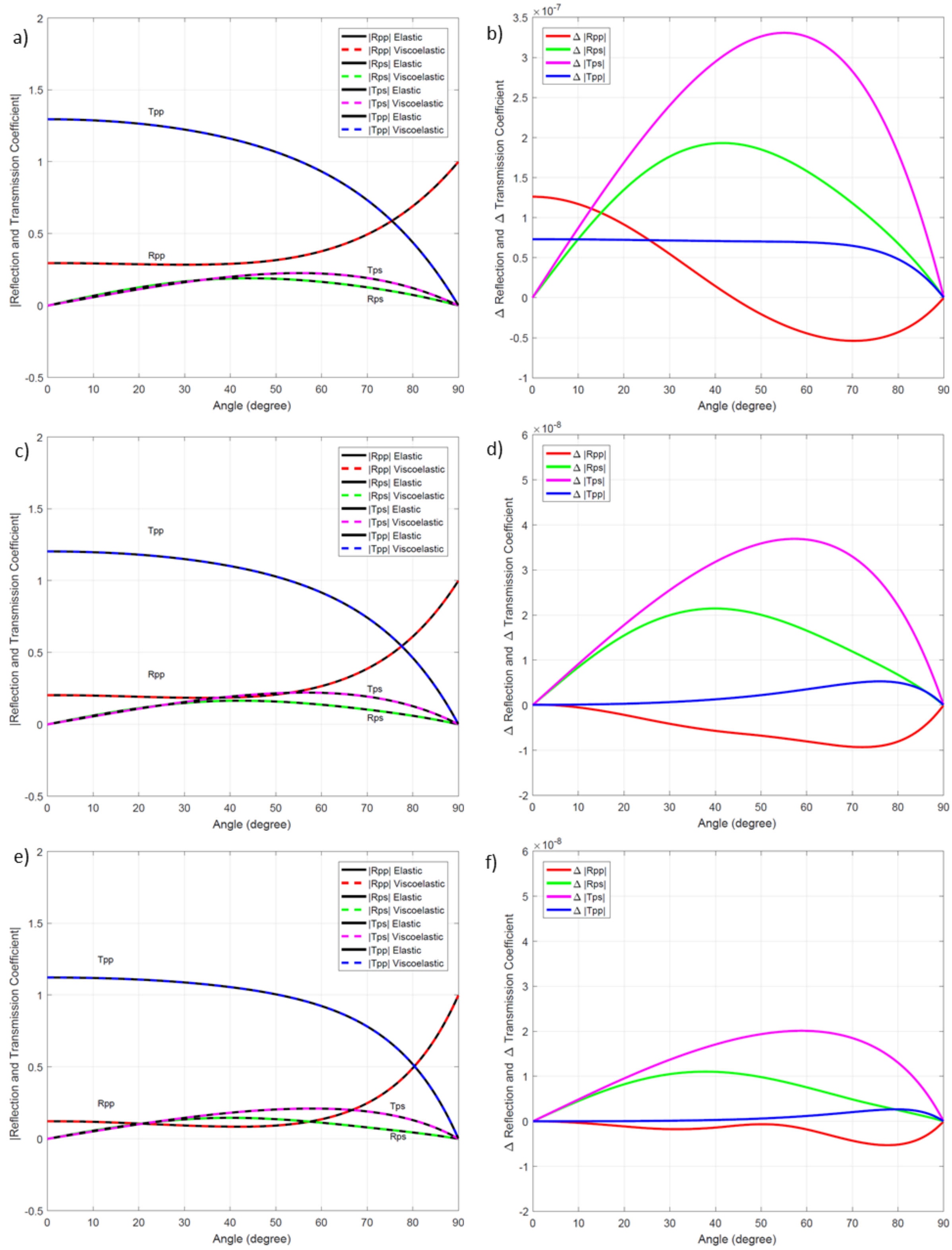

Figure A-5: *Reflection and Transmission coefficient absolute values and their corresponding difference between elastic and viscoelastic case as function of incident angle. From a), c) and e) the absolute value of reflection and transmission coefficients for elastic shale/elastic sand (solid black) and elastic shale/viscoelastic sand (dashed red, blue, green and magenta) at different water saturation levels 20, 80 and 95%, respectively. From b), d) and f) Absolute difference between the reflection and transmission coefficients elastic and viscoelastic case at 20, 80 and 95%* S_w.

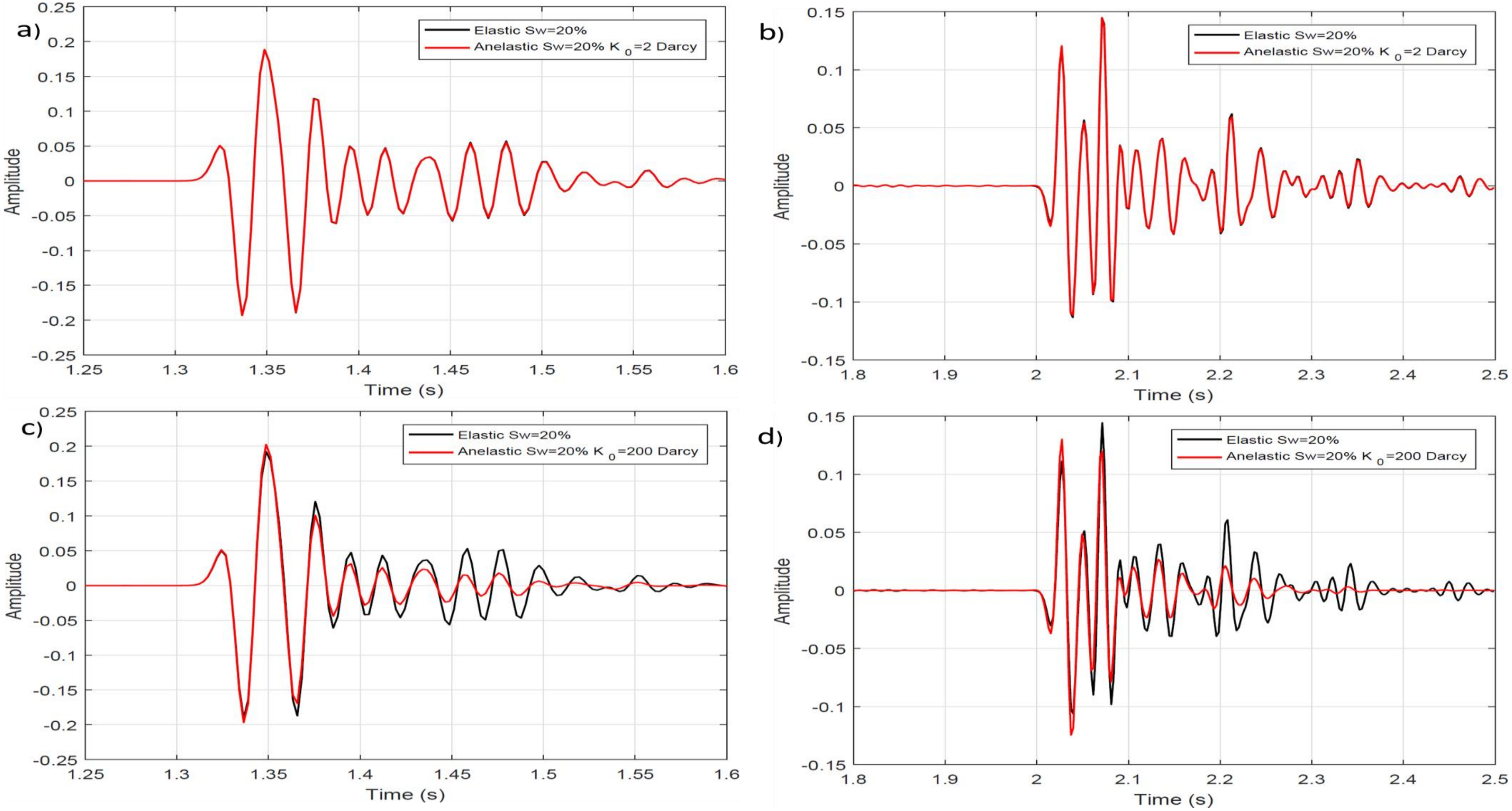

Figure A-6: *Far Trace comparison (trace 65) after the first PP reflection arrivals and the first PS reflection arrivals. Stack of periodic layers at 20% Sw. a) and c) reflection response after the first PP arrival elastic/anelastic for the Utsira sand poroelastic properties and 200 Darcy permeability (shifted attenuation peak). b) and d) reflection response after the first PS arrival elastic/anelastic for the Utsira sand poroelastic properties and 200 Darcy permeability (shifted attenuation peak).*

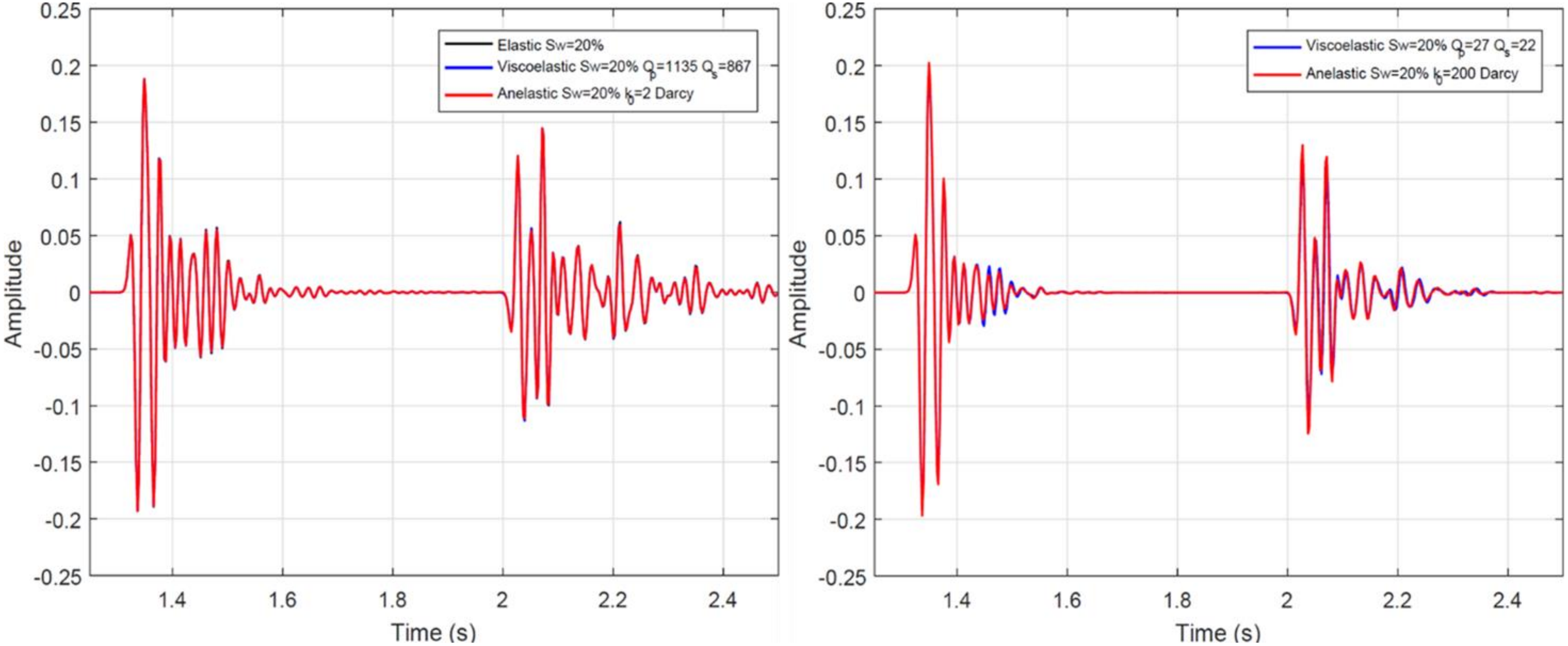

Figure A-7: *Far trace (trace 65) comparison response for elastic/viscoelastic/poroelastic for the Utsira sand reservoir at 20% Sw. Elastic sand (black), viscoelasticity introduced by Qp=1135 and Qs=867 (blue) and poroelastic sand with permeability of 2Darcy (red) all are equivalent to effective seismic properties measured at 30Hz, right panel. Viscoelastic sand with Qp=27 and Qs=22 (blue) and poroelastic sand with permeability of 200 Darcy, for an equivalent attenuation peak shift from 2500Hz to 30Hz, left panel.*

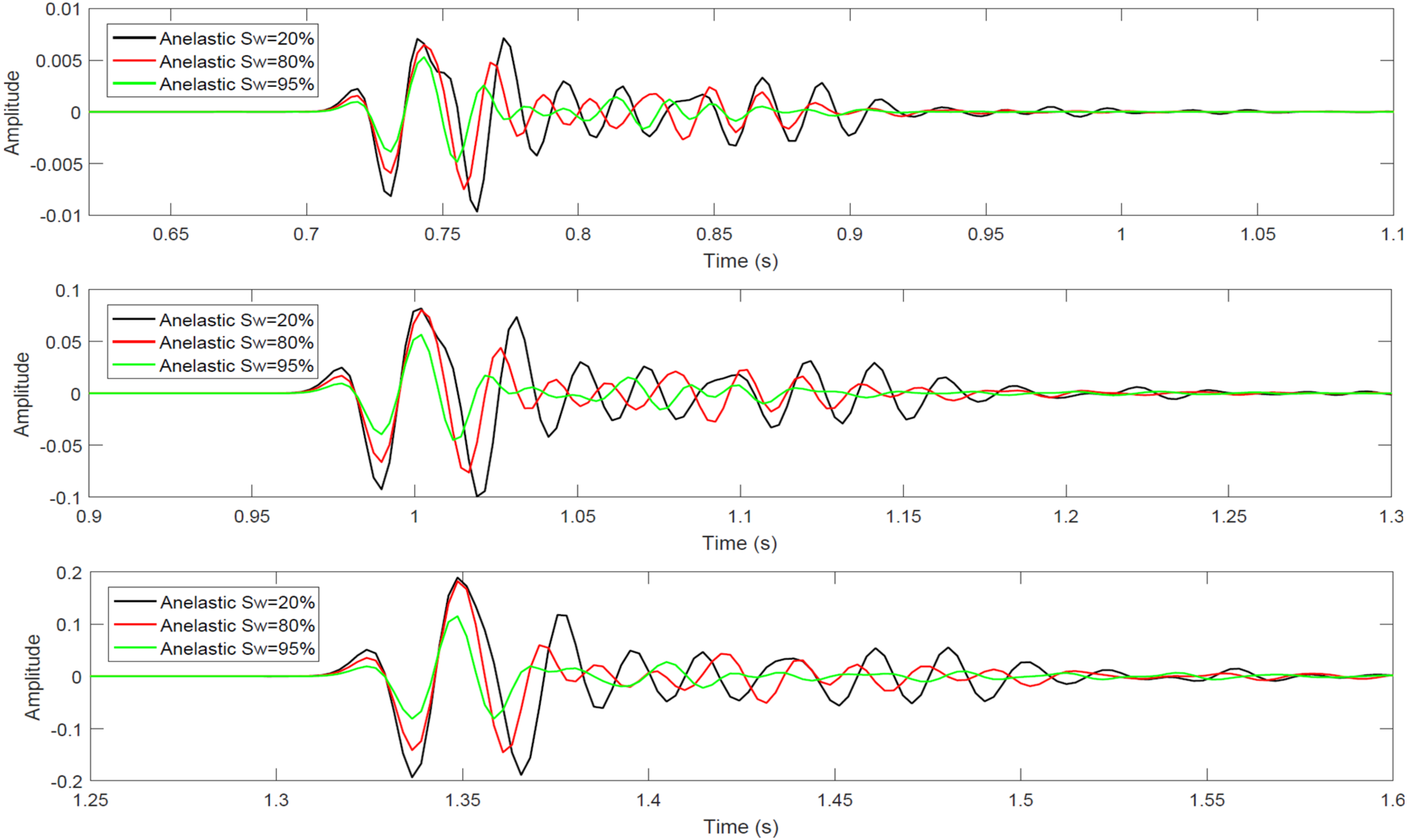

Figure A-8: *Zoom of PP reflection for a near, mid and far traces (5, 35 and 65) at different water saturations 20, 80 and 95% (black, red and green, respectively). Top panel near traces, middle panel mid traces and bottom far trace..*

Appendix B AVO Applications

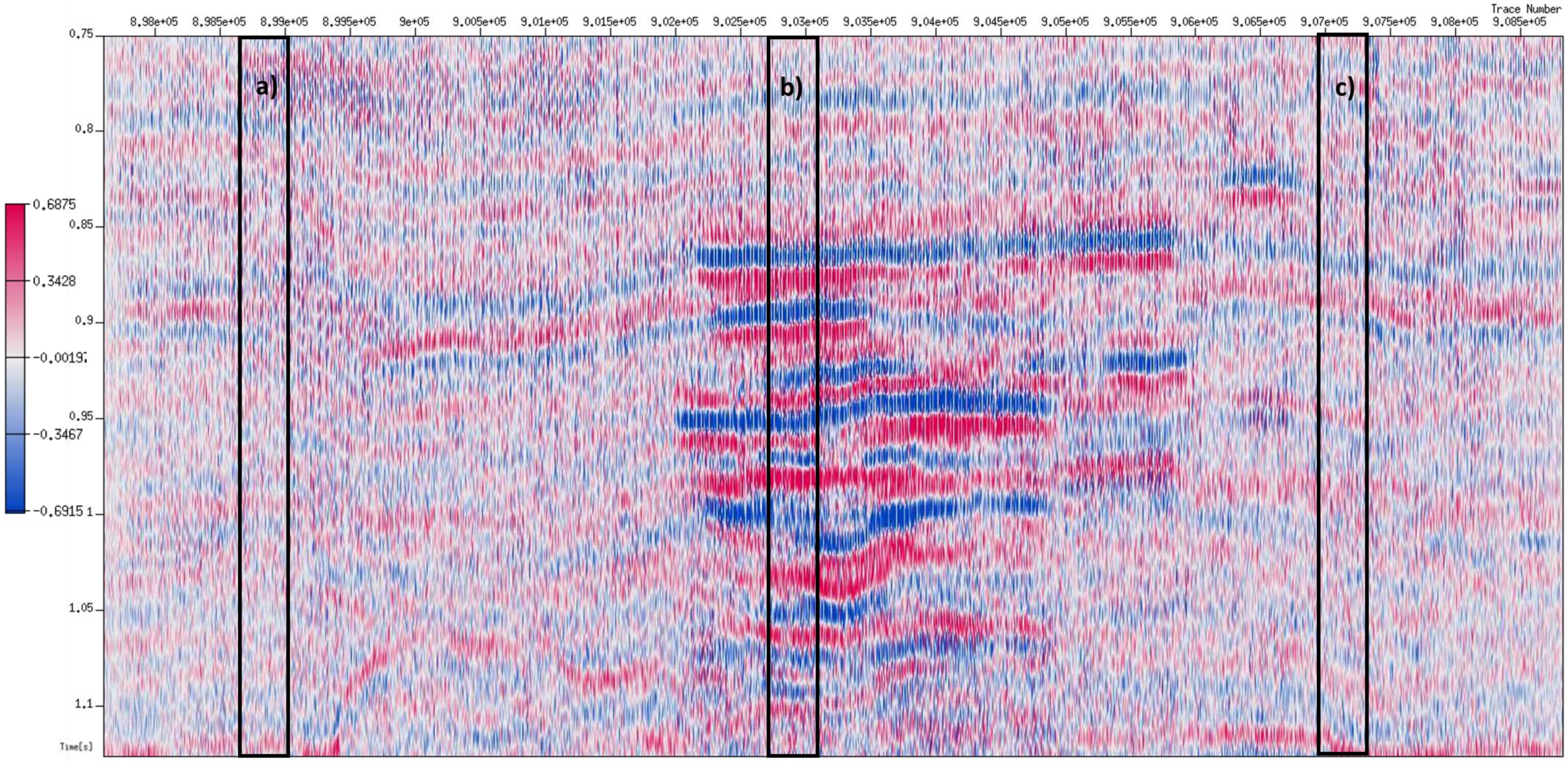

Figure B-1: *PSTM CDP gathers extracted from Inline 1880 within the time window from 0.750s to 1.125s and CDP range from 898 to 1458 (total of 561 CDP).*

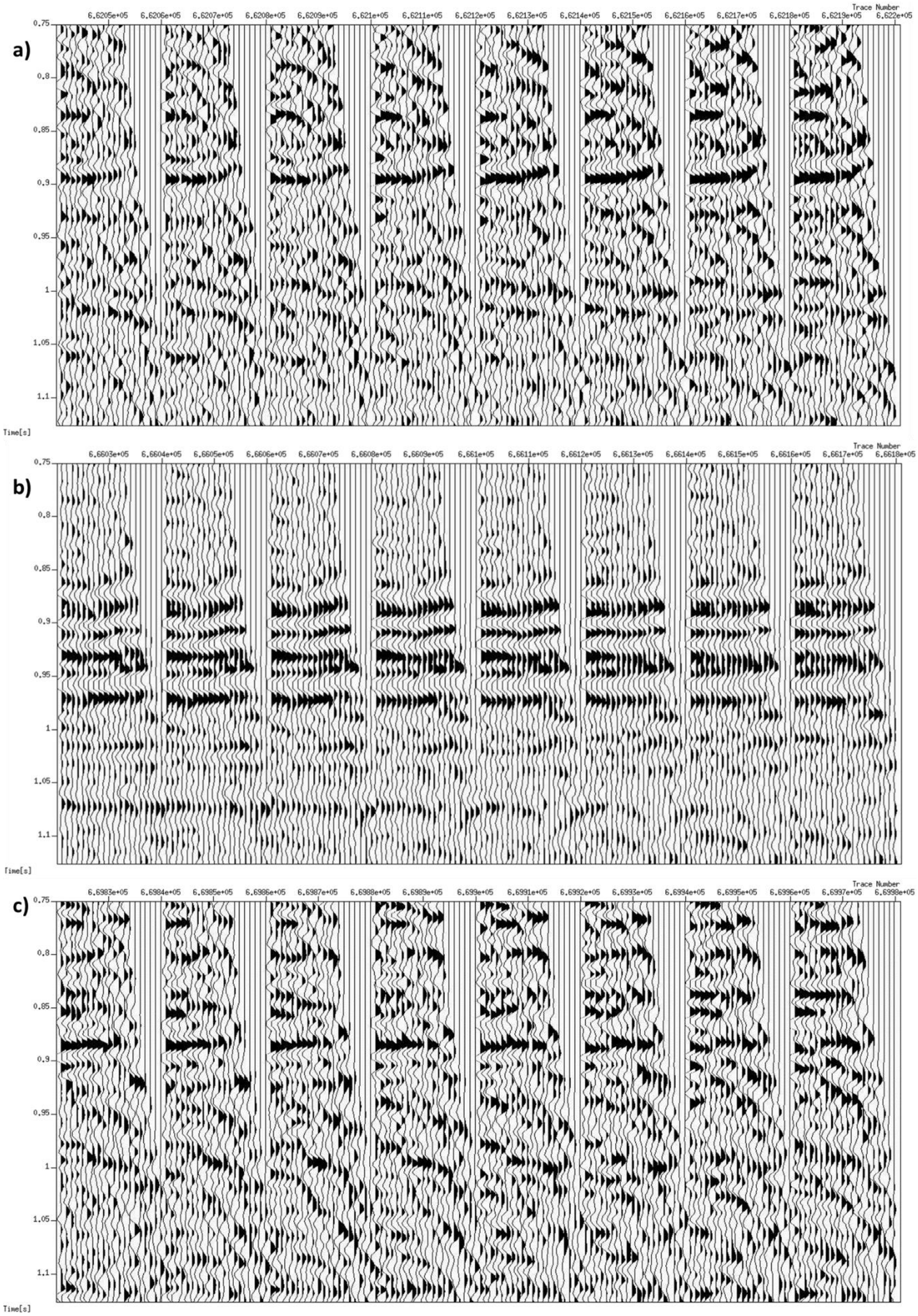

Figure B-2: *PSTM CDP gathers extraction in wiggle display from the Inline 1880.* a) CDP gather range 901-908 at the left hand side of the plume, b) CDP gather range 1160-1167 inside the CO2 plume, c) CDP gather range 1400-1407 at the right hand side of the pume as indicated in Figure B-2

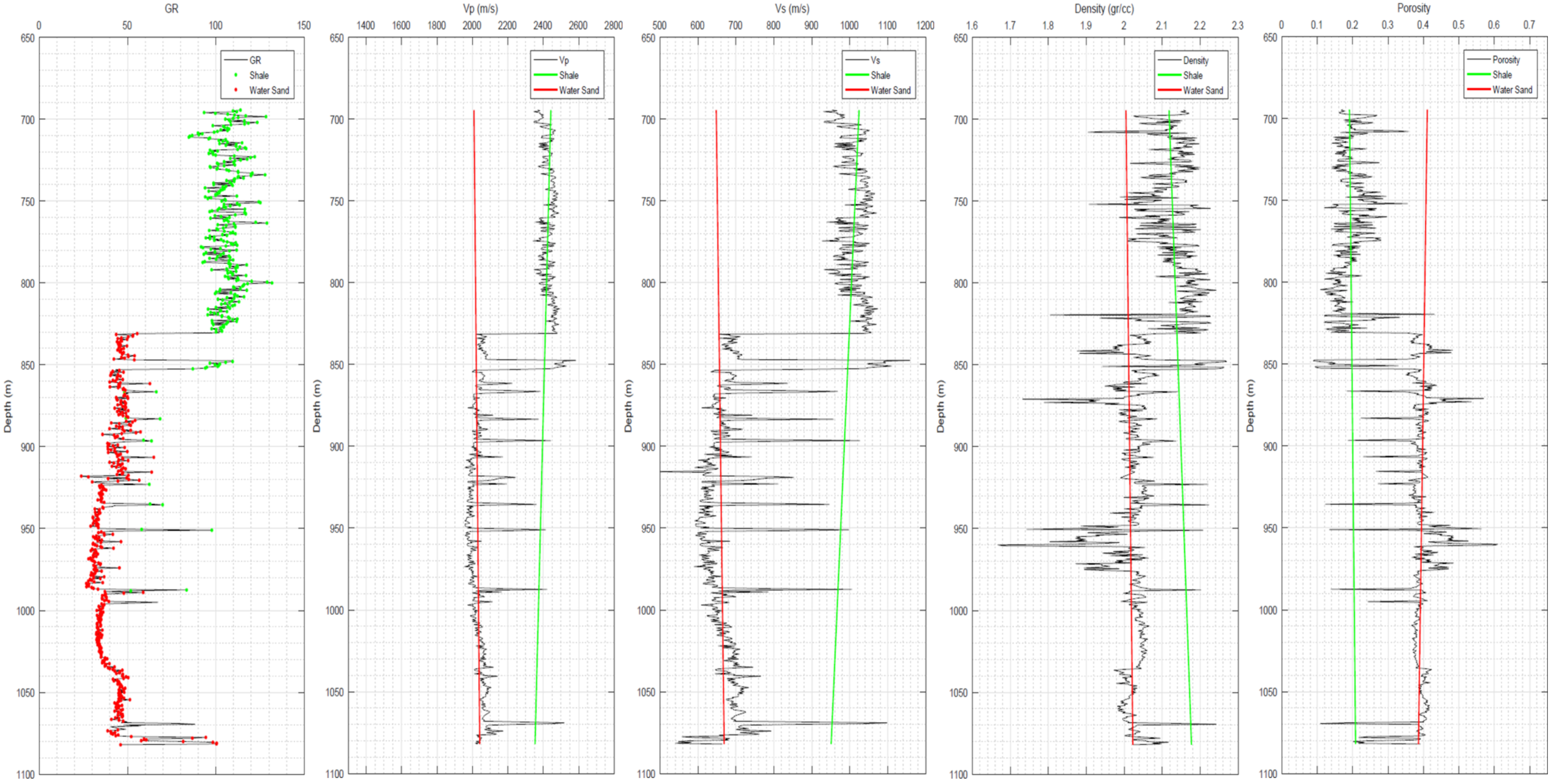

Figure B-3: *Well logs with a regular sampling rate in depth (0.5m) showing the main lithofacies and their corresponding depth trends brine sands and shales (red and Green, respectively). From left to right, GR,* V_P*,* V_S*, Density and total Porosity computed from density.*

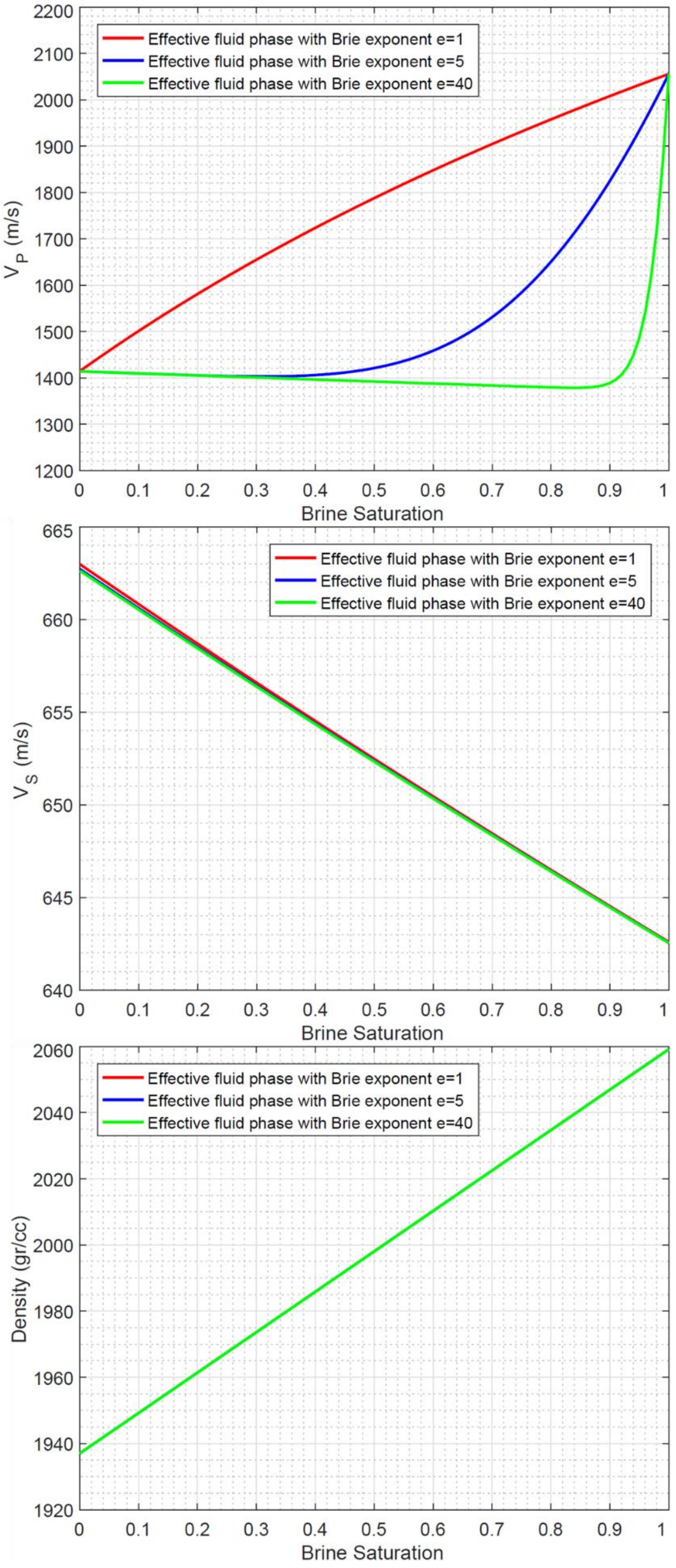

Figure B-4: *Compressional (top), Shear wave velocities (middle) and density (bottom)as a function of S_w for different fluid distributions modelled by using Brie's equation with e exponent equal to 1,5 and 40.*

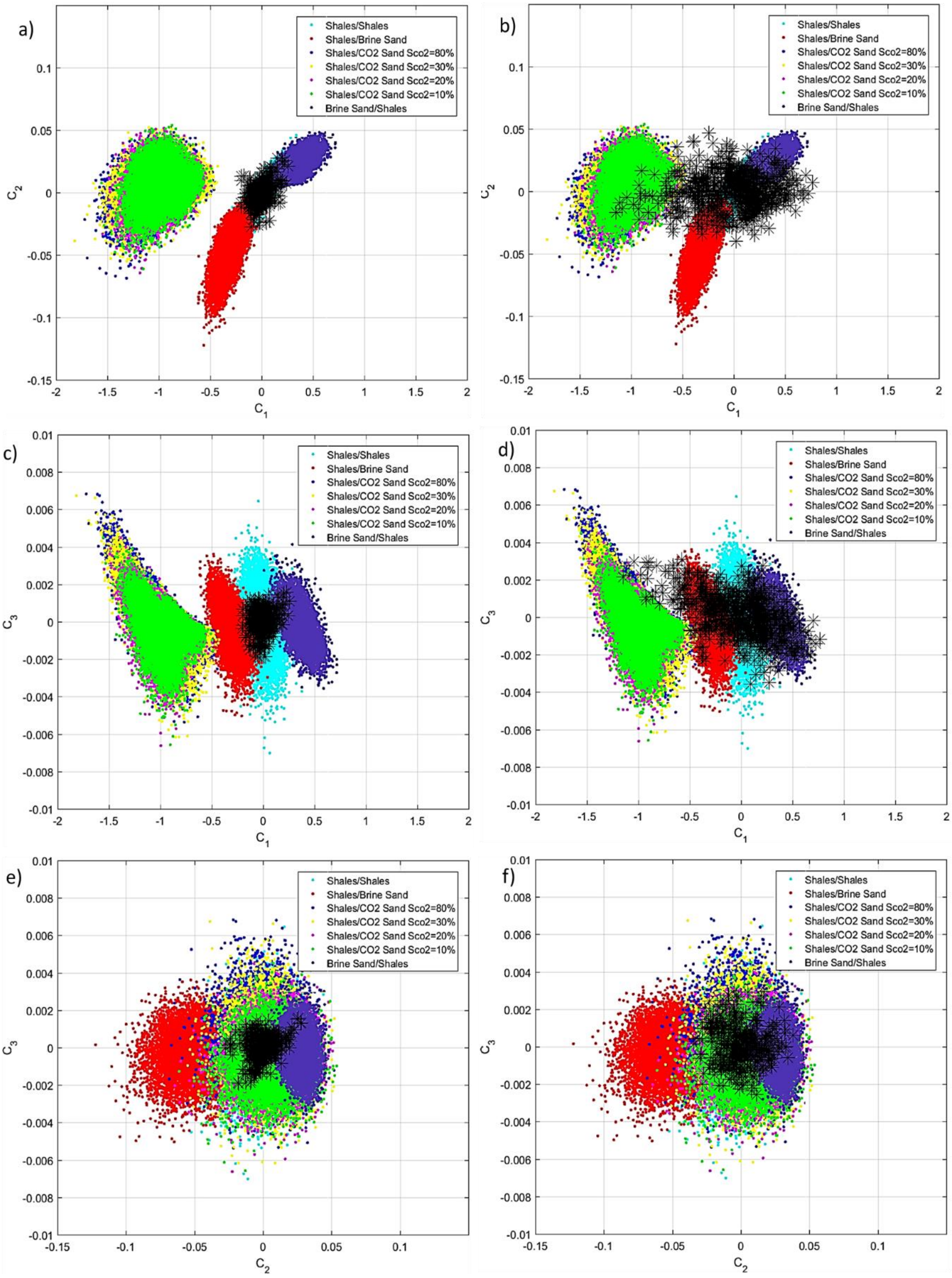

Figure B-5: *Optima AVO cross-plot for Inline 1838 within a time window from 0.85 to 0.96s inside and outside the* CO_2 *plume for Brie e exponent equal 40. a)-c)* C_1*,* C_2 *and* C_3 *cross-plot of CDP gathers outside the plume (900-910). d)-f)* C_1*,* C_2 *and* C_3 *cross-plot of CDP gathers inside the* CO_2 *plume (1100-1110).*

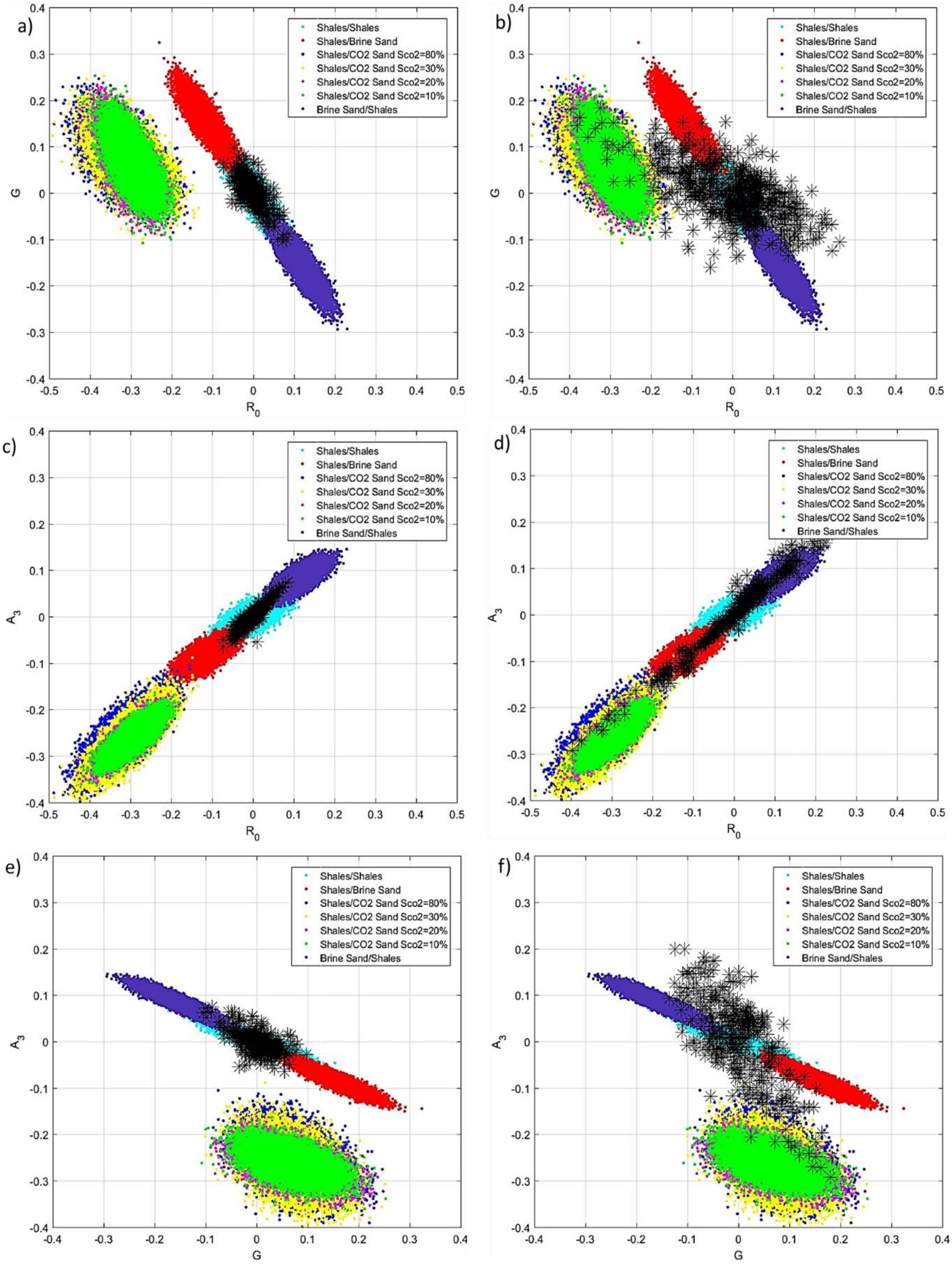

__Figure B-6:__ Convention AVO attributes estimated from C_1, C_2 and C_3 cross-plot for Inline 1838 within a time window from 0.85 to 0.96s inside and outside the CO_2 plume for Brie e exponent equal 40. a)-c) R_0, G and A_3 cross-plot of CDP gathers outside the plume (900-910). d)-f) R_0, G and A_3 cross-plot of CDP gathers inside the CO_2 plume (1100-1110).

Table B-1: Summary of the processing sequence applied to the 3D PSTM vintage 2008.

Processing Sequence and Parameters
Low cut filter (6Hz)
Deterministic zero-phase conversion using far field signature
2 pass swell noise attenuation
Tidal static and gun and cable static correction
Gap deconvolution in the Tau-p domain
Phase, time and amplitude match to baseline survey data
Data binning to match baseline survey
Fold normalization using Tau-p interpolation
Migration velocity analysis

Table B-2: Header ranges for Inline 1880 extracted from a PSTM vintage 2008.

Header Value Range	Min.	Max.
tracl	897601	908820
cdp	898	1458
offset	287m	1712m
sx	438949.49m	439053.70m
sy	6468444.94m	6475444.16m
gx	1880m	1880m
gy	898m	1458m
ns	189	189
dt	2000µs	2000 µs
Total number of traces	11220	11220